



Durham E-Theses

Structural studies of Iron (II) spin crossover compounds

Money, Victoria A.

How to cite:

Money, Victoria A. (2004) *Structural studies of Iron (II) spin crossover compounds*, Durham theses, Durham University. Available at Durham E-Theses Online: <http://etheses.dur.ac.uk/2987/>

Use policy

The full-text may be used and/or reproduced, and given to third parties in any format or medium, without prior permission or charge, for personal research or study, educational, or not-for-profit purposes provided that:

- a full bibliographic reference is made to the original source
- a [link](#) is made to the metadata record in Durham E-Theses
- the full-text is not changed in any way

The full-text must not be sold in any format or medium without the formal permission of the copyright holders.

Please consult the [full Durham E-Theses policy](#) for further details.

A copyright of this thesis rests with the author. No quotation from it should be published without his prior written consent and information derived from it should be acknowledged.

Structural Studies of Iron (II) Spin

Crossover Compounds

Victoria A. Money

Thesis submitted in part fulfilment of the requirements for the degree of

Doctor of Philosophy at the University of Durham



11 JAN 2005

Department of Chemistry
University of Durham
August 2004

Structural Studies of Iron (II) Spin Crossover Complexes

Submitted for the degree of Doctor of Philosophy by Victoria Anne Money

University of Durham

August 2004

Abstract

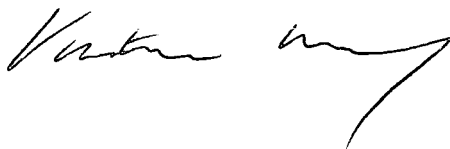
The drive for ever smaller and faster computers has, in recent years, caused much research interest to be focussed on the development of new materials in which individual molecules or assemblies of molecules can be used for information processing. Materials which show spin crossover behaviour have great potential for use not only in molecular computing but also in applications such as optical switches and display devices and are of fundamental interest due to their importance in biological and geological systems. The results of comprehensive variable temperature and excited state crystallographic studies into the spin crossover behaviour of a family of iron (II) spin crossover complexes based on the 2,6-di(pyrazol-1-yl)pyridine ligand are presented herein.

A fascinating aspect of spin crossover materials is their ability to undergo a transition from the low spin state to a metastable high spin state, with a very long lifetime, on irradiation. Crystallographic information on the structure of the metastable high spin state formed as a result of irradiation is very rare. Full structural analyses of the metastable state are reported for $[\text{FeL1}_2](\text{BF}_4)_2$, $[\text{Fe}(\text{L3})_2](\text{BF}_4)_2$, $[\text{Fe}(\text{L3})_2](\text{ClO}_4)_2$ and $[\text{Fe}(\text{L4})_2](\text{BF}_4)_2$ (L1 = 2,6-di(pyrazol-1-yl)pyridine, L3 = 2,6-(dipyrazol-1-yl)-4-hydroxymethylpyridine, L4 = 2,6-di(3-methylpyrazol-1-yl)pyridine). These studies have shown that, unlike other reported materials, the metastable high spin state is structurally identical to that reached as a result of the thermal spin transition. $[\text{Fe}(\text{L4})_2](\text{BF}_4)_2 \cdot \frac{1}{3}\text{H}_2\text{O}$ is shown to have a fascinating complexity of spin crossover behaviour including the existence of a number of metastable states. The effect of dehydration on the spin crossover behaviour has been determined.

Spin crossover compounds are extremely sensitive to changes in pressure; nonetheless there have been very few studies of the effect of pressure on the structure of these materials. The structure of the pressure induced low spin state at ambient temperature and 4.5 kbar is reported for $[\text{FeL1}_2](\text{BF}_4)_2$. The crystallographic results are supported throughout by SQUID magnetometry studies.

Declaration

The work described herein was carried out at the University of Durham between October 2001 and August 2004 under the supervision of Prof. J. K. Howard. Unless otherwise stated all the work is my own and has not been submitted previously for a degree at this or any other university.

A handwritten signature in black ink, appearing to read 'Victoria Anne Money', with a long, sweeping flourish at the end.

Victoria Anne Money

The copyright of this thesis rests with the author. No quotation from it should be published from it without prior consent and information derived from it should be acknowledged

Acknowledgements

My deepest thanks to:

Judith Howard for all her help, support and patience over the last three years, for supervising me when I needed it and standing back and letting me get on with it when I didn't

Malcolm Halcrow and Jerome Elhaïk at Leeds University for providing the fascinating crystals on which this work was carried out

Everyone in Group IX at the ICMCB in Bordeaux for their help with the photomagnetic studies and for making my visits there so very enjoyable, most especially Jean-François Létard, Chiara Carabona, Mathieu Marchivie, Philippe Guionneau, Jose Sánchez Costa and Sylvia Marcén.

Simon Parsons of Edinburgh University for letting me do the high pressure crystallography and Francesca Fabbiani both for her help with the experiments and for looking after me so well.

Andrew Harrison, Konstantin Kamenev and Fiona Coomer, at CSEC University of Edinburgh, for the SQUID studies at raised pressure.

Everyone who has worked in the Durham Crystallography group both past and present for making the last three years such fun. Particularly Ivana for her help, advice and understanding both at the beginning and right to the end and Dima and Andrés for their patience with all my silly machine related questions

My friends both in Durham and elsewhere: Amy and Elinor for providing shoulders to cry on and someone to laugh with whenever either was required; John for never once complaining about driving me round for the last six weeks; Carol and Colin for brightening my Sunday mornings.

My family; Philippa, Geoffrey, Neil and Di for their continued support, particularly my mother for her encouragement and, of course, for cups of coffee and slices of cake

Table of Contents

1. Introduction.....	1
1.1 Introduction to the spin crossover phenomenon	1
1.1.1 What is spin crossover?	1
1.1.2 Spin crossover theory	2
1.1.3 Spin crossover in iron (II)	6
1.1.4 Effect of external factors	6
1.1.5 Principle methods for examination	10
1.2 Introduction to diffraction	13
1.2.1 Diffraction of light	13
1.2.2 Diffraction of X-rays	13
1.2.3 Laue diffraction	14
1.2.4 Bragg diffraction	14
1.3 Introduction to crystallography	15
1.3.1 Single crystal diffraction	15
1.3.2 Powder diffraction	19
1.3.3 Bibliography	24
1.4 References	24
2 Instrumentation and Experimental.....	25
2.1 Single crystal X-ray diffraction	25
2.1.1 Three circle X-ray diffractometers	25
2.1.2 Generation of X-rays	26
2.1.3 Charge coupled device (CCD) detectors	28
2.1.4 Computing	28
2.1.5 Cooling systems	28
2.1.6 LIESST experiments	28
2.2 High pressure crystallography	30
2.2.1 Diamond anvil cell	30
2.2.2 Measuring the pressure in the cell	31
2.2.3 The diffractometer	31
2.2.4 Data collection, reduction and model refinement	32
2.3 High pressure Raman spectroscopy	33
2.4 Powder diffraction	34
2.4.1 Diffractometers	34

2.4.2 Indexing	35
2.4.3 Data Solution	35
2.4.4 Refinement	36
2.5 Magnetometry	36
2.5.1 High pressure SQUID magnetometry	36
2.5.2 Photomagnetic measurements	37
2.6 References	37
3 The thermal, light and pressure induced spin transitions in [FeL₁]₂(BF₄)₂ and related compounds.....	39
3.1 Introduction	39
3.2 Experimental	40
3.2.1 Synthesis	40
3.2.2 Crystallography	40
3.2.3 Variable pressure Raman spectroscopy	40
3.2.4 High pressure SQUID magnetometry	40
3.2.5 Photomagnetic measurements	41
3.3 Results and discussion	41
3.3.1 Variable temperature crystallographic study of [FeL ₁] ₂ (BF ₄) ₂	42
3.3.2 Comparison of [FeL ₁] ₂ (BF ₄) ₂ and [FeL ₁] ₂ (PF ₆) ₂	45
3.3.3 [CoL ₁] ₂ (BF ₄) ₂	46
3.3.4 The LIESST effect in [FeL ₁] ₂ (BF ₄) ₂	49
3.3.5 Investigation of the effect of pressure on the thermal spin transition	54
3.3.6 SQUID magnetometry at raised pressure	59
3.4 Conclusions	60
3.5 References	60
4. A study of the unusual thermal spin transition in [FeL₂]₂(BF₄)₂ and [FeL₂]₂(ClO₄)₂.....	62
4.1 Introduction	62
4.2 Experimental	64
4.2.1 Synthesis	64
4.2.2 Crystallography	64
4.3 Results and discussion	65
4.3.1 Variable temperature crystallographic study	65
4.3.2 The LIESST effect in [FeL ₂] ₂ (BF ₄) ₂ and [FeL ₂] ₂ (ClO ₄) ₂	71
4.4 Conclusions	72

4.5 References	73
5 The thermal and light induced spin transitions in [FeL₃]₂(BF₄)₂ and [FeL₃]₂(ClO₄)₂.....	74
5.1 Introduction	74
5.2 Experimental	75
5.2.1 Synthesis	75
5.2.2 Crystallography	75
5.2.3 Photomagnetic measurements	76
5.3 Results and Discussion	77
5.3.1 Variable temperature crystallographic study	77
5.3.2 The light induced high spin state	80
5.3.3 Photomagnetic study	84
5.4 Conclusions	86
5.5 References	87
6 The spin transition behaviour of [FeL₄]₂(BF₄)₂, [FeL₄]₂(ClO₄)₂ and [FeL₅]₂(ClO₄)₂.....	88
6.1 Introduction	88
6.2 Experimental	89
6.2.1 Synthesis	89
6.2.2 Crystallography	89
6.2.3 Magnetometry	89
6.3 Results and Discussion	90
6.3.1 [FeL ₄] ₂ (ClO ₄) ₂	90
6.3.2 Variable temperature and excited state crystallographic and magnetic studies of [FeL ₄] ₂ (BF ₄) ₂ ·xH ₂ O	95
6.3.3 Variable temperature crystallographic study of [FeL ₄] ₂ (BF ₄) ₂	100
6.3.4 Variable temperature and excited state crystallographic study of [FeL ₄] ₂ (BF ₄) ₂ ·½H ₂ O	107
6.3.5 [FeL ₅] ₂ (ClO ₄) ₂	117
6.4 Conclusions	122
7 The thermal and light induced spin transitions in [FeL₆]₂(BF₄)₂ and [FeL₆]₂(ClO₄)₂ studied by powder X-ray diffraction and SQUID magnetometry.....	124
7.1 Introduction	124
7.2 Experimental	125

7.2.1 Synthesis	125
7.2.2 Variable temperature X-ray powder diffraction	125
7.2.3 Photomagnetism	125
7.3 Results and Discussion	126
7.3.1 The structure of $[\text{FeL}_6]_2(\text{ClO}_4)_2$ at room temperature in the high spin state	126
7.3.2 Variable temperature powder X-ray diffraction study of $[\text{FeL}_6]_2(\text{ClO}_4)_2$	130
7.3.3 $[\text{FeL}_6]_2(\text{BF}_4)_2$	132
7.3.4 Photomagnetic Studies	135
7.4 Conclusions	138
7.5 References	139
8 Conclusions and Perspectives.....	140
8.1 Conclusions	140
8.2 Future perspectives	143
8.3 References	146
Appendix A: Selected crystallographic parameters.....	148
A1 $[\text{FeL}_1]_2(\text{BF}_4)_2$	148
A2 $[\text{FeL}_1]_2(\text{PF}_6)_2$	156
A3 $[\text{CoL}_1]_2(\text{BF}_4)_2$	160
A4 $[\text{FeL}_2]_2(\text{BF}_4)_2$	164
A5 $[\text{FeL}_2]_2(\text{ClO}_4)_2$	169
A6 $[\text{FeL}_3]_2(\text{BF}_4)_2$	174
A7 $[\text{FeL}_3]_2(\text{ClO}_4)_2$	180
A8 $[\text{FeL}_4]_2(\text{ClO}_4)_2$	186
A9 $[\text{FeL}_4]_2(\text{BF}_4)_2$	192
A10 $[\text{FeL}_4]_2(\text{BF}_4)_2 \cdot \frac{1}{3}\text{H}_2\text{O}$	200
A11 $[\text{FeL}_5]_2(\text{ClO}_4)_2$	221
A12 $[\text{FeL}_6]_2(\text{BF}_4)_2$	224
Appendix B: Courses, Seminars and Conferences.....	226
Appendix C: Publications.....	228

List of Tables

Table 1.1: The fourteen Bravais lattices with their restrictions	16
Table 3.1: Crystallographic data for $[\text{FeL1}_2](\text{BF}_4)_2$.	41
Table 3.2: Selected parameters for $[\text{FeL1}_2](\text{BF}_4)_2$	43
Table 3.3: Selected parameters for $[\text{FeL1}_2](\text{PF}_6)_2$	45
Table 3.4: Selected crystallographic parameters for $[\text{FeL1}_2](\text{PF}_6)_2$	46
Table 3.5: Selected parameters for $[\text{CoL1}_2](\text{BF}_4)_2$	47
Table 3.6: Selected crystallographic parameters for $[\text{CoL1}_2](\text{BF}_4)_2$	48
Table 3.7: Selected crystallographic parameters for $[\text{FeL1}_2](\text{BF}_4)_2$ 0 kbar and 4.5 kbar	56
Table 3.8: Effect of increased pressure on the thermal transition of $[\text{FeL1}_2](\text{BF}_4)_2$	59
Table 4.1: Crystallographic data for $[\text{FeL2}_2](\text{BF}_4)_2$ at 290 K, 270 K, 240 K and 30 K	63
Table 4.2: Crystallographic data for $[\text{FeL2}_2](\text{ClO}_4)_2$ at 290 K, 210 K, 180 K and 30 K	64
Table 4.3: Selected parameters for $[\text{FeL2}_2](\text{BF}_4)_2$ and $[\text{FeL2}_2](\text{ClO}_4)_2$	68
Table 5.1: Selected crystallographic parameters for $[\text{FeL3}_2](\text{BF}_4)_2$	75
Table 5.2: Selected crystallographic parameters for $[\text{FeL3}_2](\text{ClO}_4)_2$	76
Table 5.3: Selected parameters for $[\text{FeL3}_2](\text{BF}_4)_2$ and $[\text{FeL3}_2](\text{ClO}_4)_2$	78
Table 6.1: Selected crystallographic parameters for $[\text{FeL4}_2](\text{ClO}_4)_2$	90
Table 6.2: Selected molecular parameters for $[\text{FeL4}_2](\text{ClO}_4)_2$	91
Table 6.3: Selected crystallographic parameters for $[\text{FeL4}_2](\text{BF}_4)_2$ at 200 K, 130 K and 90 K	102
Table 6.4: Selected molecular parameters for $[\text{FeL4}_2](\text{BF}_4)_2$	104
Table 6.5: Selected crystallographic parameters for $[\text{FeL4}_2](\text{BF}_4)_2 \cdot \frac{1}{3}\text{H}_2\text{O}$ at 200 K, 130 K and 90 K	108
Table 6.6: Selected parameters for $[\text{FeL4}_2](\text{BF}_4)_2 \cdot \frac{1}{3}\text{H}_2\text{O}$	109
Table 6.7a: Selected crystallographic parameters for $[\text{FeL4}_2](\text{BF}_4)_2 \cdot \frac{1}{3}\text{H}_2\text{O}$ after flash freezing and cooling to 30 K	112
Table 6.7b: Selected crystallographic parameters for $[\text{FeL4}_2](\text{BF}_4)_2 \cdot \frac{1}{3}\text{H}_2\text{O}$ after irradiation and cooling from 100 K	113
Table 6.8: Selected parameters for $[\text{FeL4}_2](\text{BF}_4)_2 \cdot \frac{1}{3}\text{H}_2\text{O}$	114
Table 6.9: Selected crystallographic parameters for $[\text{FeL5}_2](\text{ClO}_4)_2$	117
Table 6.10: Selected parameters for $[\text{FeL5}_2](\text{ClO}_4)_2$	119
Table 7.1: Details of the GSAS refinement and selected crystallographic parameters for $[\text{FeL6}_2](\text{BF}_4)_2$ in the HS-1 state at room temperature	128

Table of Figures

Figure 1.1: Splitting of d orbitals caused by exposure to an octahedral field	2
Figure 1.2: Diagrams of possible thermal spin transition behaviour	3
Figure 1.3: Scheme of the mechanism for LIESST and reverse-LIESST	8
Figure 1.4: Diagram of Bragg's Law	15
Figure 2.1: The Bruker SMART 1000 diffractometer.	26
Figure 2.2: The new laser mount and focussing system	29
Figure 2.3: Diagram of the Merrill - Bassett diamond anvil cell	30
Figure 2.4: The diamond anvil cell in place on the diffractometer	32
Figure 2.5: The pressure cell used for the SQUID measurements at raised pressure.	36
Figure 3.1: L1 = 2,6-di(pyrazol-1-yl)pyridine	39
Figure 3.2: Crystal structure of $[\text{FeL}_1]_2^{2+}$ at 30 K in the low spin state.	42
Figure 3.3: Variation of unit cell volume with temperature for $[\text{FeL}_1]_2(\text{BF}_4)_2$	44
Figure 3.4: Variation of unit cell volume with temperature $[\text{CoL}_1]_2(\text{BF}_4)_2$	47
Figure 3.5: Two views of the overlay of HS-1 and HS-2 of $[\text{FeL}_1]_2(\text{BF}_4)_2$	50
Figure 3.6: Temperature dependence of $\chi_M T$ for $[\text{Fe}(\text{L}1)]_2(\text{BF}_4)_2$	52
Figure 3.7: The 2,6-di(pyrazol-3-yl)pyridine ligand	53
Figure 3.8: Raman spectra of $[\text{FeL}_1]_2(\text{BF}_4)_2$ with increasing pressure	54
Figure 3.9: The spin transition moving through the crystal at 4.5 kbar	55
Figure 3.10: The structure of the $[\text{FeL}_1]_2^{2+}$ in the low spin state at 4.5 kbar	57
Figure 3.11: Overlay of the ambient pressure and 4.5 kbar structures of $[\text{FeL}_1]_2(\text{BF}_4)_2$	57
Figure 3.12: Overlay of the low spin states of $[\text{FeL}_1]_2(\text{BF}_4)_2$ at 4.5 kbar and 30 K	58
Figure 4.1: 2,6-di(pyrazol-1-yl)pyridine and 2,6-di(3-methylpyrazol-1-yl)pyrazine	62
Figure 4.2: Temperature dependence of $\chi_M T$ for $[\text{FeL}_2]_2(\text{BF}_4)_2$ and $[\text{FeL}_2]_2(\text{ClO}_4)_2$	63
Figure 4.3: Structure of $[\text{FeL}_2]_2(\text{BF}_4)_2$ and $[\text{FeL}_2]_2(\text{ClO}_4)_2$ at 30 K	65
Figure 4.4: Crystal packing in $[\text{FeL}_2]_2(\text{BF}_4)_2$ and $[\text{FeL}_2]_2(\text{ClO}_4)_2$ at 30 K	67
Figure 4.5: Overlay of the high and low spin states	69
Figure 4.6: Variation of unit cell parameters with temperature	70
Figure 5.1: L3 = 2,6-(dipyrazol-1-yl)-4-hydroxymethylpyridine	74
Figure 5.2: $[\text{FeL}_3]_2^{2+}$ at 30 K in the low spin state	77
Figure 5.3: Crystal packing in the LS state for $[\text{FeL}_3]_2(\text{BF}_4)_2$ and $[\text{FeL}_3]_2(\text{ClO}_4)_2$	79
Figure 5.4: Variation of unit cell volume with temperature	80
Figure 5.5: An overlay of the LS and HS-2 states at 30 K for $[\text{FeL}_3]_2^{2+}$	81
Figure 5.6: Overlay of the structure of the HS-1 and HS-2 states	83
Figure 5.7: Temperature dependence of $\chi_M T$ for $[\text{FeL}_3]_2(\text{BF}_4)_2$ and $[\text{FeL}_3]_2(\text{ClO}_4)_2$	84

Figure 5.8: LITH experiment for $[\text{FeL}_3](\text{BF}_4)_2$ and $[\text{FeL}_3](\text{ClO}_4)_2$	85
Figure 6.1: 2,6-di(3-methylpyrazol-1-yl)pyridine, 2,6-di(4-methylpyrazol-1-yl)pyridine	88
Figure 6.2: Structure of the cations in $[\text{FeL}_4](\text{ClO}_4)_2$ at 290 K, 120 K and 30 K	92
Figure 6.3: Isotropic refinement of $[\text{FeL}_4](\text{ClO}_4)_2$ at 290 K and 30 K	93
Figure 6.4: Variation of unit cell volume with temperature for $[\text{FeL}_4](\text{ClO}_4)_2$	94
Figure 6.5: Thermal spin transition of $[\text{FeL}_4](\text{BF}_4)_2 \cdot x\text{H}_2\text{O}$	96
Figure 6.6: Effect of thermal quenching on $[\text{FeL}_4](\text{BF}_4)_2 \cdot x\text{H}_2\text{O}$	97
Figure 6.7: The effect of quenching to 100 K on $[\text{FeL}_4](\text{BF}_4)_2 \cdot x\text{H}_2\text{O}$	98
Figure 6.8: The LIESST effect in $[\text{FeL}_4](\text{BF}_4)_2 \cdot x\text{H}_2\text{O}$	99
Figure 6.9: Structure of the cation of $[\text{FeL}_4](\text{BF}_4)_2$ at 200 K	100
Figure 6.10: Packing diagram for $[\text{FeL}_4](\text{BF}_4)_2$ at 200 K in the high spin state	101
Figure 6.11: Packing diagram for $[\text{FeL}_4](\text{BF}_4)_2$ at 130 K in the mixed spin state	101
Figure 6.12: The three independent cations of $[\text{FeL}_4](\text{BF}_4)_2$ at 130 K	103
Figure 6.13: a) Overlay of the low spin cation with the fully high spin cation b) Overlay of the high spin cation with the 20% low spin cation	105 105
Figure 6.14: Overlay of the high spin cation at 200 K and the high spin cation at 130 K	106
Figure 6.15: Evolution of unit cell volume with temperature for $[\text{FeL}_4](\text{BF}_4)_2$	106
Figure 6.16: Overlay of the low spin state at 90 K with the low spin cation at 130 K	107
Figure 6.17: Structure of the cation of $[\text{FeL}_4](\text{BF}_4)_2 \cdot \frac{1}{3}\text{H}_2\text{O}$ at 200 K	109
Figure 6.18: Packing diagram of $[\text{FeL}_4](\text{BF}_4)_2 \cdot \frac{1}{3}\text{H}_2\text{O}$ at 200 K	110
Figure 6.19: Overlay of the structure of the hydrated and dehydrated cations at 200 K	111
Figure 6.20: Overlay of the high spin state of $[\text{FeL}_4](\text{BF}_4)_2 \cdot \frac{1}{3}\text{H}_2\text{O}$ at 30 K after irradiation and at 200 K	114
Figure 6.21: Overlay of the HS-2 structure of $[\text{FeL}_4](\text{BF}_4)_2 \cdot \frac{1}{3}\text{H}_2\text{O}$ after flash freezing and after irradiation of the crystal at 30 K	115
Figure 6.22: Structure of the cation of $[\text{FeL}_4](\text{BF}_4)_2 \cdot \frac{1}{3}\text{H}_2\text{O}$ in the LS state at 30 K	115
Figure 6.23: Structure of the cation of $[\text{FeL}_4](\text{BF}_4)_2 \cdot \frac{1}{3}\text{H}_2\text{O}$ in the LS state at 30 K	116
Figure 6.24: Overlay of the LS cation from the mixed spin state of $[\text{FeL}_4](\text{BF}_4)_2 \cdot \frac{1}{3}\text{H}_2\text{O}$ and the primarily LS state at 30 K	117
Figure 6.25: L5 = 2,6-di(4-methylpyrazol-1-yl)pyridine	118
Figure 6.26: The structure of the cation of $[\text{FeL}_5](\text{ClO}_4)_2$ in the HS-1 state at 250 K	118
Figure 6.27: Diagram of the packing of $[\text{FeL}_5](\text{ClO}_4)_2$ at 250 K in the HS-1 state	119
Figure 6.28: Diagram of the packing of $[\text{FeL}_5](\text{ClO}_4)_2$ at 30 K in the LS state	120
Figure 6.29: Temperature dependence of $\chi_M T$ for $[\text{FeL}_5](\text{ClO}_4)_2$	122
Figure 7.1: 2,6-dipyrazol-1-ylpyridine and 2,6-dipyrazol-1-ylpyrazine	124
Figure 7.2: Final Rietveld plot for $[\text{FeL}_6](\text{ClO}_4)_2$ in the HS-1 state	127
Figure 7.3: Crystal structure of $[\text{FeL}_6](\text{ClO}_4)_2$ at room temperature in the HS-1 state	129

Figure 7.4: The crystal packing in $[\text{FeL6}_2](\text{ClO}_4)_2$ in the HS-1 state at room temperature	130
Figure 7.5: The evolution of the powder pattern with temperature for $[\text{FeL6}_2](\text{ClO}_4)_2$	131
Figure 7.6: Evolution of unit cell volume with temperature for $[\text{FeL6}_2](\text{ClO}_4)_2$	132
Figure 7.7: Structure of $[\text{FeL6}_2](\text{BF}_4)_2$ in the low spin state at 120 K	133
Figure 7.8: The crystal packing in $[\text{FeL6}_2](\text{BF}_4)_2$ in the low spin state at 120 K	134
Figure 7.9: Temperature dependence of $\chi_M T$ for $[\text{FeL6}_2](\text{BF}_4)_2$ and $[\text{FeL6}_2](\text{ClO}_4)_2$	135
Figure 7.10: LITH experiment for $[\text{FeL6}_2](\text{BF}_4)_2$ and $[\text{FeL6}_2](\text{ClO}_4)_2$	137
Figure 8.1: Example of a potential target for future work	144

List of abbreviations

°	degrees
2-pic	2-(aminomethyl)pyridine
Å	angstrom
B.M	Born Magnaton
bpp	2,6-di(pyrazol-3-yl)pyridine
CCD	charge coupled device
cm	centimetre
cos	cosine
CSEC	Centre for Science at Extreme Conditions
Δ_i	$ F_o _i - F_c _i$ or $F_{o,i}^2 - F_{c,i}^2$
ΔV_{SC}	volume change on going through the spin transition
d	spacing between Miller indices
D_c	calculated density
DSC	differential scanning calorimetry
EDR	Enhanced Dynamic Range
ESRF	European Synchrotron Radiation Facility
F_o	observed structure factor
F_c	calculated structure factor
F_{hkl}	structure factor
f_j	atomic scattering factor
G	Gibbs Free Energy
g	gram
GOF	goodness of fit
H	Enthalpy
hkl	Miller indices

hr	hours
HS-1	ground high spin state
HS-2	metastable high spin state
ICMCB	Institut de Chimie de la Matière Condensée de Bordeaux
J	Joules
K	Kelvin
k_B	Boltzmann constant
λ	wavelength
L1	2,6-di(pyrazol-1-yl)pyridine
L2	2,6-di(3-methylpyrazol-1-yl)pyrazine
L3	2,6-(dipyrazol-1-yl)-4-hydroxymethylpyridine
L4	2,6-di(3-methylpyrazol-1-yl)pyridine
L5	2,6-di(4-methylpyrazol-1-yl)pyridine
L6	2,6-dipyrazol-1-ylpyrazine
LD-LISC	Ligand Driven – Light Induced Spin Change
LIESST	Light Induced Excited State Spin Trapping
LIPTH	Light Induced Perturbation of a Thermal Hysteresis
LITH	Light Induced Thermal Hysteresis
LS	low spin state
μ	absorption coefficient
M	least squares refinement minimisation function
mm	millimetre
mol	mole
mtz	methyltetrazole
nm	nanometre
NMR	Nuclear Magnetic Resonance
φ	phase
P	primitive
P(xyz)	Patterson function
Pa	Pascal
phen	1, 10-phenanthroline
phy 1	10-phenanthroline-2-carbaldehyde phenylhydrazone
ptz	1-propyltetrazole
ρ	electron density
R	R factor
rpm	revolutions per minute
S	entropy

SQUID	Superconducting Quantum Interference Device
SRS	Synchrotron Radiation Source
T	Temperature
$T_{1/2}$	Spin transition temperature, where 50% of the compound is in the high spin state
trz	4-amino-1,2,4-triazole
u,v,w	coordinates of peaks in the Patterson map
V	volume
V_p	volume of the polyhedron
V_s	volume of the circumscribed sphere
χ_M	magnetic susceptibility
W	Watt
w	weighting factor
wR	weighted R factor

1 Introduction

1.1 Introduction to the spin crossover phenomenon

1.1.1 What is spin crossover?

In an isolated transition metal ion or one exposed to a spherical field, all five d orbitals have the same energy. However on incorporation into a complex, the ligand field surrounding the ion is no longer spherical and affects different d orbitals to a different extent. For example, on exposure to an octahedral field the orbitals which are most affected by the presence of the ligand are those in which the major components lie along the metal ligand directions, the d_z^2 and the $d_{x^2-y^2}$ orbitals. These are raised in energy to form a degenerate doublet, the e_g set. The remaining three orbitals, in which the major components lie between the metal-ligand axes, are less affected by the application of the ligand field and form a degenerate triplet at lower energy, the t_{2g} set. This splitting of the d orbitals gives rise to two possible arrangements of electrons for those transition metal ions with electronic configurations between d^4 and d^7 , the so called high and low spin states, Figure 1.1. The high spin state contains the maximum number of unpaired electrons and is commonly found where the energy required to promote electrons to the higher energy e_g orbitals is less than that required to pair them in the t_{2g} . This is favoured by a weak ligand field in which the degree of orbital splitting is small. An example of an iron (II) complex which is high spin over the whole temperature range is $[\text{Fe}(\text{H}_2\text{O})_6]^{2+}$. The low spin state on the other hand is favoured where the ligand field is strong and the energy required to pair an electron in the lower energy t_{2g} orbitals is less than that required to promote it to the higher energy e_g orbitals, *e.g.* $[\text{Fe}(\text{CN})_6]^{4-}$. If the difference in energy between the high and the low spin states approaches the thermal energy, $k_B T$, where k_B is the Boltzmann constant and T is the temperature, then it is possible for a compound to switch between the two on application of an external perturbation. A transition of this type is known as a spin crossover or a spin transition. Spin transitions can be caused by a change in temperature or pressure or on irradiation with light [1,2]. For materials in which the symmetry is less than octahedral, a further loss of d orbital degeneracy will result, however the principle of a spin crossover transition taking place with a change of electronic configuration within the d orbitals remains the same.

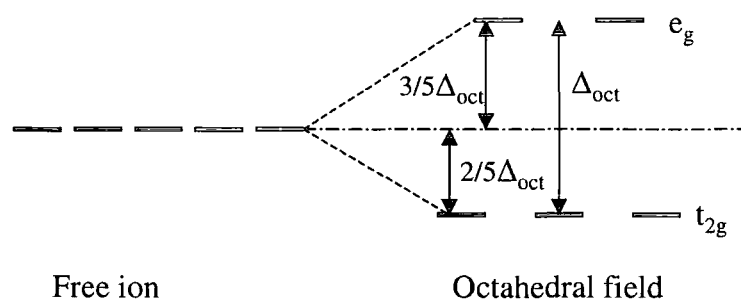


Figure 1.1: Splitting of d orbitals caused by exposure to an octahedral field

The spin crossover effect was first reported by Cambi *et al* in the 1930s during their work on iron (III) dithiocarbamates [2] although it was not until 1966 that it was correctly assigned by König and Madeja as being due to an intra-atomic transfer of two electrons with spin flip [3]. The first man made spin crossover material was reported by Baker and Bobonich in 1964 [4]. Spin crossover has been reported for all the first row transition metals with the permitted electronic configurations. It has been shown to be common for Fe(II) [1], Fe(III) [2], Co(II) and occasional for Ni(II) [5,6], Co(III) [7-9], Mn(II) [10,11], Mn(III) [12,13] and Cr(II) [2]. Thermally induced magnetic changes in Nb_6I_{11} and $\text{HNb}_6\text{I}_{11}$ have also been interpreted as due to spin crossover phenomena [14]. Two spin states are theoretically possible for d^8 , d^3 and d^2 transition metal complexes in systems with lower than octahedral symmetry and a spin equilibrium for a d^8 nickel system was reported by Melson and Busch in 1964 [15].

There is much interest in this class of materials due to their potential for use in applications such as information storage, molecular magnets and visual displays as well as for their importance in biological systems such as the metalloproteins; isopenicillin N-synthase, deoxyhemerythin and ribonucleotide reductase [16-18] and geology [19]. A variety of different systems have been synthesised including molecular complexes and polymers.

1.1.2 Spin crossover theory

Spin transitions occur both in solution and in the solid state. Transitions in solution may be interpreted as a thermal Boltzmann distribution over all the vibrational levels of the two states. They essentially take place in isolation on the molecular level and are not subject to lattice constraints as there is little, or no, interaction between the complex molecules. Solid state spin transitions are more difficult to interpret and predict, and can take a number of forms the most common, illustrated in Figure 1.2, being;

- (i) Smooth and continuous over the temperature range;
- (ii) Abrupt;
- (iii) With hysteresis;
- (iv) With steps;
- (v) Incomplete.

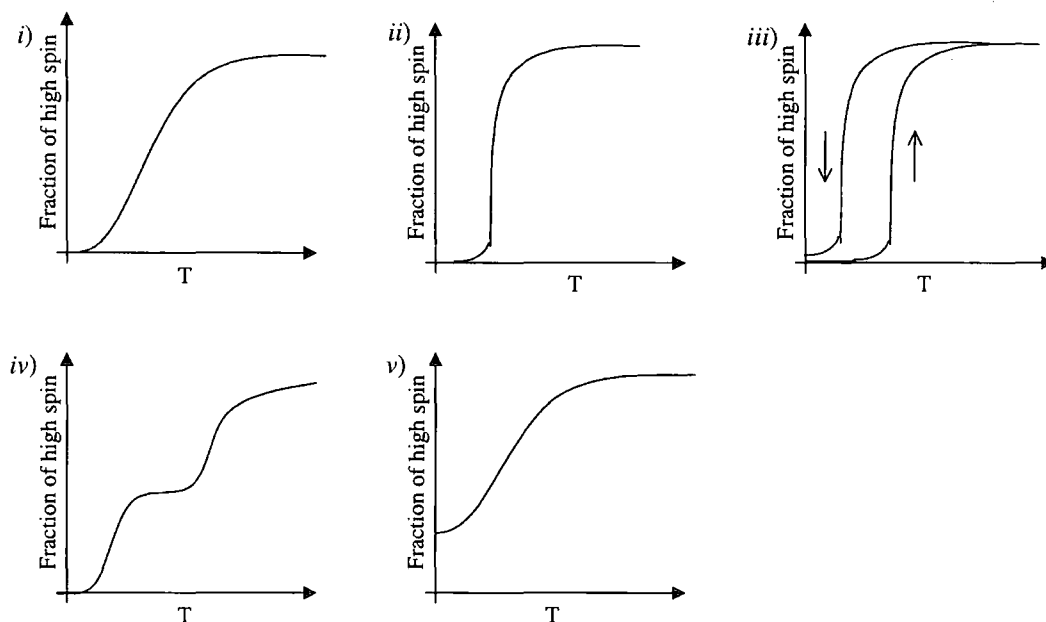


Figure 1.2: Diagrams of possible thermal spin transition behaviour *i)* smooth and continuous, *ii)* abrupt *iii)* with hysteresis, *iv)* with steps, *v)* incomplete

The form of the spin transition curves, *i.e.* a plot of high spin fraction *vs.* temperature, is diagnostic for the nature of the spin transition, the more abrupt the transition the greater the communication between metal centres in the solid state [20,21]. This communication is known as cooperativity and is a measure of the degree to which a spin transition taking place in one molecule affects neighbouring molecules and this will be discussed in more detail below. High levels of cooperativity give rise to abrupt transitions and hysteresis. The smooth transition which takes place over a very large temperature range is common in solution, but unusual in the solid state and is indicative of only very weak interactions between reacting centres as in dilute metal systems [22]. Incomplete transitions are those in which the compound is either not fully high spin even at high temperature or not fully low spin at low temperature or both. There are a number of reasons for this sort of behaviour; the kinetics of the transition may be such that some high spin material is trapped at low temperature [23] or

if there are two independent iron centres one may undergo a transition while the other remains in the same high or low spin state over the whole temperature range [24,25]. Transitions which contain steps as seen in Figure 1.2 (iv), can also be a result of different iron centres that undergo the spin transition at different temperatures [26,27] or of phonon coupling effects [28].

Hysteresis is a manifestation of bistability which is best described as the existence of two different states of the same substance under identical conditions depending on its history and it is essential for three of the applications mentioned above. For example, if a spin crossover material with a transition centred at 260 K and a hysteresis loop of ten degrees is cooled from room temperature, it will be high spin at 260 K and if the same material is warmed from 10 K it will be low spin at the same temperature. Bistability is the basis of any memory effect in these systems and so there has been considerable effort expended in designing materials with wide hysteresis loops which span room temperature. Transitions which exhibit hysteresis are frequently associated with crystallographic phase transitions and it was not until 1986 that the first transition of this type without a space group change was reported by Wiehl *et al* for $[\text{Fe}(\text{2-pic})_3]\text{Br}_2 \cdot \text{EtOH}$ (2-pic = 2-(aminomethyl)pyridine). [39]

It has been said above that if the difference in energy between the two spin states approaches the thermal energy, a spin transition can take place. However when considering the likelihood of a spin transition occurring, it is necessary not only to consider the difference in energy but also the difference in entropy, since the Gibbs Free energy (Equation 1.1) is an important factor in the determination of the spin behaviour. In order for a spin transition to be possible, ΔG for the transition must be negative.

$$\Delta G = \Delta H - T\Delta S \quad \text{Equation 1.1}$$

The critical temperature for the spin transition is defined as being the temperature at which 50% of the molecules are in the high spin state, at this temperature ΔG is equal to zero and it can be said that,

$$T_{1/2} = \Delta H / \Delta S \quad \text{Equation 1.2}$$

ΔS in this case is the combination of the vibrational and electronic entropies both of which are always positive. It therefore follows that in order for a spin transition to be possible the change in enthalpy must also be large and positive. At low temperatures the enthalpy factor

dominates and the ground spin state is low spin whereas at high temperatures the entropy factor is larger, a spin transition takes place and the high spin state is the ground state.

If a bulk spin crossover material is considered in which there are assumed to be no intermolecular interactions, it is clear that not only must the electronic and vibrational entropies be taken into account, but also the mixing entropy, that is the number of ways it is possible to arrange the number of molecules with different spin states. The mixing entropy has a maximum value at $T_{1/2}$ when the number of molecules in the high spin state is 50%. Using this sort of model predicts smooth, gradual spin transitions which are often incomplete even at very high or low temperatures [30]. While this form of transition is common in solution and in dilute metal systems it is very unusual in the solid state, and this demonstrates the importance that intermolecular interactions in the solid state play, in determining the course of the spin transition, even though it is essentially a molecular phenomenon.

The extent of intermolecular interactions in the sample is manifested by the level of cooperativity. Cooperativity is the degree to which structural and magnetic changes in a molecule undergoing the spin transition affect the neighbouring molecules. It can be thought of as a measure of the amount of communication between metal centres; the greater the amount of intermolecular bonding, such as hydrogen bonds, the more communication between reacting centres and the greater the cooperativity. Increased cooperativity leads to abrupt transitions and favours hysteresis. This is one of the reasons that small changes to the identity of spin crossover materials, such as changing the nature of the counter ion, can have such a large effect on the course of the spin transition.

Two major models have been proposed to explain and predict the cooperative nature of the spin transition; the regular solution model proposed in 1972 by Slichter and Drickamer [31] and the domain model developed by Sorai and Seki [32]. However both models have weaknesses, the latter in particular in that it is unable to predict hysteresis. The real mechanism of the spin transition has yet to be determined although attempts to explain it have been made using a variety of theories, including electron-phonon coupling [33], intermolecular coupling of Jahn-Teller type distortions [34-36] and elastic interactions between molecules of different spin states [37-39]. As mentioned previously, it is known that a high degree of cooperativity promotes abrupt transitions and can result in hysteresis. As well as theoretical studies, a number of practical examinations of this phenomenon have been made, primarily using dilute metal systems in which a certain percentage of the spin crossover centres are replaced by a similar non-active centre, zinc (II) or cobalt (II) being commonly used in studies of iron (II) systems [22]. Very dilute metal systems show gradual spin

transitions, which can be explained as a Boltzmann distribution over the vibrational levels of the two spin states as seen in solution, this experiment not only clearly shows the important role intermolecular interactions play in determining the course of the spin transition. The observation that spin crossover is still seen in very dilute metal systems and in solution, where there is essentially no communication between active centres, demonstrates that spin crossover is a property of the individual molecules rather than the bulk material.

The driving force behind the spin transition is the substantial increase in entropy on going from the low to the high spin state [40]. For Fe(II) complexes the entropy gain for this transition is *ca* 50-80 Jmol⁻¹K⁻¹ consisting of contributions from magnetism and a larger vibrational component due to the increased degrees of freedom in the high spin state. The enthalpy change associated with the transition is in the region of 6-15 kJmol⁻¹, the majority of which is due to the rearrangement of the coordination sphere caused by the alteration in bond lengths associated with the change in spin state.

1.1.3 Spin crossover in iron (II)

The majority of reported examples of this phenomenon have been for iron (II) systems in which the iron is bound to six nitrogen atoms. It seems likely that a large number of examples have been found in this area as the splitting of the *d* orbitals caused by the nitrogen ligand field is of the correct size to allow switching to take place. Much research has also focussed on this area due to links with metalloproteins such as haemoglobin [41] and ribonucleotide reductase [18].

1.1.4 Effect of external factors

The spin transition has several consequences for the physical nature of the material; on going from the low to the high spin state there is an increase in atomic radius of the metal ion associated with the increased anti-bonding nature of the e_g set of orbitals and their greater distance from the nucleus. This results in an increase in metal – ligand bond lengths; which for iron – nitrogen systems is in the order of 0.2 Å, about 10% of the bond length. The increase in the number of unpaired electrons between the low and high spin states causes a change in the magnetism of the system and this provides a very useful method of following the change in spin state. In the low spin state iron (II) compounds are diamagnetic where as the high spin state is paramagnetic with four unpaired electrons and a magnetic moment of 5 B.M. It should however be remembered that magnetism is a property of the bulk material whereas spin crossover is a property of the individual molecules and therefore a change in

magnetism alone is not proof of the spin transition. Spin transitions are frequently accompanied by strong thermochromic effects. An example of this is provided by the iron (II) compound $[\text{Fe}(\text{NH}_2\text{trz})_3](\text{NO}_3)_2$, trz = 4-amino-1,2,4-triazole, which is purple in the low spin state and white when in the high spin state [42]. This effect is also seen in $[\text{Fe}(\text{ptz})_6](\text{BF}_4)_2$, ptz = 1-propyltetrazole, which is violet in the low spin state and colourless when high spin [24,43]. A change in colour of this sort is essential for display devices.

Temperature

Most reported spin transitions have been caused by alterations in temperature; low temperatures favour the low spin state whereas high temperatures favour the high spin state, for the entropic reasons described above. The temperature of the thermal spin transition is usually described as $T_{1/2}$, the temperature at which half of the molecules are in the high spin state. Clearly for those systems which show hysteresis it is necessary to quote two temperatures, one for the branch of the transition with decreasing temperature and one for that with increasing temperature. The temperature about which the hysteresis is centred may also be quoted together with the hysteresis width.

Light

In the mid 1980s Decurtins *et al* discovered that when irradiated with a green laser, ($\lambda = 514 \text{ nm}$) a low spin compound could be promoted to a metastable high spin state with a very long lifetime at low temperatures [44]. This phenomenon is known as LIESST (Light Induced Excited Spin State Trapping) and has been found to be a common feature of spin crossover systems, particularly those containing iron (II). This behaviour is of particular interest as it is another example of the bistability essential for applications such as switches and memory devices. The existence of the reverse process termed reverse-LIESST was confirmed by Hauser in 1986 [45].

Typically irradiation of a low spin sample using an Ar^+ laser with a wavelength in the region of 514 nm at temperatures below about 50 K results in a colour change as seen in the thermal transition. For example in the case of $[\text{Fe}(\text{ptz})_6](\text{BF}_4)_2$ the crystal is completely bleached by irradiation; if the colourless crystal is then irradiated with longer wavelength light from a Ti-sapphire laser at 820 nm, it is seen to return to its original red colour [46]. During excitation the complex undergoes a spin allowed transition from the low spin, spherical $^1\text{A}_1$ state into the $^1\text{T}_1$ band, the metastable high spin, $^5\text{T}_2$ state is then reached by a two stage intersystem crossing process via the intermediate $^3\text{T}_1$ level, Figure 1.3 [44]. If the system is at sufficiently low temperature, usually below 50 K, the molecule is trapped in the low lying $^5\text{T}_2$ state; this trapped excited state has a very long lifetime at low temperatures being stable for many hours

and often days. The reverse process occurs in a similar manner by excitation with a longer wavelength of light from the 5T_2 state into the 5E state and then via intersystem crossing to the 3T_1 state and hence to the low spin 1A_1 level. The conversion from high spin to low spin was found not to be quantitative and it was noted that irradiation of the low spin sample with light of wavelength 980 nm resulted in the formation of the high spin 5T_2 state, *i.e.* LIESST is possible by direct excitation of 1A_1 to 3T_1 , in this case a spin forbidden transition. Thus the maximum fraction of low spin complex achievable through excitation of the metastable high spin state is a steady state concentration, the value of which depends on the wavelength of the excitation light and the relative energies of the two low lying states. Different term symbols apply for different metal centres.

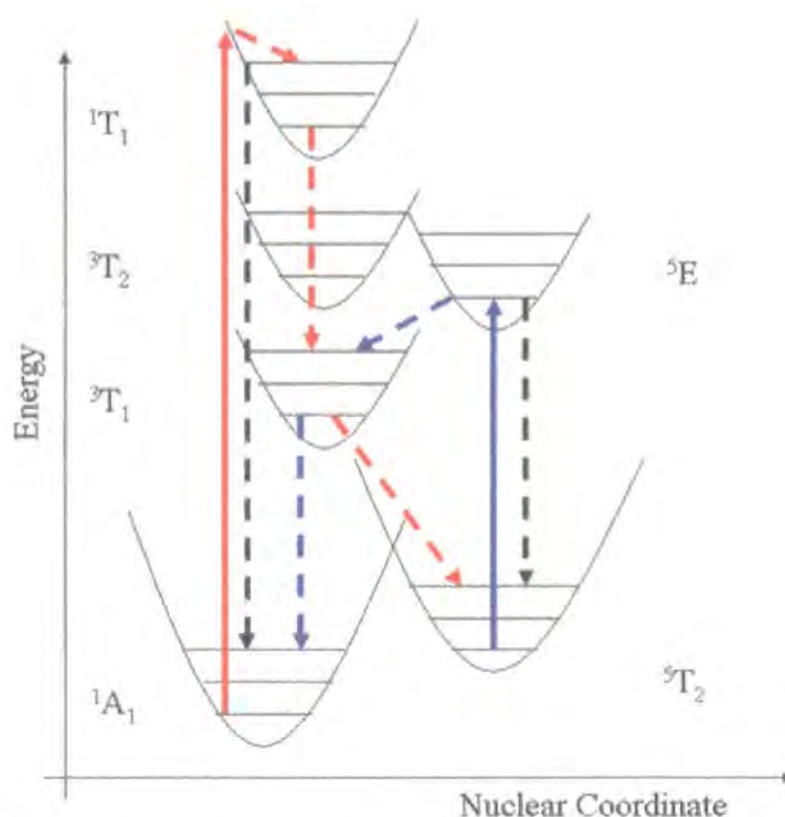


Figure 1.3: Scheme of the mechanism for LIESST and reverse-LIESST. Red lines indicate LIESST processes, blue lines reverse-LIESST process. The solid lines show excitation by irradiation while dotted lines represent relaxation pathways.

The discovery of the LIESST effect sparked interest in the photochemical and photophysical properties of iron (II) compounds which, until this point, had been largely ignored due to their lack of radiative decay processes and the short lifetimes of their optically excited states. Since then a number of new phenomena have been reported. In 1994 the first example of LD-LISC was reported [47]. Ligand Driven – Light Induced Spin Change occurs when

irradiation causes *cis-trans* isomerism in the ligand resulting in a change in ligand field strength which forces a spin transition at the metal centre. Thus far this has only been reported in solution as in order to occur in the solid state the materials need to be embedded in cellulose acetate films which are too rigid at low temperatures to allow the large degree of movement needed for the isomerism to occur. In 1998 Light Induced Thermal Hysteresis or LITH was discovered. After undergoing LIESST complete illumination is continued and under this irradiation a hysteresis develops in the light induced spin transition curve [48]. Most recently a phenomenon called LIPTH, Light Induced Perturbation of a Thermal Hysteresis, has been reported by F. Renz *et al.* Studies carried out on $[\text{Fe}(\text{phy})_2](\text{BF}_4)_2$ (phy = 1, 10-phenanthroline-2-carbaldehyde phenylhydrazone) show that it undergoes a spin crossover transition with hysteresis between 270 K and 280 K, continuous irradiation of this sample with light changes the temperature of the spin transition [49]. Green light decreases the temperature of the hysteresis and red light shifts it, albeit less significantly, towards higher temperatures.

Pressure

The spin crossover transition is known to involve a large change in the volume of the metal coordination sphere and so a related change in the volume of the crystallographic unit cell and indeed that of a crystal itself. It should come as no surprise therefore that materials of this sort are highly sensitive to the application of pressure. As described above, the high spin state has a larger volume than the low spin and so application of an increased external pressure to a spin crossover material in the high spin state at ambient pressure can cause formation of the low spin state more normally found as the ground state at low temperature. A number of studies have been performed in which the effect of pressure and of varying the temperature of the sample under raised pressure have been investigated. In the majority of cases these studies have involved spectroscopic techniques such as Mössbauer or Raman spectroscopy although a smaller number of crystallographic studies have been performed.

The effect of raised pressure on spin crossover materials was already well known when, in 1985, König *et al* reported the first study of the effect of increased pressure on the thermal transition of an iron (II) spin crossover material, $[\text{Fe}(\text{phy})_2]\text{X}_2$ where phy = 1,10-phenanthroline-2-carbaldehyde phenylhydrazone and X = BF_4 , ClO_4 [50]. This detailed study using the ^{57}Fe Mössbauer effect revealed that increasing pressure increases the temperature of the spin transition and results in a more gradual transition with an increased hysteresis loop. These features have since been confirmed by a number of other studies which have also investigated the effect of pressure on the kinetics of the transition and the equilibrium constants. As well as an increase in the hysteresis on increasing the pressure it has also been

found that in some cases a decrease in hysteresis width has been the result of exposure to increased pressure [51,52].

The first single crystal X-ray diffraction study of an iron (II) spin crossover material under pressure was performed by Granier *et al* in 1993 [53]. This study noted that the low spin structures obtained at ambient pressure at low temperature and those obtained at room temperature and high pressure are very similar with differences in iron nitrogen bond lengths of not more than 0.03 Å and bond angles of not more than 1.5°. For $[\text{Fe}(\text{phen})_2(\text{NCS})_2]$, phen = 1, 10 – phenanthroline, the volume change on going through the pressure induced spin transition was found to be the same as that reported for the thermal spin transition. It is also possible to induce a transition from the low spin state to the high spin state at room temperature by exposure of the sample to less than atmospheric pressure [54].

Magnetic field

As spin crossover alters the magnetic properties of the system it is reasonable to expect that exposure to a magnetic field would affect the transition. Theoretical calculations have predicted that this effect would be very small, a change in the critical temperature of only -0.1 K for a field of 5 Tesla. The high fields needed to obtain tiny changes in the temperature of the spin transition mean that it has proved very difficult to measure this effect. Work carried out by Qi *et al* in 1983 found a shift of -0.11 ± 0.04 K when the steep transition of $[\text{Fe}(\text{phen})_2(\text{NCS})_2]$ was exposed to fields of between 1 and 5 Tesla [55]. More recently exposure of this compound to a strong pulsed magnetic field of 30 Tesla, at the temperature of the spin transition has shown a change in the critical temperature of -1.8 K. The magnetic field caused a partial irreversible spin transition when applied to the ascending branch of the hysteresis loop and a reversible transition in the descending branch [56]. The decrease of the critical temperature under the influence of a magnetic field demonstrates that these conditions favour the high spin state.

1.1.5 Principle methods for examination

Magnetometry

As the spin crossover transition involves a change in the number of unpaired electrons in the metal ion it also has a large effect on the magnetic behaviour of the material. In the case of iron (II) the high spin state is paramagnetic with four unpaired electrons and the low spin state is diamagnetic thus there is a very large change in magnetic susceptibility on going through the spin transition. As the susceptibility of the sample is proportional to the percentage of material in the high spin state this can be used to construct a spin transition curve. It should

be remembered however that magnetism is a property of the bulk material while the spin transition is a feature of individual molecules and that a change in magnetism alone is not sufficient to prove the existence of the spin transition. This technique is much used when studying these materials as it is possible to follow the course of the transition as a function of temperature and also under light irradiation and under pressure [2]. Solid state measurements can be made using a Faraday balance or a SQUID (Superconducting Quantum Interference Device), or Fonor type magnetometer, liquids can be examined using Evans' NMR method.

Crystallography

Crystallography is of critical importance in the study of spin crossover compounds. It can be used to confirm the existence of a spin transition through determination of bond lengths above and below the transition temperature and whether the transition is associated with a change in crystallographic space group. Variable temperature techniques can be used to follow the effect of intermolecular interactions on the transition and thus the cooperativity of the sample. Correlations between structural features and the transition determined in this way may be used to aid the design of materials with specific physical properties such as abrupt spin transitions near ambient temperature.

In recent years it has also been shown to be possible to determine the effect of a LIESST transition on the structure of the material using crystallographic techniques [57-60]. Data can be collected which allow comparison of the high spin ground state at high temperature with the metastable high spin state formed as a result of irradiation. A direct comparison of the high and low spin states at the same temperature, allowing determination of the effect of the spin transition on the structure divorced from the effect of temperature is also possible using this type of technique. With the improvement of experimental techniques and computing facilities along with higher intensity X-ray sources, it is becoming easier to study the effect of pressure on spin crossover materials using diffraction techniques.

As well as X-ray diffraction, neutron diffraction has also proved useful in the study of the spin transition, since using neutrons it is possible to study the spin structure of the materials as well as their magnetic structure and the spin transition in $[\text{Fe}(\text{ptz})_6](\text{BF}_4)_2$ (ptz = 1-propyltetrazole) has been recently followed using polarised neutrons [61]. Neutrons are also expected to help with the determination of excited state structures for compounds which undergo depopulation on exposure to X-ray radiation. As the neutrons do not interact with electrons it should be possible to determine a structure of the high spin state after irradiation without risking the relaxation which is sometimes seen using X-rays.

Mössbauer spectroscopy

^{57}Fe Mössbauer has proved a valuable tool for the examination of the spin transition under a variety of conditions; variable temperature, pressure and concentration being just a few. There are clear differences in the spectra of high and low spin iron (II) compounds that facilitate their interpretation. For example the low spin spectrum of $[\text{Fe}(\text{ptz})_6](\text{BF}_4)_2$ exhibits two ligand field bands resulting from the transitions from $^1\text{A}_1$ to $^1\text{T}_1$ and $^1\text{A}_1$ to $^1\text{T}_2$ whereas the spectrum of the high spin compound has only one ligand field band due to the transition from $^5\text{T}_2$ to ^5E [1]. The relaxation rates of the two Fe(II) spin states are slow on the Mössbauer timescale and as a result the resonance lines appear sharp and well defined, on the other hand those of Fe(III) systems are much broader which complicates data analysis. The area under the resonance lines in the Mössbauer spectrum is proportional to the fraction of molecules in the high spin state and so the spin transition curve can be determined easily using this method.

Other spectroscopic methods

Other spectroscopic methods provide a very valuable source of information on both the structure and course of the spin transition. The relatively large change in the metal – ligand bond lengths on going through the transition makes vibrational spectroscopies such as Raman and infra red extremely useful. The Fe(II) – ligand bands in the region of 250 cm^{-1} for the high spin state move to around 400 cm^{-1} for the low spin state [62]. The change in bond lengths often extends into the ligand system rather than just being confined to the metal – ligand bonds, which provides a sensitive probe for Fe(II) systems containing NCS or NCSe ligands in which the $\text{N} \equiv \text{C}$ modes in the region of 2000 cm^{-1} are shifted by about 40 cm^{-1} towards higher frequencies on going from high to low spin [2,63]. These methods are also useful for determination of the spin transition under pressure or with varying temperature.

Optical absorption spectroscopy can also be used to follow the spin transition with the absorption maximum enabling determination of the fraction of compound in the high spin state and hence, with variable temperature methods, the construction of the spin transition curve.

Reflectometry and other methods

The darkening of the material on going from the high to the low spin which is frequently associated with the spin transition makes reflectivity an ideal technique to follow the spin transition. DSC (differential scanning calorimetry) can be used to determine the temperature of the spin transition and also the enthalpy and entropy of the transition.

1.2 Introduction to diffraction

1.2.1 Diffraction of light

The most well known example of diffraction is that of light by a grating such as the thin material in a net curtain or an umbrella, it is diffraction that gives rise to the patterns of light that are seen to form around street lights if viewed through one of these materials or through a steamed up window. The diffraction of light by a grating in which the spacing of the slits approaches the wavelength of the light gives rise to a pattern of light and dark lines. This phenomenon was used by Thomas Young in 1801 to demonstrate the wave like properties of light. The lines or diffraction pattern of the light can be thought of as an interference effect; on passing through the slits the light waves either recombine in phase, coherently, resulting in a band of light or out of phase, incoherently, resulting in a shadow. The diffraction pattern contains information about the grating that generated it: a grating of narrow slits will give a broad diffraction pattern whereas a grating of wide slits will result in the formation of narrow diffraction lines. This inverse relationship between the diffraction pattern and system which generated it is of critical importance in crystallography. In fact the separation of the diffraction pattern is related to the grating spacing by a Fourier transformation.

1.2.2 Diffraction of X-rays

That X-ray radiation could be diffracted from crystals was discovered in 1912 by Laue, Friedrich and Knipping and in 1915 the first crystal structure analysis was reported for sodium chloride by father and son W. H. Bragg and W. L. Bragg. The periodic regular arrangement of atoms in the crystal acts as a three dimensional diffraction grating. As X-rays are diffracted from the electrons on passing through the crystal the diffracted beams of X-rays recombine either constructively or destructively to give rise to a three dimensional pattern of peaks of X-ray intensity which can be detected as a series of spots on an image plate or photographic film. In the same way that information about the diffraction grating giving rise to a diffraction pattern of light is contained within that pattern the position and intensity of the diffracted X-ray beams hold information on the structure of the crystal from which they have been diffracted.

1.2.3 Laue diffraction

Max von Laue was the first to report the diffraction of X-rays from a crystalline sample. A white beam of X-rays was used and the diffraction pattern recorded on photographic film. This technique of using a multiple wavelength source of X-rays is still called Laue diffraction today. He and his co-workers determined that the regular pattern of spots of diffracted X-ray intensity could be interpreted by applying their understanding of the diffraction of light from a one dimensional grating to the three dimensional space of the crystal and its diffraction pattern. This treatment gave rise to the three Laue conditions for diffraction which must all be satisfied in order for constructive interference from a crystal to take place, Equations 1.3 to 1.5.

$$a(\cos\alpha_n - \cos\alpha_0) = n_x\lambda \quad \text{Equation 1.3}$$

$$a(\cos\beta_n - \cos\beta_0) = n_y\lambda \quad \text{Equation 1.4}$$

$$a(\cos\gamma_n - \cos\gamma_0) = n_z\lambda \quad \text{Equation 1.5}$$

1.2.4 Bragg diffraction

It was mentioned above that although the phenomenon of diffraction from a crystal was first observed by Laue, the first crystal structure analysis was performed by Bragg. One of the reasons that the Braggs were able to make such advances in analysis of X-ray diffraction patterns is due to the simple, yet extremely powerful way in which they considered the diffraction process. Whereas Laue thought of the crystal as a three dimensional diffraction grating, Bragg junior realised that the diffraction could be manipulated as reflection of the X-ray beam from atoms lying in a series of planes for which the angle of reflectance is equal to the angle of incidence. Although this is not strictly speaking an accurate picture of what physically occurs in the crystal it provides a simple, geometrical explanation for the processes that take place and allows interpretation of diffraction patterns. X-ray beams diffracted from successive planes interfere with each other and strong "reflections" are only found when the difference in path length between the planes is equal to an integral number of wavelengths. These planes are called Miller planes and can be identified by their Miller indices, h, k, l . These are the fractional coordinates at which they intersect the unit cell axis inverted and with the fractions cleared e.g. a plane that crosses the a axis at 1, the b at $1/2$ and the c axis at 1 will have Miller Indices of $(1, 2, 1)$.

Bragg's law states that for a given wavelength, λ , of X-rays there will be an angle, θ , for each set of Miller planes for which constructive interference will arise from the family of planes

which make up that Miller Index. This effectively means that for a specific wavelength of radiation there is a particular angle at which a diffracted beam can be expected. Although Bragg's Law tells us therefore where to expect a diffracted beam, it tells us nothing about the intensity of that diffraction peak.

Bragg's law may be derived in the following manner (Figure 1.4): the spacing between successive planes in a Miller set is d , a beam of X-rays is reflected from the planes the path difference between the first and second planes is $AB + BC$ which is equal to $2d\sin\theta$, and is normally expressed as:

$$n\lambda = 2d\sin\theta$$

Equation 1.6

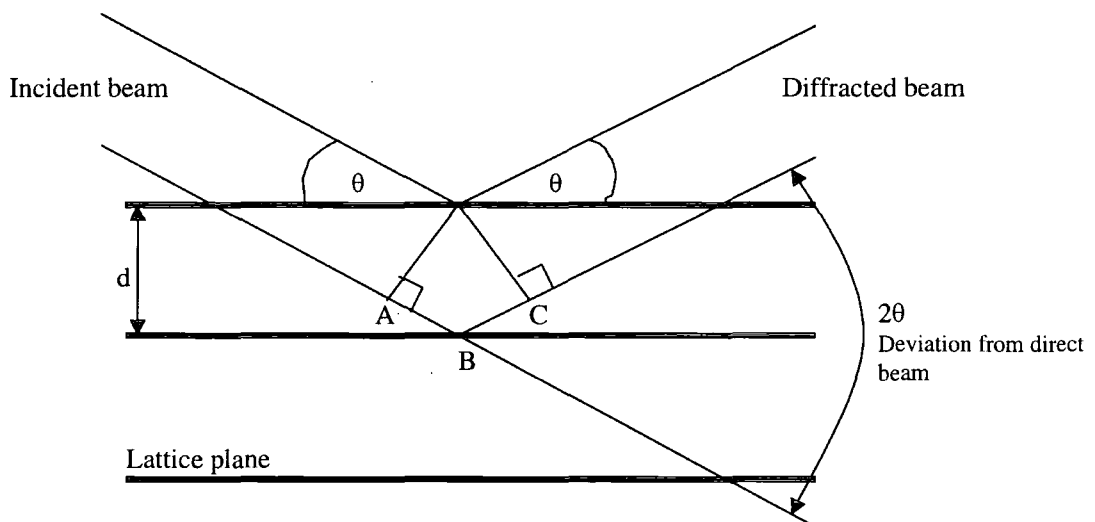


Figure 1.4: Diagram of Bragg's Law. Difference in path length is $AB + BC$.

1.3 Introduction to crystallography

1.3.1 Single crystal diffraction

The aim of a diffraction experiment

The aim of an X-ray diffraction experiment is to record the diffraction pattern of a material and then to determine a model of the structure of the material under consideration which accurately fits the recorded data. The result of a successful crystallographic analysis is precise information on the positions of individual atoms within the crystalline material. From this information it is possible to calculate other important geometrical parameters such as bond lengths and angles; torsion angles; and angles between atomic planes. These analyses

can reveal the interactions between individual atoms and molecules *e.g.* hydrogen bonding interactions or the crystal packing. In many cases this is the only technique that can determine such results, which can be of critical importance in the study of the effect of structural features on physical, chemical or biological properties.

Unit cell and space group determination

The first stage in the analysis of diffraction data from a crystal is the determination of the unit cell dimensions and symmetry, known as indexing the diffraction pattern. The unit cell is the smallest parallelepiped which can be used to generate the crystal structure by translation. The unit cell is defined by its three parallel sides; a , b and c and the angles between those edges; α , β and γ . There are seven crystal systems and four lattice types which can be combined to give fourteen possible Bravais lattices. Table 1.1. All crystalline materials have one of these Bravais lattices. Once the unit cell has been correctly assigned it is possible to predict the positions at which the diffracted beams will be found, this is essential for efficient data collection using a point detector.

Crystal system	Unit cell restrictions	Lattice types
Triclinic	None	P
Monoclinic	$\alpha = \gamma = 90^\circ$	P, C
Orthorhombic	$\alpha = \beta = \gamma = 90^\circ$	P, C, I, F
Tetragonal	$a = b; \alpha = \beta = \gamma = 90^\circ$	P, I
Trigonal	$a = b; \alpha = \beta = 90^\circ \gamma = 120^\circ$	P
Hexagonal	$a = b; \alpha = \beta = \gamma = 90^\circ$	P
Cubic	$a = b = c; \alpha = \beta = \gamma = 90^\circ$	P, I, F

Table 1.1: The fourteen Bravais lattices with their restrictions. P is primitive; C is C centred; I is body centred and F is face centred.

All the symmetry elements possible in three dimensional space can be combined with the 14 Bravais lattices to give 230 space groups. All the symmetry of the structure is contained within one unit cell and then replicated through the crystal by translation. After data collection the space group of the material is determined by examination of absences in the diffraction data. An absence is a position in which there might be expected to be a diffracted peak by geometry, but where the intensity of the diffracted beam is zero. Determination of the correct space group is essential for the successful solution of the crystal structure.

Structure factors and the phase problem

In order to determine the structure of the sample it is necessary to determine the structure factor, F_{hkl} , for the material which contains the identity of the atoms in the compound and their positions in the unit cell, Equation 1.7. This number holds information both about the

amplitude of diffraction from a given set of h,k,l planes and its phase. During a diffraction experiment the intensities and positions of the diffracted beams are measured and, once the unit cell has been determined and the orientation of the crystal on the diffractometer has been calculated, the position of the peaks can be related to the h,k,l plane from which they originated. The intensity is proportional to the square of the amplitude of the structure factor, and it is this relationship that gives rise to one of the most fundamental problems in crystallography; the phase problem. When we record the intensity of the peaks we are unable to measure directly the phase of the diffracted waves, which is required to use the structure factor equation to determine the crystal structure.

$$F_{hkl} = \sum_{j=1}^N f_j \exp[2\pi i(hx_j + ky_j + lz_j)] \quad \text{Equation 1.7}$$

where f_j is the atomic scattering factor for the j th atom with coordinates $x y z$

Once the structure factor has been determined it can be used to calculate the electron density in the unit cell using the Fourier transform relationship between the diffraction pattern and the crystal structure, Equation 1.8.

$$\rho(xyz) = \frac{1}{V} \sum_{hkl} |F_{hkl}| \exp[i\phi(hkl)] \exp[-2\pi i(hx + ky + lz)] \quad \text{Equation 1.8}$$

There are various ways in which the phase problem may be solved in order to find the structure of the crystalline material under consideration. Most commonly used in small molecule crystallography are Patterson and Direct methods.

Patterson methods

Patterson methods are normally applied when there is at least one heavy atom such as bromine or a transition metal in the compound. The Patterson function, Equation 1.9, takes the square of the amplitudes of the structure factors, effectively setting the unknown phases to zero or one. Clearly the result of the function is no longer the electron density. The result of the Patterson function is a map in which the peaks correspond to the vectors between atoms the size of each peak is proportional to the product of the atomic mass of the two atoms. This means that vectors between heavy atoms will be much larger than those between light atoms. Analysis of the Patterson map leads to the position of the heavy atoms within the unit cell. This partial solution can then be refined, as described below, to find the lighter atoms and so generate the final complete structural model.

$$P(xyz) = \frac{1}{V} \sum_{hkl} |F_{hkl}|^2 \cos[2\pi(hu + kv + lw)] \quad \text{Equation 1.9}$$

Where u , v and w are the coordinates of peaks in the Patterson map and as for atomic coordinates, these are given as fractions of the unit cell.

Direct methods

The technique known as Direct methods is frequently applied to small molecule single crystal diffraction, and is very successful when the structure only contains atoms of a similar atomic weight. This is a mathematical method of obtaining phase information direct from a set of intensities. Simply speaking, phases of a few strong reflections are “guessed” and the relationships between these reflections and others in the diffraction pattern are used to generate other phases. This procedure is repeated until the calculated phases have stabilised, as the starting values of the phases are often random the first result is unlikely to be the correct one and so the whole process is repeated a large number of times. The correctness of the phase set obtained in each case is measured using figures of merit. Frequently generation of an electron density map, known as an E-map, using the phases with the best figures of merit will reveal the majority or all of the atomic positions. This model may then be taken on to refinement.

Refinement

Once a starting model of the structure has been obtained either by Patterson or Direct methods that model must be adjusted and refined to obtain the best fit to the experimental data. This is achieved using an iterative process known as least squares refinement in which a function, M , is minimised, Equation 1.10. Many cycles of refinement are required in the course of a crystal structure analysis. Atoms missing from the initial model or wrongly assigned can be identified after least squares refinement, by examination of an electron density map or more usually a difference density map, where the difference between the observed and the calculated electron density is examined.

$$M = \sum w \cdot (Y_1 - Y_2)^2 \quad \text{Equation 1.10}$$

Where w is a weighting which reflects the errors in the data and the model, Y_1 is the observed structure factor or the observed structure factor squared, Y_2 is the calculated structure factor or the calculated structure factor squared.

Assessing the correctness of the model

The final model obtained as a result of many cycles of refinement has to be assessed for its correctness against the experimental data. There are various mathematical parameters which are used to analyse the quality of the solution. Overall residuals quoted are the R factor, Equation 1.11 and the weighted R factor Equation 1.12 and these are usually quoted as percentages. The lower the residual the better fit of the calculated model to the observed data. The goodness of fit or Gof, is also quoted and should be close to 1, Equation 1.13. Clearly the model should account for all electron density measured by the experiment, and for this reason the largest peak of residual density should be as low as possible as should the largest hole of negative electron density.

$$R = \frac{\sum_i |\Delta_i|}{\sum_i |F_o|_i} \quad \text{Equation 1.11}$$

$$wR = \frac{\sum_i w_i \Delta_i^2}{\sum_i w_i F_{o,i}^2} \quad \text{Equation 1.12}$$

$$\text{Gof} = \left(\frac{\sum (w_i \Delta_i^2)}{(n-m)} \right)^{1/2} \quad \text{Equation 1.13}$$

Where Δ_i is usually either $|F_o|_i - |F_c|_i$ or $F_{o,i}^2 - F_{c,i}^2$ and each reflection has a weight, w_i and n is the number of reflections and m is the number of parameters.

1.3.2 Powder diffraction

Diffraction of X-rays from polycrystalline materials occurs by the same physical process as diffraction from single crystals; however there are a number of differences between the two techniques. A random orientation of a large number of crystallites gives rise to a series of diffraction rings rather than the discrete spots seen from diffraction of a single crystal. Powder diffraction techniques record the angles at which these cones are found from the incident beam. This results in the collapse of the diffraction pattern to only one dimension and a subsequent loss of information. In cases where two h,k,l planes diffract at the same angle to the incident beam they overlap in the powder diffraction pattern, whereas in single crystal diffraction they would be in separate positions in reciprocal space. This can make it very difficult to index the peaks in a powder pattern and so extremely hard to determine the unit cell of the compound under consideration. For these reasons, it is almost impossible to obtain a set of h,k,l values and intensities for a polycrystalline material and so the techniques used for the solution of single crystal materials are, in the majority of cases, not suitable for powder diffraction.

Despite these difficulties, powder diffraction is an extremely powerful tool in a large number of situations. Clearly it may be used when it is not possible to obtain single crystals of sufficient size and quality for a single crystal experiment to be performed this has been particularly applied to inorganic materials. Frequently powder diffraction is the best way of finding phase transitions; accurately determining unit cell parameters; identifying unknown phases; or following the evolution of structure with temperature.

Advances in computing methods in recent years have greatly increased the number of compounds that have been solved using powder diffraction methods. These techniques include global minimisation and evolutionary methods [64]. Both methods require the input of a reliable initial molecular model and so unlike single crystal techniques it is not possible to determine the structure of materials in which the connectivity or identity of the atoms is not known.

One of the most important advances in powder diffraction techniques was the development in 1969 of Reitveld refinement methods [65]. Previous to this time least squares techniques such as those used in single crystal diffraction were used for the refinement of models from powder data. This involves treating the powder pattern as a series of discrete Bragg peaks and does not take into account peak shape, background or overlap all of which are critical for the fit of the model to the diffraction data. Reitveld methods allow refinement of not only the Bragg diffraction but the whole pattern including the background, machine constants and peak asymmetry. This allows fitting of the model to the whole pattern and gives rise to a much more complete fit of the model to the data.

As in the case of single crystal diffraction various mathematical parameters are used to assess the quality of the fit of the model to the experimental data and these include the R factor and the weighted R factor and also chi squared. Visual examination of the pattern is also greatly used to ensure that no peaks are left unfitted and that the peak shape is well accounted for.

1.3.3 Bibliography

A full, detailed discussion of the theory behind crystallography and diffraction lies outside the scope of this thesis; the interested reader is directed to any of the large number of excellent texts which cover this topic in detail, of which the list below contains just a few.

1. Glusker, J. P. *Crystal Structure Analysis A Primer*. 2nd Ed. Oxford, Oxford University Press, 1985
2. Giacovazzo, C., Monaco, H. L., Viterbo, D., Scordari, F., Gilli, G., Zanotti, G. Catti, M., *Fundamentals of Crystallography*, Oxford, Oxford University Press, 1994
3. Glusker, J. P., *Crystal Structure Analysis for Chemists and Biologists*, New York, VCH, 1994

1.4 References

1. P. Gütllich, Y. Garcia and H. A. Goodwin, *Chem. Soc. Rev.*, 2000, **29**, 419 - 427
2. P. Gütllich, A. Hauser and H. Spiering, *Angew. Chem. Int. Ed. Engl.*, 1994, **33**, 2024 - 2054
3. E. König and K. Madeja. *Chem. Commun.*, 1966, 61
4. N. A. Baker and H. M. Bobonich, *Inorg. Chem.*, 1964, **3**, 1184 - 1188
5. H. Werner, B. Ulrich, U. Schubert, P. Hofmann and B. Zimmer-Gasser, *J. Organomet. Chem.*, 1985, **297**, 27 - 42
6. W. Kläui, K. Schmidt, A. Bockmann, P. Hofmann, H. R. Schmidt and P. Stoffert, *J. Organomet. Chem.*, 1985, **286**, 407 - 418
7. W. Kläui, *J. Chem. Soc., Chem. Commun.*, 1979, 700
8. P. Gütllich, B. R. McGarvey and W. Kläui, *Inorg. Chem.*, 1980, **19**, 3704 - 3706
9. W. Eberspach, N. El Murr and W. Kläui, *Angew. Chem. Int. Ed. Engl.*, 1982, **21**, 915 - 916
10. N. Hebdanz, F. H. Köhler, G. Müller, J. Riede, *J. Am. Chem. Soc.*, 1986, **108**, 3281 - 3289
11. J. H. Ammeter, R. Bucher, N. Oswald, *J. Am. Chem. Soc.*, 1974, **96**, 7833 - 7835
12. M. E. Seitzer, R. Wang, M. F. Rettig and A. H. Maki, *J. Am. Chem. Soc.*, 1974, **96**, 7669 - 7674
13. P. G. Sin and E. Sinn, *J. Am. Chem. Soc.*, 1981, **103**, 241 - 243
14. H. Imoto, A. Simon, *Inorg. Chem.*, 1982, **21**, 308 - 319
15. G. A. Melson, D. H. Busch, *J. Am. Chem. Soc.*, 1964, **86**, 4830 - 4833

16. M. J. Headlam and R. C. Tuckey, *Archives of Biochemistry and Biophysics*, 2002, **407**, 95 - 102
17. D. R. Davydov, G. H. B. Hoa and J. A. Peterson, *Biochemistry*, 1999, **38**, 751 - 761
18. E.C. Constable, G. Baum, E. Bill, R. Dyson, R. van Eldik, D. Fenske, S. Kaderli, D. Morris, A. Neubrand, M. Neuburger, D. R. Smith, D. Wieghardt, M. Zehnder, D. Zuberbühler, *Chem. Eur. J.*, 1999, **5** (2), 498 - 508
19. J. Badro, G. Fiquet, F. Guyot, J. P. Rueff, V. V. Struzhin, G. Vanko and G. Monaco, *Science*, 2003, **300**, 789 - 791
20. J.-A. Real, A. B. Gasper, V. Niel and M. C. Muñoz, *Coord. Chem. Rev.*, 2003, **236** (1-2), 121 - 141
21. P. Gütllich, H. Köppen and G. Steinhäuser, *Chem. Phys. Lett.*, 1980, **74** (3), 475 - 480
22. I. Sanner, E. Meissner, H. Köppen, H. Spiering and P. Gütllich, *Chem. Phys.*, 1984, **86**, 227 - 233
23. A. Bousseksou, H. Constant-Macuada and F. Varret, *J. Phys. I.*, 1995, 747 - 760
24. P. L. Franke, J. G. Hassnoot and A. P. Zuur, *Inorg. Chim. Acta*, 1982, **59** (1), 5 - 9
25. L. Wiehl, *Acta Crystallogr. Sect. B*, 1993, **49**, 289 - 203
26. H. Köppen, E. W. Müller, C. P. Köhler, H. Spiering, E. Meissner and P. Gütllich, *Chem. Phys. Lett.*, 1982, **91** (5), 348 - 352
27. J.-A. Real, H. Bolvin, A. Bousseksou, A. Dworkin, O. Kahn, F. Varret and J. Zarembowitch, *J. Am. Chem. Soc.*, 1992, **114**, 4650 - 4658
28. K. Boukheddaden, J. Linares, E. Codjovi, F. Varret, V. Niel and J. A. Real, *J. Appl. Phys.*, 2003, **93**, 7103 - 7105
29. L. Wiehl, G. Kiel, C. P. Köhler, H. Spiering and P. Gütllich, *Inorg. Chem.*, 1986, **25**, 1565 - 1571
30. O. Kahn, *Molecular Magnetism*, VCH, New York, Cambridge, 1993
31. C. P. Slichter and H. G. Drickamer, *J. Chem. Phys.*, 1972, **56**, 2142 - 2160
32. M. Sorai and S. Seki, *J. Phys. Soc. Jpn.*, 1972, **33**, 575
33. R. Zimmermann, *J. Phys. Chem. Solids*, 1983, **44**, 151 - 158
34. T. Kambara, *J. Phys. Soc. Jpn.*, 1980, **49**, 1806 - 1811
35. N. Sasaki and T. Kambara, *J. Chem. Phys.*, 1981, **74**, 3472 - 3481
36. T. Kambara, *J. Chem. Phys.*, 1981, **74**, 4557 - 4565
37. S. Ohnishi and S. Sugano, *J. Phys.*, 1981, **C14**, 39 - 55
38. H. Spiering, E. Meissner, H. Köppen, E. Müller and P. Gütllich, *Chem. Phys.*, 1982, **68**, 65 - 71
39. P. Adler, L. Wiehl, E. Meissner, C. P. Köhler, H. Spiering and P. Gütllich, *J. Phys. Chem. Solids*, 1987, **48**, 517 - 525
40. M. Sorai and S. Seki, *J. Phys. Chem. Solids*, 1974, **35**, 555 - 570

41. W. R. Schiedt and C. A. Reed, *Chem. Rev.*, 1981, **81**, 543 - 555
42. O. Kahn, E. Codjovi, Y. Garcia, P. J. van Koningsbruggen, R. Lapouyade and L. Sommier, *ACS Symp. Series*, 1996, **20**, 298 - 310
43. E. W. Müller, H. Spiering and P. Gülich, *J. Chem. Phys.*, 1983, **79**, 1439 - 1443
44. S. Decurtins, P. Gülich, K. M. Hasselbach, H. Spiering and A. Hauser, *Inorg. Chem.*, 1985, **24**, 2174 - 2178
45. A. Hauser, *Chem. Phys. Lett.*, 1986, **124**, 543 - 548
46. A. Hauser, *J. Chem. Phys.*, **94** (4), 1991, 2741 - 2748
47. C. Roux, J. Zarembowitch, B. Gallois, T. Granier and R. Claude, *Inorg. Chem.*, 1994, **33**, 2273 - 2279
48. A. Desaix, O. Roubeau, J. Jeftic, J. G. Hassnoot, K. Boukheddaden, E. Codjovi, J. Linares, M. Noguez and F. Varret, *Eur. Phys. J. B.*, 1998, **6**, 183 - 193
49. F. Renz, H. Spiering, H. A. Goodwin and P. Gülich, *Hyperfine Interact.*, 2000, **126**, 155 - 158
50. E. König, G. Ritter and J. Waigel, *J. Chem. Phys.*, 1985, **83** (6), 3055 - 3061
51. E. König, G. Ritter, H. Grünsteudal, J. Dengler and J. Nelson, *Inorg. Chem.*, 1994, **33**, 837 - 839
52. C. P. Köhler, R. Jakobi, E. Meissner, L. Wiehl, H. Spiering and P. Gülich, *J. Chem. Phys. Solids*, 1990, **51**, 239 - 247
53. T. Granier, B. Gallois, J. Gaultier, J-A. Real and J. Zarembowitch, *Inorg. Chem.*, 1993, **32**, 5305 - 5312
54. E. Smit, D. de Waal and A. M. Heyns, *Mater. Res. Bull.*, 2000, **35**, 1697 - 1707
55. Y. Qi, E. W. Müller, H. Spiering and P. Gülich, *Chem. Phys. Lett.*, 1983, **101**, 503 - 505
56. A. Bousseksou, N. Negre, M. Goiran, L. Salmon, J-P. Tuchagues, M-L. Boillot K. Boukheddaden and F. Varret, *Eur. Phys. J. B*, 2000, **13**, 451- 456
57. J. Kusz, H. Spiering and P. Gülich, *J. Appl. Cryst.*, 2001, **34**, 229 - 238
58. M. Marchivie, P. Guionneau, J. A. K. Howard, A. E. Goeta, G. Chastanet, J-F. Létard and D. Chasseau, *J. Am. Chem. Soc.*, 2002, **124**, 194 - 195
59. V. A. Money, I. R. Evans, M. A. Halcrow, A. E. Goeta, and J. A. K. Howard, *Chem. Commun.*, 2003, 158 - 159
60. E. J. MacLean, C.M. McGrath, C. J. O'Conner, C. Sangregorio, J. M. W. Seddon, E. Sinn, F. E. Sowrey, S. J. Teat, A. E. Terry, G. B. M. Vaughan, N. A. Young, *Chem. Eur. J.*, 2003, **9** (21), 5314 - 5322
61. A. Goujon, B. Gillon, A. Gukasov, J. Jeftic Q. Nau, E. Codjovi and F. Varret, *Physical Rev. B*, 2003, **67**, 220401(R)
62. J. H. Takemoto and B. Hutchinson, *Inorg. Chem.*, 1973, **12**, 705 - 708

-
63. P. Gülich, *Struct. Bonding (Berlin)*, 1981, **44**, 83 - 195
 64. K. D. M. Harries, M. Tremayne and B. M. Kariuki, *Angew. Chem. Int. Ed.*, 2001, **40**, 1626 - 1651
 65. H. Rietveld, *J. Appl. Cryst.*, 1969, **2**, 65 - 71

2 Instrumentation and Experimental

This chapter contains a brief description of the instrumentation and techniques used to perform the work discussed in this thesis. No attempt has been made to present a complete overview of the many different systems available commercially or designed by individual laboratories for performing similar measurements.

2.1 Single crystal X-ray diffraction

2.1.1 Three circle X-ray diffractometers

With the development of area detectors it is no longer necessary to bring a diffraction peak into the horizontal plane of the detector in order to perform an accurate measurement of its position and intensity. As a result, a lesser degree of crystal mobility is required for the collection of sufficient diffraction data to determine a crystal structure. This has led to the development of the three circle diffractometers which were used to collect the data presented herein.

With a four circle diffractometer of the kind commonly used with point detectors and still much in use today, particularly at neutron facilities, the crystal is mounted on a goniometer head usually on a glass fibre or hair for X-ray diffraction or an aluminium pin for use with neutrons. It is possible to rotate the crystal around the axis of the mount, ϕ . The whole goniometer may be rotated around a vertical circle, the χ circle, this in turn may move relative to the detector on a horizontal circle ω and the detector may move in the same plane, 2θ . The advent of area detectors has made the use of adaptations, such as cooling devices, easier due to the removal of the physical restraints imposed by the necessity of a large χ circle. The Bruker SMART diffractometers used for this work have a goniometer head with a fixed χ angle of 54.7° . Data are collected by scanning through ω , normally in 0.3° frames for four sets of orthogonal ϕ angles, this is usually sufficient to obtain a large redundancy of data for most symmetries and orientations of crystals. The frame width may be altered to take into account the diffraction peak shape. Crystals with a high mosaicity have wide diffraction peaks and systems of this sort may be measured using wider frame widths provided that each peak appears on several frames in order to get a good measurement of peak intensity. The converse is true for crystals with very sharp diffraction peaks where it may be

necessary to use a narrower frame width in order to obtain an accurate measurement of diffracted intensity.

The single crystal diffraction experiments in this thesis were performed using a Bruker SMART 1000 diffractometer [1] and a Bruker Advance APEX fitted with a Bede molybdenum microsource generator, Figure 2.1.

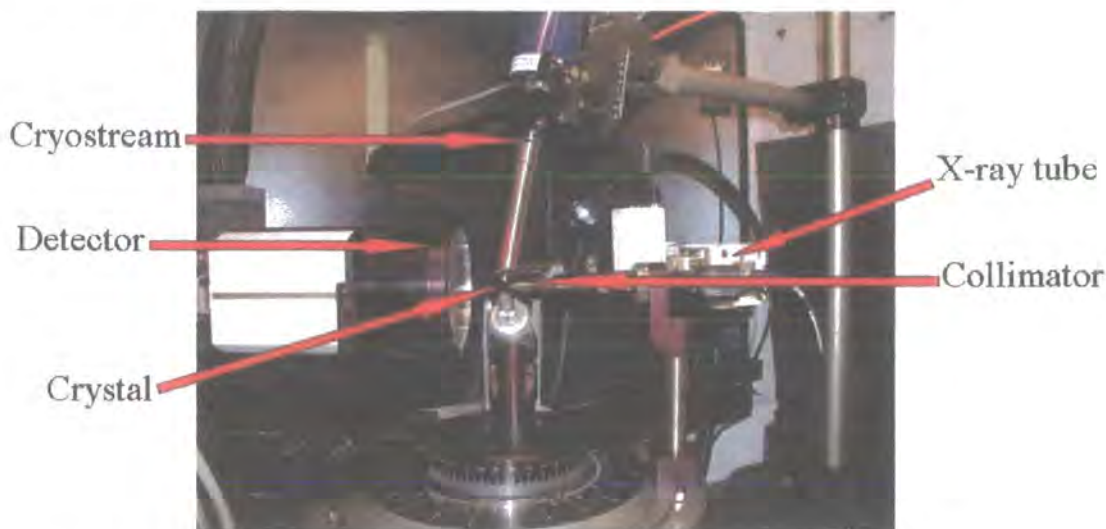


Figure 2.1: The Bruker SMART 1000 diffractometer.

2.1.2 Generation of X-rays

The laboratory sources used to generate the X-rays used in the diffraction experiments described herein were sealed tubes. X-rays are generated by the bombardment with electrons of a metal target cooled by a continuous flow of water. A high energy electron beam generated by a heated filament and accelerated through an electric field is decelerated as it hits the metal target and this results in generation of X-ray radiation with a wide range of wavelengths called Bremsstrahlung radiation. However together with this continuous white radiation are sharp peaks of high intensity which result when a high energy electron displaces an electron from a low lying metal orbital and an electron from a higher energy orbital drops into the vacancy emitting its excess energy as X-ray radiation. These peaks are at specific energies determined by the element of the metal target and the shell from which the emitting electrons originate, for example L electrons dropping into the K shell produce K_{α} radiation while those dropping from the M shell into the K produce K_{β} radiation. For the work carried out in this thesis the single crystal X-ray diffraction was performed using a molybdenum target giving rise to K_{α} radiation with a wavelength of 0.71073 \AA , a mixture of both $K_{\alpha 1}$ and $K_{\alpha 2}$ radiation. A copper target was used for the powder diffraction work generating only $K_{\alpha 1}$

radiation with a wavelength of 1.54051 Å. As the initial bombardment of the metal target results in the emission of X-rays with a continuous range of wavelengths the radiation must be filtered in such a way as to remove the unwanted energies of X-rays and leave the maximum intensity of monochromatic beam. This is done either using a metal filter which absorbs the undesired energies or using diffraction from a perfect graphite crystal, diffraction of one particular wavelength of X-rays will occur only at a specific angle as defined by Bragg's Law, Section 1.2.4. Once a monochromatic beam of X-rays has been obtained it is passed through a collimator to obtain a narrow, parallel beam which can be further focussed, if required, by a series of mirrors.

The intensity of X-rays which can be obtained from a source in this manner is limited by the efficiency with which heat can be removed from the target. A higher level of intensity may be obtained by using a rotating anode source in which the target rotates (6000 rpm), spreading the area of electron bombardment. Rotating anode sources can produce as much as ten times the intensity of a sealed tube source.

The dataset on $[\text{FeL6}_2](\text{BF}_4)_2$, presented in Chapter 7 (L6 = 2,6-dipyrazol-1-ylpyrazine) and those on $[\text{FeL4}_2](\text{BF}_4)_2$, Chapter 6 (L4 = 2,6-di(3-methylpyrazol-1-yl)pyridine), were collected using a three circle diffractometer equipped with a Bruker APEX detector and a Bede X-ray microsource generator. The microsource is capable of producing a finely focussed X-ray beam of intensity almost equivalent to that produced by a rotating anode source.

The highest intensity of X-rays is available at synchrotron sources such as the SRS at Daresbury or the ESRF in Grenoble. Applications can be made to perform experiments at these central facilities if increased intensity and also tuneable wavelengths are required. The powder X-ray diffraction experiments described in Chapter 7 were performed on Station 2.3 at Daresbury. X-rays are generated at a synchrotron by acceleration of electrons to close to the speed of light. The electrons are accelerated around a large storage ring which consists of straight and curved sections. The electrons pass through bending magnets which cause the electron beam to curve, emitting X-ray radiation tangentially to the ring.

Synchrotron radiation was used for experiments on polycrystalline samples of $[\text{Fe}(\text{L6})_2](\text{BF}_4)_2$ and $[\text{Fe}(\text{L6})_2](\text{ClO}_4)_2$, Chapter 7, the large unit cells of these compounds result in considerable peak overlap which makes indexing of the pattern impossible.

2.1.3 Charge coupled device (CCD) detectors

Since their introduction, area detectors have reduced vastly the amount of time required to collect a full data set and made rapid screening of crystals a real possibility; measurement of phase transitions has become much easier with the whole diffraction pattern being recorded not just around the Bragg peaks; accessories such as low temperature devices and pressure cells may be used more simply; and the increased sensitivity of the detectors means that poorer quality crystals can be used. The area detectors used to record the single crystal diffraction patterns in this work were all CCD (charge coupled device) detectors in which the diffracted X-rays hit a phosphor, protected by a beryllium screen, and are converted to light. Fibre optics convey the signal to the CCD chip which is cooled to reduce the electronic noise level. In the chip the light produces electron-hole pairs, the electrons are trapped in the potential wells and this is read out as current. CCDs have the advantages that they have very fast read-out times, low noise levels and efficient recording, but very high quality chips are required and the size of the detector is limited by the size of the chip, which at present remains relatively small.

2.1.4 Computing

Data collection was performed using the commercially designed software, SMART. Data reduction was performed using the Bruker SAINT [2] and XPREP [3] packages and solution and refinement of the data were carried out using the SHELX suite of programmes [3].

2.1.5 Cooling systems

Temperature control between 360 K and 100 K was carried out using an Oxford Cryosystems nitrogen Cryostream [4] in which the crystal is cooled by a flow of chilled nitrogen gas. Below 100 K cooling was performed with an Oxford Cryosystems HELIX [5,6] with the crystal cooled by a flow of chilled helium gas and a base temperature of 30 K.

2.1.6 LIESST experiments

For the LIESST (Light Induced Excited Spin State Trapping) experiments the crystal must be cooled to the base temperature of the HELIX, 30 K, and irradiated by either a green or red laser (see below). Initially the laser was placed on the base of the diffractometer cabinet and centred on the crystal using a series of mirrors and prisms and, before collecting the data, the laser had to be removed to allow the detector to move freely. Later a mount was designed to

allow constant irradiation during data collection; the laser is mounted vertically on the back of the detector arm and the laser once again centred on the crystal by means of mirrors and prisms, Figure 2.2 [7]. The laser light will remain centred throughout the experiment if continuous irradiation is required. The red laser used for these experiments was a He – Ne laser with a wavelength of 632.8 nm and power of 25 mW, the green light was provided by a Nd-YAG laser with a wavelength of 532.06 nm and power of 210 mW.

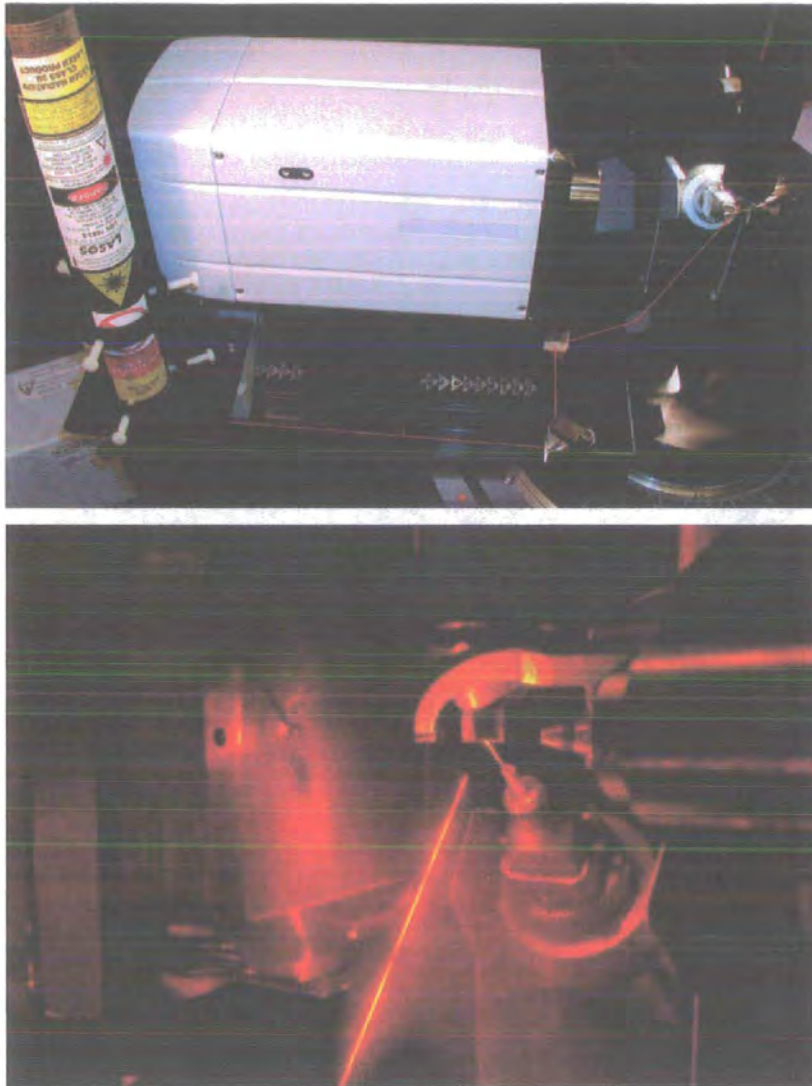


Figure 2.2: The new laser mount and focussing system (above), the laser path has been marked in red and an image of the laser in use (below) [7]

2.2 High pressure crystallography

2.2.1 Diamond anvil cell

The development of the gasketed diamond anvil cell in the mid 1960s by Van Valkenburg [8] opened up the possibilities of performing diffraction experiments at high pressures on standard diffractometers. A Merrill – Bassett cell was used for the high pressure experiments described herein, Figure 2.3 [9]. The sample chamber of the diamond anvil cell is formed by the faces (culets) of the diamonds and the hole in the metal foil of the tungsten gasket. Beryllium backing plates hold the components together while allowing X-rays to enter the sample chamber. The sample is placed in the sample chamber with a pressure calibrant and then a pressure transmitting medium is added. The pressure transmitting medium is normally a liquid capable of exerting a hydrostatic pressure on the sample over the whole pressure range under consideration. Common examples are a 4:1 ethanol:methanol mixture which is suitable for use with pressures up to about 10.4 GPa, the pressure of its glass transition [10] and petroleum ether which is hydrostatic up to 6 GPa [11]. It was not possible to use the ethanol:methanol mixture in the case studied in this thesis as the crystals are slightly soluble in these solvents. Mineral oil was used, for the experiments described in Chapter 3, this is only hydrostatic up to in the region of 2 GPa [12], however the high sensitivity of spin crossover materials to the application of pressure led us to believe that this would be more than sufficient to cause the spin transition to take place.

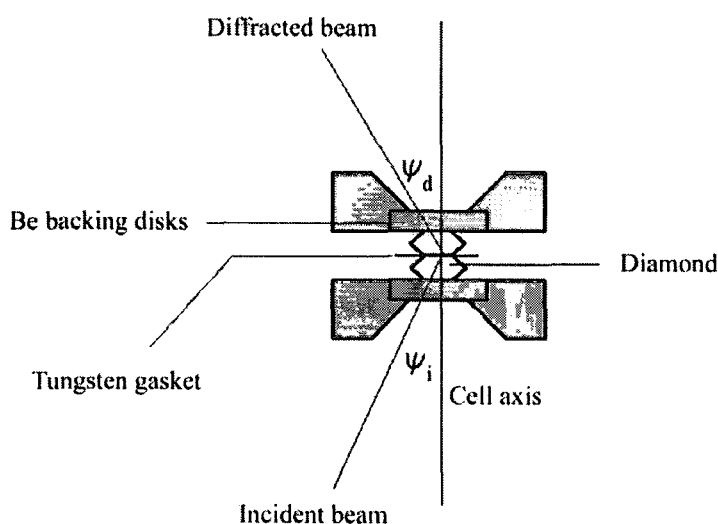


Figure 2.3: Diagram of the Merrill - Bassett diamond anvil cell [18]

Pressure is applied to the upper faces, the tables, of the diamonds by means of tightening Allen screws forcing them closer together. As the tables are much larger than the culets, typically with a ratio of the order of 3:0.6 mm, the load required to induce very high pressures in the sample chamber is only small. It is of critical importance that the diamonds remain parallel and do not touch, if the diamonds were to tilt this could cause bridging of the sample chamber by the crystal and may result in damage to the diamonds.

It is possible to use a diamond anvil cell in two ways and the one that is most appropriate depends on the nature of the experiment being performed. Transmission mode is most frequently used in X-ray diffraction, the X-rays pass through one diamond and the diffracted beams exit through the second. The second method involves both the incident and diffracted beam passing through the same diamond. Transmission cells have the advantage that the absorption correction for the incident and diffracted beams is simple to apply, however only between 40% and 50% of reciprocal space is accessible during the experiment with the exact fraction depending on opening angle of the cell and it was this geometry that was used during the spin transition experiments.

2.2.2 Measuring the pressure in the cell

The nature of the pressure calibrant is of importance in determining the accuracy with which the pressure in the sample chamber of the cell can be measured. It is not possible to calculate directly the applied pressure from the load applied to the tables of the anvils, as the distribution of the force is not fully known. The force may also be reduced by deformation or absorption of some of the load by the gasket. A small ruby chip (Cr^{3+} doped $\alpha\text{-Al}_2\text{O}_3$) was used for these experiments. Ruby is known to be stable up to megabar pressures. The pressure is measured using the strong response in the ruby Raman spectrum which shows a red shift on increased pressure [13,14,15]. The very strong nature of the ruby response to the Raman experiment means that only very small samples of ruby are required, typically only tens of microns which is a particular benefit in diffraction experiments as it means that the majority of the sample chamber can be filled by the crystal under consideration, reducing unwanted diffraction from the pressure calibrant.

2.2.3 The diffractometer

A Bruker - Nonius SMART diffractometer equipped with an APEX CCD detector was used to perform the diffraction experiments. Centring a sample in a diamond anvil cell in the X-ray beam for a diffraction experiment is not an easy matter and in this case was performed

using a camera previously focussed on the centre of the X-ray beam. The crystal can be shown to be in the focus of the beam when it can be seen to be clearly in focus when viewed using the camera through both diamond anvils. Figure 2.4 shows the diamond anvil cell mounted on the diffractometer.



Figure 2.4: The diamond anvil cell in place on the diffractometer [18]

2.2.4 Data collection, reduction and model refinement

The use of an area detector for the collection of diffraction data from a diamond anvil cell has several intrinsic problems; not only are diffraction peaks from the sample crystal recorded but the diamond anvils are also large single crystals and give rise to diffraction peaks in their own right, normally of much greater intensity than those of the sample. Powder rings may also be seen from the beryllium backing plates. This makes indexing of the data difficult. Indexing can be performed using the GEMINI programme designed for working with twinned data from Bruker [16]. Once the correct unit cell has been determined integration may be carried out this was done using the SAINT programme [2]. Absorption by the pressure cell was treated using SHADE [17]. Clearly the background of peaks on the beryllium lines or those under diamond anvil peaks will be distorted, but frequently this can be corrected for using an absorption correction programme such as SADABS [3]. As the available angle of reciprocal space is scanned in the course of the experiment absorption of the X-rays by the pressure cell results in areas of space which are inaccessible on each frame of the data and this must be accounted for when using the SAINT integration programme by applying

“masks” which effectively remove all data in the shadowed regions so that the programme no longer expects to find diffracted peaks in those places [18]. This prevents the programme from recording diffracted intensity as zero for areas which would be accessible under “normal” diffraction conditions but which cannot be reached with the diamond anvil cell in position. The data discussed herein were merged using the SORTAV programme [19].

The geometry of the cell severely limits the percentage of reciprocal space which can be sampled and this results in a low data to parameter ratio. For this reason it is frequently not possible to solve the structure of a compound using single crystal methods and a model must be obtained in another way or solved using the direct space methods, more frequently associated with powder diffraction experiments. For the experiments described in this thesis model structures were used from the variable temperature data studies, a high spin structure collected at room temperature being used for the ambient pressure experiment in the diamond anvil cell and a low temperature low spin structure used for the high pressure experiment in which the spin transition had been induced.

Refinement of the models themselves was carried out using the SHELX suite of programmes [3], however due to the low data to parameter ratio a large number of restraints were required, and these are described in Chapter 3, and it was not possible to refine the anisotropic thermal parameters. Full details of a typical X-ray diffraction experiment carried out using this experimental apparatus were described by A. Dawson *et. al.* [18]. I am very grateful to Francesca Fabbiani and Dr. Simon Parsons of the University of Edinburgh for their help with the collection and interpretation of these data.

2.3 High pressure Raman spectroscopy

While determining the pressure inside the diamond anvil cell Raman spectra were collected with varying pressure. Generally speaking peaks below 700 cm^{-1} can be attributed to the metal – ligand modes and can be seen to change dramatically on going through the spin transition. The spectra described in Chapter 3 were collected on a Jobin – Yvon LabRam 300 spectrometer. Excitation was by a He-Ne laser operating at 632.8 nm.

2.4 Powder diffraction

2.4.1 Diffractometers

As discussed in section 1.3.2 diffraction from a polycrystalline sample results in the collapse of the diffraction pattern on to one dimension giving rise to a series of rings of diffracted intensity at specific 2θ angles. Thus it is only necessary to scan through reciprocal space along one coordinate. Powder diffractometers are therefore different from their single crystal counterparts as it is no longer necessary to cover as much of three dimensional reciprocal space as possible.

Laboratory diffractometers

The laboratory data presented in Chapter 7 were collected on a Bruker *D8* Advance diffractometer. X-rays were generated by a sealed tube with a copper target and monochromated using a Ge(111) incident beam monochromator which gives rise to a beam of $K_{\alpha 1}$ radiation with wavelength of 1.54051 Å. An mBraun linear PSD detector was used.

The room temperature data were collected in capillary mode, for which the samples had been lightly ground and sieved and loaded up to about 3.5 cm in length into a glass capillary of 0.5 mm diameter. The capillary was kept spinning throughout the experiment to reduce preferred orientation of the sample. Preferred orientation can arise when, due to the shape of the individual crystallites, a random distribution of particles cannot be achieved this results in some diffraction peaks having greater intensity than others in the pattern and so can make solution and refinement of the data extremely difficult. Data were collected between 4 and 90 ° 2θ , a number of measurements of this angular range were performed and the results summed in order to accumulate the overall intensity.

Variable temperature data were collected in flat plate mode in which the sample was prepared as above but, rather than being loaded into a capillary, was sprinkled on to an aluminium plate to give an even and smooth coverage. Temperature control was achieved using an Oxford Cryosystems PHENIX helium cryostat [20]. The 2θ range for the experiment was recorded every 30 mins with a cooling rate of 17 K hr⁻¹, in effect each pattern is averaged over a change in temperature of 9 K. A series of low temperature datasets were also collected using the PHENIX cryostat and a flat plate sample environment. For these experiments the scans of between 4 and 90° 2θ were repeated a number of times and once again the data were summed.

Synchrotron data collection

Data were collected on $[\text{Fe}(\text{L6})_2](\text{ClO}_4)_2$ and $[\text{Fe}(\text{L6})_2](\text{BF}_4)_2$ (Chapter 7, L6 = 2,6-dipyrazol-1-ylpyrazine) in capillary mode on Station 2.3 at the SRS at Daresbury in the hope of obtaining better resolution and lower absorption than was possible using a laboratory source. The polychromatic incident beam was monochromated using a single crystal Si(111) monochromator, cooled to 30°C using a closed circuit water bath. The width of the monochromatic beam was defined by slits before the sample position. The beam intensity incident on the sample was monitored using a scintillation counter to measure the radiation scattered downward from a 25 μm kapton foil mounted at 45° to the incident beam. This beam monitor allowed correction of the diffracted intensity for the decay of the incident intensity over the lifetime of each beam cycle. The diffracted intensity was measured using an EDR (Enhanced Dynamic Range) [21] detector manufactured by Bede Scientific Instruments and mounted on the 2 θ arm. Maximum flux is obtained on this machine using a wavelength of 1.3 Å. The samples were loaded into 1 mm diameter glass capillaries and cooled to 120 K using an Oxford Cryosystems Cryostream [4]. The beam size was adjusted so that only the cooled portion of the capillary was in the X-ray beam.

Data acquisition was controlled using the PIN CER programme [22,23]. As for the laboratory data, a number of patterns were collected at each temperature and then summed. Data correction for beam decay was carried out using the programme PODSUM [24].

2.4.2 Indexing

The powder patterns were indexed using an in house adaptation of the Visser programme [25] or the DICVOL routine through the DASH programme [26]

2.4.3 Data Solution

Structure solution was carried out using simulated annealing in DASH [26]. In all cases the individual cations and anions were treated as rigid bodies during the solution process. At the end of the simulated annealing process the best solution was chosen as being that with the lowest χ^2 value and which made the most chemical sense on visual inspection and it was this solution that was taken forward as a model for refinement.

2.4.4 Refinement

It was necessary to apply suitable bond length and angle restraints to the models before refinement could take place and values for these were determined using searches of the Cambridge Structural Database, full details of the searches and results will be given in Chapter 7. Rietveld [27] refinement was carried out in the GSAS suite [28] on the solutions imported from DASH, once more full details are given in the relevant chapter.

2.5 Magnetometry

2.5.1 High pressure SQUID magnetometry

Raised pressure magnetometry measurements were performed using a MPMS2 Quantum Design SQUID. The cell used to achieve the raised pressure in this experiment was designed by Dr. Konstantin Kamenev of The Centre for Science at Extreme Conditions, University of Edinburgh (CSEC) and it consists of a tube made from 2% Be copper into which a teflon capsule of 2 mm internal diameter containing the polycrystalline sample, pressure calibrant and pressure medium is placed, Figure 2.5. The pressure is applied by tightening a screw, which forces a piston into the cavity of the cell acting on the sample holder and raising the internal pressure. The cell is then attached to a straw which can then be used in the SQUID in the usual manner. Fluorinert FC77 was used as the pressure medium and the pressure was calibrated using the superconducting transition of a small piece of lead wrapped in teflon tape and placed in the cell with the powdered sample. I am indebted to Fiona Coomer, Dr. Konstantin Kamenev and Prof. Andrew Harrison of CSEC for their help with the collection and interpretation of these data.



Figure 2.5: The pressure cell used for the SQUID measurements at raised pressure.

2.5.2 Photomagnetic measurements

The magnetic measurements were performed using a Spectrum Physics Series 2025 Kr⁺ laser ($\lambda = 532$ nm) coupled *via* an optical fibre to the cavity of a MPMS-55 Quantum Design SQUID magnetometer and the power at the sample surface was adjusted to 5 mW cm⁻². For the photomagnetic experiments, samples consisted of a thin layer of compound the weight of which was obtained by comparison of the thermal spin crossover curve with that of a more accurately weighed sample of the same compound. The method published by Létard *et al* for obtaining LIESST properties was followed. [29,30] After cooling slowly to 10 K the sample, now in the low spin state, was irradiated and the change in magnetism was followed. When the saturation point had been reached, the light was switched off and temperature increased at a rate of 0.3 K min⁻¹ while the magnetisation was measured every 1 K. $T(\text{LIESST})$ was determined by the extreme of the $\partial\chi_M T/\partial T$ vs. T curve for the relaxation. This work was performed in collaboration with Prof. Jean-François Létard and his team of the Groupe des Sciences Moléculaire, Institut de Chimie de la Matière Condensée de Bordeaux.

2.6 References

1. SMART-1000 CCD, Bruker AXS, Madison, Wisconsin, U.S.A.
2. G.M. Sheldrick, (1997). SHELXS-97, SHELXL 97. Program for the Refinement of Crystal Structures. University of Göttingen, Germany
3. G. M. Sheldrick, (1998). SHELXTL Version 5.1. Bruker AXS., Madison, Wisconsin, U.S.A.
4. Cryostream Cooler, Oxford Cryosystems Ltd, Oxford, UK
5. A. E. Goeta, L. K. Thompson, C. L. Sheppard, S. S. Tandon, C. W. Lehmann, J. Cosier, C. Webster and J. A. K. Howard, *Acta. Crystallogr.*, Sect. C, 1999, **55**, 1243 - 1246
6. Oxford Helix. Oxford Cryosystems Ltd, Oxford, U.K
7. A. E. Goeta, A. Beeby and A. L. Thompson, *J. Appl. Cryst.*, 2004, **37**, 652 - 653
8. A. Van Valkenburg, *Diamond Res.*, 1964, 17 - 20
9. L. Merrill and W. A. Bassett, *Rev. Sci. Instrum.*, 1974, **45**, 290 - 294
10. G. J. Piermarini, S. Block, J. D. Barnett; *J. Appl. Phys.*, 1973, **44**, 5377 - 5382
11. J. D. Barnett and C. D. Bosco, *J. Appl. Phys.*, 1969, **40**, 3144 - 3150
12. R. J. Angel, *Reviews in Mineralogy and Geochemistry*, volume 41: *High-Temperature and High-pressure crystal chemistry*, Ed; R. M. Hazen and R. T. Downs, Mineralogical Society of America 2002

13. J. H. Eggert, D. K. A. Goettel and I. F. Silvera, *Phys. Rev. B*, 1989, **40**, 5724 - 5732
14. J. H. Eggert, D. K. A. Goettel and I. F. Silvera, *Phys. Rev. B*, 1989, **40**, 5733 - 5738
15. Y. Sato-Sorenson, *In high pressure research in mineral physics*, M. Maghnani, Y. Syono (eds) p53
16. R. A. Sparks, *GEMINI*, Version 1.05, Bruker AXS Inc., Madison, Wisconsin, USA, 2000
17. S. Parsons, SHADE, 2004, The University of Edinburgh, Scotland
18. A. Dawson, D. R. Allen, S. Parsons and M. Ruf, *J. Appl. Cryst.*, 2004, **37**, 410 - 416
19. R. H. Blessing, *J. Appl. Cryst.*, 1997, **30**, 421 - 426
20. V. A. Money, I. R. Evans, M. A. Halcrow, A. E. Goeta and J. A. K. Howard, *Chem. Commun.*, 2003 158 - 159
21. S. Cockerton and B. K. Tanner, *Adv. X-ray Anal.*, 1995, **38**, 371 - 376
22. M.C. Miller, K.S. Ackroyd, G. Oszlanyi (1994). Daresbury Preprint DL/CSE/P29E and presented at ESONE 8th International Conference on Real Time Data (RT94), Dubna, Russia.
23. C.C. Tang, M.C. Miller, S.M. Clark, M.A. Player and G.R.G. Craib, *J. Synchrotron Rad.*, 1996, **3**, 6-13
24. C. C. Tang, M. C. Miller and E. J. Maclean, *Station 2.3 Manual*, <http://srs.dl.ac.uk/XRD/2.3/Manual/manual.html>
25. J. W. Visser, *J. Appl. Cryst.*, 1969, **2**, 89 - 95
26. Cambridge Crystallographic Data Centre, (2002). DASH. Version 2.1. Cambridge Crystallographic Data Centre, 12, Union Road, Cambridge, CB2 1EZ, UK
27. H. Rietveld, *J. Appl. Cryst.*, 1969, **2**, 65 - 71
28. A. C. Larson and R. B. von Dreele (1994). GSAS. LANSCE, Los Alamos National Laboratory, NM, USA
29. J-F Létard, L. Capes, G. Chastanet, N. Moliner, S. Létard, J. A. Real and O. Kahn, *Chem. Phys. Lett*, 1999, **313**, 115 - 120
30. J-F. Létard, G. Chastanet, O. Nguyen, S. Marcén, M. Marchivie, P. Guionneau, D. Chasseau, P. Gütllich, *Montash. Chem.*, 2003, **134**, 165 - 182

3 The thermal, light and pressure induced spin transitions in $[FeL_2](BF_4)_2$ and related compounds

3.1 Introduction

This chapter describes work carried out on three complexes containing the 2,6-di(pyrazol-1-yl)pyridine ligand, L1, Figure 3.1. It is easy to modify the ligand systematically and this method has been used to examine the effect that changing ligand field strength has on the form and temperature of the spin transition [1]. SQUID magnetometry shows that $[FeL_2](BF_4)_2$ undergoes an abrupt thermal spin transition with a hysteresis width of three degrees centred at 259 K [2]. These features of the thermal spin transition, and the relatively high temperature at which it occurs, mean that this compound has potential for use in the applications discussed in Chapter 1. Interestingly, on changing the anion from BF_4^- to PF_6^- the compound undergoes sufficient structural change that the spin transition no longer takes place between 300 K and 10 K. The solid state structure of $[CoL_2](BF_4)_2$ is isostructural with that of the iron (II) analogue. It is well known that cobalt complexes of this type may be used as reference compounds to deconvolute the effect of the spin transition from that of the coincident change in temperature on the structure of spin crossover materials [3]. The volumes of cobalt (II) complexes are very similar to those of iron (II) and it is this fact which makes this type of comparison applicable.

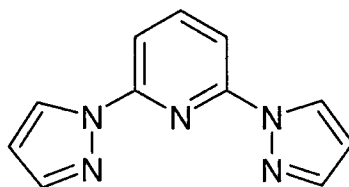


Figure 3.1: L1 = 2,6-di(pyrazol-1-yl)pyridine

Over the course of the following chapter the results of a variable temperature crystallographic study into the structures of $[FeL_2](BF_4)_2$, $[FeL_2](PF_6)_2$ and $[CoL_2](BF_4)_2$ will be discussed along with the effect of irradiation with laser light at low temperature on the structure of $[FeL_2](BF_4)_2$. The crystallographic results are supported by magnetic susceptibility measurements performed with and without light irradiation. The effect of increased pressure on the structure of $[FeL_2](BF_4)_2$ and on its magnetisation will also be described.

3.2 Experimental

3.2.1 Synthesis

All three compounds were synthesised according to literature methods by Dr. Malcolm Halcrow of the University of Leeds [2].

3.2.2 Crystallography

Variable temperature crystallographic data were collected as described in Chapter 2. The structures were solved by direct methods and refined on F^2 using full matrix least-squares methods within the SHELXTL suite. All non-hydrogen atoms were refined anisotropically. The hydrogen atoms were placed geometrically and treated with a riding model. For the LIESST (Light Induced Excited Spin State Trapping) experiments the samples were irradiated for between five and ten minutes whilst on the diffractometer using a He – Ne laser ($\lambda = 632.8$ nm, 25 mW). Selected crystallographic parameters are presented in Tables 3.1, 3.4 and 3.6.

For the high pressure crystallographic experiment a yellow block shaped crystal with dimensions of $0.25 \times 0.25 \times 0.15$ mm³ was mounted with a very small ruby chip in a diamond anvil cell using mineral oil as the pressure medium. The pressure inside the cell was determined by following evolution of the Raman spectra of the ruby chip. Selected crystallographic parameters are in Table 3.7.

3.2.3 Variable pressure Raman spectroscopy

Raman spectra were collected at differing pressures on the same crystal described above while determining the pressure inside the diamond anvil cell for the crystallographic experiment, as described in Chapter 2. Peaks below 700 cm⁻¹ were assigned to the Fe-N stretching modes while those above are due to the other modes of the ligand and counterions.

3.2.4 High pressure SQUID magnetometry

Raised pressure magnetometry measurements were performed using a MPMS2 Quantum Design SQUID. Pressure was achieved using the pressure cell previously described in

Chapter 2 and the pressure was calibrated using the super conducting transition of a fragment of lead. The pressure medium was Fluorinert FC77 oil.

3.2.5 Photomagnetic measurements

The magnetic measurements were performed using a Spectrum Physics Series 2025 Kr⁺ laser ($\lambda = 532$ nm) coupled via an optical fibre to the cavity of a MPMS-55 Quantum Design SQUID magnetometer. The data show no evidence of the sample being heated by the laser: no sudden increase in magnetic signal on turning off the laser was observed.

3.3 Results and discussion

Empirical formula	C ₂₂ H ₁₈ B ₂ F ₈ FeN ₁₀	C ₂₂ H ₁₈ B ₂ F ₈ FeN ₁₀	C ₂₂ H ₁₈ B ₂ F ₈ FeN ₁₀	C ₂₂ H ₁₈ B ₂ F ₈ FeN ₁₀
Formula weight	651.93	651.93	651.93	651.93
Temperature/K	290(2)	120(2)	30(2)	30(2)
Spin state	HS-1	LS	LS	HS-2
Shape	Prism	Prism	Plate	Block
Colour	Yellow	Brown	Brown	Yellow
Crystal system	Monoclinic	Monoclinic	Monoclinic	Monoclinic
Space group	P2 ₁	P2 ₁	P2 ₁	P2 ₁
a/ Å	8.500(2)	8.452(2)	8.4098(4)	8.462(2)
b/ Å	8.516(2)	8.518(2)	8.4731(4)	8.370(2)
c/ Å	19.067(4)	18.371(4)	18.2909(9)	18.759(4)
β/ deg	95.67(3)	98.37(3)	98.575(1)	97.15(3)
Volume/ Å³	1373.3(5)	1308.6(5)	1288.8(1)	1318.1(5)
Z	2	2	2	2
D_c/ mg/m³	1.577	1.655	1.680	1.640
μ/ mm⁻¹	0.637	0.669	0.679	0.663
Crystal size / mm	0.68 x 0.22 x 0.10	0.68 x 0.22 x 0.10	0.20 x 0.18 x 0.06	0.24 x 0.20 x 0.12
Theta range / deg	1.07 to 27.46	1.12 to 27.45.	2.65 to 27.45	2.78 to 27.46
Reflections collected	9240	8591	11476	11729
Independent reflections	6100	4676	5434	5269
R_(int)	0.0206	0.0191	0.0335	0.0281
wR(F²)(all data)	0.1204	0.0619	0.0691	0.0759
R(F)(all data)	0.0595	0.0267	0.0358	0.0310
refined parameters	460	388	388	388
GOF	1.020	1.085	1.023	1.058
$\Delta\rho_{\min,\max}$ / e.Å⁻³	0.40 and -0.22	0.36 and -0.30	0.43 and -0.45	0.58 and -0.64

Table 3.1: Crystallographic data for [FeL₁₂](BF₄)₂. Where HS-1 is the high spin ground state, LS is the low spin state and HS-2 is the metastable high spin state resulting from the LIESST effect.

3.3.1 Variable temperature crystallographic study of [FeL₁₂](BF₄)₂

X-ray diffraction data were collected on a single crystal of [FeL₁₂](BF₄)₂ at 290 K, 120 K and 30 K. [FeL₁₂](BF₄)₂ crystallises in the monoclinic space group P2₁ and there is no crystallographic phase change over the temperature range studied. The asymmetric unit consists of one complex cation and two counter anions. The anions were found to be thermally disordered at 290 K and there was no evidence of disorder at 120 K or 30 K. The iron atom is bound equatorially to two ligands through three of the ligands' five nitrogen atoms, Figure 3.2. For each ligand the Fe–N(pyridine) bond is the shortest. The cation has approximate D_{2d} symmetry with the N3 – Fe1 – N8 angle approaching 180°. Selected crystallographic data are presented in Table 3.1.

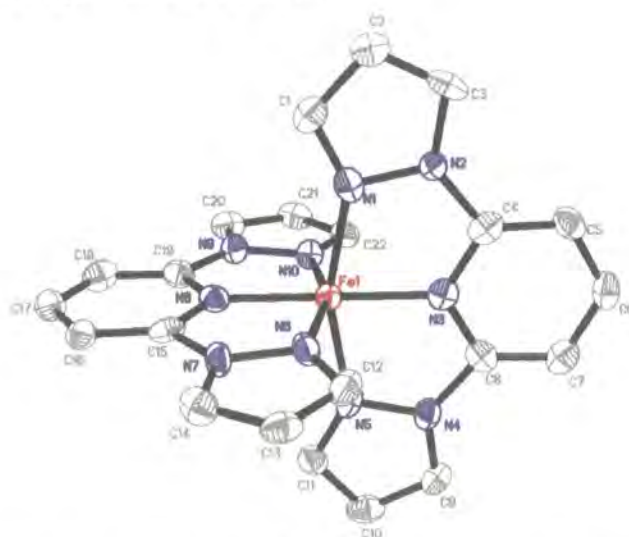


Figure 3.2: Crystal structure of [FeL₁₂]²⁺ at 30 K in the low spin state. Hydrogen atoms have been omitted for clarity and ellipsoids are shown at 90% probability

As described in section 1.1.2 the shape of the spin transition curve is closely linked to cooperativity between iron centres and so to the degree of intermolecular bonding. The more intermolecular bonding that is present in the system, the more abrupt the transition and the more likely it is to show hysteresis. [FeL₁₂](BF₄)₂ contains a high degree of edge to face and face to face π interactions which are orientated along the *a* and *b* axis directions and weak hydrogen bonding between CH groups in the ligand and the fluorine atoms of the anions; this hydrogen bonding lies along the crystallographic *c* axis. These bonds link the molecules into a three dimensional net and provide the communication between iron centres which gives rise to the abrupt transition and the hysteresis loop.

On cooling the crystal below the temperature of the spin transition, there is a decrease in the mean metal – ligand (Fe – N) bond length of 0.213 Å from 2.166(6) Å at 290 K to 1.953(2) Å

at 120 K. This is within the range of reductions reported for similar spin crossover compounds and agrees well with the previously published data [2]. As the metal ligand bonds decrease, there is an associated decrease in the volume of the coordination polyhedron (V_p) of 2.771 Å³ or 22% between 290 K and 120 K. Compounds in the low spin state generally approach ideal octahedral symmetry more closely than when in the high spin state, this is true of [FeL₁₂](BF₄)₂ and can be illustrated by examining the symmetry parameters Σ and ν introduced by Guionneau *et al* [3,4], Equations 3.1 and 3.2. Both of the terms Σ and ν demonstrate the deviation of the coordination octahedron from ideal geometry, although the latter also uses information on the dimensions of that deviation, and both are equal to zero for an ideal octahedron. The increase in regularity on going from the high spin state at 290 K to the low spin state at 120 K and 30 K is clearly illustrated for this compound by the decrease in these values, Table 3.2. Σ and ν are well suited for use in the analysis of this class of materials, as they show a large change on going through the spin transition, but are only very slightly affected by changes in temperature. This means that these parameters can be used to determine approximately the percentage of the compound that is either in the high or the low spin state. A demonstration of this is the fact that the values of both parameters are the same within error at both 120 K and 30 K, when it is certain from magnetic data that [FeL₁₂](BF₄)₂ has been converted completely to the low spin state.

$$\Sigma = \sum_{i=1}^{12} |90 - \phi_i| \quad \text{Equation 3.1}$$

Where ϕ_i is the deviation from 90° of each of the twelve cis angles in the octahedron.

$$\nu = 100 \left(1 - \pi \frac{V_p}{V_s} \right) \quad \text{Equation 3.2}$$

Where V_p is the volume of the octahedron and V_s is the volume of the equivalent sphere.

$$V_s = \frac{4}{3} \pi r^3 \quad \text{Equation 3.3}$$

Where r is the mean metal - ligand distance

T/K	Spin state	Unit cell volume /Å ³	Mean Fe-N /Å	ν / %	Σ °	Bite angle°	V_p / Å ³
290	HS-1	1373.3(5)	2.166(6)	8.53	151.2	73.4(2)	12.394
120	LS	1308.6(5)	1.953(2)	3.11	86.03	80.09(8)	9.623
30	LS	1288.8(1)	1.950(2)	3.10	86.11	80.08(8)	9.580
30	HS-2	1318.1(5)	2.165(2)	8.89	149.03	73.52(7)	12.327

Table 3.2: Selected parameters for [FeL₁₂](BF₄)₂ Where HS-1 is the high spin ground state, LS is the low spin state and HS-2 is the metastable high spin state resulting from the LIESST effect.

Anisotropy in the change in the unit cell parameters and iron – ligand bond lengths during the spin transition is also of interest and may be related to the molecular and crystallographic directions in which the spin transition has the most effect. The crystallographic c parameter is seen to be subject to a far greater change than either the a or b parameters; this may be due, in this case, to the iron to pyridine nitrogen bonds, Fe-N3 and Fe-N8, which lie parallel to the c axis and undergo the greatest change on going through the spin transition. It is also possible that the differences in intermolecular bonding cause the differences in the effect of the spin crossover in the different crystallographic directions, there being weak hydrogen bonding along the c direction and π interactions along the a and b directions.

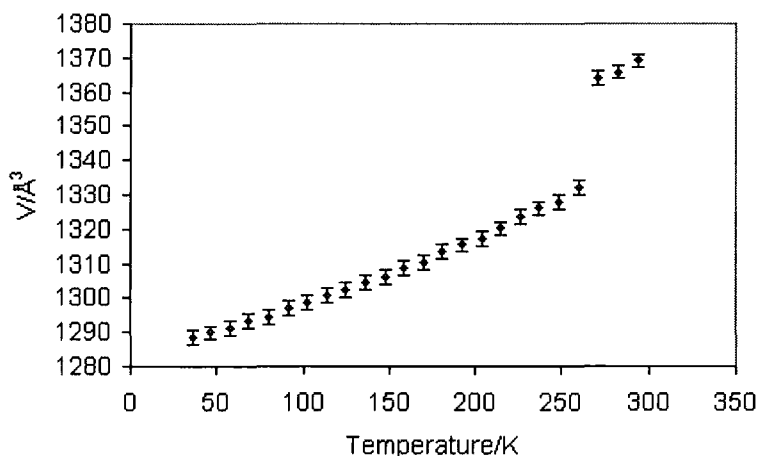


Figure 3.3: Variation of unit cell volume with temperature for $[FeL1_2](BF_4)_2$ determined from powder diffraction data

The crystallographic structure at 30 K is identical to that determined at 120 K with the expected minor alterations due to thermal contraction. It was necessary to flash freeze the single crystals used in this experiment from room temperature by quenching to 30 K in a stream of chilled helium, as they were so badly damaged during slow cooling as to be unsuitable for use. This raised the question as to why the crystals were destroyed by slow cooling, whereas they survived the relatively violent process of flash freezing. It was thought that a crystallographic phase transition might be taking place between 120 K and 30 K and that rapid flash freezing inhibited this transition by trapping the phase stable at 120 K. In order to test this possibility powder X-ray diffraction data were collected every 9 K between 300 K and 30 K on both warming and cooling and the unit cell parameters were refined using the structural models obtained from the single crystal studies. Figure 3.3 shows the variation of the unit cell volume with temperature on cooling, the volume decreases sharply at 260 K which is in good agreement with the temperature of the spin transition determined by SQUID

magnetometry. There is then a steady decline from 250 K to 30 K which has the same slope as the portion of the graph before the spin transition. There is no evidence of a phase transition which might be responsible for the destruction of the single crystals on cooling. Damage of the crystals during slow cooling on the single crystal diffractometer is most likely a result of the crystal mounting conditions. An added benefit of having performed a powder diffraction study of this sort, is that it confirms that the single crystals used for analysis are representative of the bulk material; an important consideration for technical applications.

3.3.2 Comparison of [FeL₂](BF₄)₂ and [FeL₂](PF₆)₂

Data were also collected on [FeL₂](PF₆)₂ at 290 K, 120 K and 30 K. This compound was found not to be isomorphous with [FeL₂](BF₄)₂ but to crystallise in the monoclinic space group C2/c with the asymmetric unit consisting of half a cation and one anion and the unit cell containing four formula units. The iron atom is situated on a two fold axis and the cation has C₂ symmetry. There is no change in space group over the temperature range under consideration and the compound remains in the high spin state throughout. The Fe - N bond lengths remain indicative of a high spin material over the whole temperature range and the symmetry parameters Σ and ν are also unchanged, Table 3.3.

T/K	Spin state	Unit cell volume /Å ³	Mean Fe-N /Å	ν / %	Σ /°	Bite angle /°	V_p /Å ³
290	HS-1	2827.5(1)	2.194(8)	17.76	191.3	71.9(3)	11.581
120	HS-1	2752(1)	2.199(2)	18.62	198.0	71.87(7)	11.538
30	HS-1	2713.2(9)	2.197(4)	18.85	200.2	72.0(1)	11.459

Table 3.3: Selected parameters for [FeL₂](PF₆)₂

It is well documented that small changes in the composition of spin crossover materials can have a very large effect on the temperature and nature of the spin transition and this is illustrated by [FeL₂](PF₆)₂ and [FeL₂](BF₄)₂. However it is unlikely that the nature of the anion is solely responsible for the suppression of the spin transition. Changing the anion would change the intermolecular bonding and thus the cooperativity resulting in a different shaped transition curve; more gradual with a narrower hysteresis loop if the communication were reduced and a wider hysteresis loop, if it were improved. As spin transitions take place in the absence of cooperative effects, for example in dilute metal systems or solution, it follows that another effect must be responsible for the repression of the spin transition in [FeL₂](PF₆)₂. Halcrow *et al* have determined that the C₂ symmetry of this salt results in a total loss of the degeneracy of the metal *d* orbitals, reducing the energy required to promote electrons to the high spin state and leading to a gain of 400 cm⁻¹ in the ligand field stabilisation energy relative to the D_{2d} form [2]. The C₂ form is favoured by the small ligand

bite angle formed by the 2,6-di(pyrazol-1-yl)pyridine ligand. If this were the only consideration, both salts would have the C₂ form and clearly the nature of the anion therefore plays a critical role in determining the geometry of the cation. That the PF₆ salt favours the high spin state may also be seen by the longer metal ligand bond lengths.

Empirical formula	C ₂₂ H ₁₈ F ₁₂ FeN ₁₀ P ₂	C ₂₂ H ₁₈ F ₁₂ FeN ₁₀ P ₂	C ₂₂ H ₁₈ F ₁₂ FeN ₁₀ P ₂
Formula weight	768.25	768.25	768.25
Temperature/K	290	120	30
Spin state	HS-1	HS-1	HS-1
Shape	Irregular	Irregular	Irregular
Colour	Yellow	Yellow	Yellow
Crystal system	Monoclinic	Monoclinic	Monoclinic
Space group	C2/c	C2/c	C2/c
a/ Å	14.648(3)	14.260(3)	14.128(3)
b/ Å	9.481(2)	9.5035(19)	9.490(2)
c/ Å	20.600(4)	20.582(4)	20.516(4)
β/ deg	98.76(3)	99.33(3)	99.47(3)
Volume/ Å³	2827(1)	2752.4(10)	2713.2(9)
Z	4	4	4
D_c/ Mg/m³	1.805	1.854	1.881
μ/ mm⁻¹	0.762	0.783	0.794
Crystal size / mm	0.20 x 0.18 x 0.14	0.20 x 0.18 x 0.14	0.18 x 0.16 x 0.10
Theta range / deg	2.57 to 28.99	2.59 to 27.46	2.60 to 27.44
Reflections collected	9334	9162	7759
Independent reflections	3739	3142	2924
R_(int)	0.0163	0.0315	0.0426
wR(F²)(all data)	0.0878	0.0896	0.1438
R(F)(all data)	0.0379	0.0468	0.0843
Refined parameters	322	213	213
GOF	1.045	1.155	1.178
Δρ_{min,max} / e.Å⁻³	0.30 and -0.43	0.49 and -0.50	0.66 and -0.73

Table 3.4: Selected crystallographic parameters for [FeL₁₂](PF₆)₂. Where HS-1 is the high spin ground state.

3.3.3 [CoL₁₂](BF₄)₂

It is of paramount importance for complete understanding of the spin crossover phenomenon to be able to determine exactly what effect the transition has on the structure of the material under consideration. When studying the thermal spin transition, structural data will always be affected by the change in temperature on going through the transition, particularly as it is necessary not to collect data at a temperature very close to that of the spin transition in order to ensure that the transition is complete. In order to decouple the effect of the transition from that of temperature, a second compound may be used which is as similar as possible to the spin crossover compound, excepting the presence of the spin transition. Clearly [FeL₁₂](PF₆)₂ may not be used for this comparison as it is structurally substantially different from

[FeL₁₂](BF₄)₂. Although there have been many spin crossover systems containing Co (II), it is normally possible to use the Co (II) analogue of an Fe (II) spin crossover compound for this type of study, as the ligand fields required to promote a spin transition are different for the two metal ions. Cobalt has been used often for this work, although Sanner *et al* showed during their work on the dilute metal system, [Fe_xM_{1-x}(2-pic)₃]Cl₂·EtOH, (2-pic = 2-(aminomethyl)pyridine), that the Zn (II) lattice was of a more similar size to the Fe (II) [5]. It is assumed that the contraction or expansion of the cobalt compound on heating or cooling is the same as that of the iron. Once the thermal behaviour of the cobalt compound has been determined, this knowledge may be applied to the spin crossover compound and the precise effect of the spin transition determined.

T/K	Spin state	Unit cell volume /Å ³	Mean Co-N /Å	v/ %	Σ/°	Bite angle/°	V _p /Å ³
120	HS-1	1342.65(8)	2.128(4)	10.66	133.37	75.2(1)	11.4950
30	HS-1	1328.1(5)	2.126(4)	7.136	133.46	75.2(1)	11.898

Table 3.5: Selected parameters for [CoL₁₂](BF₄)₂. v and Σ are defined in section 3.3.1

[CoL₁₂](BF₄)₂ was found to be isostructural with [FeL₁₂](BF₄)₂, crystallising in the monoclinic space group P2₁. It remains in the high spin state throughout the temperature range and this is demonstrated by the small changes in unit cell volume, metal ligand bonds and symmetry parameters. Table 3.5. The variation in unit cell volume with temperature is shown in Figure 3.4 and it can be seen that there is no discontinuity in the cooling curve. There is a slight decrease in the gradient of the curve at very low temperatures, which is probably due to the compound reaching its limit of compression due to thermal contraction.

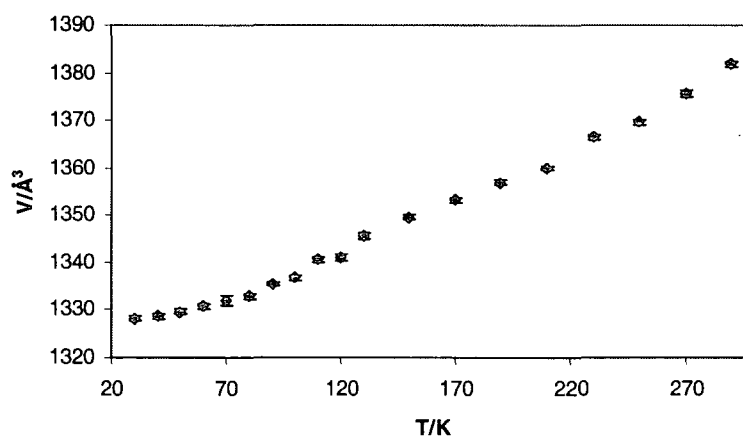


Figure 3.4: Variation of unit cell volume with temperature [CoL₁₂](BF₄)₂

Examination of the straight part of the cooling curve for [CoL₁₂](BF₄)₂, shows a decrease in unit cell volume of 40.8 Å³ or 2.9% on cooling between 290 K and 120 K. This implies a ΔV_{SC} of approximately 2% of the room temperature unit cell volume for [FeL₁₂](BF₄)₂, which is slightly lower than that estimated previously from examination of the temperature

dependence of the unit cell parameters of [FeL1₂](BF₄)₂ alone. It has been assumed above, that the anisotropy in the changes in bond length with temperature in [FeL1₂](BF₄)₂, is due to the spin transition rather than a preferred direction for contraction in the crystal lattice itself. That the much larger decrease along the *c* parameter is due to the spin transition, may be seen by comparison with the changes in the unit cell parameters of [CoL1₂](BF₄)₂ with temperature. On cooling from 290 K to 120 K the *a* parameter undergoes a decrease of 0.048 Å (0.6%), the *b* parameter of 0.088 Å (1.0%) and the *c* parameter 0.206 Å (1.1%). This is a marked difference to [FeL1₂](BF₄)₂ in which over the same temperature range the *a* parameter decreases by 0.048 Å (0.6%), the *b* parameter remains unchanged and the *c* parameter decreases by 0.696 Å (3.7%). This comparison suggests that the *a* parameter is effectively unaffected by the spin transition, decreasing by the same amount as observed for the cobalt analogue, that the *b* parameter actually increases slightly on going through the transition and that the *c* parameter is most effected. The spin transition probably has the greatest effect on the *c* parameter as the iron – pyridine nitrogen (N3 and N8) bonds are those which undergo the greatest contraction on going from the high to the low spin state.

Empirical formula	C ₂₂ H ₁₈ B ₂ CoF ₈ N ₁₀	C ₂₂ H ₁₈ B ₂ CoF ₈ N ₁₀
Formula weight	655.01	655.01
Temperature/K	120(2)	30(2)
Spin state	HS-1	HS-1
Shape	Plate	Plate
Colour	Red	Red
Crystal system	Monoclinic	Monoclinic
Space group	P2 ₁	P2 ₁
a/ Å	8.4897(3)	8.465(2)
b/ Å	8.4868(3)	8.451(2)
c/ Å	18.8031(6)	18.751(4)
β/ deg	97.669(2)	98.05(3)
Volume/ Å³	1342.65(8)	1328.1(5)
Z	2	2
D_c/ Mg/m³	1.620	1.638
μ/ mm⁻¹	0.729	0.737
Crystal size / mm	0.28 x 0.16 x 0.05	0.28 x 0.16 x 0.05
Theta range / deg	1.09 to 27.49	2.65 to 28.11
Reflections collected	9694	7737
Independent reflections	6047	4755
R_(int)	0.0570	0.0449
wR(F²)(all data)	0.1254	0.1068
R(F)(all data)	0.0704	0.0622
Refined parameters	388	388
GOF	1.063	1.050
Δρ_{min,max} / e.Å⁻³	0.51 and -0.51	0.48 and -0.52

Table 3.6: Selected crystallographic parameters for [CoL1₂](BF₄)₂. Where HS-1 is the high spin ground state.

3.3.4 The LIESST effect in [FeL1₂](BF₄)₂

Although the LIESST (Light Induced Excited Spin State Trapping) effect is a subject of great interest in the field of spin crossover research, very little was hitherto known about the structure of the metastable high spin state (HS-2) formed on irradiation. On irradiation with laser light, normally in the green region of the spectrum, a metastable high spin state may be formed which, at low temperatures (generally < 50 K), can have a lifetime of several days. The reverse transition, reverse-LIESST, may be caused by irradiation with red light. Examination of the structure of the HS-2 state allows a direct comparison of the low and high spin states, without the complication of having to take into account the effects of temperature, allowing direct isolation of the effect of the spin transition on the structure. Since its discovery by Decurtins *et al* in the 1980s LIESST has been found to be relatively common for iron (II) compounds with the metastable state stabilised by the large difference in bond lengths between the high and low spin states [6]. For this reason it is postulated that long lived excited states will not be accessible in compounds containing cobalt (II).

The first crystallographic study of this phenomenon was performed by Kusz *et al* in 2000 where they undertook a study of the effect of irradiation on the unit cell parameters of [Fe(ptz)₆](BF₄)₂ (ptz = propyltetrazole) [7]. Later the same authors reported a similar study on [Fe(mtz)₆](BF₄)₂ (mtz = methyltetrazole) in which they describe the collection of data for a full structural analysis, but the results of this have never been published [8]. More recent results have included the full structural analysis of [Fe(phen)₂(NCS)₂] [9] and [Fe(phen)₂(NCSe)₂] [10] (where phen = 1,10-phenanthroline) however, despite these advances, information on the effect of light irradiation on the structure of spin crossover materials remains relatively rare.

Excited state crystallographic study

After irradiation with red laser light ($\lambda = 632.8$ nm, 25 mW) at 30 K for ten minutes the crystal of [FeL1₂](BF₄)₂ had changed colour from brown to yellow indicating that at least a partial spin transition had taken place. A full data collection showed that the crystal was in the high spin state (HS-2) as evidenced by the increase in unit cell volume of 29.3 Å³ or 2.3 %. This increase is slightly greater than that predicted for the thermal spin transition by comparison with the thermal behaviour of [CoL1₂](BF₄)₂ and more in line with the 2.6 % suggested by examination of the variation of unit cell parameters alone [2]. The similarity of ΔV_{sc} for the thermal and the light induced transition is unusual; the two studies which attempted a comparison, recorded a significant difference between ΔV_{sc} for the thermal transition and ΔV_{sc} for the light induced transition [7,9]. A change in unit cell volume alone

does not prove the presence of a spin transition and further evidence has been provided by the increase in Fe-N bond lengths of 0.213 Å from 1.950(2) Å to 2.165(2) Å, the latter being indicative of a high spin iron (II) complex. The HS-2 state still occupies the monoclinic space group P2₁, with the iron (II) ion bound equatorially to two ligands through three of their five nitrogen atoms. There is no evidence of disorder in the BF₄⁻ anions. That conversion to the HS-2 state was quantitative, is demonstrated by the Σ and ν parameters being the same at both 290 K and at 30 K after irradiation (Table 3.2). The volume of the coordination polyhedron shows only a small decrease on going from the HS-1 state to the HS-2 state, which is to be expected from the difference in temperature. The unit cell parameters show the same pronounced anisotropy on going from the LS to the HS-2 state as they do on going through the thermal spin transition. The change in the *c* parameter is more than five times that in either *a* or *b* and the Fe-N(pyridine) bond lengths change by 0.233 Å, while those from the pyrazole rings to the iron atoms increase by only 0.207 Å.

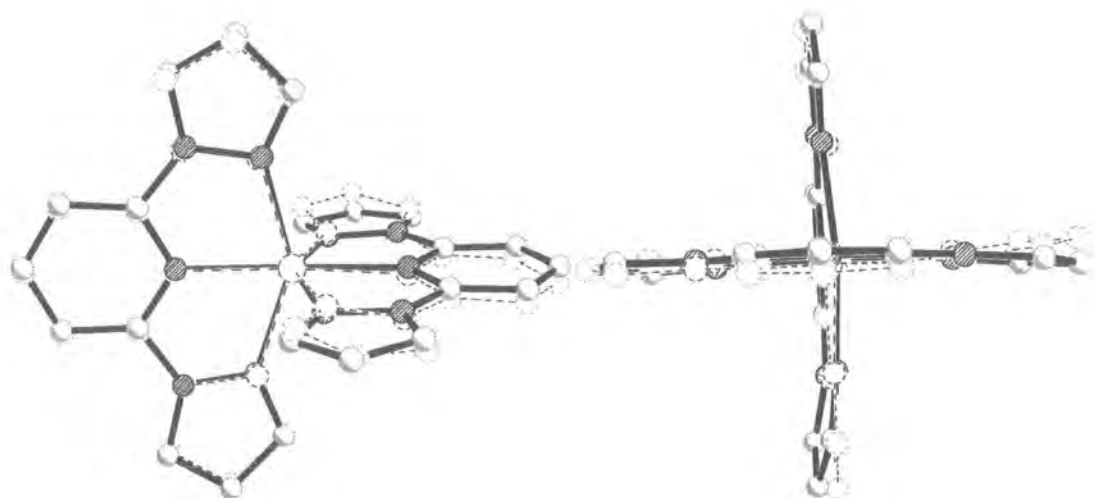


Figure 3.5: Two views of the overlay of HS-1 and HS-2 of [FeL₁₂](BF₄)₂, showing the minor differences in ligand twist. The solid lines are for the HS-2 structure at 30 K and the dashed lines HS-1 at 290 K.

Comparison of the structure of the HS-1 state at 290 K with the HS-2 state at 30 K adds to the conformation provided by the Σ and ν parameters that both high spin states are very similar, Figure 3.5. Bond lengths throughout the ligands are the same in the HS-2 state as in the HS-1 state. It can be seen from the overlay diagrams (Figure 3.5) that the ligands twist slightly more out of the plane in the HS-1 state. Despite these very small differences, the two high spin states are essentially identical. The smaller unit cell volume determined for the metastable state at 30 K is most likely due to the change in temperature and the consequent decrease in thermal motion. Guionneau *et al* noted that the metastable state of

$[Fe(phen)_2(NCS)_2]$ shows stronger intermolecular interactions than the HS-1 state, indicating that it was more cooperative and the same behaviour was noted during the study of $[Fe(phen)_2(NCSe)_2]$ by MacLean *et al* [9,10]. There is no evidence of substantial changes taking place in the intermolecular bonding of the HS-2 state in comparison to that of the HS-1, however the face to face π - π interactions between neighbouring cations are shorter in the HS-2 state, probably as a result of the decrease in temperature.

The critical LIESST temperature ($T(LIESST)$) has been defined by Létard *et al* as the temperature at which 50% of the molecules are in the HS-2 state; this definition relies upon following a very strict experimental procedure [11,12]. In the majority of cases, the HS-2 state is only stable at relatively low temperatures with the highest recorded LIESST temperature being 130 K. Clearly in order for this type of material to be applied in devices, $T(LIESST)$ must be as close to ambient temperature as possible. The evolution of unit cell parameters with temperature was monitored on warming after irradiation at 30 K and the subsequent full data collection. There was a sharp decrease in unit cell volume between 75 K and 80 K which indicates that $T(LIESST)$ should lie between these two values. This temperature range coincides with the change in colour of the crystal from yellow in the HS-2 state to brown. This value is of necessity only an estimate of the $T(LIESST)$ as we were unable to obtain the conditions required under the definition described above using the available diffraction equipment.

Trapping of the high spin state by thermal quenching

In a number of cases it has been shown to be possible to trap a spin crossover material in the high spin state by cooling very rapidly to very low temperatures [13]. This quenching provides a different way of obtaining bistability at low temperatures in the absence of light. As has been described above, it was necessary to flash freeze the crystals of $[FeL1_2](BF_4)_2$ from room temperature to 30 K. That the low spin state was obtained by this procedure proves that in this case the high spin state is not trapped by quenching. The comparatively high temperature of the spin transition may be responsible for the absence of spin state trapping on quenching.

Photomagnetic behaviour

A detailed magnetic study was carried out to examine the effect of the irradiation on the spin state of $[FeL1_2](BF_4)_2$. As reported previously the $[FeL1_2](BF_4)_2$ was found to undergo an abrupt spin transition with a 3 K hysteresis loop centred at 259 K [2]. The magnetic properties of $[FeL1_2](BF_4)_2$ both with and without light irradiation are shown in Figure 3.6a.

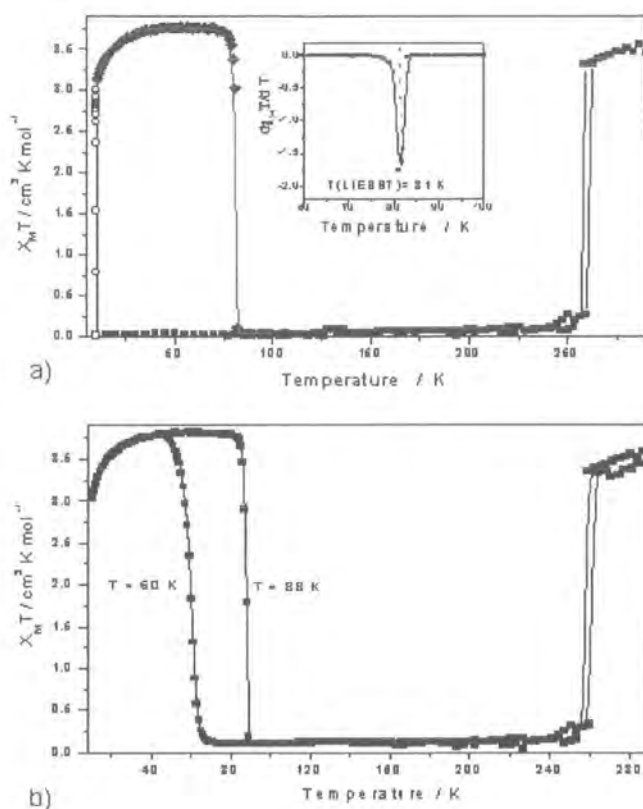


Figure 3.6: a) Temperature dependence of $\chi_M T$ for [Fe(L1)₂](BF₄)₂. ■ = data recorded in the cooling and warming mode without irradiation; ○ = data recorded with irradiation at 10 K; ♦ = T(LIESST) measurement, data recorded in the warming mode with the laser turned off after irradiation for one hour; b) LITH experiment, the temperature dependence of $\chi_M T$ recorded in the warming and cooling modes with irradiation

The values of $\chi_M T$ at 300 K and 30 K are indicative of an iron (II) complex completely in the high and low spin state respectively. Under irradiation at 10 K with a Kr⁺ laser ($\lambda = 532$ nm) the $\chi_M T$ value is seen to increase, when a photostationary point is reached the laser was switched off and the temperature raised at a rate of 0.3 K min⁻¹. Initially $\chi_M T$ is seen to increase slightly due to zero field splitting, the anisotropy of the iron ion in an octahedral field, before levelling off, the plateau has a similar value to that at room temperature. There is an abrupt decrease in magnetisation from 3.0 cm³ K mol⁻¹ to nearly 0 cm³ K mol⁻¹. This decrease indicates the complete relaxation of the compound from the HS-2 to the LS state. T(LIESST) is estimated from the extreme of the $\partial\chi_M T/\partial T$ versus T curve for the relaxation as being 81 K which is in good agreement with the estimation made using X-ray diffraction. The shape of the LIESST curve is abrupt which suggests that cooperativity plays as important a role in the LIESST transition as it does in the thermal spin transition and that there is a

similar degree of intermolecular bonding in the two high spin states, as supported by the crystallographic evidence. An examination of the effect of continuous irradiation on the spin transition reveals the existence of a LITH (Light Induced Thermal Hysteresis) loop, Figure 3.6 b. This phenomenon was first reported in 1998 and is associated with systems in which cooperativity is involved in the LIESST transition [14]. Thus the presence of LITH in the photomagnetic behaviour of this system provides further evidence for cooperative interactions in the HS-2 state.

Létard *et al* have carried out pioneering work in improving our understanding of the photoexcited HS-2 state and recently they have reported a large body of experimental evidence supporting the existence of a reciprocal relationship between $T_{1/2}$ for the thermal spin transition and $T(\text{LIESST})$ proposed by Hauser [11,15]. Further examination of a large set of spin crossover materials revealed that when these values were plotted on a graph of $T_{1/2}$ vs. $T(\text{LIESST})$, related compounds lie on straight lines at varying positions on the graph with different y intercepts, T_0 . The intercept of the straight line formed by related points gives its name to the line. For example the solvates of complexes of the bpp ligand (bpp = 2,6-di(pyrazol-3-yl)pyridine, Figure 3.7) which is similar to the ligand discussed in this chapter, form a line at $T_0 = 150$ K.

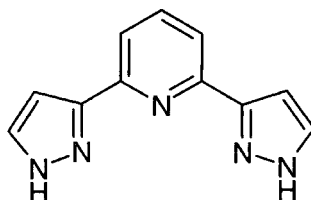


Figure 3.7: The 2,6-di(pyrazol-3-yl)pyridine ligand

Kinetic measurements were also performed on [FeL1₂](BF₄)₂ and have been reported elsewhere [16]; a complete analysis of these results lies outside the scope of this thesis. In summary; data were collected at the temperatures accessible using the SQUID equipment in Bordeaux. Below 65 K, relaxation is in the temperature independent tunnelling region and no change in occupancy of the HS-2 state is noted over the time scale of the experiment. Above 65 K the relaxation shows strong deviation from the single exponential decay that would be expected if Arrhenius behaviour were being followed. This deviation from simple Arrhenius decay is normal for materials which experience a strong self accelerating effect, as might be predicted for strongly cooperative systems. Above 70 K, the relaxation took place faster than the SQUID time frame and it was not possible to collect kinetic data above this temperature.

3.3.5 Investigation of the effect of pressure on the thermal spin transition

The behaviour of spin crossover materials under pressure has not been much studied by crystallographic techniques due to the intrinsic problems in obtaining data under these conditions and the normally comparatively complex structures of spin crossover materials. In this section the results of a single crystal diffraction study of $[\text{FeL}_2](\text{BF}_4)_2$ in a diamond anvil cell will be described, as well as the behaviour of the compound at variable pressures monitored by Raman spectroscopy. The problems of heating or cooling a sample concurrently with applying increased pressure have led to studies of the effect of raised pressure on the thermal spin transition being relatively rare. However, we have obtained results of this type for a polycrystalline sample of $[\text{FeL}_2](\text{BF}_4)_2$ using SQUID magnetometry.

Raman Spectroscopy

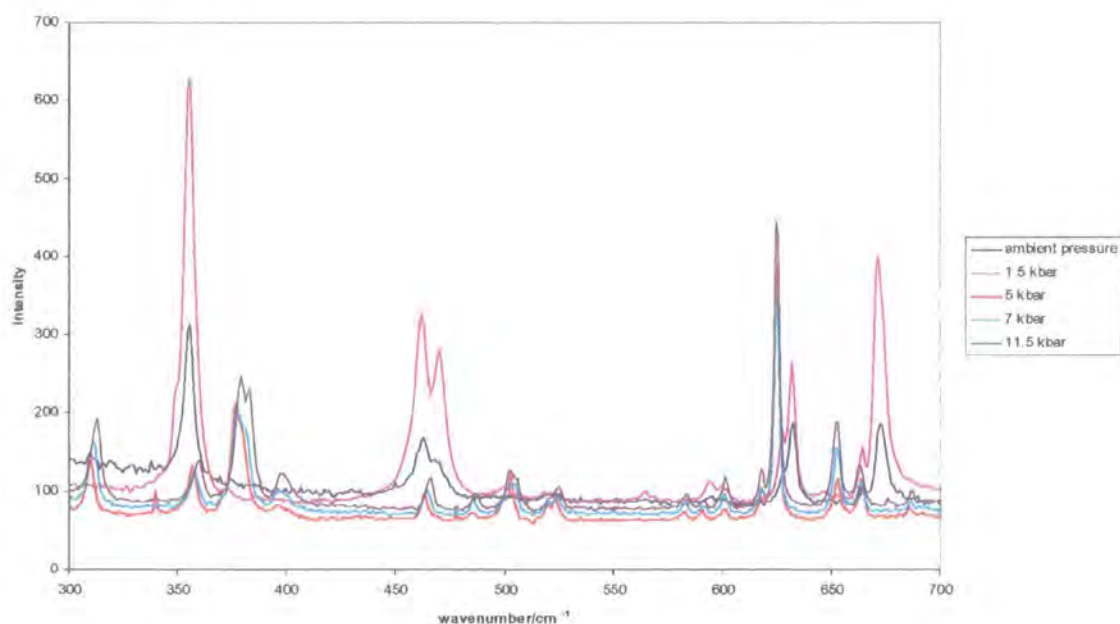


Figure 3.8: Variation of the low wavenumber region of the Raman spectra of $[\text{FeL}_2](\text{BF}_4)_2$ with increasing pressure.

Spectra were collected between 250 cm^{-1} and 700 cm^{-1} successively at the following pressures: 1.5 kbar, 5 kbar, 7 kbar, 11.5 kbar, 7 kbar, 3.5 kbar, between 1 kbar and 1.5 kbar and finally at ambient pressure once more. Figure 3.8 shows the change in spectra, between 300 cm^{-1} and 700 cm^{-1} observed on raising the pressure. The shift to higher wavenumber which is clearly visible here is commonly observed with increasing pressure. New peaks can be seen to appear with increasing pressure at 310 cm^{-1} and 380 cm^{-1} , whilst the peak at

460 cm^{-1} becomes less intense and loses a degree of splitting. These changes in peaks can be assigned to the decrease in metal – ligand bond distances on going from the high spin state at ambient pressure, to the low spin state between 1.5 kbar and 5 kbar.

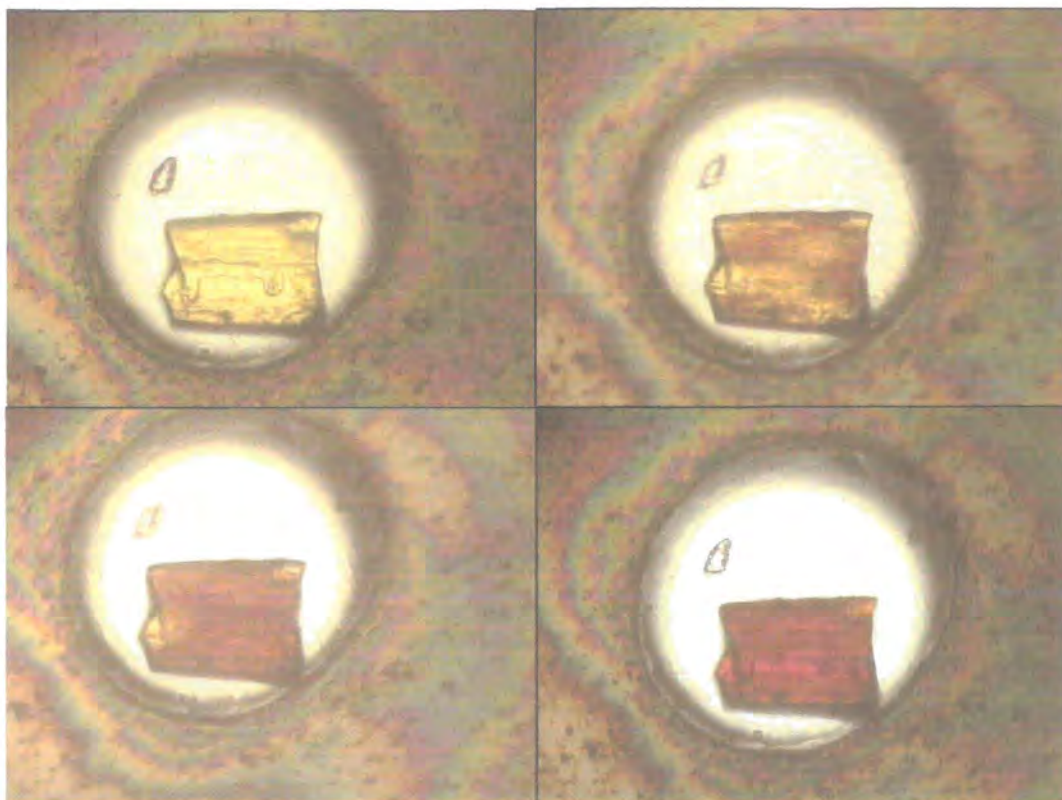


Figure 3.9: The spin transition moving through the crystal of $[\text{FeL}_2](\text{BF}_4)_2$ at 4.5 kbar, looking down through the diamond anvil. The top left hand picture shows the fully high spin state, the bottom left hand picture the crystal completely in the low spin state, the other two pictures show the crystal in an mixed spin state. The smaller crystal on the left is the ruby chip used for calibrating the pressure in the sample chamber.

The nature of the diamond anvil cell used for these experiments is such that it is possible to see the crystal through the diamond when using the spectrometer, in this manner we were able to see the colour change associated with the spin transition at first hand. Figure 3.9 shows the transition moving through the crystal at 4.5 kbar. This observation coupled with the spectra collected confirms that the spin transition in $[\text{FeL}_2](\text{BF}_4)_2$ can be induced by an increase in pressure and that a relatively low applied pressure can move the transition from 260 K to room temperature. The colour change from yellow to brown was first observed in the diamond anvil cell at 2.5 kbar, which suggests that the spin transition is induced initially at this pressure.

Crystallography at raised pressure

Empirical formula	C ₂₂ H ₁₈ B ₂ F ₈ FeN ₁₀	C ₂₂ H ₁₈ B ₂ F ₈ FeN ₁₀
Formula weight	651.93	651.93
Applied pressure/ kbar	0	4.5
Spin state	HS-1	LS
Shape	Block	Block
Colour	Yellow	Brown
Crystal system	Monoclinic	Monoclinic
Space group	P2 ₁	P2 ₁
a/ Å	8.473(1)	8.311(1)
b/ Å	8.489(1)	8.295(2)
c/ Å	19.034(5)	18.295(6)
β/ deg	95.51(3)	98.21(3)
Volume/ Å³	1362.9(4)	1248.4(5)
Z	2	2
D_c/ Mg/m³	1.589	1.734
μ/ mm⁻¹	0.642	0.701
Crystal size / mm	0.25 x 0.25 x 0.15	0.25 x 0.25 x 0.15
Theta range / deg	2.399 to 22.520	2.455 to 22.563
Reflections collected	3380	3012
Independent reflections	1298	1179
R_(int)	0.1267	0.1583
wR(F²)(all data)	0.2870	0.2771
R(F)(all data)	0.1580	0.1549
Refined parameters	101	77
GOF	1.081	1.080
Δρ_{min,max} / e.Å⁻³	0.294 and -0.234	0.506 and -0.476

Table 3.7: Selected crystallographic parameters for [FeL1₂](BF₄)₂ in the diamond anvil cell at 0 kbar and 4.5 kbar. Where HS-1 is the high spin ground state and LS is the low spin state.

After the pressure in the diamond anvil cell had been determined using Raman spectroscopy, X-ray diffraction data were collected using the method described in Chapter 2. It was possible to refine a model for the structure using the crystallographic structure already obtained for the high and low spin states at ambient pressures on either side of the thermal spin transition. Due to the restrictions placed on the data collection by the pressure cell, the data to parameter ratios for the full data sets are such that it has not been possible to determine anisotropic temperature factors and a set of restraints has been applied to the model. However given these restrictions, it has still proved possible to refine the structure at ambient pressure and at 4.5 kbar. The following restraints were applied to the structures to aid the refinement: the pyrazole rings were restrained to be regular pentagons while the pyridine rings were restrained as hexagons; the anions were restrained to be regular tetrahedral with one boron – fluorine bond length refined for each anion; only one isotropic temperature factor was refined for each chemical element. Figure 3.10 shows the structure of the low spin cation determined at 4.5 kbar.

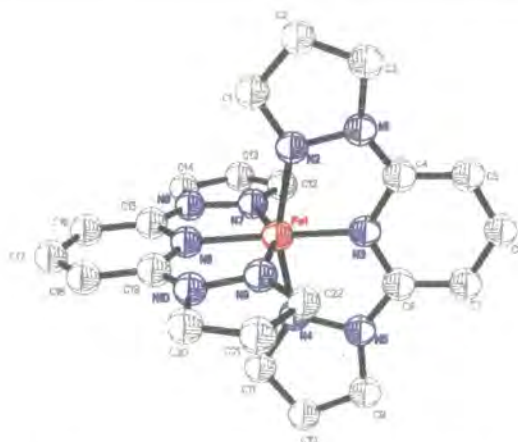


Figure 3.10: The structure of the [FeL₂]²⁺ cation in the low spin state at 4.5 kbar. Hydrogen atoms have been omitted for clarity.

There is no space group change over the pressure range studied with the crystal remaining in the monoclinic space group $P2_1$ at 4.5 kbar. At this pressure the mean metal – ligand bond length of 1.91(2) Å is indicative of a low spin iron (II) centre. Despite the relatively high error on this value, due mainly to a high level of uncertainty in the crystallographic c parameter and hence the metal – pyridine nitrogen bonds, it is nonetheless possible to distinguish the two spin states. The mean Fe – N bond distance for the crystal from the data collected in the diamond anvil cell at ambient pressure is 2.14(2) Å a difference of 0.23 Å from that determined at 0 kbar. Figure 3.11 shows an overlay of the high and low spin structures determined in the pressure cell. It can be seen that the differences in the two structures are those that be expected for a spin transition with a shortening of the metal – ligand bond lengths and an opening of the ligand bite angle. At ambient pressure both the BF₄ anions are found to be disordered over two positions, this disorder is not present in the high pressure low spin structure.

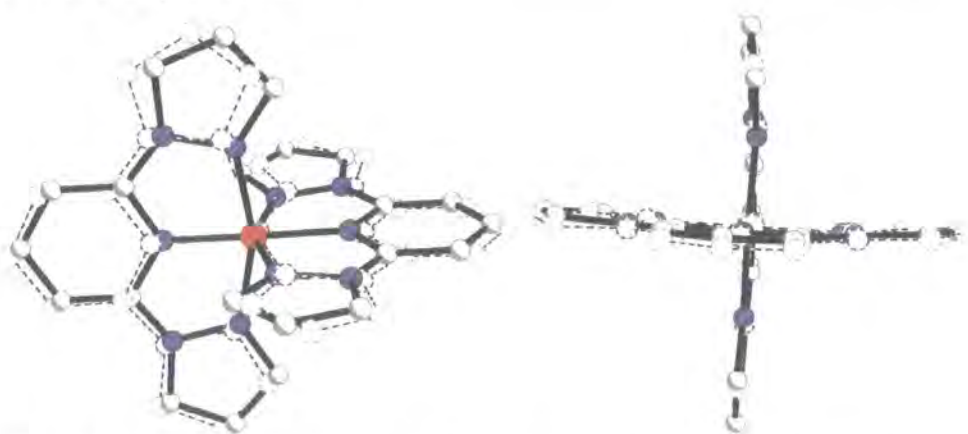


Figure 3.11: Overlay of the structure of the high spin cation of [FeL₂](BF₄)₂ (dashed lines) recorded at ambient pressure in the diamond anvil cell with the structure of the low spin cation at 4.5 kbar (solid lines)

The structure of the low spin state at ambient temperature and 4.5 kbar can be compared with that found at low temperature and atmospheric pressure, Figure 3.12. It may be seen that the differences in the two low spin states are not significant. The low spin state induced by raised pressure is the same as that found at low temperature. In other words for this system increasing the pressure has the same physical effect as lowering the temperature. It is likely that if the pressure were increased further from the comparatively low pressures used for this experiment, that further phase transitions might be observed. The spin transition is the first effect to be seen on raising the pressure because the difference in energy between the high and low spin states is so small and the reduction in volume so large.

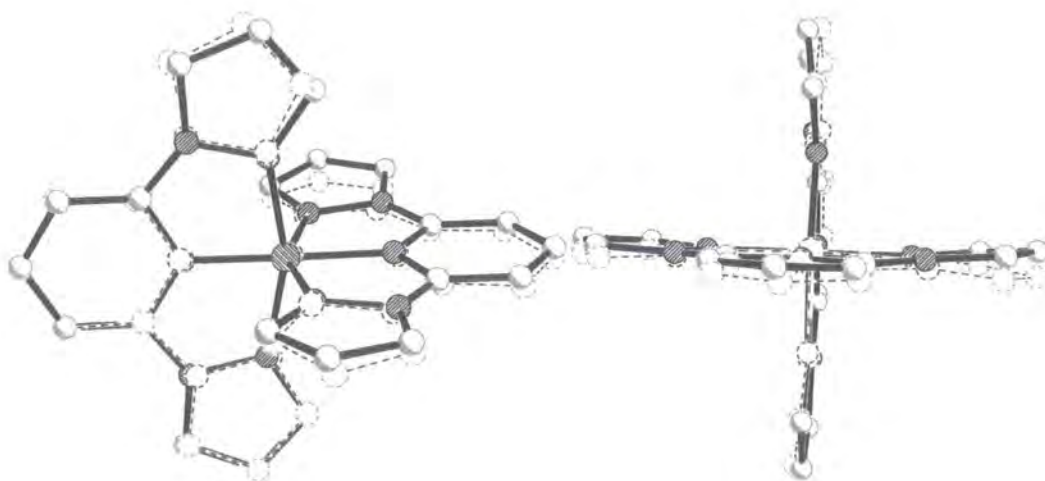


Figure 3.12: Overlay diagrams of the structure of the low spin state of [FeL1₂](BF₄)₂ induced at room temperature and raised pressure (solid lines) and that found at 30 K (dashed lines)

One of the most noticeable differences between the thermal spin transition and that induced by raised pressure, is the far greater decrease in unit cell volume seen for the latter. For the thermal spin transition, ΔV_{sc} is estimated as being 2.6% and for the light induced transition ΔV_{sc} is estimated as 2.3%. On increasing the pressure from ambient to 4.5 kbar, the unit cell volume decreases by 114.5 Å³, equal to 8.4% of the ambient pressure volume. The high pressure structure shows extensive $\pi - \pi$ interactions between the ligands of neighbouring cations which lie in the crystallographic *a* and *b* directions and weak hydrogen bonds between the cations and the fluorine atoms of the counter ions which lie along the crystallographic *c* direction. These are the same packing features observed at ambient pressure. These extensive intermolecular interactions in the low spin state induced by the increase in pressure imply that it retains a high level of cooperativity.

3.3.6 SQUID magnetometry at raised pressure

The design of a pressure cell that can be used inside the cavity of a SQUID magnetometer allows the examination of the effect of pressure on the thermal spin transition. The pressure cell used in this experiment was designed by Dr. Konstantin Kamenev and is described in Section 2.5.1. Data were collected at six pressures between 1.86 kbar and 0 kbar with the pressure being calibrated using the superconducting transition of a very small piece of lead wrapped in Teflon tape and mixed into the polycrystalline sample. Table 3.8 shows the results of this investigation.

Applied pressure/ kbar	T _{1/2} ↑ /K	T _{1/2} ↓ /K	Hysteresis /K
1.856	317.80	308.09	9.71
1.656	307.95	306.29	1.66
0.826	288.32	282.95	5.37
0.500	274.91	270.76	4.15
0.050	262.75	261.73	1.02
0.000	261.51	261.28	0.23

Table 3.8: Effect of increased pressure on the thermal spin transition of [FeL₁₂](BF₄)₂

It is quite clear that, as predicted, the transition moves to higher temperature with application of raised pressure. Under an applied pressure of less than 2 kbar, the [FeL₁₂](BF₄)₂ is low spin at room temperature and the spin transition is centred at approximately 312 K, this is in good agreement with the crystallographic data in which the change in colour associated with the spin transition was first observed between 1.5 kbar and 2.5 kbar. It is not possible to draw conclusions on the effect of pressure on the hysteresis width of the spin transition from the data collected in this experiment, due to the varying spacing of the collected data points. However unlike many of the other reported examples, the spin transition here would appear to remain relatively abrupt, even at raised pressures taking place over only a few degrees in temperature. This implies that a high degree of cooperativity remains in the structure of [FeL₁₂](BF₄)₂ even a higher pressures and this hypothesis is supported by the extensive intermolecular interactions seen from the crystallographic study.

3.4 Conclusions

A full structural analysis of the spin crossover compound [FeL1₂](BF₄)₂ has been performed, determining the changes in structure on going through the thermal spin transition. A similar study carried out on [FeL1₂](PF₆)₂ has shown that this material does not undergo a spin crossover transition in the temperature range studied, but remains in the high spin state throughout and is not isomorphous with [FeL1₂](BF₄)₂. A variable temperature study of the cobalt (II) compound [CoL1₂](BF₄)₂ has shown that this too remains in the high spin state over the same temperature range. Comparison with the behaviour of the analogous iron (II) compound has allowed an estimation of the variation in unit cell volume with the spin transition and of the anisotropy of the effects of the spin crossover on the crystal structure. The crystallographic structure of [FeL1₂](BF₄)₂ in the metastable high spin state after irradiation with red laser light at 30 K has been determined and similarities between the HS-1 and HS-2 states have been observed. The *T*(LIESST) has been estimated as 81 K by SQUID magnetometry and this is supported by single crystal diffraction methods. Examination of the HS-2 state has enabled the decoupling of the effects of the spin transition from those of temperature. The existence of a LITH loop in the magnetisation curve under constant irradiation reveals the cooperative nature of the transition between the HS-2 and LS states.

There are very few examples of structural studies of the effect of pressure on spin crossover materials. It has been possible to obtain the crystal structure of the pressure induced low spin state at ambient temperature using a diamond anvil cell. SQUID studies of the effect of raised pressure on the thermal spin transition have shown that the transition may be induced at room temperature by a small increase in pressure and that, contrary to a number of reported examples, the transition remains abrupt even at raised pressure.

3.5 References

1. T. Ayers, S. Scott, J. Goins, N. Caylor, D. Hathcock, S. J. Slattery, D. L. Jameson, *Inorg. Chim. Acta.*, **307**, 7-12
2. J. M. Holland, J. A. McAllister, C. A. Kilner, M. Thornton-Pett, A. J. Bridgeman and M. A. Halcrow, *J. Chem. Soc., Dalton Trans.*, 2002, 548 - 554
3. P. Guionneau, M. Marchivie, G. Bravic, J-F. Létard and D. Chasseau, *J. Mater. Chem.*, 2002, **12**, 2546 - 2551

4. P. Guionneau, C. Brigonteix, Y. Barrans, A. E. Goeta, J-F Létard, J. A. K. Howard, J. Gaultier, D. Chasseau, *C. R. Acad. Sci, Ser, Ili. Chim.*, 2001, **4**, 161 - 171
5. I. Sanner, E. Meissner, H. Köppen, H. Spiering and P. Gülich, *Chem. Phys.*, 1984, **86**, 227
6. S. Decurtins, P. Gülich, K. M Hasselbach, H. Spiering and A. Hauser, *Inorg. Chem.*, 1985, **24**, 2174 - 2178
7. J. Kusz, H. Spiering and P. Gülich, *J. Appl. Cryst.*, 2000, **33**, 201-205
8. J. Kusz, H. Spiering and P. Gülich, *J. Appl. Cryst.*, 2001, **31**, 229-238
9. M. Marchivie, P. Guionneau, J. A. K. Howard, A. E. Goeta, G. Chastanet, J-F Létard and D. Chasseau, *J. Am. Chem. Soc.*, 2002, **124**, 194 - 195
10. E. J. MacLean, C.M. McGrath, C. J. O'Conner, C. Sangregorio, J. M. W. Seddon, E. Sinn, F. E. Sowrey, S. J. Teat, A. E. Terry, G. B. M. Vaughan, N. A. Young, *Chem. Eur. J.*, 2003, **9** (21), 5314 - 5322
11. J-F Létard, L. Capes, G. Chastanet, N. Moliner, S. Létard, J. A. Real and O. Kahn, *Chem. Phys. Lett*, 1999, **313**, 115 - 120
12. J-F Létard, G. Chastanet, O. Nguyen, S. Marcén, M. Marchivie, P. Guionneau, D. Chasseau, P. Gülich, *Montash. Chem.*, 2003, **134**, 165 - 182
13. M. Marchivie, P. Guionneau, J-F Létard, D. Chasseau and J. A. K. Howard, *J. Phys. Chem. Solids*, 2004, **65**, 17 - 23
14. A. Desaix, O. Roubeau, J. Jętic, J. G. Hassnoot, K. Boukheddaden, E. Codjovi, J. Linares, M. Nogues and F. Varret, *Eur. Phys. B.*, 1998, **6**, 183 - 193
15. A. Hauser, *Coord. Chem. Rev.*, 1991, **111**, 275 - 290
16. V. A. Money, J. Sánchez Costa, S. Marcén, G. Chastanet, J. Elhäik, M. A. Halcrow, J. A. K. Howard and J-F Létard, *Chem. Phys. Lett.*, 2004, 273- 277

4 A study of the unusual thermal spin transition in [FeL₂](BF₄)₂ and [FeL₂](ClO₄)₂

4.1 Introduction

As previously mentioned, one of the main goals in spin crossover research is to obtain a large range of materials which may be modified to give a spin transition with the desired features. For the majority of potential applications it is necessary that the transition occur close to room temperature and that it be abrupt, whereas for a number of applications, such as memory devices, a wide hysteresis loop is also desirable. Transitions of this sort are favoured by materials in which there is a large degree of communication between iron centres [1,2]. With this in mind systematic alterations were made to the 2,6-di(pyrazol-1-yl)pyridine ligand (L1) with the hope of increasing cooperativity and also with furthering our understanding of the effect of structural changes on the spin transition. The following chapter describes work on one of these modified ligands; 2,6-di(3-methylpyrazol-1-yl)pyrazine (L2), Figure 4.1.

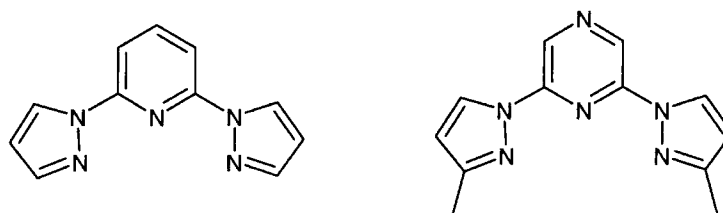


Figure 4.1: 2,6-di(pyrazol-1-yl)pyridine (L1) and 2,6-di(3-methylpyrazol-1-yl)pyrazine (L2)

The synthesis and initial unit cell parameter determinations of [FeL₂](ClO₄)₂ and [FeL₂](BF₄) were performed in Leeds by Jerome Elhiak and reported in 2003 [3]. It was noted in this publication that the crystals were tetragonal and probably I centred, however analysis of the crystal structure was taken no further than this. Also reported in this paper were the magnetic curves which show that both compounds undergo unusual spin transitions in which there is a clear change in gradient at the temperature at which 50% of the compound is in the high spin state, Figure 4.2. The transition for [FeL₂](ClO₄)₂ takes place between 210 K and 90 K with the change in gradient at 190 K whereas that for [FeL₂](BF₄)₂ shows a change in gradient at 240 K and occurs between 280 K and 130 K. Neither compound shows any hysteresis. That the spin transitions for these two compounds are much less abrupt and show no evidence of bistability, seems to imply that the materials have less cooperativity and so less intermolecular bonding than [FeL₁](BF₄)₂ (Chapter 3). However the shape of the

transitions is of interest; although stepped transitions are relatively common in spin crossover research and arise for a number of reasons described in Section 1.1.2, the spin transition curves displayed by these compounds are not of that type as they show a change in gradient rather than an obvious step.

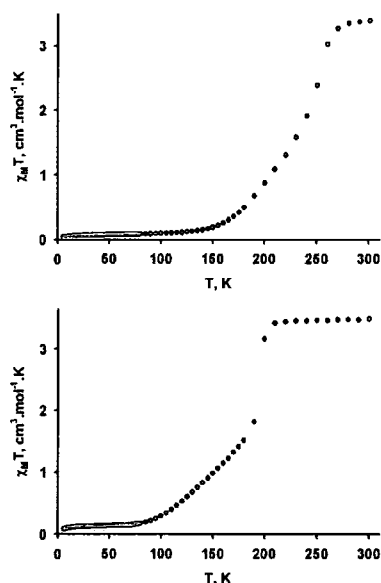


Figure 4.2: Variation of magnetic susceptibility with temperature for [FeL₂](BF₄)₂ (top) and [FeL₂](ClO₄)₂ (bottom)

Empirical formula	C ₂₄ H ₂₄ B ₂ F ₈ FeN ₁₂	C ₂₄ H ₂₄ B ₂ F ₈ FeN ₁₂	C ₂₄ H ₂₄ B ₂ F ₈ FeN ₁₂	C ₂₄ H ₂₄ B ₂ F ₈ FeN ₁₂
Formula weight	710.02	710.02	710.02	710.02
Temperature/K	290(2)	270(2)	240(2)	30(2)
Spin state	HS-1	Mixed spin	Mixed spin	LS
Shape	Diamond	Diamond	Diamond	Diamond
Colour	Yellow	Yellow	Brown	Brown
Crystal system	Tetragonal	Tetragonal	Tetragonal	Tetragonal
Space group	I4	I4	I4	I4
a/ Å	9.307(1)	9.273(1)	9.153(1)	9.025(1)
c/ Å	17.592(4)	17.600(4)	17.694(4)	17.547(4)
Volume/ Å³	1523.7(4)	1513.4(4)	1482.3(4)	1429.2(4)
Z	2	2	2	2
D_c/ Mg/m³	1.548	1.558	1.591	1.650
μ/ mm⁻¹	0.583	0.587	0.599	0.622
Crystal size / mm	0.24 x 0.16 x 0.16	0.24 x 0.16 x 0.16	0.24 x 0.16 x 0.16	0.24 x 0.16 x 0.16
Theta range / deg	2.32 to 27.47°	2.31° to 27.42°	2.30 to 27.46°	3.95° to 26.67°
Reflections collected	5227	8173	8079	3522
Independent reflections	1743	1718	1694	1407
R_(int)	0.0368	0.0408	0.0427	0.0263
wR(F²)(all data)	0.1025	0.1009	0.1079	0.0839
R(F)(all data)	0.0477	0.0439	0.0439	0.0358
refined parameters	123	117	108	108
GOF	1.055	1.064	1.055	1.183
Δρ_{min,max} / e.Å⁻³	0.35 and -0.39	0.23 and -0.26	0.22 and -0.37	0.35 and -0.39

Table 4.1: Crystallographic data for [FeL₂](BF₄)₂ at 290 K, 270 K, 240 K and 30 K.

Where HS-1 is the high spin ground state and LS is the low spin state.

4.2 Experimental

4.2.1 Synthesis

[FeL₂](BF₄)₂ and [FeL₂](ClO₄)₂ were synthesised according to literature methods by Jerome Elhik of the University of Leeds [3].

4.2.2 Crystallography

Data collection was carried out as described in Chapter 2. The structures were solved by direct methods and refined on F² using full matrix least-squares methods within the SHELXTL suite. All non-hydrogen atoms were refined anisotropically. The hydrogen atoms were placed geometrically and treated with a riding model. For the LIESST experiments the samples were irradiated for between five and ten minutes whilst on the diffractometer, using a He – Ne laser ($\lambda = 632.8$ nm, 25 mW) or a Nd-YAG laser ($\lambda = 532.06$ nm, 210 mW)

Empirical formula	C ₂₄ H ₂₄ Cl ₂ FeN ₁₂ O ₈	C ₂₄ H ₂₄ Cl ₂ FeN ₁₂ O ₈	C ₂₄ H ₂₄ Cl ₂ FeN ₁₂ O ₈	C ₂₄ H ₂₄ Cl ₂ FeN ₁₂ O ₈
Formula weight	735.30	735.30	735.30	735.30
Temperature/K	290(2)	210	180	30(2)
Spin state	HS-1	Mixed spin	Mixed spin	LS
Shape	Diamond	Diamond	Diamond	Diamond
Colour	Yellow	Yellow	Brown	Brown
Crystal system	Tetragonal	Tetragonal	Tetragonal	Tetragonal
Space group	$\overline{14}$	$\overline{14}$	$\overline{14}$	$\overline{14}$
a/ Å	9.419(1)	9.380(1)	9.201(1)	9.133(1)
c/ Å	17.645(4)	17.650(4)	17.771(4)	17.676(4)
Volume/ Å³	1565.4(4)	1552.9(4)	1504.5(4)	1474.4(4)
Z	2	2	2	2
D_c/ Mg/m³	1.560	1.573	1.623	1.656
μ/ mm⁻¹	0.720	0.725	0.749	0.764
Crystal size / mm	0.34 x 0.22 x 0.18	0.34 x 0.22 x 0.18	0.34 x 0.22 x 0.18	0.34 x 0.22 x 0.18
Theta range / deg	2.31 to 27.45	2.31 to 27.45	2.29 to 27.47	3.91 to 27.03
Reflections collected	5370	5262	5180	3837
Independent reflections	1810	1782	1705	1458
R_(int)	0.0264	0.0302	0.0269	0.0232
wR(F²)(all data)	0.0763	0.0740	0.0593	0.0587
R(F)(all data)	0.0354	0.0376	0.0285	0.0244
Refined parameters	118	125	109	109
GOF	1.059	1.086	1.048	1.056
$\Delta\rho_{\min,\max}$ / e.Å⁻³	0.15 and -0.28	0.27 and -0.18	0.17 and -0.23	0.23 and -0.29

Table 4.2: Crystallographic data for [FeL₂](ClO₄)₂ at 290 K, 210 K, 180 K and 30 K

Where HS-1 is the high spin ground state and LS is the low spin state.

4.3 Results and discussion

4.3.1 Variable temperature crystallographic study

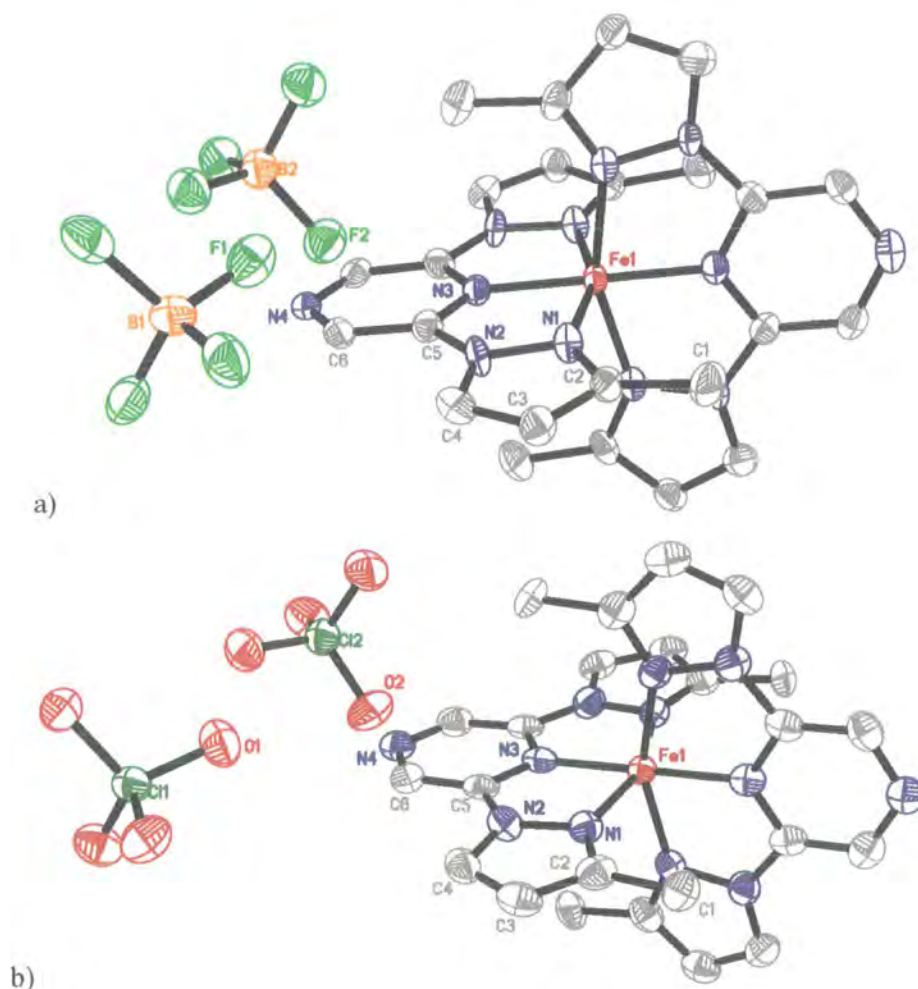


Figure 4.3: Crystal structure of the low spin states of a) [FeL₂](BF₄)₂ and b) [FeL₂](ClO₄)₂ at 30 K showing the numbering scheme used throughout. Hydrogen atoms have been omitted for clarity and thermal ellipsoids are at 90% probability.

Data were collected on both compounds at various temperatures along the spin transition curves. [FeL₂](BF₄)₂ and [FeL₂](ClO₄)₂ are isomorphous and were found to crystallise in the tetragonal space group $I\bar{4}$. This high symmetry space group is very unusual in molecular crystallography with only 441 records in the Cambridge Structural Database (out of 298097 entries in the November 2003 release) [4]. There is no space group change over the temperature range under examination. [FeL₂](ClO₄)₂ was found to be merohedrally twinned

about the two fold axis of the tetragonal unit cell, this was modelled using the appropriate commands in the SHELX suite. The iron ions have a distorted octahedral geometry and are bound equatorially to two ligands through three of each ligands' six nitrogen atoms, Figure 4.3. The iron atoms of the cations and central atoms of the anions lie on fourfold improper axes and the asymmetric unit is a quarter of the cation and a quarter of each anion. In both compounds one of the anions is disordered at 290 K and both are found to be ordered at 30 K. The iron – pyrazine nitrogen bonds lie parallel to the crystallographic *c* direction whilst the iron – pyrazole nitrogen bonds are at 45° to both the *a* and *b* directions and deviate slightly from 90° to the *c* axis, Figure 4.4.

In other complexes of modified versions of the 2,6-di(pyrazol-1-yl)pyridine ligand, there is an extensive network of edge to face and face to face π interactions which links the iron centres and contributes to the cooperativity of the compounds, thus aiding abrupt transitions. [FeL₂](ClO₄)₂ and [FeL₂](BF₄)₂ show no such intermolecular bonding, with the only intermolecular interactions being weak hydrogen bonds between the anions and the CH groups of the ligands, primarily the methyl moieties. As in [FeL₁](BF₄)₂, Chapter 3, these hydrogen bonds lie along the direction of the crystallographic *c* axis and as a result there are very few or no intermolecular interactions along the crystallographic *a* and *b* directions. The hydrogen bonding is facilitated by disorder in one of the anions in each compound at 290 K, which is shown to be resolved on cooling. [FeL₂](BF₄)₂ contains two hydrogen bonds from the methyl groups one to the disordered and one to the ordered anion, with CH...F of 3.38(2) Å and 3.529(6) Å and CĤ...F of 144.67° and 161.07° respectively at 270 K. The bonding in [FeL₂](ClO₄)₂ is slightly different with the methyl groups forming three hydrogen bonds to the anions two to the disordered perchlorate and one to the ordered at 210 K. The hydrogen bonds to the disordered anion have CH...O of 3.35(2) Å and 3.49(4) Å with CĤ...O of 133.68° and 158.72° and those to the ordered 3.40(9) Å and 152.72°. From the point of view of designing compounds with a greater degree of cooperativity, it is interesting to note that the nitrogen atoms of the pyrazine rings, N4, do not form intermolecular bonds and so in this case cannot be said to increase the level of cooperativity. This reduced intermolecular bonding compared with other members of this series is consistent with lower cooperativity and hence a more gradual spin crossover transition.

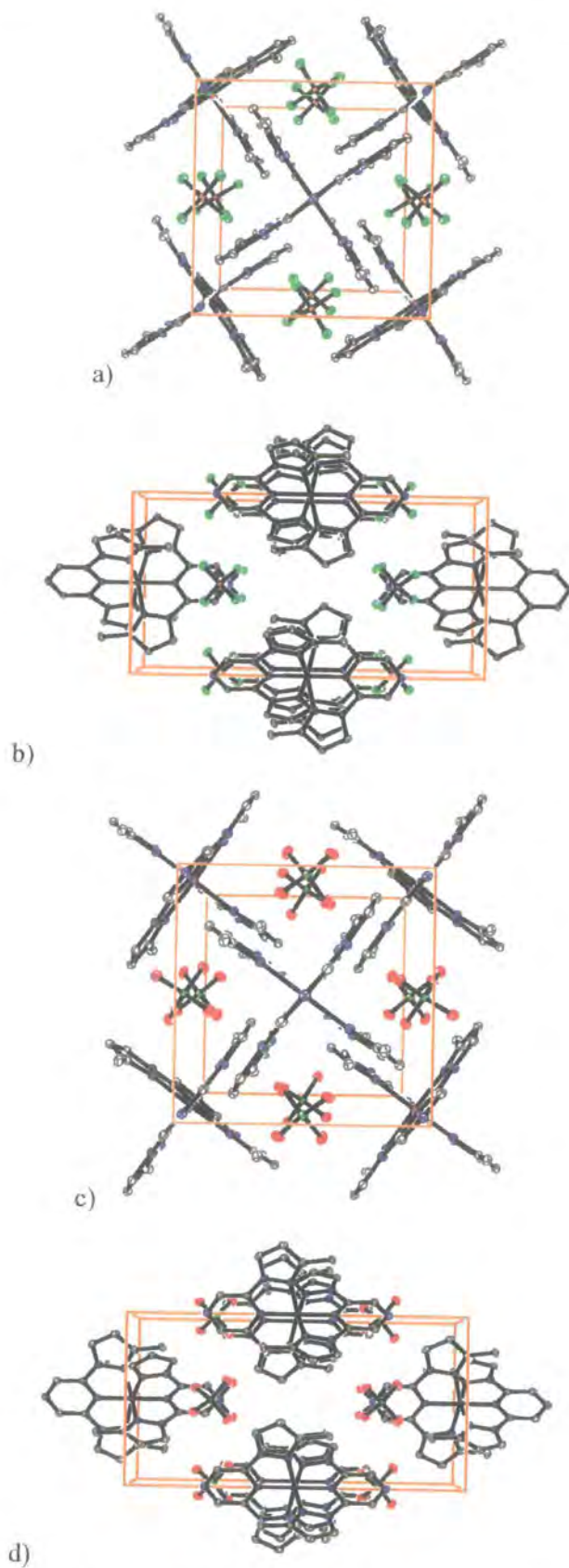


Figure 4.4: Crystal packing in $[\text{FeL}_2](\text{BF}_4)_2$ at 30 K, a) view normal to 001, b) view normal to 010 and $[\text{FeL}_2](\text{ClO}_4)_2$ c) view normal to 001, d) view normal to 010. Hydrogen atoms have been omitted for clarity.

	T/ K	% HS	Mean Fe-N/ Å	Bite angle/ ^o	Σ/ ^o	v /%	Anions
[FeL ₂](BF ₄) ₂	290	100	2.164(3)	73.52(6)	150.32	8.04	One disordered
	270	96	2.154(3)	73.70(6)	148.36	7.86	One disordered
	240	52	2.057(3)	76.2(1)	123.16	5.76	Both ordered
	30	0	1.973(3)	79.25(7)	94.00	3.55	Both ordered
[FeL ₂](ClO ₄) ₂	290	100	2.176(2)	72.97(6)	156.12	8.64	One disordered
	210	95	2.173(3)	73.25(6)	153.08	8.26	One disordered
	180	32	2.047(2)	77.05(6)	115.12	5.04	Both ordered
	30	0	1.988(2)	79.03(6)	96.08	3.72	Both ordered

Table 4.3: Selected parameters for [FeL₂](BF₄)₂ and [FeL₂](ClO₄)₂. See Chapter 3 section 3.3.1 for definitions of Σ and v.

At 290 K the mean iron – nitrogen bond lengths for both materials are indicative of iron (II) complexes in the high spin state, Table 4.3, and this is in agreement with the magnetic data. On lowering the temperature from 290 K to 30 K through the thermal spin transition there is a marked decrease in the iron – nitrogen bond lengths, of 0.191(4) Å for [FeL₂](BF₄)₂ and 0.188(3) Å for [FeL₂](ClO₄)₂, Figure 4.5. During this change, the ligand bite angle increases as is the case for other members of this series and the cation has a less distorted octahedral geometry, which is demonstrated by the change in Σ and v parameters [5,6], Table 4.3. The unit cell volumes decrease by 6.2 % for [FeL₂](BF₄)₂ and 5.8 % for [FeL₂](ClO₄)₂. This decrease is due to both the spin transition and the change in temperature, which causes thermal contraction, however it is greater than would be expected if it were due to thermal contraction alone. The spin transition is accompanied by a thermochromic change from yellow in the high spin state at 290 K to brown in the low spin state at 30 K.

In order to determine the cause of the unusual thermal spin transition, the unit cell parameters were followed as a function of temperature for both [FeL₂](BF₄)₂ and [FeL₂](ClO₄)₂. This study revealed that, although the unit cell volume and crystallographic *a* parameter follow the same trends with temperature as the magnetic curve, Figure 4.6, the *c* parameter shows different behaviour actually increasing in length between 270 K and 240 K for [FeL₂](BF₄)₂ and between 210 K and 180 K for [FeL₂](ClO₄)₂. In both compounds the increase in *c* parameter occurs until there is 50 % of the compound in the high spin state and after this point it begins to decrease, Figure 4.6. The percentage of material in the high spin state may be confirmed using both the magnetic susceptibility curves and the Σ parameter. X-ray diffraction data were collected for each compound at temperatures coincident with the rise in *c* parameter and it became clear that it was during the range of temperatures where the magnetic susceptibility decreases steeply and the *c* parameter increases, that the one anion disordered at 290 K becomes ordered. One anion is disordered at 270 K and both are ordered at 240 K for [FeL₂](BF₄)₂ in which the change in gradient in the magnetic curve is at 240 K. For [FeL₂](ClO₄)₂ the change in gradient is at 190 K and at 180 K both anions are found to

be ordered, whereas at 210 K one is disordered. The structures of the cations during the increase in c parameter show no significant changes, besides those expected for an increase in high spin population. The data sets collected at temperatures where 50 % of the compounds are in the high spin state, provide no evidence for local ordering of the high and low spin states.

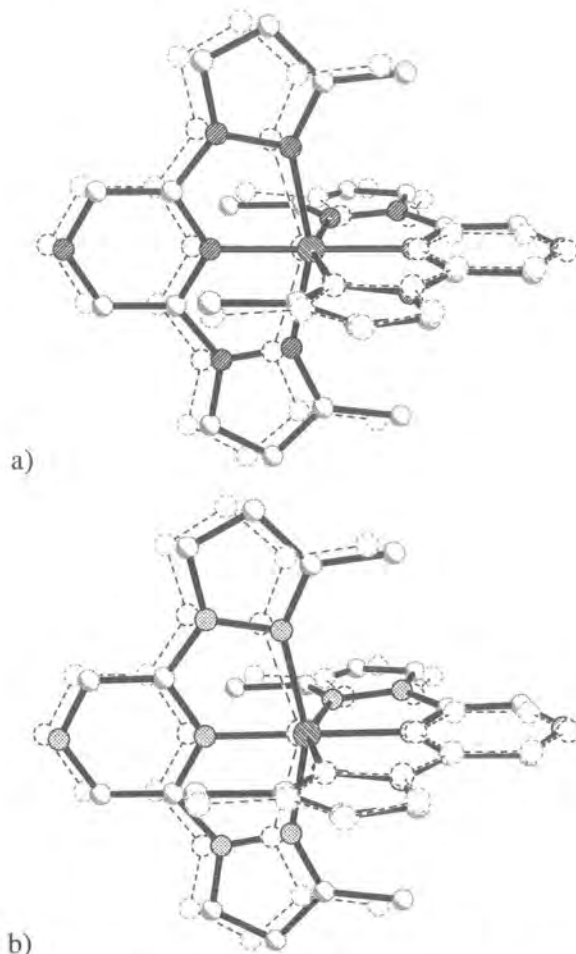


Figure 4.5: Overlay of the high spin state at 290 K (dashed lines) with the low spin state at 30 K (solid lines) for a) $[\text{FeL}_2](\text{BF}_4)_2$ and b) $[\text{FeL}_2](\text{ClO}_4)_2$

The anion order – disorder transition increases the distance between the iron centres. The ordering of the anion decreases the number of hydrogen bonds with the cation, such that both compounds now form only one hydrogen bond between the methyl groups of the ligands and the anions. In $[\text{FeL}_2](\text{BF}_4)_2$ $\text{CH}\cdots\text{F}$ is 3.489(8) Å and $\text{CH}\cdots\text{F}$ is 162.90° at 240 K. In the perchlorate salt, $\text{CH}\cdots\text{O}$ is 3.403(5) Å and $\text{CH}\cdots\text{O}$ is 158.79° at 180 K. This reduction in the number of intermolecular interactions reduces the communication between the iron centres and thus the cooperativity of the system, resulting in a slower rate of conversion to the low spin state and hence a reduction in the gradient of the magnetic susceptibility curve. Therefore the order – disorder transition of one of the anions is primarily responsible for the unusual shape of the spin transition curve.

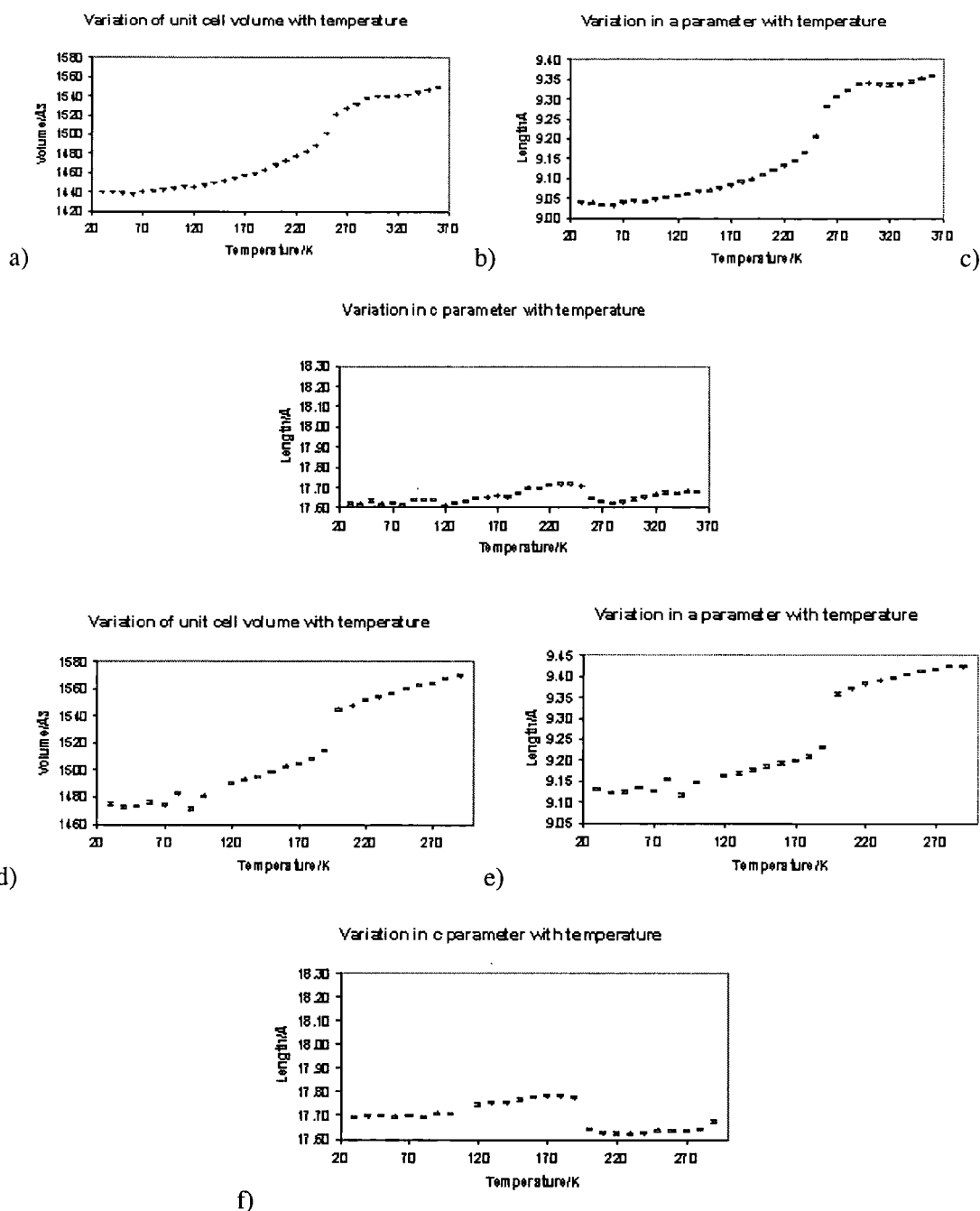


Figure 4.6: a to c: Variable temperature study of $[\text{FeL}_2](\text{BF}_4)_2$; variation of unit cell parameters with temperature; a) unit cell volume, b) a unit cell parameter and c) c unit cell parameter. **Figure 4.6 d to f:** Variable temperature study of $[\text{FeL}_2](\text{ClO}_4)_2$; variation of unit cell parameters with temperature; d) unit cell volume, e) a unit cell parameter and f) c unit cell parameter.

4.3.2 The LIESST effect in [FeL₂](BF₄)₂ and [FeL₂](ClO₄)₂

Crystallographic study

Irradiation of [FeL₂](BF₄)₂ with a red laser ($\lambda = 632.8$ nm, 25 mW) at 30 K resulted in a change in colour of the crystal from brown to yellow indicating that a transition from the low to the metastable high spin state (HS-2) had been induced. However a unit cell determination revealed only the low spin ground state unit cell parameters.

[FeL₂](ClO₄)₂ behaves in a different manner to [FeL₂](BF₄)₂: irradiation with the red laser ($\lambda = 632.8$ nm, 25 mW) at 30 K results in a colour change as described above, but also a unit cell determination shows an increase in unit cell volume of 21 Å³ and new tetragonal unit cell parameters of $a = 9.169(6)$ Å, $c = 17.77(1)$ Å and volume = 1496(4) Å³. Relaxation to the low spin ground state was too fast to allow collection of a full crystallographic data set. It is possible to estimate the increase in unit cell volume that would be expected at this temperature, if 100 % conversion to the HS-2 state had been achieved, by extrapolation backwards from the high spin portion of the unit cell volume vs. temperature curve. This method predicts a unit cell volume for the high spin state of 1500 Å³, an increase of 25 Å³ or about 2 % relative to the low spin state at this temperature. The unit cell parameters suggest that we have obtained close to 100 % conversion from the ground low spin state to the HS-2 state on irradiation, assuming that the HS-2 state is similar to the high spin state at room temperature (HS-1).

After irradiation with a green laser ($\lambda = 532.06$ nm, 210 mW), the unit cell of [FeL₂](BF₄)₂ had increased in volume by 42.8 Å³ or 3 % to give new tetragonal unit cell parameters of $a = 9.11(1)$ Å, $c = 17.75(2)$ Å and Volume = 1472(5) Å³. Unhappily, the crystal was found once more to relax back to the low spin ground state during the unit cell determination and so it was not possible to collect sufficient data to perform a full crystallographic analysis. Extrapolating backward from the high spin portion of the unit cell volume vs temperature graph gives an expected high spin unit cell volume of 1506 Å³ at 100 K, an increase of about 4 %. This is a much larger increase than that observed after irradiation and suggests that either the HS-2 state is different in structure to the HS-1 or that complete conversion was not possible, under these conditions. It is also possible that relaxation during the unit cell determination gives rise to an average unit cell, with a volume somewhere between that of the low spin and HS-2 states.

Photomagnetic studies

Photomagnetic studies of $[\text{FeL}_2](\text{BF}_4)_2$ and $[\text{FeL}_2](\text{ClO}_4)_2$, carried out with Prof. Jean-François Létard and his team at the Groupe des Sciences Moléculaire, Institut de Chimie de la Matière Condensée de Bordeaux, have revealed the existence of a long lived HS-2 state at low temperatures. This suggests that the relaxation of the HS-2 state observed on the single crystal diffractometer may be caused by the interaction of X-rays with the metastable state of the iron (II) complex thus resulting in a reverse – LIESST type effect and depopulation of the HS-2 state.

Kinetic studies of both the thermal and light induced transitions have proved complicated to interpret and work on these is still on going in Bordeaux.

Trapping of the high spin state by thermal quenching

Attempts were made to trap the HS-1 state by flash freezing the crystals to 30 K but these attempts were unsuccessful, which may be a result of the comparatively high temperature of the thermal spin transition.

4.4 Conclusions

The change in rate of the thermal spin transition in $[\text{FeL}_2](\text{BF}_4)_2$ and $[\text{FeL}_2](\text{ClO}_4)_2$, caused by an order – disorder transition in the counter anions, is another example of the critical role that anions play in determining the course of the spin transition. It has long been known that seemingly small changes in the nature of anions can have dramatic effects on the temperature and type of the spin transition, as demonstrated by $[\text{FeL}_1](\text{BF}_4)_2$ and $[\text{FeL}_1](\text{PF}_6)_2$, Chapter 3. In the unusual example described in this chapter, an order – disorder transition in the anion actually changes the course of the spin transition. It is possible that this order – disorder transition is not solely a result of thermal factors, but that it is linked to the spin transition itself. To the best of my knowledge this is the first example of anions playing this sort of role in a spin transition and in which their behaviour can be so clearly characterised.

Both $[\text{FeL}_2](\text{BF}_4)_2$ and $[\text{FeL}_2](\text{ClO}_4)_2$ undergo the LIESST effect; the former on irradiation with green light and the latter on irradiation with red light. The unit cell parameters determined for the HS-2 states suggest that the HS-2 state of $[\text{FeL}_2](\text{ClO}_4)_2$ is similar to the HS-1 state, but that

either complete conversion was not achieved for $[FeL_2](BF_4)_2$ or the two high spin states have different structures. Given the behaviour of other materials in the 2,6-di(pyrazol-1-yl)pyridine series, it would seem probable that the former is the case. Due to fast relaxation it was not possible to determine the crystal structure of the HS-2 state for either compound. As long lived states have been observed using SQUID magnetometry, the relaxation is most likely to be a result of an interaction between the metastable high spin state and the X-ray radiation. For this reason, the most reliable manner in which to obtain the structure of the HS-2 state for these materials would be on a suitably modified neutron diffractometer in which the sample chamber has been altered such that an optical fibre can be used to focus the laser light on the sample. The sample environment normally used to obtain low sample temperatures at neutron facilities is completely enclosed and so the method of irradiation described herein cannot be used. An optical fibre could be attached to the sample holder such that the crystal could be irradiated whilst at low temperature. In this way it would be possible to determine the LIESST state using neutron diffraction.

4.5 References

1. P. Gülich, A. Hauser and H. Spiering, *Angew. Chem. Int. Ed. Engl.*, 1994, **33**, 2024 - 2054
2. P. Gülich, Y. Garcia and H. A. Goodwin, *Chem. Soc. Rev.*, 2000, **29**, 419 -427
3. J. Elhaik, V. A. Money, S. A. Barrett, C. A. Kilner, I. R. Evans, M. A. Halcrow, *Dalton Discussion*, 2003, 2053 - 2060
4. F. H. Allen, *Acta Cryst.*, 2002, **B58**, 380 - 388
5. P. Guionneau, C. Brigonteix, Y. Barrans, A. E. Goeta, J-F Létard, J. A. K. Howard, J. Gaultier, D. Chasseau, *C. R. Acad. Sci, Ser, Ili. Chim.*, 2001, **4**, 161 - 171
6. P. Guionneau, M. Marchivie, G. Bravic, J-F Létard, D. Chasseau, *J. Mater. Chem.*, 2002, **12**, 2546 - 2551

5 The thermal and light induced spin transitions in $[FeL_3_2](BF_4)_2$ and $[FeL_3_2](ClO_4)_2$,

5.1 Introduction

This chapter describes a detailed crystallographic study into the thermal and light induced spin transitions of $[FeL_3_2](BF_4)_2$ and $[FeL_3_2](ClO_4)_2$, where $L_3 = 2,6$ -(dipyrazol-1-yl)-4-hydroxymethylpyridine, Figure 5.1. These complexes form part of the series of iron (II) spin crossover complexes derived from L_1 , 2,6-(dipyrazol-1-yl)-pyridine. By making further systematic changes to the ligand, it is hoped that trends in the spin crossover behaviour will become clear, augmenting the available information on these materials and aiding the design of compounds with specific, tailored properties. By addition of a CH_2OH group, with strong hydrogen bonding potential, to the 4-position of the central pyridine ring of the ligand, the intention was to improve the formation of strong intermolecular interactions leading to an abrupt transition with a wide hysteresis loop. Also presented here are the results of photomagnetic studies performed in collaboration with Dr. Jean-François Létard and his team at the Groupe des Sciences Moléculaire, Institut de Chimie de la Matière Condensée de Bordeaux.

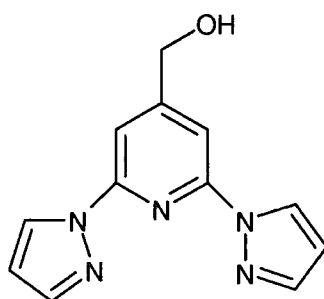


Figure 5.1: $L_3 = 2,6$ -(dipyrazol-1-yl)-4-hydroxymethylpyridine

The two compounds, $[FeL_3_2](BF_4)_2$ and $[FeL_3_2](ClO_4)_2$, have abrupt spin transitions with very small hysteresis loops close to ambient temperature, Figure 5.5. Both materials are shown to exhibit LIESST transitions on irradiation with red laser light and the crystal structures of the metastable states have been determined at 30 K. The effect of the thermal and light induced spin transitions on the structures have been determined and direct comparisons are made between the structure of the low spin state and the metastable high spin state at 30 K and between the metastable high spin state and that found at room temperature

for both compounds. The effect of the change of the ligand on the intermolecular bonding and the form of the spin transition compared with other members of this family of spin crossover complexes is discussed.

5.2 Experimental

5.2.1 Synthesis

Both compounds were synthesised by Jerome Elhaik of the School of Chemistry, University of Leeds. Details of the syntheses have been published previously [1].

5.2.2 Crystallography

Empirical formula	C ₂₄ H ₂₂ B ₂ F ₈ FeN ₁₀ O ₂	C ₂₄ H ₂₂ B ₂ F ₈ FeN ₁₀ O ₂	C ₂₄ H ₂₂ B ₂ F ₈ FeN ₁₀ O ₂
Formula weight	711.99	711.99	711.99
Temperature/ K	300	30	30
Spin state	HS-1	LS	HS-2
Shape	Pyramid	Pyramid	Pyramid
Colour	Yellow	Brown	Yellow
Crystal system	Monoclinic	Monoclinic	Monoclinic
Space group	Cc	Cc	Cc
a/ Å	12.112(2)	11.904(2)	11.974(2)
b/ Å	12.125(2)	11.935(2)	12.001(2)
c/ Å	20.451(4)	20.007(4)	20.014(4)
β/ deg	99.53(3)	99.71(3)	98.44(3)
Volume/ Å ³	2962(1)	2801(1)	2844(1)
Z	4	4	4
D _c / Mg/m ³	1.597	1.688	1.662
μ/ mm ⁻¹	0.603	0.638	0.628
Crystal size / mm	0.26 x 0.18 x 0.12	0.26 x 0.18 x 0.12	0.26 x 0.18 x 0.12
Theta range / deg	2.39 to 27.60	2.43 to 27.49	2.42 to 28.21
Reflections collected	9181	6996	8019
Independent reflections	4722	5050	5414
R _(int)	0.0564	0.0364	0.0373
wR(F ²)(all data)	0.1994	0.1220	0.1071
R(F)(all data)	0.0835	0.0461	0.0416
Refined parameters	447	431	431
GOF	1.043	1.064	1.029
Δρ _{min,max} / e.Å ⁻³	0.51, -0.58	0.66, -0.44	0.72 and -0.36

Table 5.1: Selected crystallographic parameters for [FeL₃]₂(BF₄)₂. Where HS-1 is the high spin ground state, LS is the low spin state and HS-2 is the metastable high spin state resulting from the LIESST effect.

Variable temperature and excited state crystallographic experiments were performed as described in Chapter 2 (section 2.1). The structures were solved by direct methods and refined on F² using full matrix least-squares methods within the SHELXTL suite. For

[FeL₃]₂(BF₄)₂ all non – hydrogen atoms were refined anisotropically. However, for [FeL₃]₂(ClO₄)₂, either due to crystal damage during the magnetic transition, or the intrinsically poor quality of the crystal, the quality of the data obtained was such that it was only possible to refine non-hydrogen atoms anisotropically for the data collected at 340 K. It is likely that only poorly diffracting crystals were obtainable for the perchlorate compound as a result of the spin transition being centred around ambient temperature, the same temperature at which the crystal growth was performed. For the LIESST experiments the sample was irradiated for ten minutes whilst on the diffractometer using a He – Ne laser ($\lambda = 632.8$ nm, 25 mW). Selected crystallographic data are shown in Tables 5.1 and 5.2 for [FeL₃]₂(BF₄)₂ and [FeL₃]₂(ClO₄)₂ respectively.

Empirical formula	C ₂₄ H ₂₂ Cl ₂ FeN ₁₀ O ₁₀	C ₂₄ H ₂₂ Cl ₂ FeN ₁₀ O ₁₀	C ₂₄ H ₂₂ Cl ₂ FeN ₁₀ O ₁₀
Formula weight	737.27	737.27	737.27
Temperature/K	340	30	30
Spin state	HS-1	LS	HS-2
Shape	Pyramid	Pyramid	Pyramid
Colour	Yellow	Brown	Yellow
Crystal system	Monoclinic	Monoclinic	Monoclinic
Space group	Cc	Cc	Cc
a/ Å	12.269(3)	12.027(2)	12.052(2)
b/ Å	12.216(2)	12.038(2)	12.043(2)
c/ Å	20.572(4)	20.184(4)	20.105(4)
β/ deg	99.61(3)	99.90(3)	98.66(3)
Volume/ Å³	3040(1)	2878(1)	2884(1)
Z	4	4	4
D_c/ Mg/m³	1.611	1.701	1.697
μ/ mm⁻¹	0.744	0.786	0.784
Crystal size/ mm	0.22 x 0.18 x 0.18	0.22 x 0.18 x 0.18	0.22 x 0.18 x 0.18
Theta range/ deg	2.01 to 27.46	2.50 to 27.50	2.51 to 27.47
Reflections collected	9681	6091	6507
Independent reflections	5388	4122	4353
$R_{(int)}$	0.0632	0.0812	0.0700
$wR(F^2)$(all data)	0.2367	0.3700	0.3200
$R(F)$(all data)	0.1260	0.1602	0.1344
Refined parameters	437	192	192
GOF	1.019	1.170	1.184
$\Delta\rho_{min,max}$ / e.Å⁻³	0.86 and -1.30	4.01 and -3.22	3.87 and -4.58

Table 5.2: Selected crystallographic parameters for [FeL₃]₂(ClO₄)₂. Where HS-1 is the high spin ground state, LS is the low spin state and HS-2 is the metastable high spin state resulting from the LIESST effect.

5.2.3 Photomagnetic measurements

The magnetic measurements were performed at the ICMCB as described in Chapter 2 and according to literature methods [2,3]. The data show no evidence of the sample being heated by the laser, namely there was no sudden increase in magnetic signal observed when turning off the laser, Figure 5.5.

5.3 Results and Discussion

5.3.1 Variable temperature crystallographic study

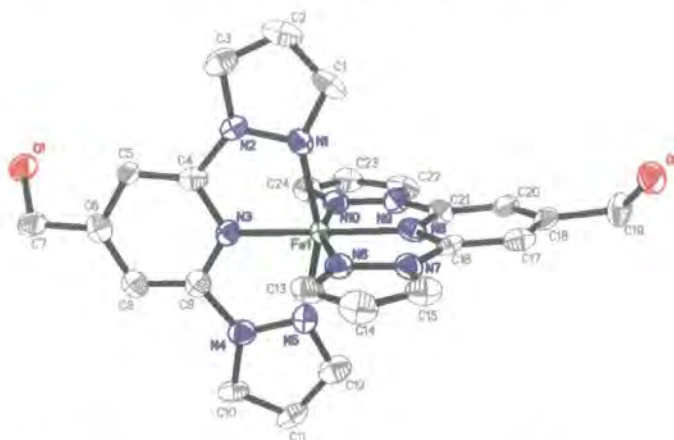


Figure 5.2: $[\text{FeL}_3]_2^{2+}$ at 30 K in the low spin state. Hydrogen atoms have been omitted for clarity and the thermal ellipsoids are at 90% probability

Preliminary magnetic data, collected using a SQUID magnetometer, show that both compounds undergo abrupt changes in magnetisation which can be interpreted as complete thermal spin transitions with very small hysteresis loops of less than 2 K, Figure 5.5. The thermal spin transition of $[\text{FeL}_3]_2(\text{BF}_4)_2$ is centred at 271 K and that of $[\text{FeL}_3]_2(\text{ClO}_4)_2$ at 285 K.

$[\text{FeL}_3]_2(\text{BF}_4)_2$ and $[\text{FeL}_3]_2(\text{ClO}_4)_2$ are isostructural and crystallise in the monoclinic space group *Cc* with no crystallographic phase transition over the temperature range of the experiments; 360 K to 30 K. The asymmetric unit consists of one cation and two anions and there are four formula units in the unit cell. The iron atoms occupy a distorted octahedral environment with the two ligands bound equatorially through three of their five nitrogen atoms, Figure 5.2. The hydroxyl groups of the ligands are found to be thermally disordered at 300 K for $[\text{FeL}_3]_2(\text{BF}_4)_2$ and 340 K for $[\text{FeL}_3]_2(\text{ClO}_4)_2$. However this disorder is resolved on cooling to 30 K and appears to play no role in determining the course of the spin transition. The importance of intermolecular interactions in the determination of the form and temperature of the spin transition has been emphasised already on several occasions, Chapter 4. The addition of the CH_2OH groups to the 4 position of the pyridine ring of L1, 2,6-dipyrazol-1-yl-pyridine, does allow the formation of weak hydrogen bonds between the OH groups and the anions in each case, as planned. However, these weak hydrogen bonds do not link the metal centres into a three dimensional network and it is probable that they cannot

therefore be considered as adding greatly to the cooperativity. In common with the complexes of L1 already described, and those of other members of this series discussed in the following chapters, both [FeL₃]₂(BF₄)₂ and [FeL₃]₂(ClO₄)₂ show extensive edge to face and face to face π interactions between neighbouring cations. In comparison with [FeL₁]₂(BF₄)₂ and the complexes of L2, 2,6-di(3-methylpyrazol-1-yl)pyrazine, discussed in Chapter 4, the level of hydrogen bonding found in [FeL₃]₂(BF₄)₂ and [FeL₃]₂(ClO₄)₂ is much reduced. Despite this apparent reduction in the level of intermolecular communication, the thermal spin transitions are still abrupt, with small hysteresis loops. It seems likely, therefore, that for the complexes of ligands derived from L1, it is the π interactions between the pyrazole rings of neighbouring cations which play the most important role in determining the level of cooperativity and not the weak intermolecular hydrogen bonding. This hypothesis finds further support when it is considered that [FeL₂]₂(BF₄)₂ and [FeL₂]₂(ClO₄)₂ have gradual spin transitions and that their structure is such that they contain no extensive network of π interactions similar to that observed in the other examples, Chapter 4.

	T/K	Spin state	Volume/Å ³	Mean Fe-N/Å	Bite Angle/°	Σ /°	ν /%
[FeL ₃] ₂ (BF ₄) ₂	300	HS-1	2962(1)	2.143(5)	73.8(2)	147.6	7.699
	30	LS	2801(1)	1.962(3)	79.5(1)	91.2	3.369
	30	HS-2	2844(1)	2.161(3)	73.8(1)	147.0	8.001
[FeL ₃] ₂ (ClO ₄) ₂	340	HS-1	3040(1)	2.153(8)	74.0(3)	147.7	7.920
	30	LS	2839(1)	1.973(10)	79.2(4)	94.0	3.750
	30	HS-2	2884(1)	2.150(6)	73.8(2)	146.4	7.895

Table 5.3: Selected parameters for [FeL₃]₂(BF₄)₂ and [FeL₃]₂(ClO₄)₂. Σ and ν were defined in section 3.3.1

Data were collected in the high spin state at 300 K for [FeL₃]₂(BF₄)₂ and at 340 K for [FeL₃]₂(ClO₄)₂ and in the low spin state at 30 K for both compounds. Selected parameters for both compounds, under various conditions, are shown in Table 5.3. At 300 K and at 340 K the mean iron – nitrogen bond lengths for both compounds are diagnostic for a high spin iron (II) species; 2.143(5) Å for [FeL₃]₂(BF₄)₂ and 2.153(8) Å for [FeL₃]₂(ClO₄)₂. On cooling through the thermal spin transition to 30 K there is a decrease in the mean metal – ligand bond lengths of 0.181 Å for the former and 0.180 Å for the latter. The reduction in the volume of the unit cell observed on cooling is related to the decrease in the iron – nitrogen bond lengths caused by the change in electronic configuration associated with the spin transition. Monitoring the unit cell parameters with temperature reveals this decrease to be equal to 1.6% between 280 K and 260 K for [FeL₃]₂(BF₄)₂ and 1.7% between 300 K and 270 K for [FeL₃]₂(ClO₄)₂, Figure 5.4. These changes in volume are clearly much greater than

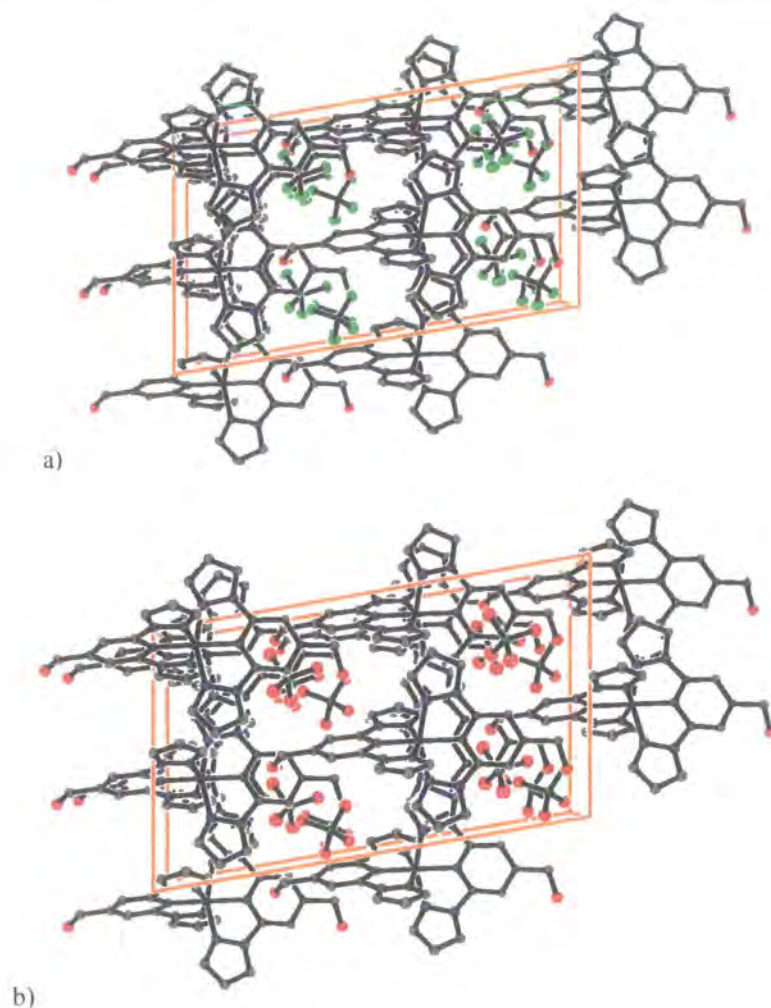


Figure 5.3: Crystal packing in the low spin state at 30 K for a) $[\text{FeL}_3]_2(\text{BF}_4)_2$ and b) $[\text{FeL}_3]_2(\text{ClO}_4)_2$. Hydrogen atoms have been omitted for clarity.

might be expected for thermal contraction alone and given that there is only a difference of 20 K and 30 K respectively, between the high and low spin measurements, we can assume that the values obtained in this way, do not differ significantly from the volume change due to the thermal spin transition alone, ΔV_{SC} . Close examination of the variation of the unit cell parameters with temperature shows that there is only a small degree of anisotropy in these compounds, with the a and b unit cell parameters decreasing by 0.4% in $[\text{FeL}_3]_2(\text{BF}_4)_2$ between 280 K and 260 K, and by 0.5% between 290 K and 270 K for $[\text{FeL}_3]_2(\text{ClO}_4)_2$, while the c parameter decreases by 0.8% for the former and 1% for the latter over the same temperature ranges. The β angles increase by 0.05% and 0.06% respectively. As in the HS-I state, there are weak hydrogen bonds between the anions and the OH groups of the cations which do not form a three dimensional network of hydrogen bonding. However, there are still a high number of face – to – face and edge – to – face π interactions, which do link the cations into a three dimensional network. The reduction in metal – ligand bond lengths on

going from the high to the low spin state results in an increase in ligand bite angle, Table 5.3. In common with the majority of spin crossover compounds, the low spin state has a closer to ideal geometry than the high spin state, as demonstrated by the lower values of the Σ and ν parameters.

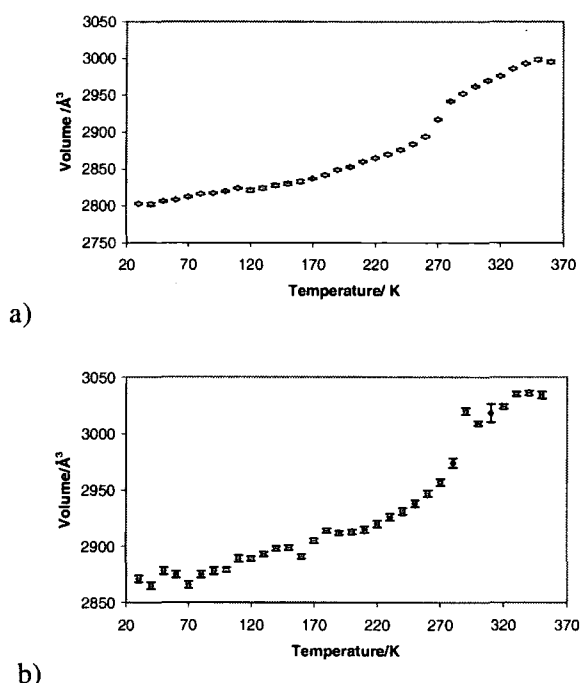


Figure 5.4: Variation of unit cell volume with temperature for a) [FeL₃]₂(BF₄)₂ and b) [FeL₃]₂(ClO₄)₂

5.3.2 The light induced high spin state

Excited state crystallographic study

Irradiation with red laser light ($\lambda = 632.8$ nm, 25 mW) at 30 K promotes both [FeL₃]₂(BF₄)₂ and [FeL₃]₂(ClO₄)₂ to the metastable high spin state and initial evidence for this is provided by the observed change in crystal colour from brown to dark yellow. Confirmation of the conversion from the low spin ground state to the HS-2 state is obtained by the increase in unit cell volume seen after irradiation, equal to 1.4% for [FeL₃]₂(BF₄)₂ and 1.6% for [FeL₃]₂(ClO₄)₂. The similarity between these values and those obtained for the thermal spin transitions, not only suggests that 100% conversion has been achieved, but it is unusual as two of three publications in which attempts were made to decouple the effect of temperature from that of the change in spin state for the thermal spin transition, report a much smaller increase in volume for the light induced transition than for the thermal transition. Only the study into the behaviour of [FeL₁]₂(BF₄)₂, the results of which are described in Chapter 3, reported a similar change in volume on going through the thermal and LIESST transitions

[4,5,6]. It therefore seems probable that this is a feature of this particular family of compounds. It is most likely that this behaviour is a result of the relatively high packing density of these materials and hence the very slight effect that changing the temperature has on their volume.

Full structural determination of the HS-2 state was possible for both compounds, however due to the reasons previously stated, (Section 5.2.2), it was not possible to refine anisotropic temperature factors for $[FeL_3_2](ClO_4)_2$. Nonetheless the results are sufficiently accurate to allow differentiation between the high and low spin states based on the metal – ligand bond lengths. After irradiation both compounds remain in the monoclinic Cc space group and selected crystallographic parameters are presented in Tables 5.1 and 5.2. Proof that a spin transition has taken place is given by the increase in mean metal – ligand bond lengths on irradiation from 1.962(3) Å to 2.161(3) Å, an increase of 0.20 Å, for $[FeL_3_2](BF_4)_2$ and from 1.982(10) Å to 2.150(6) Å, an increase of 0.17 Å, for $[FeL_3_2](ClO_4)_2$. As can be seen from Table 5.3, as well as evidence from the ligand – metal bond lengths, the Σ parameters of the HS-2 states are the same as those of the HS-1 which demonstrates that complete conversion to the metastable high spin state has taken place. Comparison of the LS and HS-2 states at 30 K shows that aside from the obvious lengthening of the metal – ligand bond lengths on irradiation, there are a number of differences between the high and low spin states; a decrease in ligand bite angle; a decrease in the symmetry of the coordination core and some slight changes to the internal angles within the ligands. Figure 5.5 shows the two spin states at 30 K superimposed in order to facilitate the comparison.

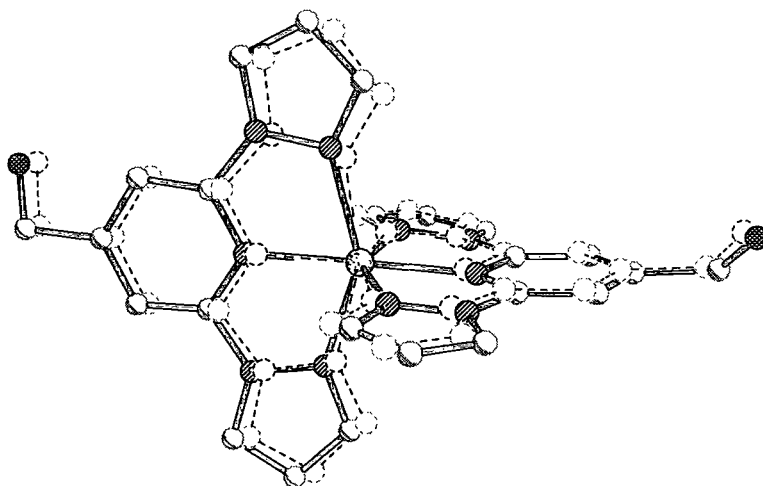


Figure 5.5: An overlay of the LS and HS-2 states at 30 K for $[FeL_3_2]^{2+}$, showing the difference in coordination around the metal centre. Solid lines represent the HS-2 state and dashed lines the LS state.

Although the increase in unit cell volume on irradiation is similar to that observed over the course of the thermal spin transition, a closer examination of the unit cell parameters reveals some differences in behaviour during the LIESST transition. The crystallographic a and b parameters change by a slightly larger percentage than during the thermal transition; 0.6 % and 0.5% for $[FeL_3_2](BF_4)_2$ respectively and 0.7% and 0.5% for $[FeL_3_2](ClO_4)_2$. The most noticeable difference is that, whereas over the course of the thermal transition the crystallographic c parameters change by 1% and 0.8%, after the LIESST transition there is no significant difference in the length of this cell edge between the high and low spin states. The difference in anisotropy of the transition results in a larger decrease in the β angle of 1% for $[FeL_3_2](BF_4)_2$ and 1.2% for $[FeL_3_2](ClO_4)_2$, than was observed in the thermal spin transition.

Research into the LIESST behaviour of $[Fe(phen)_2(NCS)_2]$ and $[Fe(phen)_2(NCSe)_2]$ (phen = 1,10-phenanthroline) has shown that for these compounds there are significant differences between the structures of the HS-1 and HS-2 states, which lead to increased cooperativity in the HS-2 state through shorter intermolecular bonds [5,7]. Comparison of the two high spin states for $[FeL_3_2](BF_4)_2$ and $[FeL_3_2](ClO_4)_2$ demonstrates that the HS-1 and HS-2 states are essentially identical. Although the iron – nitrogen bond lengths for the HS-2 states appear to be longer than those observed for the HS-1 states, this is an artefact of the crystallographic experiment caused by the reduction in thermal motion of the atoms on cooling. The diagrams in Figure 5.6 show the two HS-2 states overlaid and it can be seen that, aside from very small differences in the twists of the ligands, which are most likely due to the change in bond lengths associated with cooling, the two high spin states of both compounds are the same. The intermolecular $\pi - \pi$ and hydrogen bonding in these complexes it is the same in both the HS-1 and HS-2 states, allowing once again for the effect of thermal contraction which will bring neighbouring molecules more closely together. The similarities between the intermolecular bonding in the two states imply that the cooperativity of the two is the same and this is borne out by the photomagnetic studies described in the following section. When taken in conjunction with the results from the determination of the structure of the HS-2 state of $[FeL_1_2](BF_4)_2$, in which the two high spin states are shown to have the same structure (Chapter 3), these results suggest that it is a property of the family of 2,6-dipyrazol-1-ylpyridine derivatives that there is no significant difference between the two high spin states. This feature of their behaviour is likely to be related to the fact that these complexes of two tridentate ligands have less intrinsic flexibility than either $[Fe(phen)_2(NCS)_2]$ or $[Fe(phen)_2(NCSe)_2]$ which contain two bidentate and two monodentate ligands. This point is particularly pertinent when it is considered that the changes observed in both earlier studies, concern the conformation of the monodentate NCS^- or $NCSe^-$ ligands.

$T(\text{LIESST})$ has been defined previously as the temperature at which 50% of the molecules are in the HS-2 state and in order to determine this important parameter it is necessary to follow a specific experimental method, as defined by Létard *et al* [2,3]. It is not possible to obtain the rigorous experimental conditions required using the routinely available diffraction equipment and so any measurement of $T(\text{LIESST})$ is of necessity an estimate. However by monitoring the change in unit cell parameters with temperature on warming from 30 K after irradiation it is possible to estimate the temperature at which relaxation from the HS-2 state takes place. By this method $[\text{FeL}_3]_2(\text{BF}_4)_2$ is found to undergo relaxation between 70 K and 80 K while $[\text{FeL}_3]_2(\text{ClO}_4)_2$ relaxes back to the low spin ground state between 65 K and 70 K. These results fit the inverse relationship proposed by Hauser between $T_{1/2}$ and $T(\text{LIESST})$ [8].

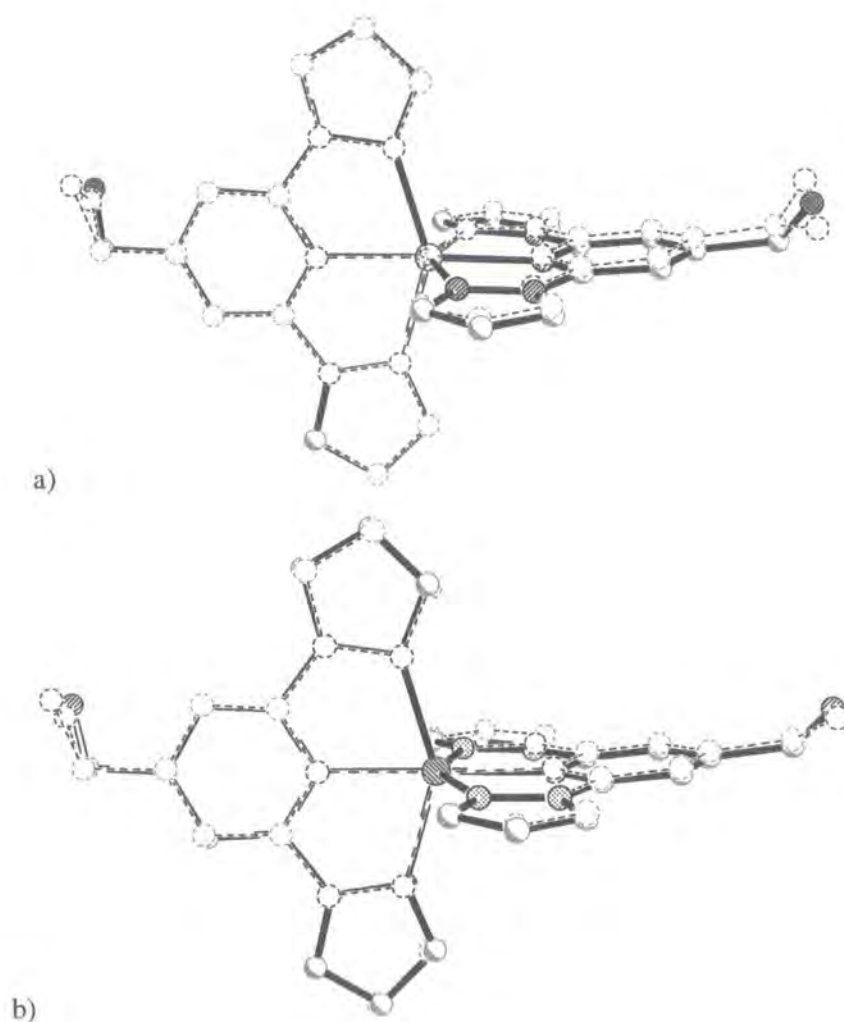


Figure 5.6: Overlay of the structure of the HS-1 and HS-2 states of a) $[\text{FeL}_3]_2(\text{BF}_4)_2$; and b) $[\text{FeL}_3]_2(\text{ClO}_4)_2$. Solid lines show the HS-2 states at 30 K while dashed lines represent the HS-1 states at 300 K a) and 340 K b).

5.3.3 Photomagnetic study

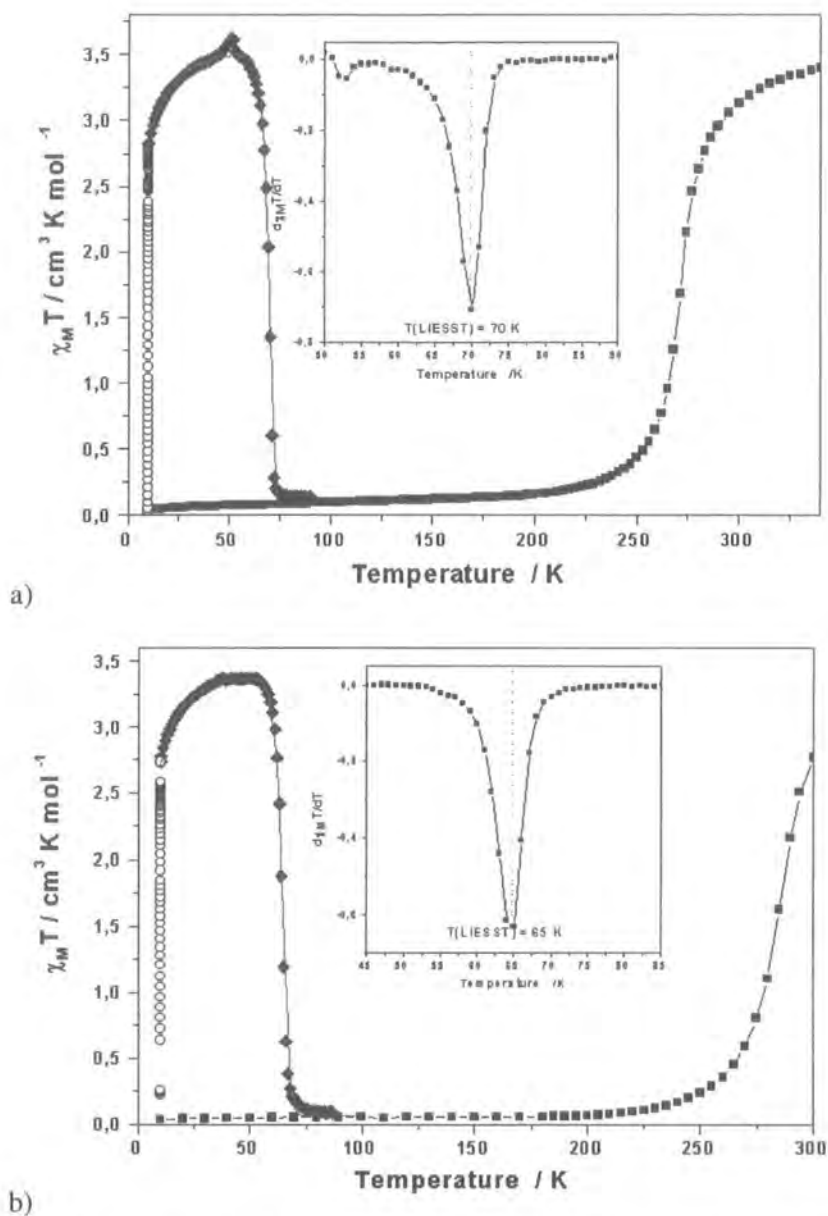


Figure 5.7: Temperature dependence of $\chi_M T$ for a) [FeL₃]₂(BF₄)₂ and b) [FeL₃]₂(ClO₄)₂. ■ = data recorded in the cooling and warming mode without irradiation; ○ = data recorded with irradiation at 10 K; ◆ = T(LIESST) measurement, data recorded in the warming mode with the laser turned off after irradiation for one hour

Figure 5.7 shows the results of a detailed examination into the magnetic behaviour of [FeL₃]₂(BF₄)₂ and [FeL₃]₂(ClO₄)₂, both the effect of the thermal spin transition and the effect of irradiation. The values of $\chi_M T$ at 300 K and at 10 K before irradiation are as predicted for fully high spin and fully low spin iron (II) compounds respectively. On irradiation at 10 K $\chi_M T$ increases sharply to reach a plateau with a value close to that seen at 300 K, indicating

complete conversion to the HS-2 state. On warming in the dark there is a sudden decrease in the value of $\chi_{\text{M}}T$ to close to $0 \text{ cm}^3 \text{ K mol}^{-1}$ indicative of complete relaxation to the low spin ground state. Determination of the extreme of the $\partial\chi_{\text{M}}T/\partial T$ versus T curve for the relaxation shows that $T(\text{LIESST})$ can be estimated as being 70 K and 65 K for $[\text{FeL}_3]_2(\text{BF}_4)_2$ and $[\text{FeL}_3]_2(\text{ClO}_4)_2$ respectively, in good agreement with the crystallographic results. The abrupt nature of the relaxation and the similarity of its shape to that of the thermal spin transition curve, indicates that there is a comparable degree of cooperativity in the two high spin states and so that the intermolecular interactions are closely related, as supported by the crystallographic results.

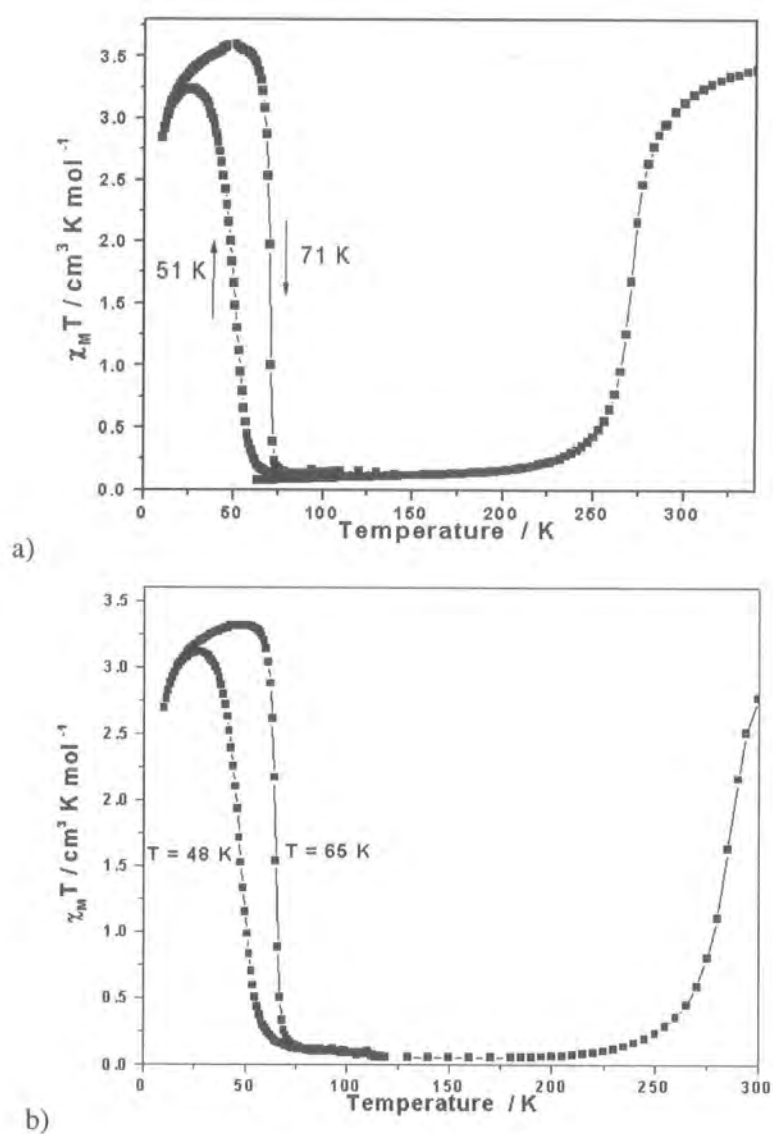


Figure 5.8: LITH experiment; the temperature dependence of $\chi_{\text{M}}T$ recorded in the warming and cooling modes with irradiation for a) $[\text{FeL}_3]_2(\text{BF}_4)_2$; b) $[\text{FeL}_3]_2(\text{ClO}_4)_2$

Constant irradiation of spin crossover materials whilst warming from 10 K to a temperature above $T(\text{LIESST})$ and then cooling to 10 K has shown the existence of LITH loops (Light Induced Thermal Hysteresis) when the compounds involved have a high degree of cooperativity. This provides another method for examining the degree of cooperativity in the sample. The results of the LITH experiments for $[\text{FeL}_3](\text{BF}_4)_2$ and $[\text{FeL}_3](\text{ClO}_4)_2$ are shown in Figure 5.8. The solid lines through the graphs in Figures 5.7 are the results obtained from calculation of the spin transitions using parameters obtained from a kinetic study of the relaxation of the compounds. Detailed discussion of the results of these calculations lies beyond the scope of this thesis, and will be published elsewhere [1], but it can be seen from the figures that an excellent fit to the experimental data has been achieved.

5.4 Conclusions

The title compounds undergo abrupt spin transitions close to room temperature with small hysteresis loops. The structures of the high and low spin states have been determined on either side of the thermal spin transition. The addition of a CH_2OH group to the 4 position of the central pyridine ring of the 2,6-dipyrazol-1-yl-pyridine ligand allows the formation of some weak hydrogen bonds, but in comparison with $[\text{FeL}_1](\text{BF}_4)_2$, $[\text{FeL}_2](\text{BF}_4)_2$ and $[\text{FeL}_2](\text{ClO}_4)_2$ the amount of hydrogen bonding is reduced. Despite the reduced hydrogen bonding, both $[\text{FeL}_3](\text{BF}_4)_2$ and $[\text{FeL}_3](\text{ClO}_4)_2$ show abrupt thermal spin transitions with narrow hysteresis loops, indicative of high levels of cooperativity. This observation suggests that it is the extensive network of π interactions in these structures which is responsible for the cooperative nature of the transitions. This hypothesis is further supported by the absence of these interactions in $[\text{FeL}_2](\text{BF}_4)_2$ and $[\text{FeL}_2](\text{ClO}_4)_2$, in which the thermal spin transition is gradual and for which hydrogen bonding plays a critical role, Chapter 4.

On irradiation with red laser light at 30 K $[\text{FeL}_3](\text{BF}_4)_2$ and $[\text{FeL}_3](\text{ClO}_4)_2$ are promoted to the metastable high spin state. The HS-2 state has a sufficiently long lifetime at this temperature to allow for a full data collection. Comparison of the structures of the two high spin states for the materials shows that, in common with $[\text{FeL}_1](\text{BF}_4)_2$, the HS-1 and HS-2 states are metrically the same. These three results are different for those obtained from an examination of the excited state structures of $[\text{Fe}(\text{phen})_2(\text{NCS})_2]$ and $[\text{Fe}(\text{phen})_2(\text{NCSe})_2]$ in which significant differences were observed between the two high spin states. That the two states are the same, is a feature of this class of compounds and can be reasonably considered as being a result of the rigidity conferred on them by the presence of two tridentate ligands,

when compared with the relative flexibility of the monodentate NCS^- and NCS_2^- ligands used in conjunction with the bidentate phen ligands.

5.5 References

1. J. Elhaik, V. A. Money, C. Carabonera, J. Sánchez, J-F. Létard, M. A. Halcrow and J. A. K. Howard, *Chem. Eur. J.*, 2004 in preparation
2. J-F Létard, L. Capes, G. Chastanet, N. Moliner, S. Létard, J. A. Real and O. Kahn, *Chem. Phys. Lett*, 1999, **313**, 115 - 120
3. J-F. Létard, G. Chastanet, O. Nguyen, S. Marcén, M. Marchivie, P. Guionneau, D. Chasseau, P. Gülich, *Montash. Chem.*, 2003, **134**, 165 - 182
4. J. Kusz, H. Spiering and P. Gülich, *J. Appl. Cryst.*, 2001, **34**, 229 - 238
5. M. Marchivie, P. Guionneau, J. A. K. Howard, A. E. Goeta, G. Chastanet, J-F. Létard and D. Chasseau, *J. Am. Chem. Soc.*, 2002, **124**, 194 - 195
6. V. A. Money, I. R. Evans, M. A. Halcrow, A. E. Goeta, and J. A. K. Howard, *Chem. Commun.*, **2003**, 158 - 159
7. E. J. MacLean, C. M. McGrath, C. J. O'Connor, C. Sangregorio, J. M. W. Seddon, E. Sinn, F. E. Sowrey, S. J. Teat, A. E. Terry, G. B. M. Vaughan and N. A. Young, *Chem. Eur. J.*, 2003, **921**, 5314 - 5322
8. A. Hauser, *Coord. Chem. Rev.*, 1991, **111**, 275 - 290

6 The spin transition behaviour of $[FeL_4_2](BF_4)_2$, $[FeL_4_2](ClO_4)_2$ and $[FeL_5_2](ClO_4)_2$

6.1 Introduction

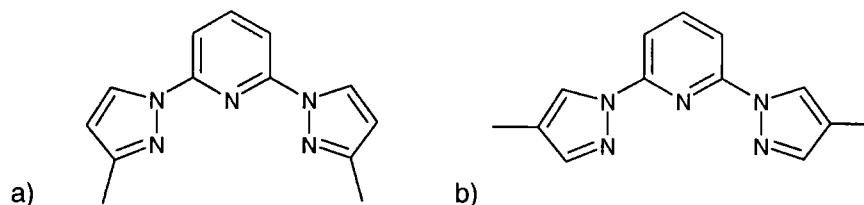


Figure 6.1: a) $L_4 = 2,6\text{-di}(3\text{-methylpyrazol-1-yl})\text{pyridine}$; b) $L_5 = 2,6\text{-di}(4\text{-methylpyrazol-1-yl})\text{pyridine}$

With the aim of extending our library of spin crossover compounds with differing spin transition behaviour, iron (II) complexes of L_4 and L_5 were made, where $L_4 = 2,6\text{-di}(3\text{-methylpyrazol-1-yl})\text{pyridine}$ and $L_5 = 2,6\text{-di}(4\text{-methylpyrazol-1-yl})\text{pyridine}$, Figure 6.1. $[FeL_4_2](ClO_4)_2$, $[FeL_4_2](BF_4)_2$ and $[FeL_5_2](ClO_4)_2$ are related to those described in Chapter 4, $[FeL_2_2](BF_4)_2$ and $[FeL_2_2](ClO_4)_2$, in which intermolecular bonding between the anions and the methyl groups of the ligands plays a critical role in determining the course of the thermal spin transition. Synthesis of $[FeL_4_2](ClO_4)_2$ yields a mixture of unsolvated and solvated crystals, impossible to separate on sight. For this reason it has not been possible to obtain a good spin transition curve using SQUID magnetometry. A detailed variable temperature crystallographic study was performed on this material in the hope of gaining an insight into its spin transition behaviour in the absence of magnetic data.

Prior to this study, no magnetic data were available for $[FeL_4_2](BF_4)_2$ or $[FeL_5_2](ClO_4)_2$; described herein are the results of a variable temperature and excited state SQUID magnetometry study into the spin transition behaviour of these compounds, performed in collaboration with the ICMCB in Bordeaux. To compliment these studies, variable temperature and excited state crystallographic investigations were carried out on both materials and the results of this work are described below.

6.2 Experimental

6.2.1 Synthesis

$[FeL_4_2](BF_4)_2$, $[FeL_4_2](ClO_4)_2$ and $[FeL_5_2](ClO_4)_2$ were synthesised by Jerome Elhaik of the School of Chemistry, University of Leeds.

6.2.2 Crystallography

The variable temperature crystallographic study was performed as described in Chapter 2. The structures were solved by direct methods and refined on F^2 using full matrix least-squares methods within the SHELXTL suite. The hydrogen atoms were placed geometrically and treated with a riding model. For the LIESST experiments the samples were irradiated for between five and ten minutes whilst on the diffractometer using a He – Ne laser ($\lambda = 632.8$ nm, 25 mW). Selected crystallographic parameters are presented in Tables 6.1, 6.3, 6.5, 6.7 and 6.9.

X-ray diffraction data for $[FeL_4_2](ClO_4)_2$ and $[FeL_5_2](ClO_4)_2$ were collected on a Bruker SMART 1000 diffractometer using a sealed tube X-ray source. Due to the weaker nature of the diffraction observed from $[FeL_4_2](BF_4)_2$ a Bruker Proteum diffractometer equipped with an APEX detector and a Bede molybdenum X-ray Microsource was used for the experiments on this compound.

6.2.3 Magnetometry

Excited state and variable temperature SQUID magnetometry experiments were carried out on $[FeL_4_2](BF_4)_2$ and $[FeL_5_2](ClO_4)_2$ as described in Chapter 2. The data show no evidence of the sample being heated by the laser: no sudden increase in magnetic signal on turning off the laser was observed as shown in Figures 6.8 and 6.29.

6.3 Results and Discussion

6.3.1 [FeL₂](ClO₄)₂

Variable temperature crystallographic study

Empirical formula	C ₂₆ H ₂₆ Cl ₂ FeN ₁₀ O ₈	C ₂₆ H ₂₆ Cl ₂ FeN ₁₀ O ₈	C ₂₆ H ₂₆ Cl ₂ FeN ₁₀ O ₈
Formula weight	733.32	733.32	733.32
Temperature/K	290	120	30
Spin state	HS-1	Mixed spin	LS
Shape	Plate	Plate	Plate
Colour	Yellow	Yellow - brown	Yellow - brown
Crystal system	Monoclinic	Monoclinic	Monoclinic
Space group	C2/c	C2/c	C2/c
a/ Å	35.394(7)	34.397(1)	34.201(4)
b/ Å	11.380(2)	11.1552(3)	11.102(1)
c/ Å	17.260(4)	17.0325(5)	16.986(2)
β/ deg	114.30(3)	113.817(2)	113.667(2)
Volume/ Å ³	6336(2)	5978.9(3)	5907(1)
Z	8	8	8
D _c / Mg/m ³	1.537	1.629	1.649
μ/ mm ⁻¹	0.709	0.752	0.761
Crystal size / mm	0.24 x 0.20 x 0.06	0.24 x 0.20 x 0.06	0.24 x 0.20 x 0.06
Theta range / deg	1.26 to 27.47	1.29 to 27.47	2.60 to 27.51
Reflections collected	16418	20278	24965
Independent reflections	6213	6857	6523
R _(int)	0.1929	0.0688	0.0565
wR(F ²)(all data)	0.1592	0.1480	0.2154
R(F)(all data)	0.2183	0.0966	0.1043
refined parameters	455	455	464
GOF	0.754	1.208	1.364
Δρ _{min,max} / e.Å ⁻³	0.31 and -0.23	0.59 and -0.69	0.70 and -0.77

Table 6.1: Selected crystallographic parameters for [FeL₂](ClO₄)₂. Where HS-1 is the high spin ground state and LS is the low spin state.

[FeL₂](ClO₄)₂ was found to crystallise in the monoclinic space group C2/c and there is no crystallographic phase transition over the temperature range studied. The iron atom occupies a distorted octahedral geometry bound to two ligands through three of their five nitrogen atoms, Figure 6.2. One of the anions is found to be disordered over the whole temperature range. In common with the other members of this family of spin crossover compounds, apart from [FeL₂](BF₄)₂ and [FeL₂](ClO₄)₂, there are extensive edge - to - face and face - to - face π interactions between neighbouring cations. There are also weak hydrogen bonds between the central pyridine ring of the ligands and the oxygen atoms of the anions. The disordered anion plays the most important role in the intermolecular bonding, forming weak hydrogen

bonds to both the methyl groups and the pyridine ring of the ligands and so linking neighbouring cations. It is possible that these extensive interactions are the reason why this anion is found to be disordered over the whole temperature range rather than becoming ordered on cooling as has been seen in other compounds. The asymmetric unit consists of one cation and two anions. At 290 K the iron – nitrogen bond lengths are indicative of iron in the high spin state with a mean value of 2.112(8) Å. On cooling to 120 K there is a decrease in iron – nitrogen bond length of 0.143 Å to 1.969(6) Å. This value for the change in Fe - N bond lengths is rather low for a complete spin transition but does suggest that at least a partial spin transition has taken place, certainly the mean iron – nitrogen bond distances do indicate that the compound is in the low spin state at this temperature. Further cooling to 30 K leads to iron – nitrogen bond lengths identical, within error, to those observed at 120 K, 1.964(7) Å, suggesting that no further spin transition has taken place between these two temperatures.

	T/ K	Mean Fe-N/ Å	Bite angle ^o	Σ ^o	v/ %
[FeL ₄](ClO ₄) ₂	290	2.112(8)	75.6(2)	131.4	6.67
	120	1.969(6)	79.9(2)	92.5	3.30
	30	1.964(7)	80.0(2)	91.8	3.33

Table 6.2: Selected molecular parameters for [FeL₄](ClO₄)₂

Examination of the anisotropic temperature factors for [FeL₄](ClO₄)₂ reveals that the model does not adequately describe the data. Severe elongation of the ellipsoids was noted at all three temperatures at which full data sets were collected, Figure 6.2. Refinement with isotropic temperature factors reveals the position of electron density at positions that suggest that there is some residual high spin compound left at 30 K and some residual low spin at 290 K, Figure 6.3. This is in line with the direction of elongation seen for the anisotropic temperature factors. At 290 K there is a peak of residual electron density in the correct position for a ligand nitrogen atom, at a distance of 1.982 Å from the central iron atom; a distance indicative of a low spin iron – nitrogen bond. The situation is less clear at 30 K but two peaks appear at distances of 2.321 Å and 2.251 Å. These distances would be rather long for an iron (II) compound in the high spin state but are suggestive of the presence of a residual high spin fraction. It was not possible to model the fraction of material in the minor state using a disorder model and so, in the absence of diffraction data collected either 100 % in the high or low spin state, it was also not possible to estimate the fraction of compound that had not gone through the spin transition. Examination of the variation in the unit cell parameters with temperature between 360 K and 30 K shows no sign of the discontinuity normally associated with a spin transition, Figure 6.4. This provides evidence of a very gradual spin transition, incomplete at the upper end of the accessible temperature range. The unit cell

volume stops decreasing at low temperature indicating that the transition has reached completion at 30 K. A further data set collected at 400 K provided no convincing evidence for a completed spin transition even at this temperature.

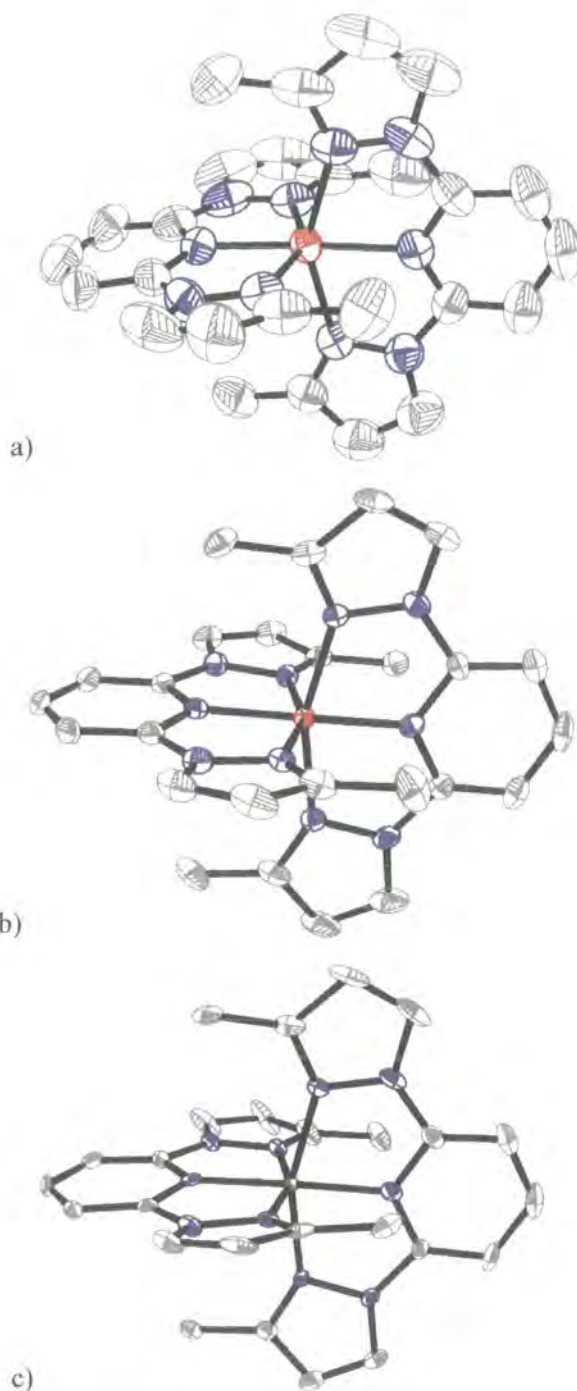


Figure 6.2: Structure of the cation from $[FeL_4](ClO_4)_2$ at a) 290 K b) 120 K and c) 30 K. Hydrogen atoms have been removed for clarity and thermal ellipsoids are at 50% probability for a) and b) and 90% for c).

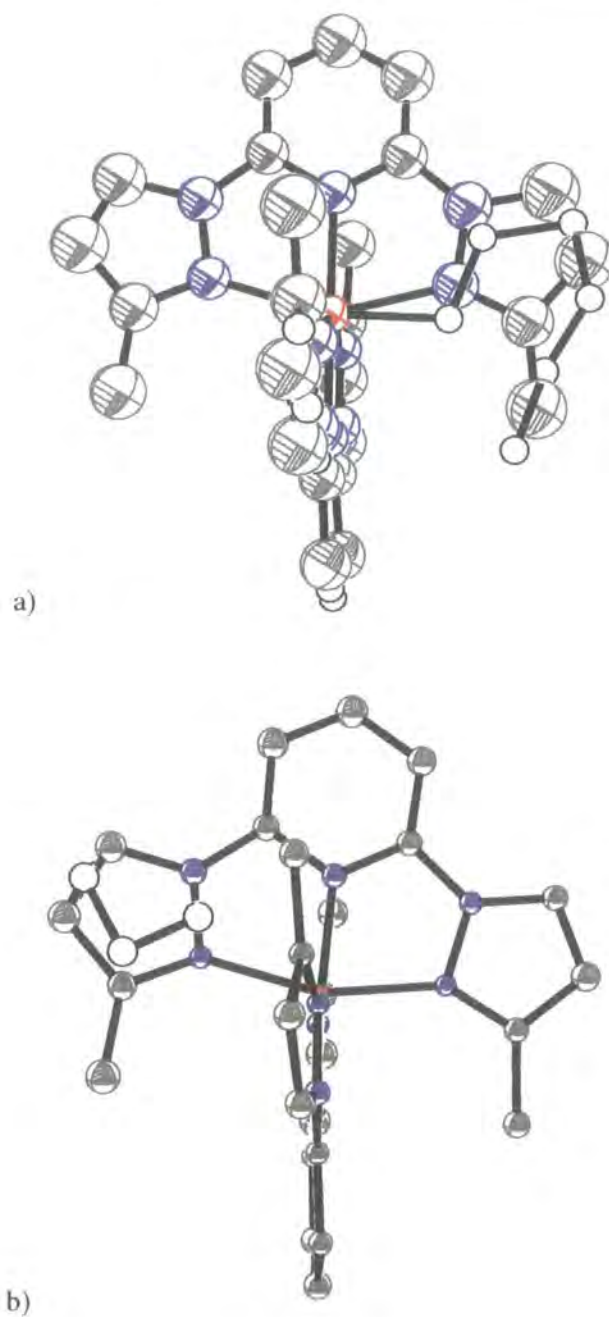


Figure 6.3: Isotropic refinement of $[\text{FeL}_4](\text{ClO}_4)_2$ at a) 290 K, primarily high spin and b) 30 K, primarily low spin, showing the residual electron density peaks at positions suggestive of residual low and high spin respectively.

The solid state structure provides no reason as to why $[\text{FeL}_4](\text{ClO}_4)_2$ could not undergo a complete spin transition. Gradual spin transitions such as this are common in solution but relatively rare in the solid state where interactions between neighbouring molecules generally lead to more abrupt transitions. This would imply that the intermolecular interactions in $[\text{FeL}_4](\text{ClO}_4)_2$ are weaker than found in other members of this series of spin crossover

compounds. It has already been suggested in Chapter 5 that it is the intermolecular π interactions that play the most important role in determining the course of the thermal spin transition in these materials. Nonetheless, given that $[\text{FeL}_2](\text{ClO}_4)_2$ and $[\text{FeL}_2](\text{BF}_4)_2$ do not undergo very gradual transitions, it would appear that the weak hydrogen bonding interactions also play a role. Indeed the hydrogen bonds formed by the disordered anion in $[\text{FeL}_4](\text{ClO}_4)_2$ are longer than those shown by either $[\text{FeL}_2](\text{ClO}_4)_2$ or $[\text{FeL}_2](\text{BF}_4)_2$ and the π interactions are also longer than those observed in $[\text{FeL}_3](\text{ClO}_4)_2$ and $[\text{FeL}_3](\text{BF}_4)_2$. These weaker interactions reduce the cooperativity of the system and thus result in a more gradual transition.

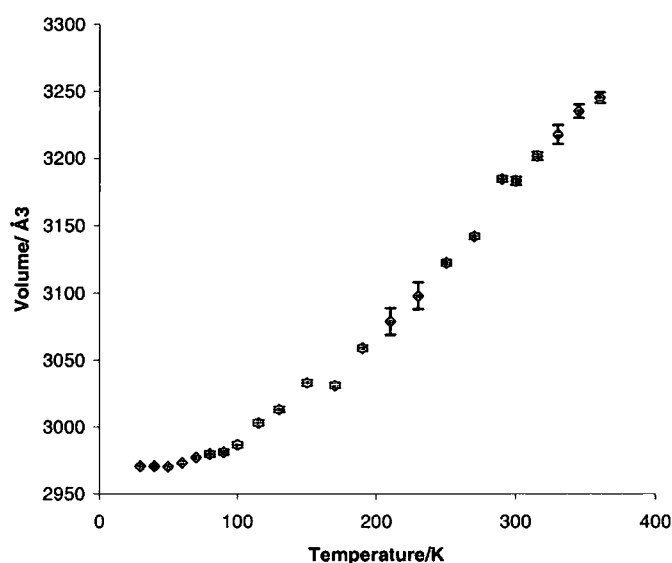


Figure 6.4: Variation of unit cell volume with temperature for $[\text{FeL}_4](\text{ClO}_4)_2$.

Excited state crystallography

Attempts were made to trap the high spin state of $[\text{FeL}_4](\text{ClO}_4)_2$ both by irradiation and by flash freezing the crystal to 30 K. The crystal was destroyed on irradiation and flash freezing only gave rise to the unit cell seen at 30 K after slow cooling. Nonetheless, it was observed that after irradiation what little remained of the crystal had changed colour from brownish yellow to yellow, which suggests that $[\text{FeL}_4](\text{ClO}_4)_2$ does undergo a LIESST transition on irradiation with red laser light ($\lambda = 632.8$ nm, 25 mW).

6.3.2 Variable temperature and excited state crystallographic and magnetic studies of [FeL₄]₂(BF₄)₂·xH₂O

Initial crystallographic studies were performed on a Bruker SMART 1000 diffractometer equipped with a sealed tube X-ray source. The results of these studies showed that the sample was hydrated, the formula being [FeL₄]₂(BF₄)₂·½H₂O. It was found that the crystal underwent a partial spin transition from fully high spin at room temperature to ⅔ high spin at 30 K. This partial spin transition was accompanied by ordering of the spin states in the crystal giving rise to the generation of a super cell with three times the volume of the room temperature unit cell. This super cell was responsible for the low intensity of some of the diffraction from the sample and thus the relatively poor quality of the structure solution for the low temperature phase. Some months after these results had been obtained, a careful study of the magnetic and photomagnetic behaviour of a polycrystalline sample of [FeL₄]₂(BF₄)₂·xH₂O revealed a fascinating complexity of spin crossover behaviour, including the existence of a number of metastable spin states. It was decided to re-examine the compound using single crystal X-ray diffraction techniques to try to determine the structural effects that might be behind this complex behaviour. For the second set of crystallographic experiments on [FeL₄]₂(BF₄)₂·xH₂O, a diffractometer fitted with an APEX detector and a Bede molybdenum X-ray microsource was used in order to provide higher incident and hence diffracted intensity, particularly from the super cell peaks expected for the mixed spin state. It was hoped that the greater intensity gained in this way would make it possible to obtain a better structural model than those determined from the preliminary experiments.

SQUID magnetometry study

This work was performed in collaboration with Dr. Chiara Carabonera in the group of Prof. Jean - François Létard of the ICMCB in Bordeaux. Figure 6.5 shows the thermal spin transition obtained on both warming and cooling. It can be seen from this plot that the polycrystalline sample of [FeL₄]₂(BF₄)₂·xH₂O is completely high spin at 300 K with a $\chi_{\text{M}}T$ value of near to 3.5 cm³ K mol⁻¹, as expected for a high spin iron (II) species. On cooling the compound undergoes a partial spin transition between 150 K and 90 K with a plateau in the transition situated at between 100 K and 130 K for the cooling curve and between 120 K and 140 K for the warming curve. The spin transition is not complete with the final $\chi_{\text{M}}T$ value being 1.5 cm³ K mol⁻¹ rather than the 0 cm³ K mol⁻¹ expected for a completely low spin iron (II) species. This value suggests that between ⅓ and ½ of the material remains in the high spin state after cooling, in contrast to the preliminary crystallographic results which suggested that ⅓ of [FeL₄]₂(BF₄)₂·½H₂O was in the high spin state after cooling.

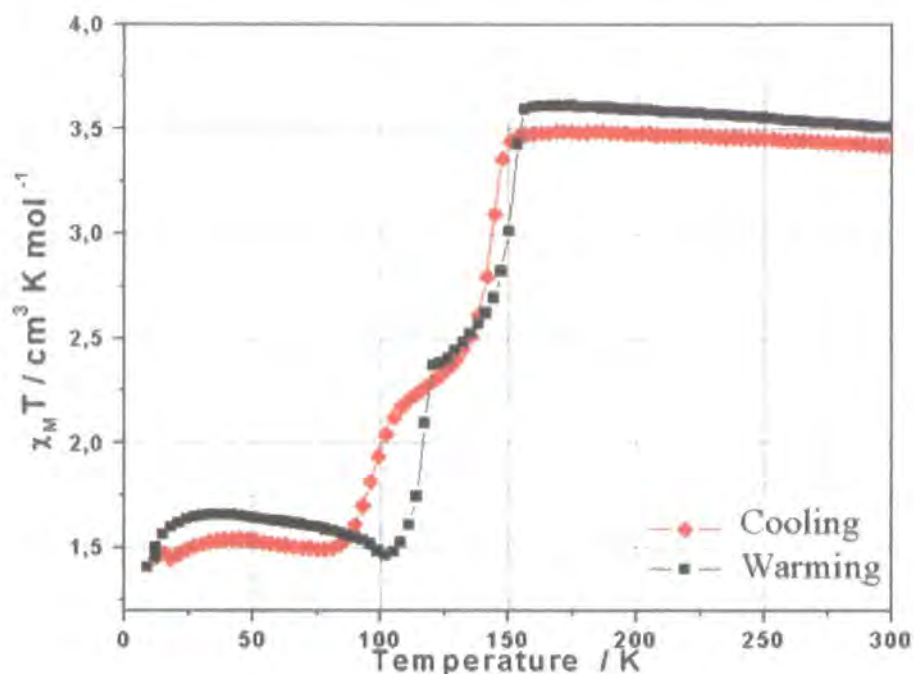


Figure 6.5: Thermal spin transition of [FeL₄]₂(BF₄)₂·xH₂O. Red: cooling at 0.5 K min⁻¹; black: warming at 1 K min⁻¹.

Trapping of the high spin state at 10 K

Quenching the sample to 10 K in the SQUID cavity was found to trap the high spin state. The red line in Figure 6.6 shows the effect of quenching superimposed on the thermal spin transition curve, black line, described above. The $\chi_M T$ value of 2.5 cm³ K mol⁻¹ at 10 K suggests that the compound may not be trapped completely in the high spin state. On warming there is a slight increase in the magnetic signal, due to zero field splitting, before it reaches a plateau at a value of 2.75 cm³ K mol⁻¹. The peak in the plot at around 40 K is due to some residual oxygen being present in the SQUID cavity. The signal decreases abruptly between 75 K and 90 K to 0 cm³ K mol⁻¹, suggesting complete and quantitative relaxation to the low spin state. The low spin state is only stable over a very small temperature range with an abrupt increase in magnetic signal observed at 120 K. Above 125 K the plot from the quenched sample follows the same course as the thermal spin transition; there is a plateau in the curve between 125 K and 150 K before the signal increases abruptly once more, reaching a final value of 3.5 cm³ K mol⁻¹ at 160 K indicating that the material is now completely in the high spin state. If the sample is then cooled again it undergoes a thermal spin transition, following the same path as seen previously.

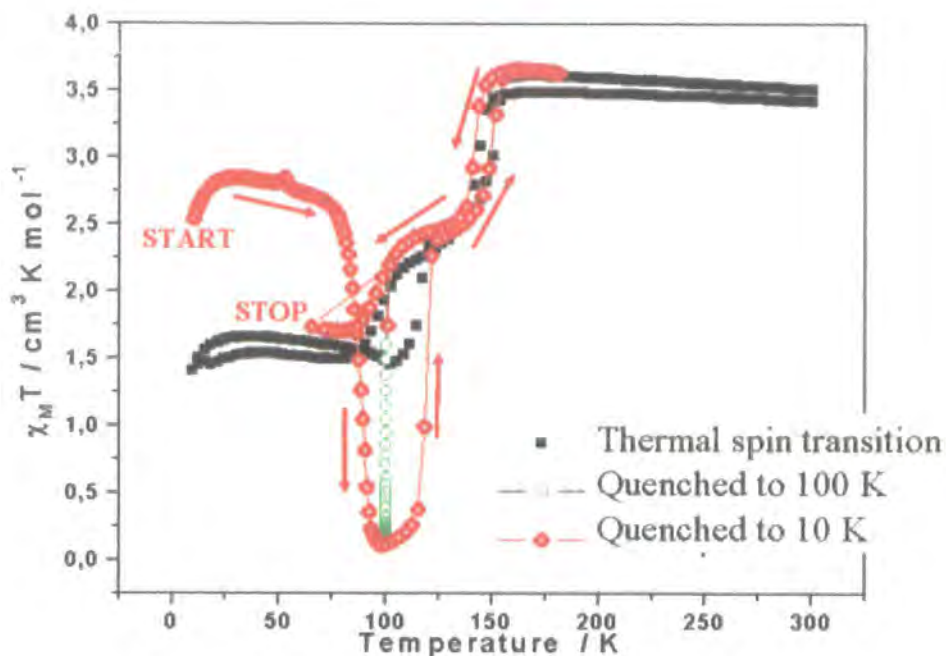


Figure 6.6: Effect of thermal quenching on $[\text{FeL}_4]_2(\text{BF}_4)_2 \cdot x\text{H}_2\text{O}$. Red line: after quenching to 10 K; green: after quenching to 100 K; black: thermal spin transition for comparison.

Quenching to 100 K; the low spin state

An alternative route to the fully low spin state was found by quenching the sample to 100 K and leaving it at this temperature to relax. This experiment is shown by the green points in Figure 6.6. On initial quenching the magnetic signal of $[\text{FeL}_4]_2(\text{BF}_4)_2 \cdot x\text{H}_2\text{O}$ is such that it is in a mixed spin state, $\chi_M T = 1.5 \text{ cm}^3 \text{ K mol}^{-1}$. The signal then falls over time to reach a final value of close to $0 \text{ cm}^3 \text{ K mol}^{-1}$ after a period of three hours. Figure 6.7 shows the effect of changing the temperature on the low spin state. The orange points show what happens when the sample is quenched to 100 K and then allowed to relax to the low spin state, stage 1. The sample was then cooled to 10 K, 2, and it can be seen that the value of $\chi_M T$ remains close to $0 \text{ cm}^3 \text{ K mol}^{-1}$. On warming from 10 K the sample remains fully low spin until 115 K, 3, when there is a sudden increase in $\chi_M T$ to $2.5 \text{ cm}^3 \text{ K mol}^{-1}$, 4, followed by a short plateau, 5, then another abrupt increase, in line with the thermal spin transition, 6, reaching the fully high spin state at 160 K with a $\chi_M T$ value of close to $3.5 \text{ cm}^3 \text{ K mol}^{-1}$, 7. The sample was then cooled from this temperature and was found to undergo a thermal spin transition identical to that initially observed before cycling through the metastable and low spin states, stages 8 to 12.

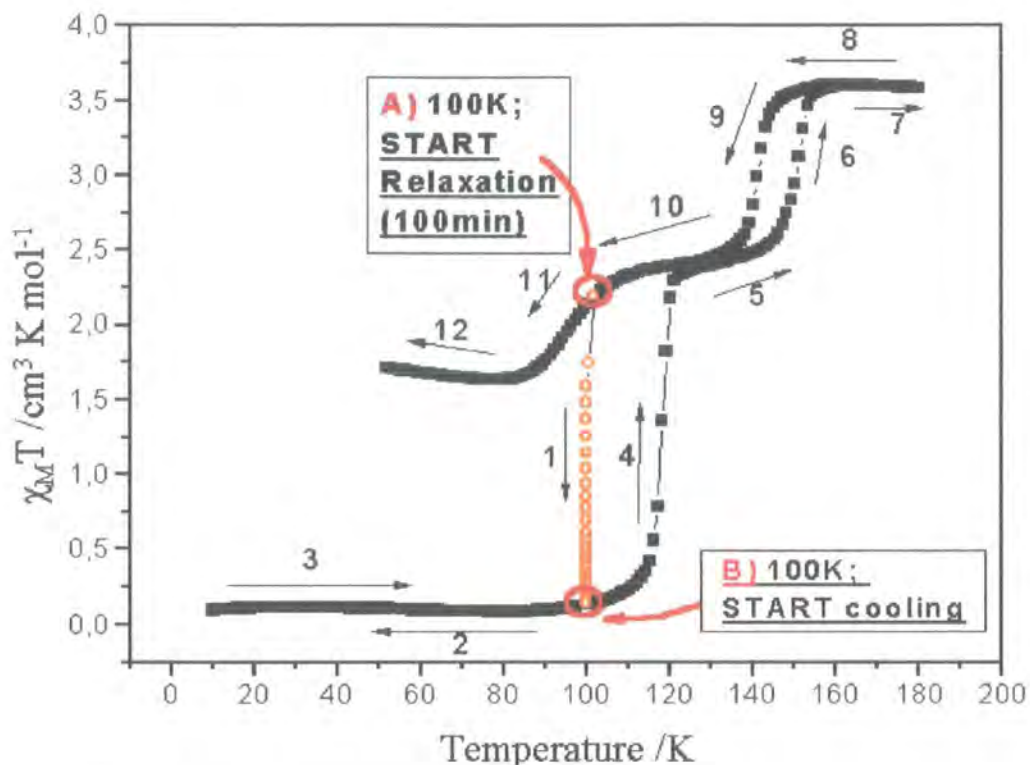


Figure 6.7: The effect of quenching to 100 K on [FeL₄]₂(BF₄)₂·xH₂O. Orange: quenching to 100 K then relaxation for 100 mins; black: effect of cooling from 100 K to 10 K after relaxation then warming from 10 K to 180 K before cooling from 180 K to 50 K.

The LIESST effect

Figure 6.8 shows the results of an investigation into the effect of irradiation on [FeL₄]₂(BF₄)₂·xH₂O, the LIESST (Light Induced Excited Spin State Trapping) effect. The sample was irradiated with green laser light ($\lambda = 532.06$ nm) and the magnetic response monitored. There was an abrupt increase in magnetic susceptibility which reached saturation at a value for $\chi_M T$ of $3.5 \text{ cm}^3 \text{ K mol}^{-1}$ indicating complete conversion to the metastable high spin state. The light was then turned off and the sample warmed, in the dark, according to the method described in Chapter 2. The material remains in the high spin state until 85 K when there is sudden fall in the $\chi_M T$ value to close to $0 \text{ cm}^3 \text{ K mol}^{-1}$ equivalent to a complete relaxation to the ground low spin state. The increase in signal at low temperature is due to zero field splitting and the discontinuity in the plateau at 40 K is due to residual oxygen. On cooling from 90 K to 10 K the sample remains in the low spin state. If the low spin state is then irradiated with green laser light it is also converted to the metastable high spin state and on warming follows the same LIESST curve. On warming from 90 K

when the compound is in the low spin state there is an abrupt increase in magnetisation at 115 K, as observed for the trapped spin state, rising to a plateau at $2.5 \text{ cm}^3 \text{ K mol}^{-1}$ before increasing again after 150 K, to reach a plateau indicative of complete conversion to the high spin state at 160 K. Cooling from this state gives rise once more to the thermal spin transition behaviour initially observed.

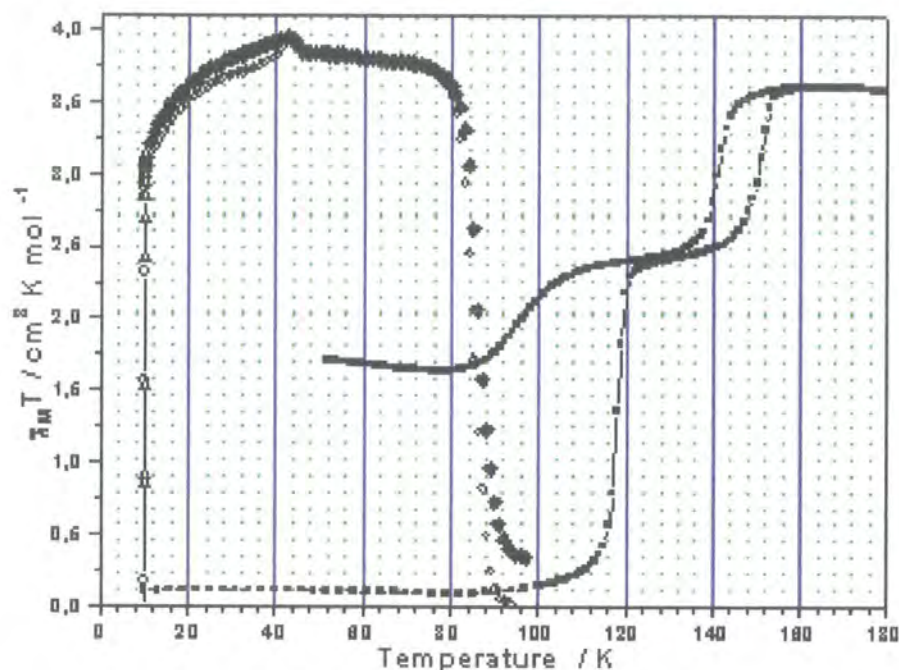


Figure 6.8: The LIESST effect in $[\text{FeL}_4]_2(\text{BF}_4)_2 \cdot x\text{H}_2\text{O}$.

This thorough investigation revealed the real complexity behind the spin crossover behaviour of $[\text{FeL}_4]_2(\text{BF}_4)_2 \cdot x\text{H}_2\text{O}$. The compound can exist in the high spin state as a result of the thermal spin transition above 160 K and as a mixed spin state below 100 K. The low spin state may be reached by allowing the sample to relax at 100 K for a period of some hours. It is also possible to reach a metastable high spin state at 10 K either by quenching to this temperature or by irradiation of either the mixed spin state or the low spin ground state, Figure 6.8. Finally the low spin state may be obtained by the relaxation of the metastable high spin state on warming from 10 K although it is only stable between 90 K and 115 K. This richness of spin crossover behaviour is indicative of how finely balanced the energy difference between the high and low spin states is in $[\text{FeL}_4]_2(\text{BF}_4)_2 \cdot x\text{H}_2\text{O}$. Despite being cycled through the metastable high spin states and relaxation to the low spin state $[\text{FeL}_4]_2(\text{BF}_4)_2 \cdot x\text{H}_2\text{O}$ still shows the same thermal spin transition behaviour, which indicates that the spin transitions cause no permanent alteration to the structure.

6.3.3 Variable temperature crystallographic study of $[FeL_4_2](BF_4)_2$

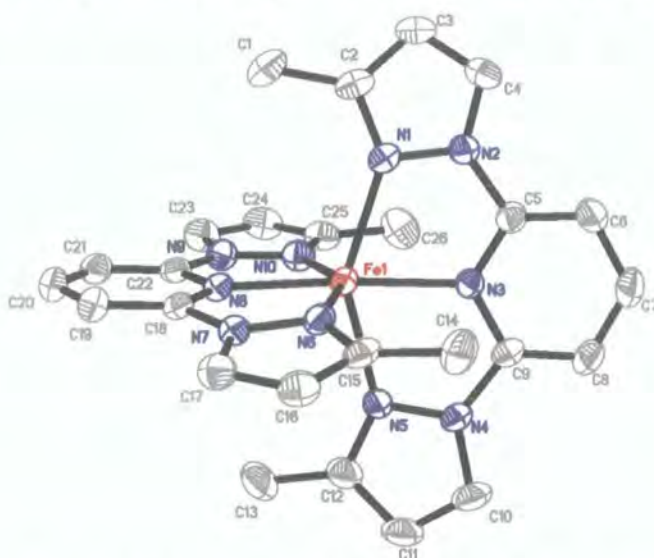


Figure 6.9: Structure of the cation of $[FeL_4_2](BF_4)_2$ at 200 K. Hydrogen atoms have been omitted for clarity and thermal ellipsoids are at 50% probability

Re-examination of the crystal on which the preliminary experiments had been performed showed that it had lost the disordered water molecule previously observed. Despite this it had retained its crystallinity and it was possible to determine the structure of the high and low spin states and the mixed spin state. X-ray diffraction data were collected at 200 K, 130 K and 90 K. However, on this occasion, the spin transition behaviour observed was different to that seen initially. $[FeL_4_2](BF_4)_2$ was found to crystallise in the monoclinic space group $C2/c$ at 200 K with unit cell parameters of $a = 23.341(5) \text{ \AA}$, $b = 11.000(2) \text{ \AA}$, $c = 24.037(5) \text{ \AA}$, $\beta = 95.44(3)^\circ$ and $V = 6144(2) \text{ \AA}^3$. Selected crystallographic parameters for the variable temperature study of $[FeL_4_2](BF_4)_2$ are presented in Table 6.3. The asymmetric unit consists of one formula unit; two anions and one cation. The iron atom occupies a distorted octahedral geometry bound equatorially to two ligands through three of their five nitrogen atoms, Figure 6.9. The mean iron – nitrogen bond length is indicative of a fully high spin iron (II) centre at this temperature, in agreement with the magnetic data, Table 6.4. The methyl groups at the three positions on the ligand pyrazole rings disrupt the solid state packing such that $[FeL_4_2](BF_4)_2$ is unable to form the edge to face and face to face π interactions, which have been observed to be common for this family of spin crossover materials. There are weak interactions between the methyl groups and the pyrazole rings of neighbouring cations which link the cations into a chain. There are also extensive weak CH – F hydrogen bonds between the anions and the ligands. Figure 6.10 shows the packing in the crystal for $[FeL_4_2](BF_4)_2$ at 200 K. Neither of the counter anions is disordered at this temperature. Some residual

electron density is visible around the fluorine atoms of the anion; B2, F5, F6, F7, F8, but examination of the Fourier map shows that there is only one discrete peak present and this does not warrant modelling as either thermal or static disorder.

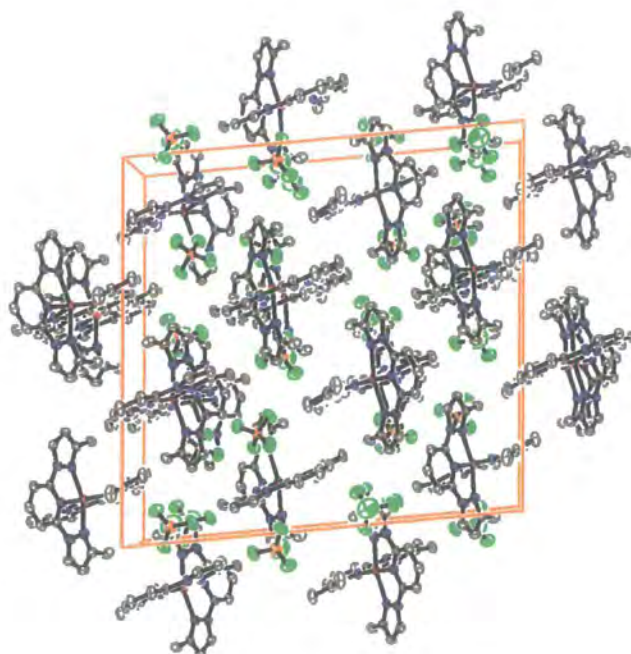


Figure 6.10: Packing diagram for $[FeL_4_2](BF_4)_2$ at 200 K in the high spin state. Hydrogen atoms have been omitted for clarity. View normal to 010.

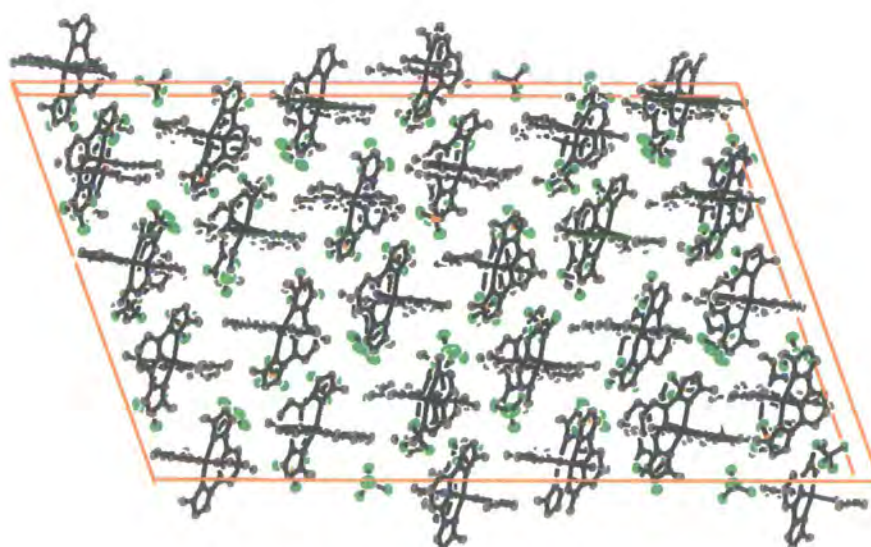


Figure 6.11: Packing diagram for $[FeL_4_2](BF_4)_2$ at 130 K in the mixed spin state. Hydrogen atoms have been omitted for clarity. View normal to 010.



Empirical formula	C ₂₆ H ₂₆ B ₂ F ₈ FeN ₁₀	C ₂₆ H ₂₆ B ₂ F ₈ FeN ₁₀	C ₂₆ H ₂₆ B ₂ F ₈ FeN ₁₀
Formula weight	708.04	708.04	708.04
Spin state	HS-1	Mixed spin	LS
Temperature/K	200	130	90
Shape	Irregular	Irregular	Irregular
Colour	Yellow	Yellow	Brown
Crystal system	Monoclinic	Monoclinic	Monoclinic
Space group	C2/c	C2/c	C2/c
a/ Å	23.341(5)	54.88(1)	22.707(5)
b/ Å	11.000(2)	10.892(2)	10.817(2)
c/ Å	24.037(5)	31.997(6)	24.162(5)
β /deg	95.44(3)	109.77(3)	93.11(3)
Volume/ Å³	6144(2)	17999(6)	5926(2)
Z	8	24	8
D_c/ Mg/m³	1.531	1.568	1.587
μ/ mm⁻¹	0.576	0.590	0.598
Crystal size / mm	0.20 x 0.16 x 0.12	0.20 x 0.16 x 0.12	0.20 x 0.16 x 0.12
Theta range / deg	1.70 to 23.26	1.32 to 35.00	1.69 to 35.02
Reflections collected	8676	49319	14609
Independent reflections	4105	28791	9088
R_(int)	0.0382	0.0583	0.0712
wR(F²)(all data)	0.1437	0.2331	0.2944
R(F)(all data)	0.0510	0.1361	0.1421
Refined parameters	428	1282	428
GOF	1.132	1.017	1.027
Δρ_{min,max} / e.Å⁻³	0.47 and -0.49	2.09 and -1.34	2.04 and -2.32

Table 6.3: Selected crystallographic parameters for [FeL₄](BF₄)₂ at 200 K, 130 K and 90 K. Where HS-1 is the high spin ground state and LS is the low spin state.

On cooling to 130 K [FeL₄](BF₄)₂ is found to undergo a crystallographic phase transition. The bulk packing of the compound remains the same, Figure 6.11, and at this temperature it is still in the monoclinic C2/c space group. However the unit cell is seen to treble in volume having parameters of: $a = 54.88(1)$ Å, $b = 10.892(2)$ Å, $c = 31.997(3)$ Å, $\beta = 109.77(3)^\circ$ and $V = 17999(6)$ Å³. The asymmetric unit now contains three formula units and the unit cell twenty four. This trebling of the unit cell and asymmetric unit is a result of ordering of a mixed spin state. Examination of the three independent iron (II) ions reveals that the mean metal – ligand bond lengths indicate that two are high spin and one is low spin. The only very minor alterations in solid state structure which arise from this partial spin transition explain why the peaks for this larger unit cell appear as weak super cell peaks, it being nearly possible to refine the structure in the smaller unit cell with a volume of only 6000 Å³ with averaged bond lengths and symmetry parameters. This accounts for the poor quality of the data collected. Figure 6.12 shows the structure of the three independent cations at 130 K.

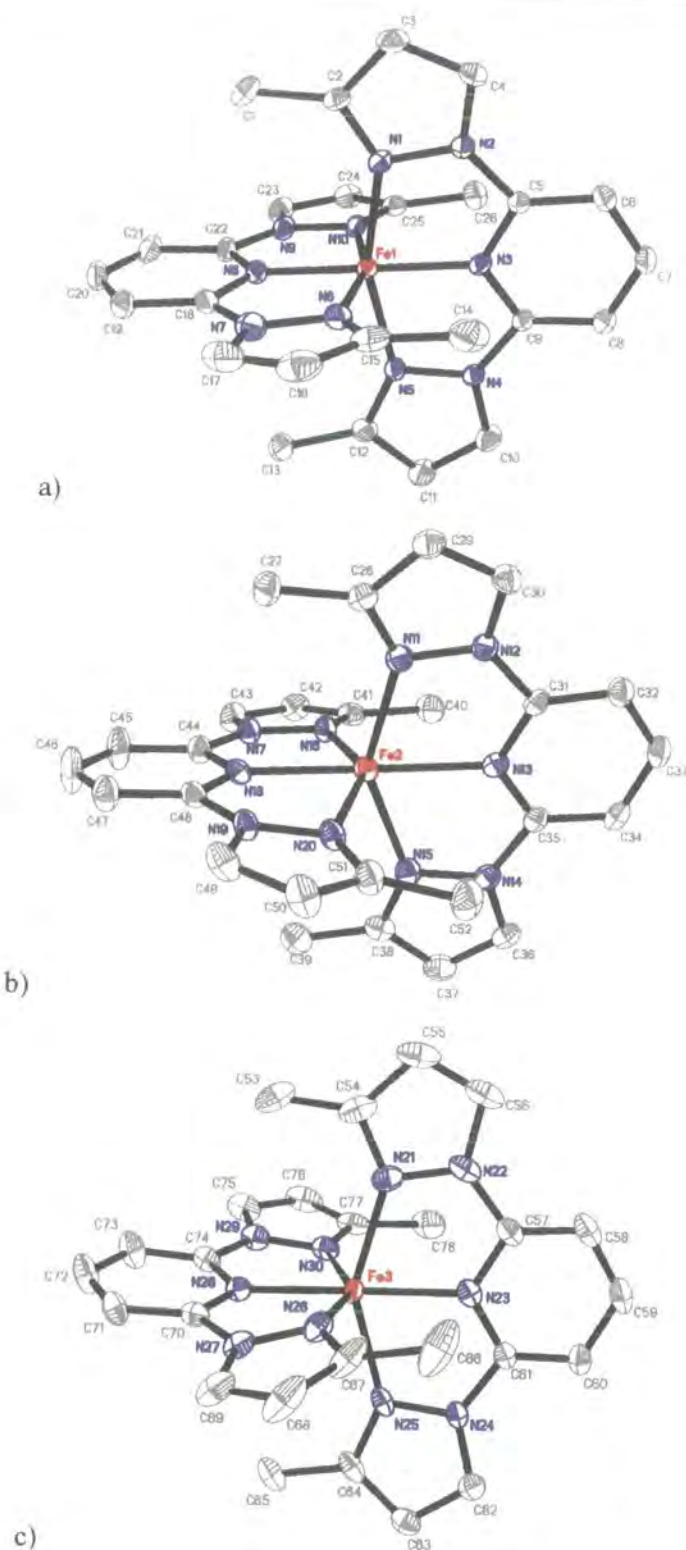


Figure 6.12: The three independent cations of $[FeL_4_2](BF_4)_2$ at 130 K. Hydrogen atoms have been omitted for clarity. a) Low spin iron Fe1; b) High spin iron Fe2; c) 20% low spin iron Fe3.

Comparison of the independent cations reveals the differences in structure that lead to the tripling of the unit cell volume and asymmetric unit. The mean metal – ligand bond lengths indicate that Fe1 is in the low spin state whereas Fe2 is in the high spin state and this is supported by the higher value of the Σ and ν parameters obtained for Fe2. Although the value of the mean metal – ligand bond length for Fe3 is in line with expectations for a high spin iron (II) compound of this type it is significantly lower than that observed for Fe2, or for the single independent high spin cation at 200 K, and this, together with the lower value of Σ , suggests that this iron centre is at least partly low spin. All these molecular parameters indicate that only a small percentage of the iron atoms on this site are in the low spin state. It is possible to estimate the percentage of the iron site in the low spin state by comparison of the Σ parameter for this site with that for Fe2, which is assumed to be 100 % high spin, and Fe1 which is assumed to be 100 % in the low spin state. Using this method the percentage of the iron in the Fe3 site in the low spin state may be estimated as 20%.

	T/ K	Fe	Spin state	Mean Fe-N/ Å	Bite angle ^o	Σ / ^o
[FeL ₄](BF ₄) ₂	200	1	HS	2.166(3)	73.7(1)	153.1
	130	1	LS	1.975(3)	80.1(1)	90.6
		2	HS	2.168(3)	73.5(1)	158.9
		3	HS/LS	2.130(3)	74.8(1)	143.7
	90	1	LS	1.968(3)	80.08(1)	101.8

Table 6.4: Selected molecular parameters for [FeL₄](BF₄)₂. The Σ parameter was defined in Section 3.3.1

Figure 6.13a shows an overlay of the cations containing Fe1 and Fe2, this shows clearly the differences between the high and low spin states. That both states exist independently in one compound, with essentially identical coordination environments, provides another method by which the effect of the spin transition on the structure may be determined, divorced from thermal effects. The differences in the two cations are those that are expected for a spin transition and have been seen frequently in the compounds described herein. There is a clear lengthening of the metal ligand bond lengths on going from the low to the high spin state and a decrease in the bite angle. Other changes within the ligands derive from these major alterations, the most noticeable being the greater twist away from planarity in the ligands seen for the high spin Fe2. The pyrazole ring N16, N17, C41, C42 and C43 is moved out of the ligand plane and this is further demonstrated by the small angle formed between this ring and the neighbouring pyrazole ring of the other ligand, 87.3(1)^o. There are also significant differences between Fe2 and Fe3 and these are shown in Figure 6.13b. That Fe3 is not fully in the high spin state is demonstrated by the slightly shorter bonds visible when the two structures are overlaid and in the elongation of the anisotropic temperature factors along the

direction of the metal ligand bonds and in the opening of the bite angle seen on going from the high to the low spin state, Figure 6.12c. The twist in the ligands is much more pronounced in the Fe3 containing cation than in either of the other two independent cations.

It is possible to compare the high spin cation, Fe2, with that of the cation at 200 K, Figure 6.14. From this comparison it can be seen that although the bond angles and lengths within the ligands are very similar at both temperatures, there is considerably more twist in the ligands at 130 K in the mixed spin state.

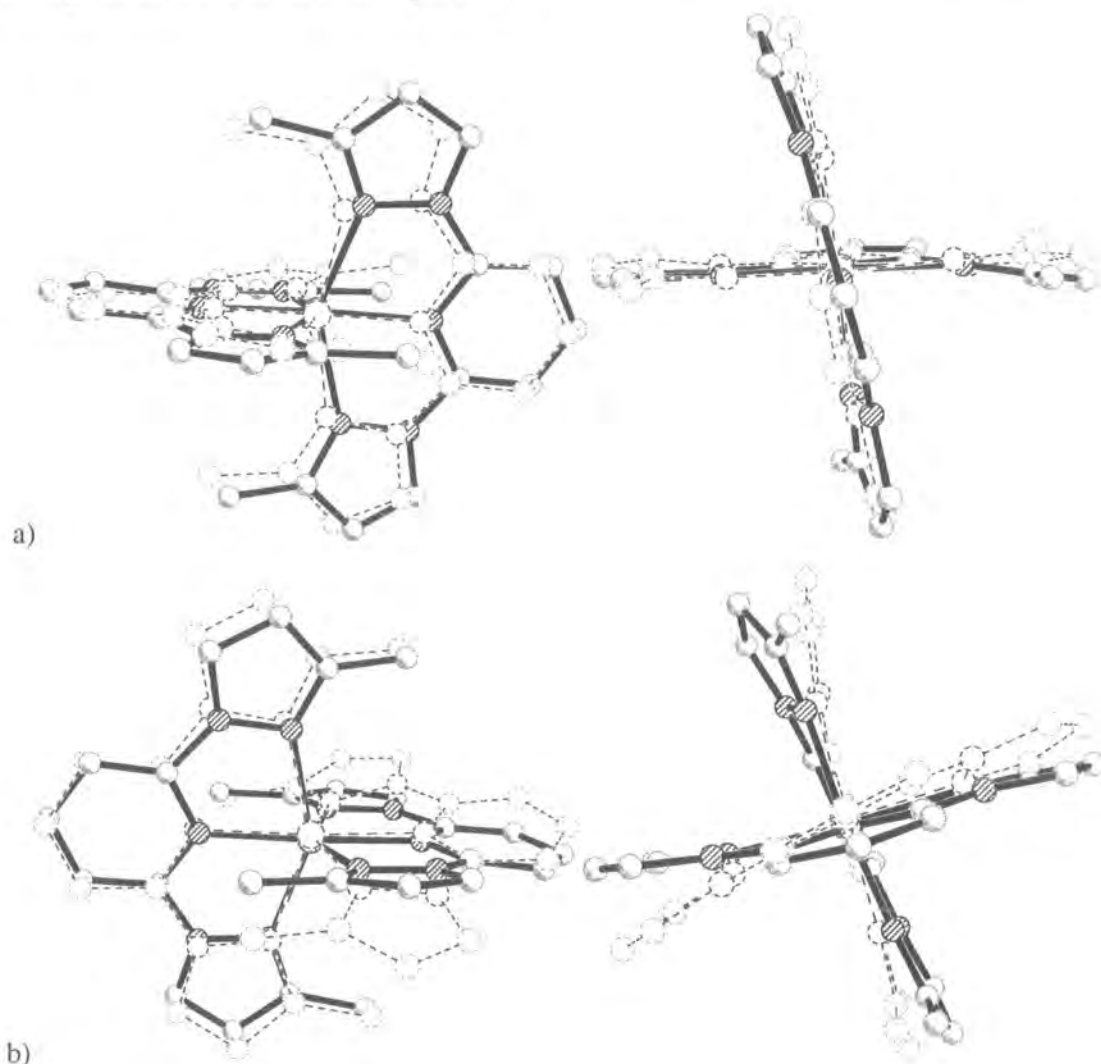


Figure 6.13: a) Overlay of the low spin cation, Fe1 (dashed line) with the fully high spin cation, Fe2 (solid line); b) overlay of the high spin cation, Fe2 (dashed line) with the 20% low spin Fe3 (solid line). Hydrogen atoms have been omitted for clarity.

Examination of the intermolecular bonding provides no conclusive evidence for why only a third of the iron molecules undergo a complete thermal spin transition. As in the fully high spin state at 200 K there are weak interactions between the methyl groups and the pyrazole rings of the ligands and hydrogen bonds between the anions and the cations.

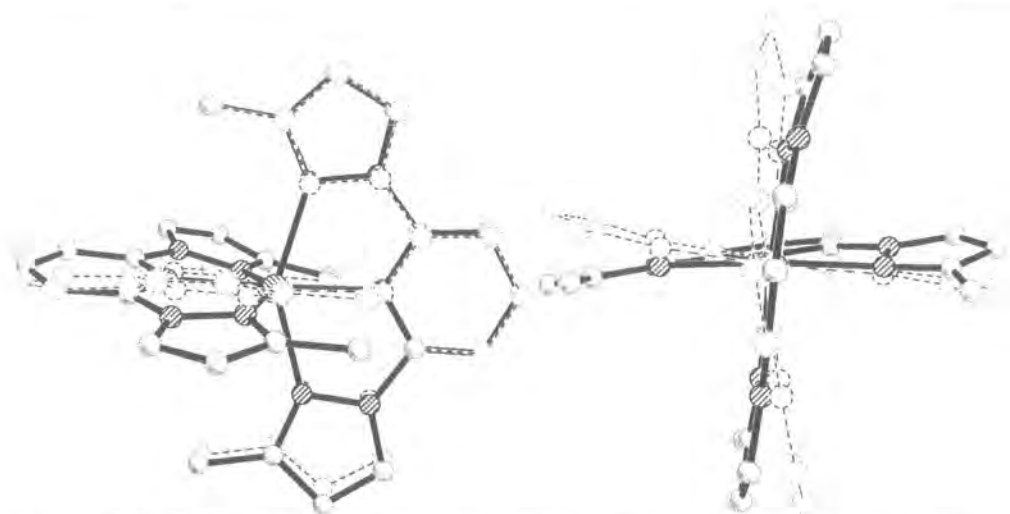


Figure 6.14: Overlay of the high spin cation at 200 K (solid line) and the high spin cation, Fe2, at 130 K (dashed line). Hydrogen atoms have been omitted for clarity.

In order to follow the evolution of the unit cell parameters with temperature the sample was cooled at a rate of 3 K/hr between 300 K and 90 K. Short data collections were made during the cooling. The duration of each data collection was three hours, the unit cells obtained in this fashion being, therefore averaged over 9 K. Figure 6.15 shows a plot of the unit cell volume with temperature. $[FeL_4](BF_4)_2$ has a unit cell volume of, in the region of, 6000 \AA^3 between 300 K and 160 K at this latter temperature it then undergoes a transition to give a unit cell of three times the volume. The mixed spin state is stable between 150 K and 120 K when the smaller unit cell is again reformed and $[FeL_4](BF_4)_2$ remains in this state until 90 K. A full structural analysis of X-ray diffraction data collected at 90 K showed that the compound was completely low spin at this temperature. The rate of temperature change during this experiment was sufficiently slow to allow the compound to relax to the low spin state, which is the same behaviour observed on flash freezing to 100 K in the SQUID diffractometer.

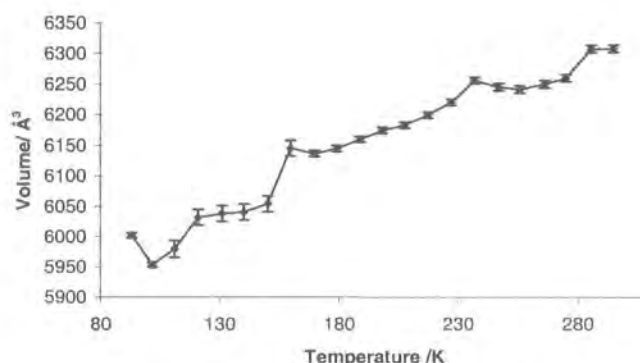


Figure 6.15: Evolution of unit cell volume with temperature during a continuous ramping (3 K/hr) experiment for $[FeL_4](BF_4)_2$. Values between 150 K and 120 K have been divided by three to allow for ease of comparison

[FeL₄](BF₄)₂ is still in the monoclinic space group C2/c in the low spin state and the asymmetric unit consists of one cation and two counter anions. The symmetry parameters reported in Table 6.4 show that, as expected, the low spin state is closer to ideal octahedral geometry than the high spin state. Figure 6.16 shows a comparison of the cation at 130 K containing the low spin iron Fe1 and the only independent low spin cation at 90 K. It can be seen that although the bond lengths and angles of the two ligands are similar there is a much greater degree of twist away from planarity in the cation at 130 K. This is the same result seen when comparing the high spin cation in the mixed spin state with that seen at 200 K. It appears that this high degree of ligand twist is a feature of the mixed spin state.

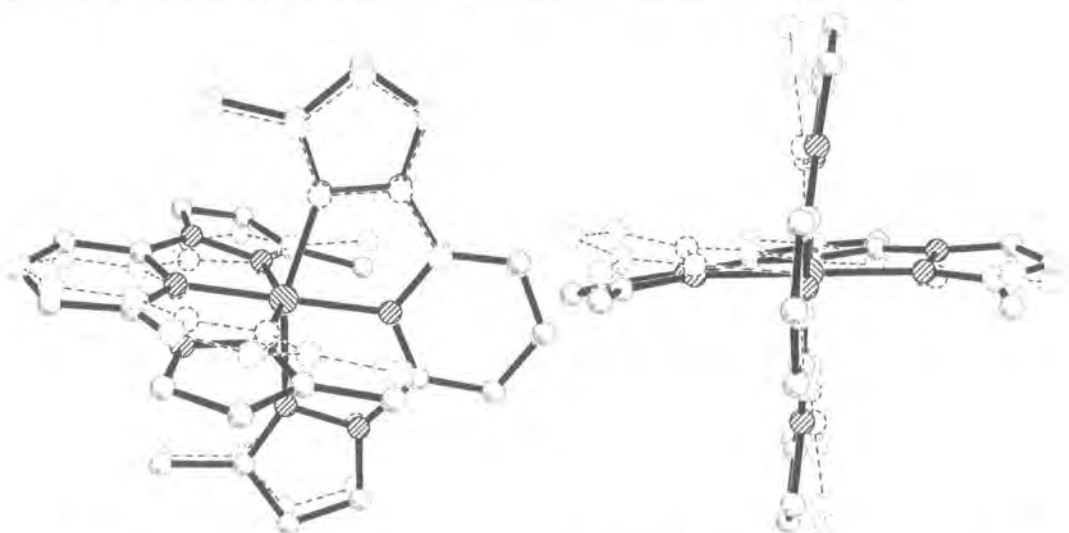


Figure 6.16: Overlay of the low spin state at 90 K (solid line) with the low spin cation at 130 K, Fe1 (dashed line). Hydrogen atoms have been omitted for clarity.

Unfortunately on cooling to 30 K the crystal used for all the above work collapsed and so examination of the excited state behaviour on irradiation or quenching was not possible.

6.3.4 Variable temperature and excited state crystallographic study of [FeL₄](BF₄)₂· $\frac{1}{3}$ H₂O

The thermal spin transition

Given that preliminary studies had shown that this compound was hydrated, it was decided to obtain new crystals and to re-examine their structure to determine if the water content had any role to play in the spin transition. This was deemed to be of particular interest as it appeared to be possible for the water to migrate out of the crystal with only minor loss of crystal quality and there were some discrepancies in the behaviour of the water containing crystals compared with their behaviour after dehydration: predominately the fact that it had been possible to

determine the structure of the mixed spin state at 100 K. This is unusual when it is considered that the dehydrated crystal was in the low spin state at this temperature and that the time taken for the crystallographic data collection was much longer than that required in the SQUID cavity for full relaxation to the low spin state.

Empirical formula	C ₂₆ H ₂₆ B ₂ F ₈ FeN ₁₀ O _{0.33}	C ₂₆ H ₂₆ B ₂ F ₈ FeN ₁₀ O _{0.33}	C ₂₆ H ₂₆ B ₂ F ₈ FeN ₁₀ O _{0.33}
Formula weight	713.38	713.38	713.38
Spin state	HS-1	HS-1	Mixed spin
Temperature/K	200	130	90
Shape	Prism	Prism	Prism
Colour	Yellow	Yellow	Brown
Crystal system	Monoclinic	Monoclinic	Monoclinic
Space group	C2/c	C2/c	C2/c
a/ Å	23.425(5)	23.285(5)	55.28(1)
b/ Å	11.000(2)	10.965(2)	10.957(2)
c/ Å	24.017(5)	23.914(5)	31.973(6)
β /deg	95.56(3)	95.63(3)	108.88(3)
Volume/ Å³	6159(2)	6076(2)	18325(6)
Z	8	8	24
D_c/ Mg/m³	1.540	1.560	1.551
μ/ mm⁻¹	0.577	0.584	0.581
Crystal size / mm	0.16 x 0.13 x 0.11	0.16 x 0.13 x 0.11	0.16 x 0.13 x 0.11
Theta range / deg	1.70 to 26.33	1.71 to 26.05	0.78 to 26.06
Reflections collected	16308	15666	41067
Independent reflections	5371	5220	15090
R_(int)	0.0219	0.0230	0.1135
wR(F²)(all data)	0.1462	0.1537	0.4464
R(F)(all data)	0.0606	0.0630	0.2352
Refined parameters	432	432	585
GOF	1.120	1.139	1.285
Δρ_{min,max} / e.Å⁻³	0.87 and -0.38	1.02 and -0.45	3.86 and -1.46

Table 6.5: Selected crystallographic parameters for [FeL₂](BF₄)₂· $\frac{1}{3}$ H₂O at 200 K, 130 K and 90 K. Where HS-1 is the high spin ground state.

Analysis of X-ray diffraction data collected on this new sample at 200 K shows it to be isostructural with the dehydrated compound crystallising in the monoclinic space group C2/c with unit cell parameters of $a = 23.425(5)$ Å, $b = 11.000(2)$ Å, $c = 24.017(5)$ Å, $\beta = 95.56(3)^\circ$ and $V = 6159(2)$ Å³ but to contain a disordered water molecule with an occupancy of a third. The iron atom has a distorted octahedral geometry, bound equatorially to two ligands through three of their five nitrogen atoms, Figure 6.17. The iron – nitrogen bond distances indicate that the compound is in the high spin state at 200 K, as does the symmetry parameter, Σ , Table 6.6. These parameters are the same within error to those observed for the dehydrated compound at 200 K. The disordered water molecule is sited in a cavity of 30 Å³ and the water oxygen atom forms a hydrogen bond with the methyl group of one of the ligands. The other intermolecular bonds formed by [FeL₂](BF₄)₂· $\frac{1}{3}$ H₂O are the same as those formed by the dehydrated compound: weak hydrogen bonding between the anions and the methyl groups

of the ligands. Again the methyl groups in the 3 position of the ligand pyrazole rings disrupt the packing such that it is not possible for the cations to form the π interactions so common in this family of spin transition compounds, Figure 6.18.

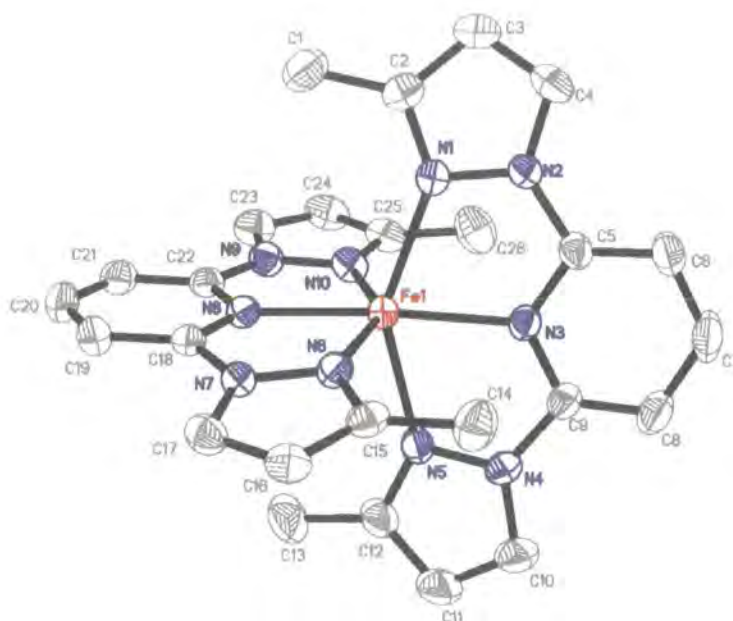


Figure 6.17: Structure of the cation of $[FeL_4_2](BF_4)_2 \cdot \frac{1}{2}H_2O$ at 200 K in the high spin state. Hydrogen atoms have been omitted for clarity and thermal ellipsoids are at 50% probability.

	T/ K	Fe	Spin state	Mean Fe-N/ Å	Bite angle/ $^\circ$	Σ / $^\circ$
$[FeL_4_2](BF_4)_2 \cdot \frac{1}{2}H_2O$	200	1	HS	2.165(2)	73.68(9)	155.9
	130	1	HS	2.159(3)	73.8(1)	154.8
	90	1	LS	1.985(9)	79.9(4)	95.8
		2	HS	2.168(9)	73.7(3)	156.0
		3	HS	2.15(1)	73.7(4)	158.2

Table 6.6: Selected parameters for $[FeL_4_2](BF_4)_2 \cdot \frac{1}{2}H_2O$. The Σ parameter was defined in Section 3.3.1

Comparison of the high spin cation from the hydrated compound with that from the dehydrated compound shows that there are no significant differences in the structures of the two cations, Figure 6.19. The loss of the water molecule from the crystal does not appear to affect the packing of the compound, the geometry of the cations or the intermolecular bonding of the high spin state.

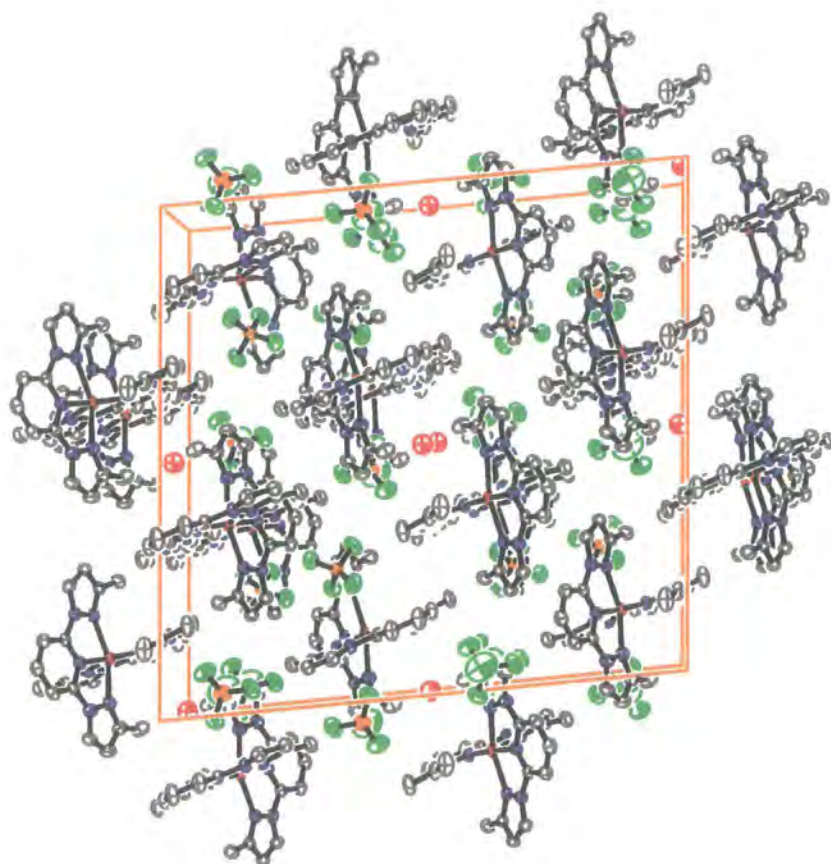


Figure 6.18: Packing diagram of [FeL₄](BF₄)₂· $\frac{1}{3}$ H₂O at 200 K, view normal to 010. Hydrogen atoms have been omitted for clarity.

Cooling [FeL₄](BF₄)₂· $\frac{1}{3}$ H₂O at 120 K/hr to 130 K yields the fully high spin state. The iron – nitrogen bond lengths and symmetry parameters are the same within error to those observed at 200 K. This is in contrast to the behaviour of the dehydrated compound, which is found to be in the mixed spin state at 130 K.

At 90 K [FeL₄](BF₄)₂· $\frac{1}{3}$ H₂O is found to be in the mixed spin state with unit cell parameters of $a = 55.28(1)$ Å, $b = 10.957(2)$ Å, $c = 31.973(6)$ Å, $\beta = 108.88(3)^\circ$ and $V = 18325(6)$ Å³ and to be in the monoclinic space group C2/c. As seen in the mixed spin state observed at 130 K for the hydrated compound the asymmetric unit consists of one low spin iron atom, Fe1, and two high spin iron centres, Fe2 and Fe3, as indicated by the metal – ligand bond lengths, Table 6.6. Examination of the Σ parameters shows that both Fe2 and Fe3 are fully high spin. This behaviour is different to that observed for the dehydrated compound which is fully low spin at this temperature, it is also the case that in the mixed spin state of the dehydrated compound the iron atom Fe3 exists 20% in the low spin state. However comparison of the cations for the dehydrated and hydrated compounds in this mixed spin state reveals that there

are no significant differences between the structures of the cations. $[\text{FeL}_4]_2(\text{BF}_4)_2 \cdot \frac{1}{3}\text{H}_2\text{O}$ at this temperature also shows different behaviour to that seen during the SQUID experiments in which relaxation from the mixed spin state occurs within a few hours under these conditions. This implies that the polycrystalline sample used for the magnetic measurements has a different composition to the single crystals used for the X-ray diffraction experiments. If this were the case it might explain the fact that the mixed spin state observed in the SQUID experiments seems to be between half and a third high spin rather than the two thirds high spin observed crystallographically.

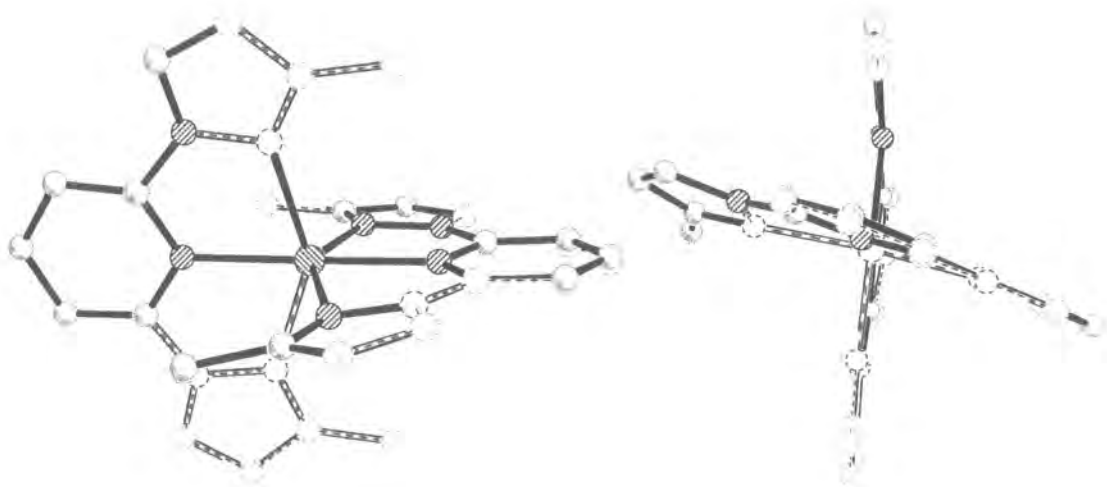


Figure 6.19: Overlay of the cation from the hydrated compound at 200 K in the high spin state (solid line) with the cation from the dehydrated compound at the same temperature (dashed line)

It is extremely interesting to observe that not only do the spin states become ordered in this mixed spin state but so do the water molecules. At this temperature the asymmetric unit contains only two independent water sites each with an occupancy of 50%. This is a very interesting feature of the spin crossover behaviour of $[\text{FeL}_4]_2(\text{BF}_4)_2 \cdot \frac{1}{3}\text{H}_2\text{O}$ but it is unlikely to be the reason why only two thirds of the molecules undergo a complete thermal spin transition as this partial transition is also observed in the dehydrated compound. It is perhaps self evident that the water cannot be closely involved in the process as it is possible for a single crystal to dehydrate and still retain its crystallinity. To support this proposal, the cations each form one close intermolecular contact with a water molecule and the bulk packing and intermolecular interactions remain the same as those observed at 200 K.

A number of attempts were made to determine the structure of the low spin state of $[\text{FeL}_4]_2(\text{BF}_4)_2 \cdot \frac{1}{3}\text{H}_2\text{O}$ at 90 K by both cooling very slowly, the way that this state was reached

for the hydrated compound, and by leaving the crystal at 90 K and 100 K for extended periods of time to allow relaxation. In all cases the result was that the crystal was found to be in the mixed spin state. Comparison of the thermal spin transition behaviour of the hydrated and dehydrated compounds shows that the high spin state of the hydrated compound is more stable, this is demonstrated by the difficulty found in obtaining a fully low spin structure of the compound under conditions in which the dehydrated compound was found to exist as completely low spin. The presence of water within the crystal lattice of [FeL₄]₂(BF₄)₂·xH₂O stabilises the high spin state.

The LIESST effect and thermal trapping

	Flash freezing	Cool at 120 K/hr
Empirical formula	C ₂₆ H ₂₆ B ₂ F ₈ FeN ₁₀ O _{0.33}	C ₂₆ H ₂₆ B ₂ F ₈ FeN ₁₀ O _{0.33}
Formula weight	713.38	713.38
Spin state	HS-2	Mixed spin
Temperature/K	30	30
Shape	Irregular	Irregular
Colour	Yellow	Brown
Crystal system	Monoclinic	Monoclinic
Space group	C2/c	C2/c
a/ Å	23.229(5)	54.91(1)
b/ Å	10.935(2)	10.872(2)
c/ Å	23.801(5)	31.710(6)
β /deg	96.02(3)	108.94(3)
Volume/ Å³	6012(2)	17905(6)
Z	8	24
D_c/ Mg/m³	1.576	1.588
μ/ mm⁻¹	0.590	0.595
Crystal size / mm	0.25 x 0.24 x 0.12	0.25 x 0.24 x 0.12
Theta range / deg	1.76 to 28.31	0.78 to 28.30
Reflections collected	22123	42076
Independent reflections	6696	18466
R_(int)	0.0372	0.0790
wR(F²)(all data)	0.1486	0.3255
R(F)(all data)	0.0742	0.1802
Refined parameters	432	585
GOF	1.041	1.039
Δρ_{min,max} / e.Å⁻³	1.62 and -0.57	3.56 and -1.38

Table 6.7a: Selected crystallographic parameters for [FeL₄]₂(BF₄)₂·½H₂O after flash freezing to 30 K and after cooling from 300 K at 120 K/hr. Where HS-2 is the metastable high spin state resulting from flash freezing to 30 K.

On cooling from 300 K to 30 K at a rate of 120 K/hr the mixed spin state is obtained, as seen during the SQUID experiment. Under these conditions [FeL₄]₂(BF₄)₂·½H₂O has unit cell parameters of $a = 54.91(1)$ Å, $b = 10.872(2)$ Å, $c = 31.710(6)$ Å, $\beta = 108.94(3)^\circ$ and $V = 17905(6)$ Å³. Once again examination of the iron – nitrogen bond lengths indicates that of the

	After irradiation	Cooling from 100 K
Empirical formula	C ₂₆ H ₂₆ B ₂ F ₈ FeN ₁₀ O _{0.33}	C ₂₆ H ₂₆ B ₂ F ₈ FeN ₁₀ O _{0.33}
Formula weight	713.38	713.38
Spin state	HS-2	LS
Temperature/K	30	30
Shape	Irregular	Prism
Colour	Yellow	Brown
Crystal system	Monoclinic	Monoclinic
Space group	C2/c	C2/c
a/ Å	23.078(5)	22.789(5)
b/ Å	10.948(2)	10.836(2)
c/ Å	23.797(5)	24.023(5)
β /deg	95.66(3)	93.86(3)
Volume/ Å³	5983(2)	5919(2)
Z	8	8
D_c/ Mg/m³	1.584	1.601
μ/ mm⁻¹	0.593	0.600
Crystal size / mm	0.25 x 0.24 x 0.12	0.25 x 0.20 x 0.15
Theta range / deg	2.63 to 28.02	0.170 to 28.40
Reflections collected	16766	15639
Independent reflections	5856	6466
R_(int)	0.0190	0.0311
wR(F²)(all data)	0.0965	0.4885
R(F)(all data)	0.0433	0.2035
Refined parameters	432	197
GOF	1.072	2.060
Δρ_{min,max} / e.Å⁻³	0.59 and -0.33	4.98 and -1.86

Table 6.7b: Selected crystallographic parameters for [FeL₄](BF₄)₂·½H₂O after irradiation of the slow cooled crystal and after cooling from 100 K to 30 K. Where LS is the low spin state and HS-2 is the metastable high spin state resulting from the LIESST effect.

three independent cations one iron centre is in the low spin state, Fe1, and two are in the high spin state, Fe2 and Fe3. There are very small differences in the metal to ligand bond distances, bite angle and Σ parameter between those for Fe2 and Fe3 which suggest that the iron atom at site 3 may have a very small amount of low spin character; however this would only be a very small percentage. Comparison of the structure of the independent cations in the mixed spin state at 30 K and at 90 K shows that there are no significant differences between the structures at the two temperatures.

Irradiation of this mixed spin state at 30 K with red laser light (λ = 632.8 nm, 25 mW) for ten minutes results in promotion of the crystal to the metastable high spin state, HS-2. The unit cell parameters after irradiation are *a* = 23.078(5) Å, *b* = 10.948(2) Å, *c* = 23.797(5) Å, β = 95.66(3)° and *V* = 5983(2) Å³. The symmetry parameters and iron – nitrogen bond lengths show that the compound is in the high spin state, Table 6.8. The asymmetric unit now consists of just one formula unit and the compound is in the space group C2/c. There are no significant differences, aside from those which can be associated with a decrease in

temperature of 270 K, between the structure of the high spin cation at 200 K and the one generated as a result of the LIESST effect at 30 K, Figure 6.20.

On warming from 30 K after irradiation, the crystal remains in the metastable high spin state until 90 K when it relaxes back into the mixed spin state. This is in contrast to the SQUID experiment in which the low spin state was reached between 90 K and 100 K on warming from 10 K. The crystal was cycled several times through this process in an attempt to obtain the low spin state that occurred during the SQUID experiment, however all of these attempts proved unsuccessful.

[FeL ₄](BF ₄) ₂ · $\frac{1}{3}$ H ₂ O	T/ K	Fe	Spin state	Mean Fe-N/ Å	Bite angle/°	Σ /°
Flash frozen	30	1	HS	2.162(3)	73.8(1)	149.0
Cool at 120 K/hr	30	1	LS	1.983(6)	79.6(3)	98.0
		2	HS	2.163(6)	73.5(2)	157.9
		3	HS	2.142(7)	74.3(3)	151.8
After irradiation	30	1	HS	2.165(1)	73.81(7)	154.0
Cool from 90 K	30	1	LS	2.001(7)	79.0(3)	104.7

Table 6.8: Selected parameters for [FeL₄](BF₄)₂· $\frac{1}{3}$ H₂O. The Σ parameter was defined in Section 3.3.1

A second method of obtaining the metastable high spin state at low temperature is by trapping the high spin state by very rapid cooling. This was achieved by flash freezing the crystal in a flow of chilled helium to 30 K. After flash freezing in this manner [FeL₄](BF₄)₂· $\frac{1}{3}$ H₂O was found to be in the high spin state with unit cell parameters of $a = 23.229(5)$ Å, $b = 10.935(2)$ Å, $c = 23.801(5)$ Å, $\beta = 96.02(3)^\circ$ and $V = 6012(2)$ Å³. Comparison of the structure of the flash frozen crystal with that of the metastable high spin state resulting from irradiation at 30 K reveals that there are no significant differences between the two metastable states, Figure 6.21.

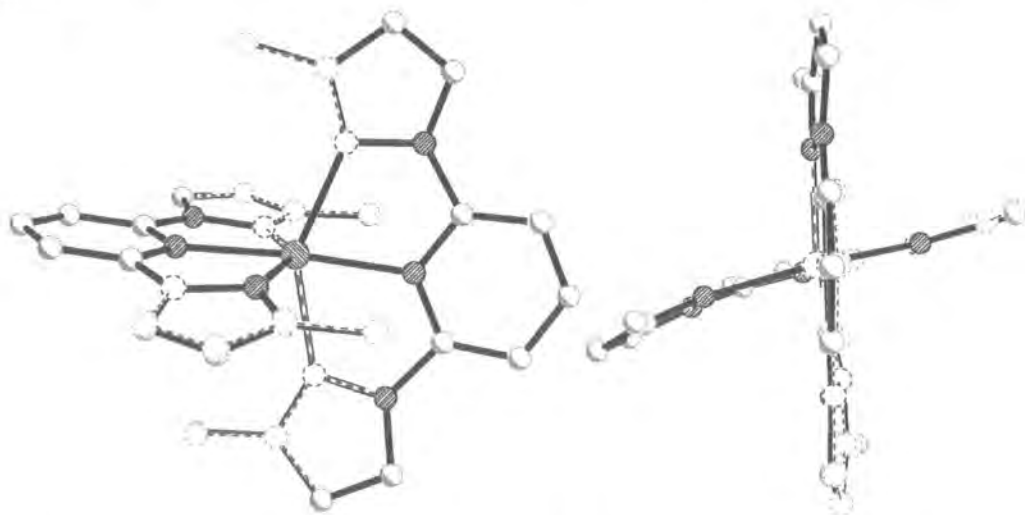


Figure 6.20: Overlay of the high spin state of [FeL₄](BF₄)₂· $\frac{1}{3}$ H₂O at 30 K after irradiation (solid line) with that at 200 K (dashed line)

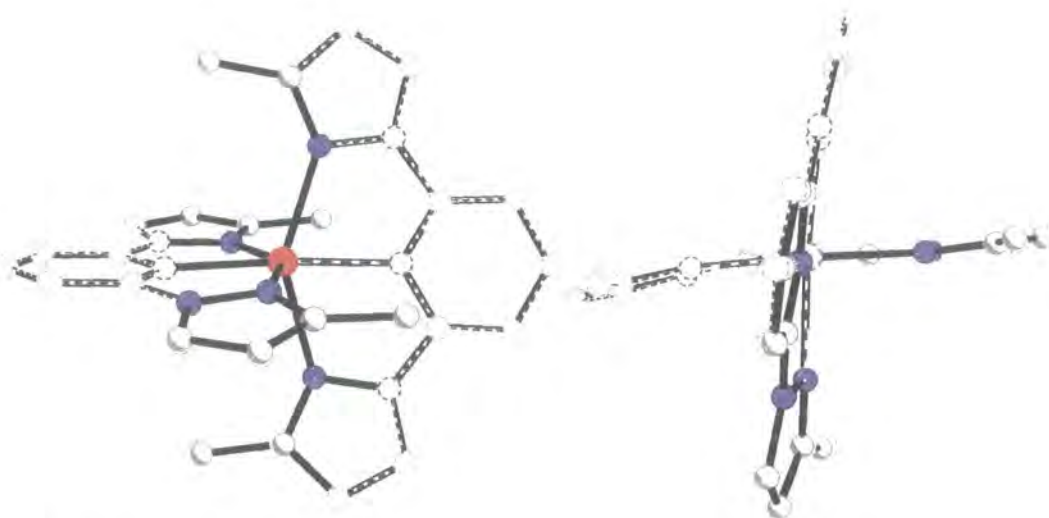


Figure 6.21: Overlay of the high spin structure of $[FeL_4_2](BF_4)_2 \cdot \frac{1}{2}H_2O$ resulting from flash freezing to 30 K (dashed line) with that reached by irradiation of the crystal at 30 K (solid line)

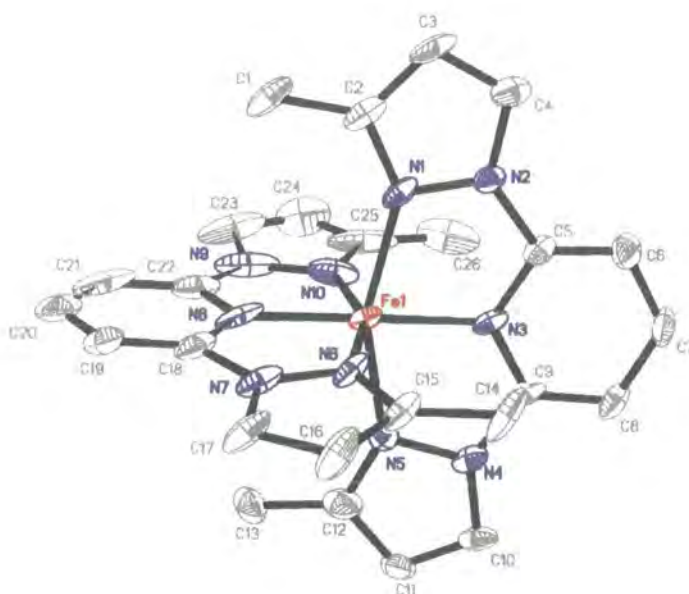


Figure 6.22: Structure of the cation of $[FeL_4_2](BF_4)_2 \cdot \frac{1}{2}H_2O$ in the low spin state at 30 K showing the distortion of the thermal parameters

The low spin state of $[FeL_4_2](BF_4)_2 \cdot \frac{1}{2}H_2O$ was finally obtained by warming a crystal flash frozen to 30 K, at a rate of 120 K/hr to 90 K and then allowing it to relax for one hour. If the temperature is allowed to rise above this, the compound makes a transition to the mixed spin state. Once the low spin state had been obtained, as determined by examination of the unit

cell parameters, the crystal was cooled to 30 K and X-ray diffraction data were collected. Visual examination of the data shows that there is some evidence of diffracted X-ray intensity between the sharp diffraction peaks, suggesting that under these conditions some of the crystal is still in the mixed spin state. Further evidence for this is provided by the refinement of the structural model. If the anisotropic temperature factors are refined a pronounced degree of distortion is observable both along the metal ligand bonds and, for the pyrazole nitrogen atoms in particular, in the direction of the ligand bite angle, Figure 6.22. Refinement of only the isotropic temperature factors shows that there is some high spin component present, with residual electron density clearly visible at positions indicative of a high spin state, Figure 6.23. This residual high spin component is most probably responsible for the slightly longer iron – nitrogen bond lengths and higher Σ parameter observed for this low spin state compared with the cation containing FeI of the mixed spin state at 30 K. This residual high spin fraction means that it is better to draw comparisons between the low spin cation of the mixed spin state and the high spin states when examining the effect of the spin transition, than to use this low spin state. Comparison of the low spin state cation at 30 K with that of the cation containing FeI (low spin) of the mixed spin state at 30 K clearly shows the differences between the two states, Figure 6.24. There is a more pronounced twist of the ligands away from planarity which is associated with the high spin state. In the absence of a fully low spin structure of the hydrated compound it is not possible to determine the change in unit cell volume due to the spin transition alone.

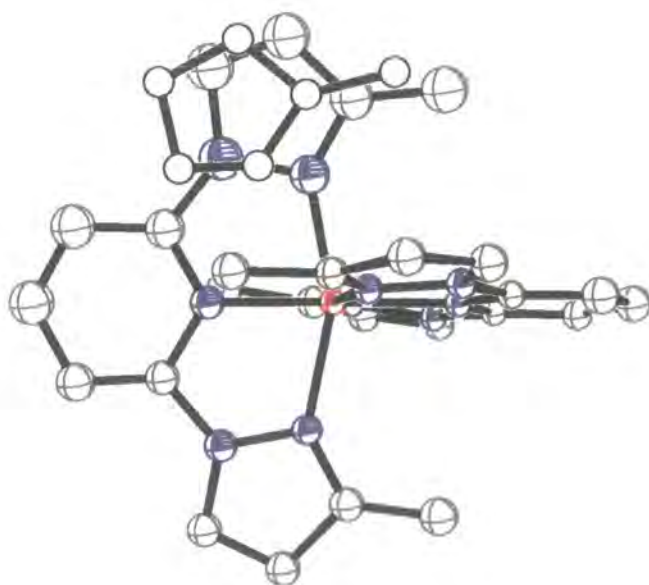


Figure 6.23: Structure of the low spin cation of $[FeL4_2](BF_4)_2 \cdot \frac{1}{2}H_2O$ in the low spin state at 30 K showing the residual electron density indicative of a high spin component

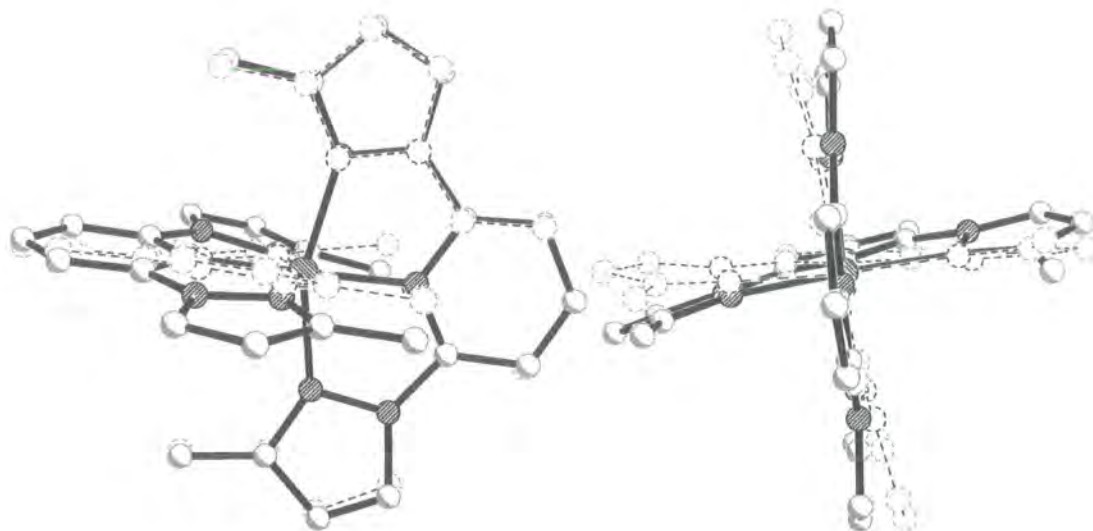


Figure 6.24: Overlay of the structure of the low spin cation from the mixed spin state of [FeL₄](BF₄)₂·½H₂O at 30 K (dashed line) with that of the primarily low spin state at 30 K (solid line)

6.3.5 [FeL₅](ClO₄)₂

Variable temperature crystallography

Empirical formula	C ₂₆ H ₂₆ Cl ₂ FeN ₁₀ O ₈	C ₂₆ H ₂₆ Cl ₂ FeN ₁₀ O ₈
Formula weight	733.32	733.32
Temperature/K	250	30
Spin state	HS-1	LS
Shape	Irregular	Irregular
Colour	Yellow	Brown
Crystal system	Tetragonal	Orthorhombic
Space group	P $\bar{4}$ 2 ₁ c	P2 ₁ 2 ₁ 2 ₁
a/ Å	9.587(1)	9.600(2)
b/ Å		9.625(2)
c/ Å	17.933(4)	33.470(7)
Volume/ Å³	1648.1(5)	3092(1)
Z	2	4
D_r/ Mg/m³	1.478	1.575
μ/ mm⁻¹	0.682	0.727
Crystal size / mm	0.18 x 0.12 x 0.08	0.18 x 0.12 x 0.08
Theta range / deg	2.27 to 27.42	2.20 to 27.48
Reflections collected	11139	16491
Independent reflections	1893	6915
R_(int)	0.0756	0.0998
wR(F²)(all data)	0.2192	0.3182
R(F)(all data)	0.1149	0.1440
refined parameters	115	194
GOF	1.041	1.125
Δρ_{min,max} / e.Å⁻³	1.00 and -0.38	3.47 and -1.59

Table 6.9: Selected crystallographic parameters for [FeL₅](ClO₄)₂. Where HS-1 is the high spin ground state and LS is the low spin state

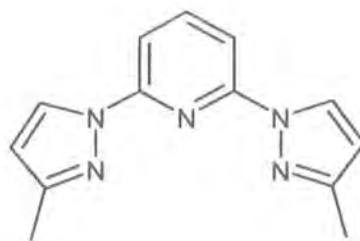


Figure 6.25: L5 = 2,6-di(4-methylpyrazol-1-yl)pyridine

[FeL₅](ClO₄)₂ crystallises in the tetragonal space group $P\bar{4}2_1c$ with unit cell parameters of $a = 9.587(1) \text{ \AA}$, $c = 17.933(4) \text{ \AA}$ and $V = 1648.1(5) \text{ \AA}^3$ at 250 K. The asymmetric unit consists of quarter of the cation and half of one anion, although at this temperature the anion is found to be disordered over the two fold axis. The iron atom is situated on a four fold improper axis and, like all the compounds in this series, has a distorted octahedral geometry; bound equatorially to two ligands through three of their five nitrogen atoms. Figure 6.26 shows the structure of the cation at this temperature. The mean iron – nitrogen distance at this temperature is consistent with the compound being in the high spin state, Table 6.10.

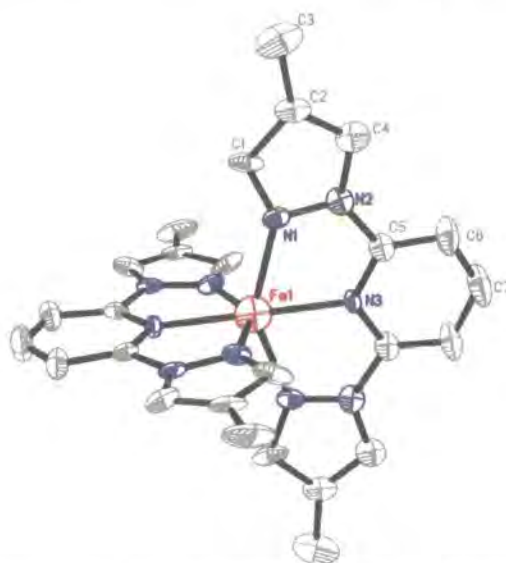


Figure 6.26: The structure of the cation of [FeL₅](ClO₄)₂ in the high spin state at 250 K. Hydrogen atoms have been omitted for clarity and the thermal ellipsoids are at 50 % probability.

Intermolecular bonding in this member of the series of complexes based on the 2,6-dipyrazol-1-yl pyridine ligand, differs from that of the majority of examples in that there are no π interactions between the rings of neighbouring ligands. The presence of the methyl groups at

the 4 position of the pyrazole rings forces the cations sufficiently far apart that they no longer overlap. However, there are interactions between the methyl groups and the pyrazole rings and these link the cations into a tilted chain along the crystallographic *a* axis. Weak hydrogen bonds link the cations along the crystallographic *c* axis.

	T/K	Space Group	Spin State	Mean Fe-N/ Å	Bite angle/ ^o	Σ/ ^o	v/%
[FeL5 ₂](ClO ₄) ₂	250	P $\bar{4}$ 2 ₁ c	HS	2.149(8)	72.7(2)	158.8	8.90
	30	P2 ₁ 2 ₁ 2 ₁	LS	1.947(9)	79.8(4)	96.3	3.44

Table 6.10: Selected parameters for [FeL5₂](ClO₄)₂

The iron atom lies on the origin with the iron - pyridine nitrogen (N3) bonds along the crystallographic *c* axis. Neighbouring iron atoms, therefore, are separated by a distance equal to the length of the *c* axis and are sited on a straight line through the unit cell. This is similar to the packing observed in [FeL2₂](BF₄)₂ and [FeL2₂](ClO₄)₂, and discussed in Chapter 4. In the case of [FeL5₂](ClO₄)₂ the unit cell is not body centred as the central cation is rotated by forty-five degrees relative to those at the corners, this is a result of the bulky methyl groups at the four position, Figure 6.27.

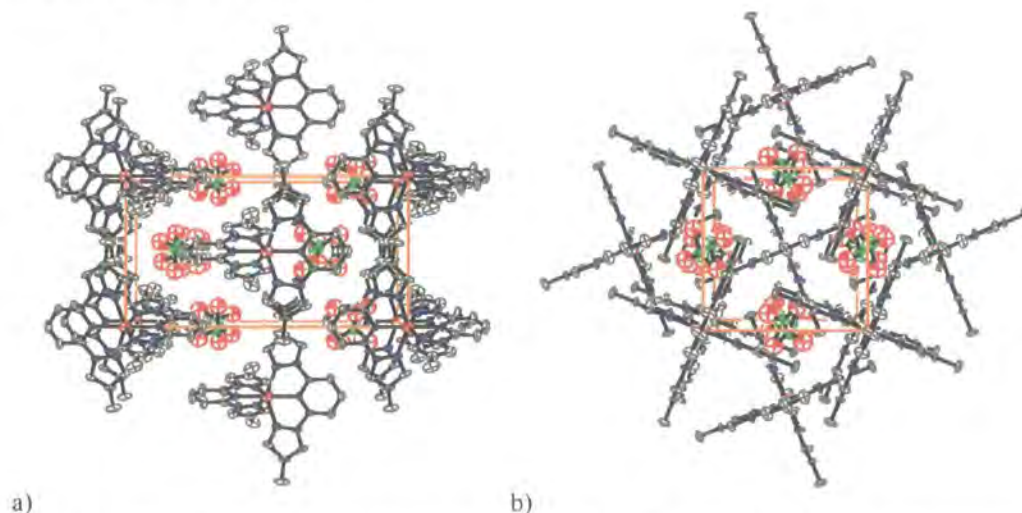


Figure 6.27: Diagram of the packing of [FeL5₂](ClO₄)₂ at 250 K in the high spin state. a) view along *a*, b) view along *c*. Hydrogen atoms have been omitted for clarity

Cooling to 30 K results in a crystallographic phase transition from P $\bar{4}$ 2₁c to the orthorhombic space group P2₁2₁2₁ which involves a doubling of the crystallographic *c* axis. At 30 K the unit cell parameters are *a* = 9.600(2) Å, *b* = 9.625(2) Å, *c* = 33.470(7) Å and *V* = 3092(1) Å³. The asymmetric unit is one cation and two anions and there are four formula units in the unit cell. The mean iron - nitrogen distance of 1.947(9) Å, and the symmetry parameters, indicate

that the iron (II) centre is in the low spin state, Table 6.10. Both anions are found to be ordered at this temperature.

The loss of symmetry is caused by displacement of the cations, which in the high spin state are arranged such that the iron atoms are situated on a straight line along the c axis. On going through the spin transition and symmetry change from the tetragonal space group $P\bar{4}2_1c$ to the orthorhombic $P2_12_12_1$ the cations are displaced such that the iron atoms are no longer aligned parallel to c , Figure 6.28. Rather than forming a straight line, the iron atoms now form a zigzag parallel to the c direction being displaced from each other in both the a and b directions and no longer being situated at the origin of the unit cell. This distortion of the packing prevents clashing of the methyl groups on contraction of the unit cell due to the spin transition. The interactions between the methyl groups and the pyrazole rings link the cations into a tilted chain along the b direction and once more weak hydrogen bonds formed with the anions link the cations in the other cell directions. Close comparison of the structures of the cations in the high and low spin states shows that there are very few differences other than those expected as being due to the change in spin state and these are tabulated in Table 6.10.

Monitoring the unit cell parameters with temperature demonstrates that the spin transition takes place abruptly between 240 K and 230 K. This is in good agreement with the results of magnetic experiments performed in Bordeaux which estimate $T_{1/2}$ as being 232 K.

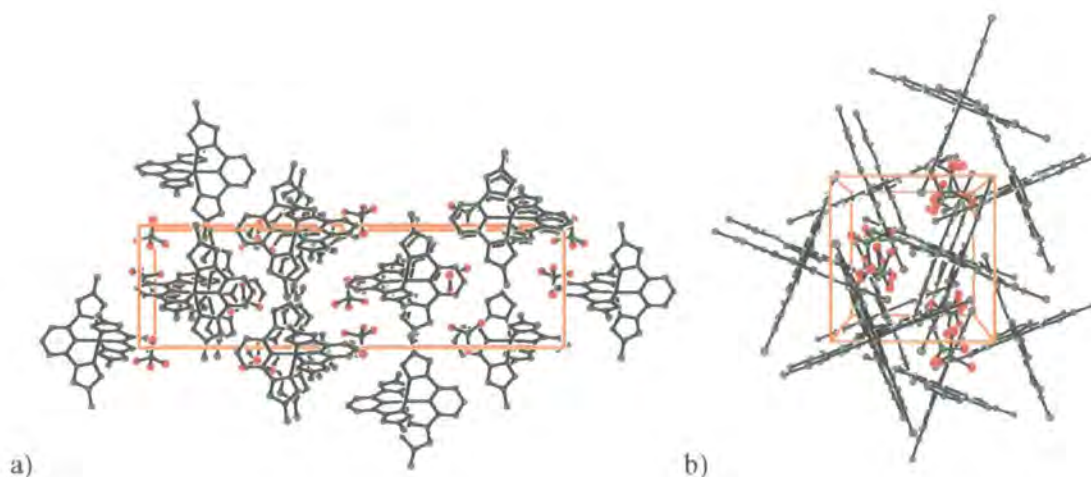


Figure 6.28: Diagram showing the packing in $[FeL5_2](ClO_4)_2$ at 30 K in the low spin state; a) view along a , b) view along c . Hydrogen atoms have been omitted for clarity.

Excited state crystallography

Irradiation of the crystal on the diffractometer at 30 K with red laser light ($\lambda = 632.8$ nm, 25 mW) results in a change in colour of the crystal from the dark yellow - brown associated with the low spin state to the yellow of the high spin state. However, on attempting to determine the unit cell parameters of the compound after irradiation, it was found that the crystal had been irreversibly damaged and the diffraction peaks had become very broad and diffuse. Thus, this material does undergo LIESST on irradiation, in common with other members of this series, but it is likely that it also undergoes a crystallographic phase transition which destroys the crystallinity.

SQUID magnetometry

A preliminary examination of the magnetic curve determined using SQUID magnetometry with the purpose of determining the effect of irradiation on the spin state of this material reveals the existence of a small hysteresis loop < 2 K and an abrupt transition, as expected for a compound with a crystallographic phase transition coincident with the spin transition. Irradiation with red laser light ($\lambda = 532$ nm) results in promotion of the compound to the metastable high spin state. Figure 6.29 shows the SQUID curve obtained by both varying the temperature and on irradiation. On warming in the dark from 10 K after irradiation approximately 10% of the compound is found to undergo relaxation at 50 K whereas the rest of the compound remains in the metastable high spin state up to 84 K. This is evidence of the existence of a second polymorph in the polycrystalline sample used for this experiment. The far lower relaxation temperature from the metastable high spin state suggests that, according to the inverse law relationship, it should have a higher thermal spin transition temperature than the majority polymorph, the SQUID curve of which is in good agreement with the single crystal X-ray diffraction data. The thermal spin transition temperature of the minor polymorph is almost certainly above the top temperature obtainable by this SQUID set up and so cannot be observed in the thermal spin transition curve.

In order to confirm the presence of a second polymorph in the bulk sample, a room temperature powder diffraction pattern was collected. Comparison of this pattern with that simulated from the single crystal data showed that there was at least one other phase in the bulk powder sample. It can be clearly seen that there are extra peaks in the powder diffraction pattern which do not correspond to those seen in the ideal pattern generated from the single crystal data.

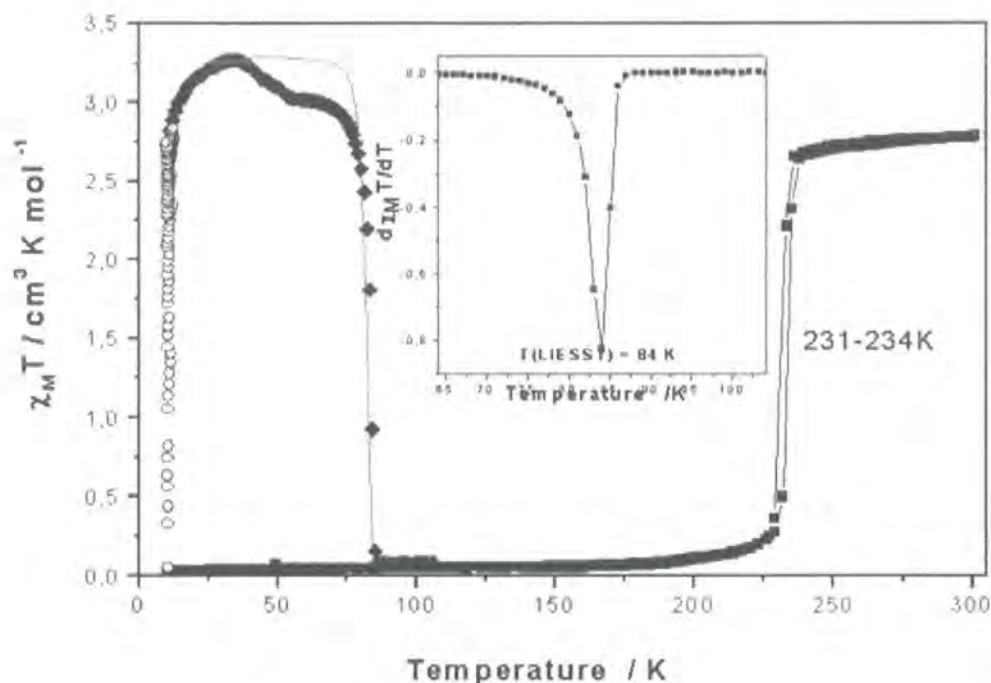


Figure 6.29: Temperature dependence of $\chi_M T$ for [FeL₅]₂(ClO₄)₂. ■ = data recorded in the cooling and warming mode without irradiation; ○ = data recorded with irradiation at 10 K; ♦ = T(LIESST) measurement, data recorded in the warming mode with the laser turned off after irradiation for one hour

6.4 Conclusions

[FeL₄]₂(ClO₄)₂ was found to undergo only a partial spin transition with a residual low spin component remaining at 290 K and a residual high spin component at 30 K. Attempts to promote the compound to the metastable high spin state by irradiation resulted in the destruction of the crystal.

Unlike its perchlorate analogue, [FeL₄]₂(BF₄)₂·xH₂O shows a very rich array of spin crossover behaviour of a level unprecedented in the family of spin crossover compounds derived from the 2,6-di(pyrazol-1-yl)pyridine ligand. The ordering of the spin states to give a very stable mixed spin state, revealed by this thorough X-ray diffraction study, is highly unusual in spin crossover compounds. It is particularly unusual that the mixed spin state should be so stable in a compound in which there is no clear reason as to why two thirds of the cations should undergo the transition and the third not. In other reported examples of stable mixed spin states of this type there are either two independent iron centres over the

whole temperature range or a physical reason why it is not possible for all the iron centres to undergo a spin transition.

Examination of both a dehydrated and hydrated sample of $[FeL_2](BF_4)_2 \cdot xH_2O$ has revealed that the water does affect the course of the spin transition. The mixed spin state is more stable in the hydrated compound of which it has proved impossible to obtain a fully low spin state. This indicates that the water acts to stabilise the high spin state. It is possible that the contraction of the unit cell which takes place during the transition from the high to the low spin state is inhibited by the presence of water in the crystal lattice.

This extremely rich spin crossover behaviour emphasises once more, how finely balanced is the relationship between the high and low spin states.

$[FeL_5_2](ClO_4)_2$ exhibits a complete spin transition accompanied by a crystallographic phase transition which involves a loss of symmetry, going from tetragonal in the high spin state at 250 K to orthorhombic in the low spin state at 30 K. This loss of symmetry is a result of the contraction of the unit cell which leads to the cations having to be displaced from the crystallographic *c* axis to avoid clashing of the ligand methyl groups.

7 The thermal and light induced spin transitions in $[\text{FeL}_6_2](\text{BF}_4)_2$ and $[\text{FeL}_6_2](\text{ClO}_4)_2$ studied by powder X-ray diffraction and SQUID magnetometry

7.1 Introduction

The first part of this chapter concerns a variable temperature study of the spin crossover behaviour of $[\text{FeL}_6_2](\text{BF}_4)_2$ and $[\text{FeL}_6_2](\text{ClO}_4)_2$, where L6 = 2,6-dipyrazol-1-ylpyrazine, Figure 7.1. Attempts to obtain unsolvated, diffraction quality single crystals were unsuccessful and so variable temperature powder X-ray diffraction studies were performed. Magnetic studies of $[\text{FeL}_6_2](\text{BF}_4)_2$ and $[\text{FeL}_6_2](\text{ClO}_4)_2$ show that they undergo complete, abrupt spin transitions centred at 223 K, with a hysteresis width of 5K, and 208 K, with a hysteresis width of 3 K, respectively, Figure 7.8 [1]. It was hoped that the adaptation of the ligand to include a central pyrazine ring in place of the pyridine would aid the hydrogen bonding functionality, leading to more cooperativity between iron centres and a compound with a wide hysteresis loop. It can be seen from the results of the magnetic study that the spin transitions for these compounds are very similar to that seen for the parent complex, $[\text{FeL}_1_2](\text{BF}_4)_2$, discussed in Chapter 3, Figure 7.1.

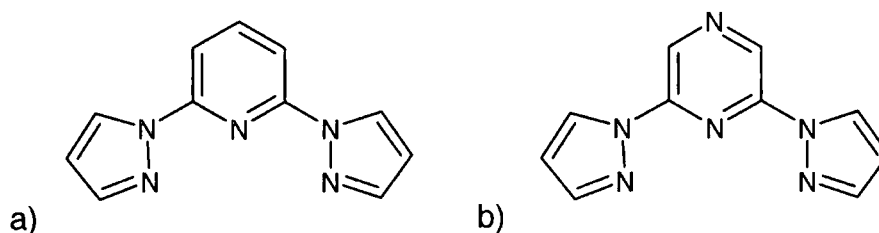


Figure 7.1: a) L1 = 2,6-dipyrazol-1-ylpyridine b) L6 = 2,6-dipyrazol-1-ylpyrazine

The second part of this chapter describes the results of a detailed photomagnetic study into the behaviour of these materials on irradiation. This study shows that both compounds undergo the LIESST effect; forming long lived excited states on irradiation at low temperature. Comparison of the excited state behaviour of $[\text{FeL}_6_2](\text{ClO}_4)_2$ and $[\text{FeL}_6_2](\text{BF}_4)_2$ with that of $[\text{FeL}_1_2](\text{BF}_4)_2$ shows that they obey the inverse law between $T_{1/2}$ and $T(\text{LIESST})$.

7.2 Experimental

7.2.1 Synthesis

$[\text{FeL6}_2](\text{BF}_4)_2$ and $[\text{FeL6}_2](\text{ClO}_4)_2$ were synthesised by Jerome Elhaïk, of the University of Leeds, according to literature methods [1].

7.2.2 Variable temperature X-ray powder diffraction

Laboratory data

Laboratory powder X-ray diffraction data were collected as described in Section 2.4. For the room temperature experiment, 9 powder patterns over the 2θ range 4° to 90° were collected for $[\text{FeL6}_2](\text{ClO}_4)_2$ and 8 between 4° and 90° for $[\text{FeL6}_2](\text{BF}_4)_2$ with a step size of 0.0144° and step time of 7 s. In addition, variable temperature data were collected for $[\text{FeL6}_2](\text{ClO}_4)_2$ in the temperature range 300 K to 130 K

Synchrotron data

As described in Chapter 2 variable temperature powder X-ray diffraction data were collected at station 2.3 of the Daresbury synchrotron. Data were collected with a wavelength of 1.3 \AA between 5° and 60° 2θ in all cases with a step size of 0.01° and a step time of 1 s. 6 scans were collected for $[\text{FeL6}_2](\text{ClO}_4)_2$ at room temperature and 4 scans at 120 K. 3 scans were recorded at room temperature for $[\text{FeL6}_2](\text{BF}_4)_2$. The data were summed and treated as described previously.

7.2.3 Photomagnetism

Photomagnetic data were collected using the method outlined in Chapter 2. The data show no evidence of the sample being heated by the laser, *i.e.* no sudden increase in magnetic signal on turning off the laser was observed.

7.3 Results and Discussion

7.3.1 The structure of [FeL6₂](ClO₄)₂ at room temperature in the high spin state

Indexing

The room temperature X-ray powder diffraction patterns were summed and then indexed, using 20 peaks between 5° and 50° 2 θ , with an in-house modification of the indexing programme of Visser [2]. This gave an orthorhombic unit cell with parameters of $a = 8.44$ Å, $b = 8.45$ Å and $c = 19.4$ Å. Comparison with the related compound [FeL1](BF₄)₂ indicated that this unit cell was probably monoclinic with a β angle close to 90°. From inspection of the systematic absences it was determined that the possible space groups were P2₁ and P2₁/m. Second harmonic generation measurements were performed by Dr. Marek Szablewski of the Department of Physics, University of Durham and the results of these measurements showed SHG activity for [FeL6₂](ClO₄)₂, confirming that the compound must be non-centrosymmetric and the space group was determined to be P2₁. The volume of this unit cell (1383 Å³) suggested that it contained two formula units, indicating that the asymmetric unit consisted of one cation and two anions.

Structure solution

Structure solution was performed using the DASH programme [3]. Three Z-matrices were used, one for the cation and one for each unique anion in the asymmetric unit. The Z-matrix, containing the structural model, for the [FeL6₂]²⁺ cation was based on the structure of [FeL1₂]²⁺ at 290 K in the high spin state as solved by single crystal X-ray diffraction and this was treated as a rigid body during the simulated annealing process. Fifty runs of ten million moves were performed with the lowest χ^2 being 40.88 after 8,305,500 moves. Visual inspection of the results confirmed that this best solution was also the one which made the most physical sense and so this was taken forward to refinement.

Refinement

It was necessary to introduce a set of restraints into the model to allow refinement to proceed. Searches for suitable fragments were made using the CSD (Cambridge Structural Database) [4].

It had been determined previously by magnetic measurements that [FeL₆](ClO₄)₂ is fully high spin at room temperature [1]. A search for iron (II) compounds bound to six nitrogen atoms reveals a histogram of bond lengths with two maxima; one centred at 1.95 Å and the other at 2.2 Å. The former group of iron – nitrogen bond distances is due to low spin iron centres and the latter to high spin. In order to determine the optimal distance for the metal to ligand bond restraints, a search was performed for high spin iron centres bound to six nitrogen donors and the mean value of these bonds determined. To ensure only high spin iron centres were considered, the search was restricted to bond lengths between 2.0 Å and 2.3 Å. This search found 121 fragments with a mean iron – nitrogen distance of 2.170 Å. Iron – nitrogen bond distances in the refinement of [FeL₆](ClO₄)₂ were, therefore, restrained to be 2.17(1) Å.

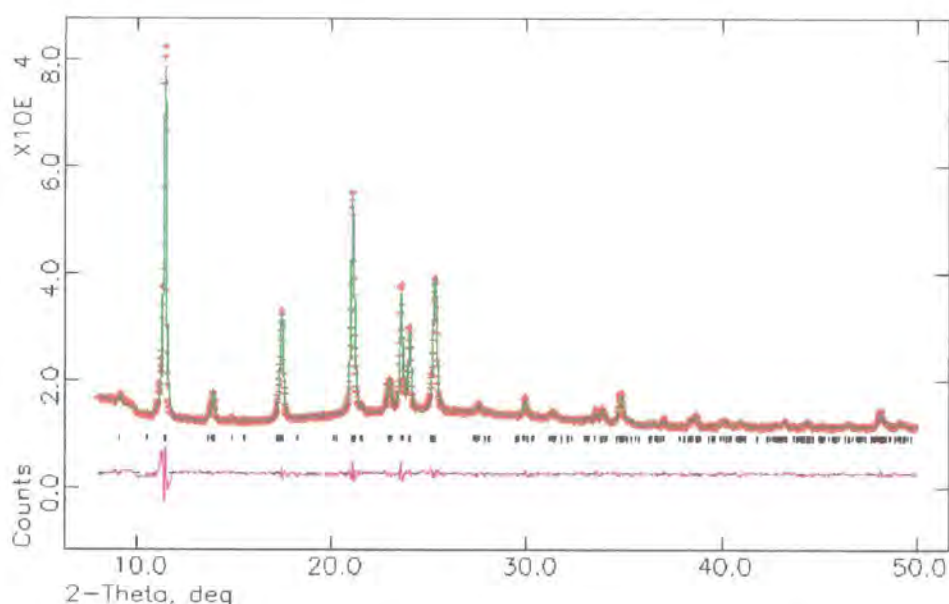


Figure 7.2: Final Rietveld plot for [FeL₆](ClO₄)₂ at room temperature in the high spin state, observed: red; calculated: green; difference: pink.

The aromatic rings within the ligands were restrained to be planar by the application of the following planar restraints: ring 1 (N1,N2,C1–C3); ring 2 (C4,C5,N11,C7,C8,N3); ring 3 (C9–C11,N4,N5); ring 4 (N6,N7,C12–C14); ring 5 (N8,C15,C16,N12,C18,C19); and ring 6 (N9,N10,C20–C22). The bond angles within the five membered rings were restrained to be 108.0(1)^o and those within the six membered rings to 120.0(1)^o. Results from a search for pyrazole rings bound to a carbon atom through one of their nitrogen atoms gave 129 hits and allowed the following restraints to be applied. Pyrazole carbon – carbon bonds were restrained to 1.37(1) Å, nitrogen – nitrogen bonds to 1.36(1) Å and nitrogen – carbon bonds to 1.34(1) Å. A search of the CSD for pyrazine rings bound to a transition metal through one of their nitrogen atoms gave 228 hits. The pyrazine carbon – carbon bonds were restrained to

1.38(1) Å and carbon – nitrogen bonds to 1.33(1) Å. Restraints were also applied to the tetrahedral perchlorate anions; the bond angles were restrained to be 109.5(1)°. A search of the CSD revealed that the mean chlorine – oxygen bond length in perchlorate is 1.39 Å and so these bonds were restrained to be 1.39(1) Å. This gives a total of 94 restraints.

After application of these restraints, Rietveld refinement of the model could proceed [5] using the GSAS suite of programmes [6]. Non – hydrogen atoms were refined isotropically. The isotropic displacement parameters were constrained to be the same for each element with only one parameter refined for carbon and nitrogen. The background was refined using a Chebyshev polynomial function with nine terms. A total of 152 parameters were refined: four unit cell parameters; a zero point; a histogram scale factor; four profile parameters; nine terms of the Chebyshev background function; 129 atomic positional parameters and four isotropic displacement parameters. Details of the refinement are given in Table 7.1 and Figure 7.2 shows the final Rietveld plot.

Formula	[Fe(C ₁₀ H ₈ N ₆) ₂](ClO ₄) ₂
Wavelength (Å)	1.54051 (Cu K _{α1})
Data range (°2θ)	5 – 50
Step size (°2θ)	0.0144
Space group	P2 ₁
a (Å)	8.4538(8)
b (Å)	8.4462(7)
c (Å)	19.436(2)
β (°)	90.450(5)
Volume (Å³)	1387.7(2)
Z	2
Number of degrees of freedom	18
Number of Z-matrices	3
Number of Bragg reflections	280
Number of profile points	3011
Number of restraints	94
Number of observations	3105
Number of refined parameters	152
R_p (%)	3.03
wR_p (%)	4.73
R_F² (%)	7.86

Table 7.1: Details of the GSAS refinement and selected crystallographic parameters for [FeL6₂](BF₄)₂ in the high spin state at room temperature.

Description of the structure

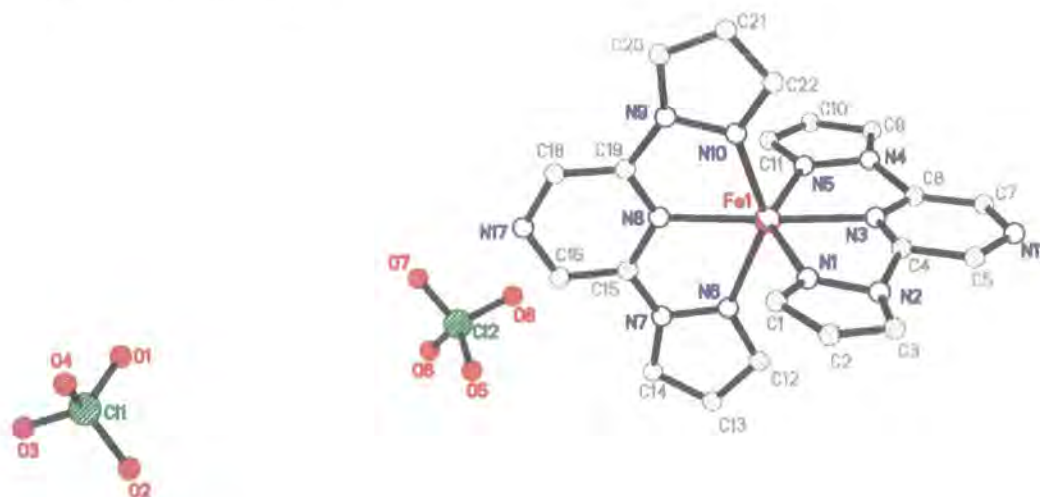


Figure 7.3: Crystal structure of $[\text{FeL}_6_2](\text{ClO}_4)_2$ at room temperature in the high spin state, determined by X-ray powder diffraction. Hydrogen atoms have been omitted for clarity.

At room temperature $[\text{FeL}_6_2](\text{ClO}_4)_2$ was found to crystallise in the monoclinic space group $P2_1$ and is isostructural with $[\text{FeL}_1_2](\text{BF}_4)_2$, described in Chapter three. The iron atom has a distorted octahedral geometry with the iron atom bound to two ligands through three of their six nitrogen atoms, Figure 7.3. The iron atom forms four bonds to the pyrazole rings and two to the pyrazine rings. Of these bonds the ones to the pyrazine rings are the shortest. The iron – pyrazine nitrogen bonds lie parallel to the crystallographic c axis and the iron – pyrazole bonds are at approximately 45° to the a and b axes, Figure 7.4. Like other members of this family of iron (II) spin crossover compounds, $[\text{FeL}_6_2](\text{ClO}_4)_2$ exhibits extensive $\pi - \pi$ interactions which are orientated along the a axis and weak hydrogen bonds between the ligands and the counter anions. It is interesting to note that the replacement of the central pyridine ring of the ligands in the parent compound, $[\text{FeL}_1_2](\text{BF}_4)_2$, with a pyrazine ring, in L6, has had little effect on the intermolecular bonding or bulk packing of this system. The uncoordinated nitrogen atom of the pyrazine ring forms no new significant interactions. It is probable that it is these similarities in cooperativity are responsible for $[\text{FeL}_1_2](\text{BF}_4)_2$ and $[\text{FeL}_6_2](\text{ClO}_4)_2$ having comparable shaped spin transition curves, Figure 7.9b (the spin transition curve for $[\text{FeL}_1_2](\text{BF}_4)_2$ can be found on page 52, Figure 3.6). The lower transition temperature of $[\text{FeL}_6_2](\text{ClO}_4)_2$ is most likely a result of the differences in ligand field caused by changing the central pyridine ring of the ligand to a pyrazine.

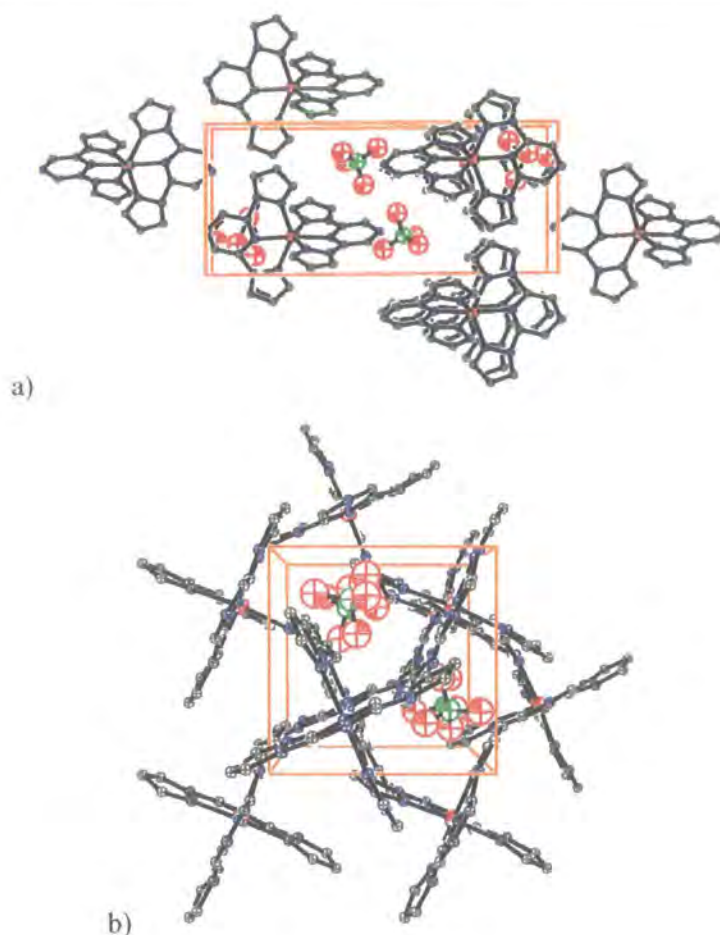


Figure 7.4: The crystal packing in $[\text{FeL}_6]_2(\text{ClO}_4)_2$ in the high spin state at room temperature; a) view normal to 010; b) view normal to 001. Hydrogen atoms have been omitted for clarity

7.3.2 Variable temperature powder X-ray diffraction study of $[\text{FeL}_6]_2(\text{ClO}_4)_2$

Figure 7.5 illustrates the evolution of the diffraction pattern with temperature between 298 K and 120 K. A phase transition is evident between 217 K and 194 K; this is in good agreement with the magnetic data which show a transition from the high to the low spin state at 208 K. The eight patterns above the phase transition were treated using the structural model obtained from structure solution at room temperature and Rietveld refinement. The unit cell parameters, an overall temperature factor, sample displacement, profile and background coefficients were refined. The data set collected at 206 K was found to be a mixture of the high and low spin phases. The pattern collected at 195 K is representative of the low spin state and this was indexed to give a monoclinic unit cell with parameters of $a = 16.571(3) \text{ \AA}$, $b = 8.568(1) \text{ \AA}$, $c = 18.839(4) \text{ \AA}$, $\beta = 92.33(1)^\circ$ and $V = 2673(2) \text{ \AA}^3$. This corresponds to a

doubling along the crystallographic a axis on going from the high to the low spin state. It is expected that the crystal retains its symmetry and, if this is the case, the asymmetric unit in the low spin state would consist of six independent molecules; four perchlorate anions and two cations. Given the current state of systems for the solution of structures from powder data, this renders the solution of this structure extremely difficult. The unit cell parameters for the low temperature, low spin state were refined using Pawley fitting [7]. The unit cell parameters, sample displacement and background and profile parameters were refined. Figure 7.6 shows the evolution of the unit cell parameters with temperature, the unit cell volumes for $[\text{FeL}_6]_2(\text{ClO}_4)_2$ in the low spin state *i.e.* below 206 K have been halved to allow for direct comparison. It can be seen that the discontinuity in the unit cell volume curve is in good agreement with the magnetic data.

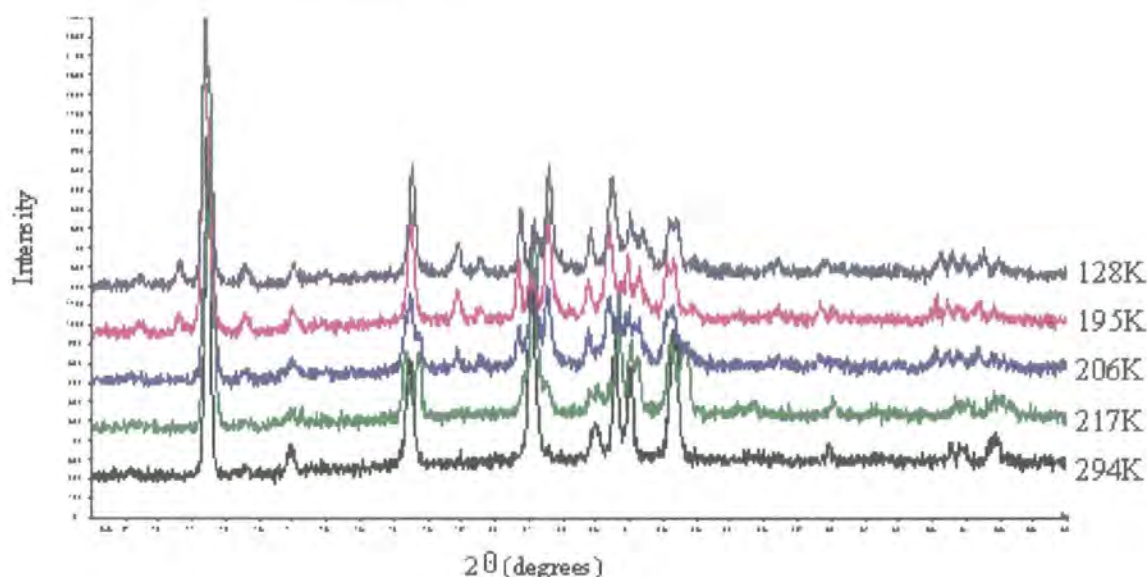


Figure 7.5: The evolution of the powder pattern with temperature for $[\text{FeL}_6]_2(\text{ClO}_4)_2$.

Only selected temperatures have been shown for clarity.

Without structural determination of the solid state structure of the low spin state, it is not possible to predict the cause of the crystallographic phase transition which accompanies the spin transition. The magnetic data indicate that $[\text{FeL}_6]_2(\text{ClO}_4)_2$ undergoes a complete spin transition from the high spin state above 208 K to the low spin below this temperature, for this reason it is unlikely that the crystallographic phase transition is associated with an ordering of spin states after a partial spin transition, as is observed under some conditions, for example for $[\text{FeL}_4]_2(\text{BF}_4)_2$, Chapter 6.

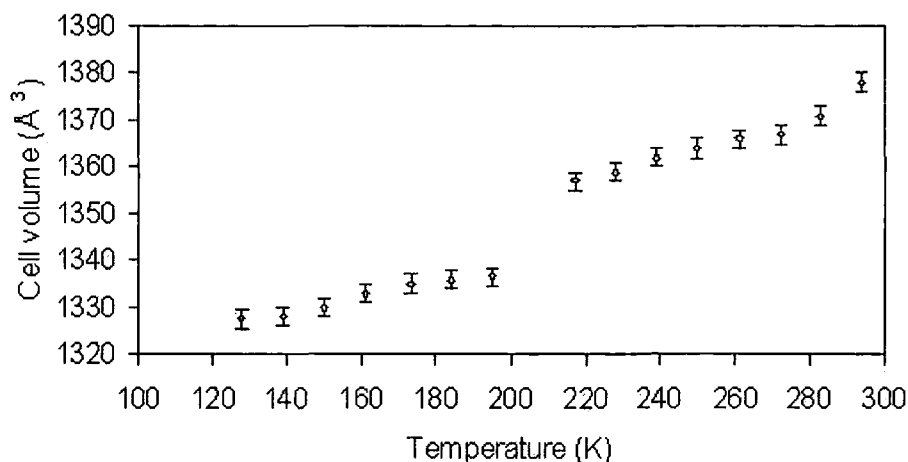


Figure 7.6: Evolution of unit cell volume with temperature for [FeL₆₂](ClO₄)₂. Values in the low spin state, below 195 K, have been halved for ease of comparison.

7.3.3 [FeL₆₂](BF₄)₂

Powder X-ray diffraction

Powder X-ray diffraction data were collected on a polycrystalline sample of this compound in capillary geometry at room temperature. Indexing the pattern obtained in this way yielded a monoclinic unit cell, with unit cell parameters of; $a = 11.886(2) \text{ \AA}$, $b = 11.878(2) \text{ \AA}$, $c = 19.093(3) \text{ \AA}$, $\beta = 92.291(9)^\circ$ and $V = 2693.4(8) \text{ \AA}^3$ [1]. As in the case of the low spin, low temperature state of [FeL₆₂](ClO₄)₂ this large unit cell results in a high degree of overlap of reflections in the diffraction pattern and, for the same reasons mentioned above, with the current state of structure solution from powder data, it has not been possible to solve the structure of the high spin state of this compound at room temperature.

Further X-ray powder diffraction data were collected on station 2.3 at the Daresbury synchrotron, as described in Chapter 2, which had the added benefit of not only providing a much higher level of intensity of X-rays but also a tuneable wavelength. The data were collected at a wavelength of 1.3 \AA ; this is a shorter wavelength than that of the copper radiation (1.54051 \AA) used in the laboratory experiment, described in the previous paragraph. Nonetheless, the greater intensity and reduced absorption was not sufficient to allow for reliable unit cell determination and so structure solution was unsuccessful.

Single crystal X-ray diffraction

Attempts were made to grow diffraction quality, solvent free single crystals of [FeL6₂](BF₄)₂; unfortunately the crystals, obtained by vapour diffusion of ether into acetone, were of bad overall quality being very small, thin and twinned. X-ray diffraction data were collected on one of these crystals at 120 K and, despite its poor quality, it was possible to refine a solution and it was hoped that this would allow us to solve the powder diffraction data. Intriguingly the unit cell of this low temperature phase was found to have unit cell parameters of $a = 8.4104(9) \text{ \AA}$, $b = 8.5683(9) \text{ \AA}$, $c = 18.096(2) \text{ \AA}$, $\beta = 96.151(5)^\circ$ and $V = 1296.6(2) \text{ \AA}^3$. This cell is similar to that determined for [FeL6₂](ClO₄)₂ at room temperature. It was possible to solve the structure of [FeL6₂](BF₄)₂ at 120 K and to refine the model isotropically, Figure 7.7. The compound was found to crystallise in the monoclinic space group P2₁ and to be isostructural with [FeL6₂](ClO₄)₂ at room temperature. Despite the poor quality of the final refinement, inspection of the iron – nitrogen bond lengths shows that, in agreement with the magnetic data, the compound is in the low spin state under these conditions. The mean metal – ligand distance is 1.94(2) \AA.

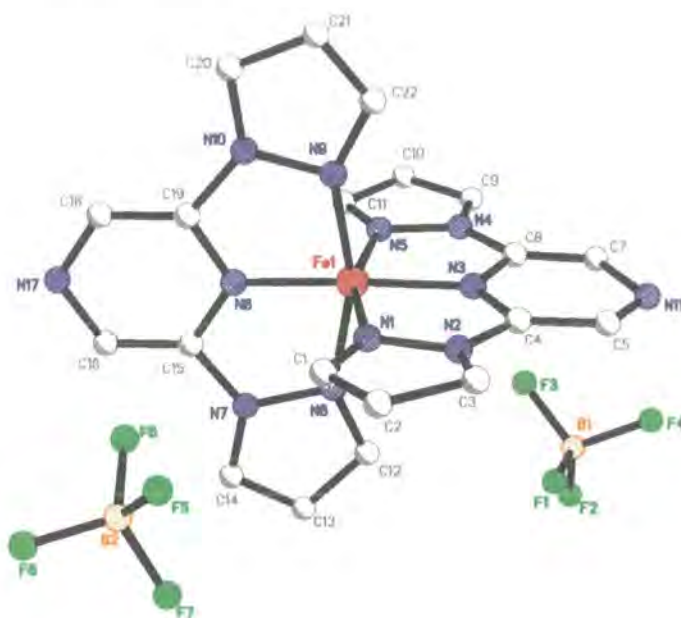


Figure 7.7: Structure of [FeL6₂](BF₄)₂ in the low spin state at 120 K solved from single crystal X-ray diffraction data. Hydrogen atoms have been omitted for clarity.

This result is particularly interesting as it suggests that despite their similar spin transition behaviour, demonstrated by the magnetic data discussed below, [FeL6₂](ClO₄)₂ and [FeL6₂](BF₄)₂ have very different solid state behaviour. From the powder diffraction data it can be seen that both materials undergo crystallographic phase transitions. In the case of the

perchlorate, the transition coincides with the spin transition and the low temperature phase of $[\text{FeL6}_2](\text{BF}_4)_2$ and is observed to be isostructural with the high temperature phase of $[\text{FeL6}_2](\text{ClO}_4)_2$, Figure 7.8 shows the solid state packing of $[\text{FeL6}_2](\text{BF}_4)_2$. This latter result is somewhat unusual, but attempts to model the high temperature, high spin, diffraction pattern of $[\text{FeL6}_2](\text{BF}_4)_2$ using the result from the low temperature single crystal study were unsuccessful, with the smaller cell failing to fit the pattern. Indeed it would appear that the high temperature, high spin, phase of $[\text{FeL6}_2](\text{BF}_4)_2$ has a similar structure to the low spin, low temperature phase of $[\text{FeL6}_2](\text{ClO}_4)_2$. Sadly, as previously mentioned, attempts to solve either of these structures from the powder diffraction data have been unsuccessful thus far.

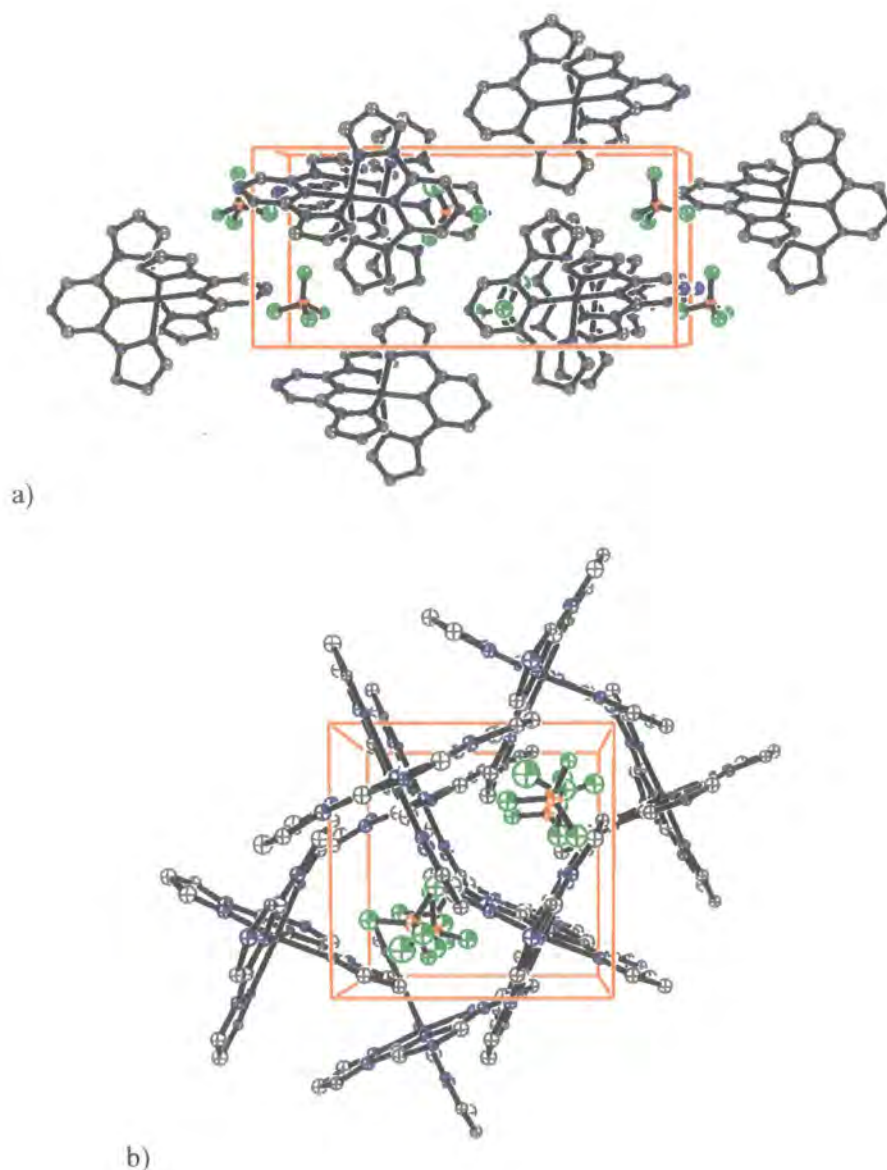


Figure 7.8: The crystal packing in $[\text{FeL6}_2](\text{BF}_4)_2$ in the low spin state at 120 K; a) view normal to 010; b) view normal to 001. Hydrogen atoms have been omitted for clarity

7.3.4 Photomagnetic Studies

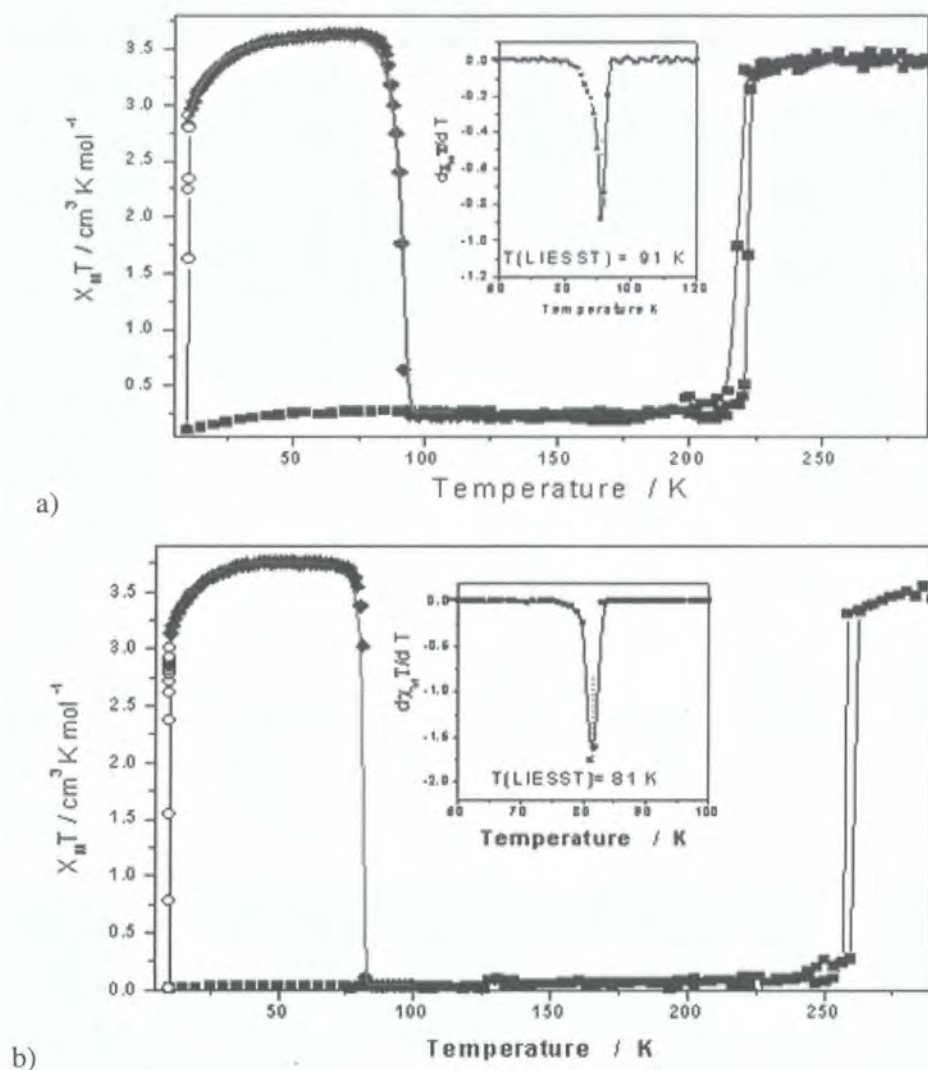


Figure 7.9: Temperature dependence of $\chi_M T$ for a) $[\text{FeL6}_2](\text{BF}_4)_2$ and b) $[\text{FeL6}_2](\text{ClO}_4)_2$. ■ = data recorded in the cooling and warming mode without irradiation; ○ = data recorded with irradiation at 10 K; ◆ = T(LIESST) measurement, data recorded in the warming mode with the laser turned off after irradiation for one hour.

These magnetic data were collected in collaboration with Prof. Jean-François Létard at the ICMCB and were published in 2004 [8]. This detailed SQUID magnetometry study focussed on the effect of irradiation on the magnetic behaviour of $[\text{FeL6}_2](\text{BF}_4)_2$ and $[\text{FeL6}_2](\text{ClO}_4)_2$. Both compounds were found to exhibit abrupt, complete spin transitions with small hysteresis loops with $T_{1/2\uparrow} = 221 \text{ K}$ and $T_{1/2\downarrow} = 218 \text{ K}$ for $[\text{FeL6}_2](\text{BF}_4)_2$ and $T_{1/2\uparrow} = 203 \text{ K}$ $T_{1/2\downarrow} = 199 \text{ K}$ for $[\text{FeL6}_2](\text{ClO}_4)_2$ in good agreement with previously published results [1]. The variation of the magnetic susceptibility with temperature is shown in Figure 7.9. It can be seen that both

[FeL6₂](BF₄)₂ and [FeL6₂](ClO₄)₂ show very similar spin transition behaviour. In both cases at 290 K the $\chi_M T$ product is near to 3.0 cm³ K mol⁻¹ (where χ_M is the magnetic susceptibility and T is temperature) which would be expected for a quintet ground state, suggesting that the compound is completely in the high spin state. $\chi_M T$ drops suddenly to close to 0 cm³ K mol⁻¹, as expected for a singlet ground state, over the course of only a few degrees at the spin transition temperature. The abrupt transitions and hysteresis loops provide evidence of cooperative interactions in the solid state.

Figure 7.9 also shows the effect of irradiation at 10 K. Irradiation of both samples at 10 K causes a sudden increase in $\chi_M T$; saturation was reached at a value close to 3.0 cm³ K mol⁻¹ indicating complete transition from the low spin ground state to the metastable high spin state. The laser was then switched off and the temperature increased, in the dark, at 0.3 K min⁻¹. [FeL6₂](BF₄)₂ and [FeL6₂](ClO₄)₂ show an initial increase in $\chi_M T$ before reaching a plateau at a similar value to that seen at 290 K, indicating a complete and quantitative conversion to the metastable high spin state. This initial increase is due to zero field splitting; the anisotropy of high spin iron (II) in octahedral surroundings. $\chi_M T$ decreases suddenly to a value close to 0 cm³ K mol⁻¹ showing complete relaxation back to the ground low spin state. $T(\text{LIESST})$ was estimated, by taking the extreme of the $\partial\chi_M T/\partial T$ versus T curve for the relaxation, to be 91 K and 100 K for [FeL6₂](BF₄)₂ and [FeL6₂](ClO₄)₂ respectively. In both cases the relaxation curve is seen to be abrupt, which indicates that the metastable high spin state retains a high degree of cooperativity. This is seen in the related compound [FeL1₂](BF₄)₂ (Chapter 3) in which the relaxation from the metastable high spin state is also abrupt and determination of the structure of this metastable state, by single crystal X-ray diffraction, confirms a high level of cooperativity. It was described in Chapter 3 how a large body of experimental work by Létard *et al* had confirmed the reciprocal relationship between $T_{1/2}$ (the temperature of the thermal spin transition) and $T(\text{LIESST})$ proposed by Hauser [9]. A study of a large number of spin crossover compounds for which these values had been determined showed that, when plotted on a graph of $T_{1/2}$ vs. $T(\text{LIESST})$, points for related compounds lie on straight lines with different y intercepts, T_0 . Comparison of the $T(\text{LIESST})$ and $T_{1/2}$ values for [FeL6₂](BF₄)₂ and [FeL6₂](ClO₄)₂ with that of [FeL1₂](BF₄)₂ show that these compounds also exhibit this relationship with the points lying on a straight line with $T_0 = 150$ K.

Continuous irradiation of [FeL6₂](BF₄)₂ and [FeL6₂](ClO₄)₂ in the SQUID cavity on both warming and cooling, reveals the existence of LITH (Light Induced Thermal Hysteresis) [10] in the two compounds, Figure 7.10. The hysteresis loops for these compounds are found to be 11 K for [FeL6₂](BF₄)₂ and 31 K for [FeL6₂](ClO₄)₂. The presence of LITH provides further evidence that the metastable high spin states of these two materials show high levels of

cooperativity. Nonetheless, in the absence of crystallographic information, very few conclusions can be drawn concerning the differences between the high spin state found as a ground state at room temperature, and that formed as a result of the LIESST effect.

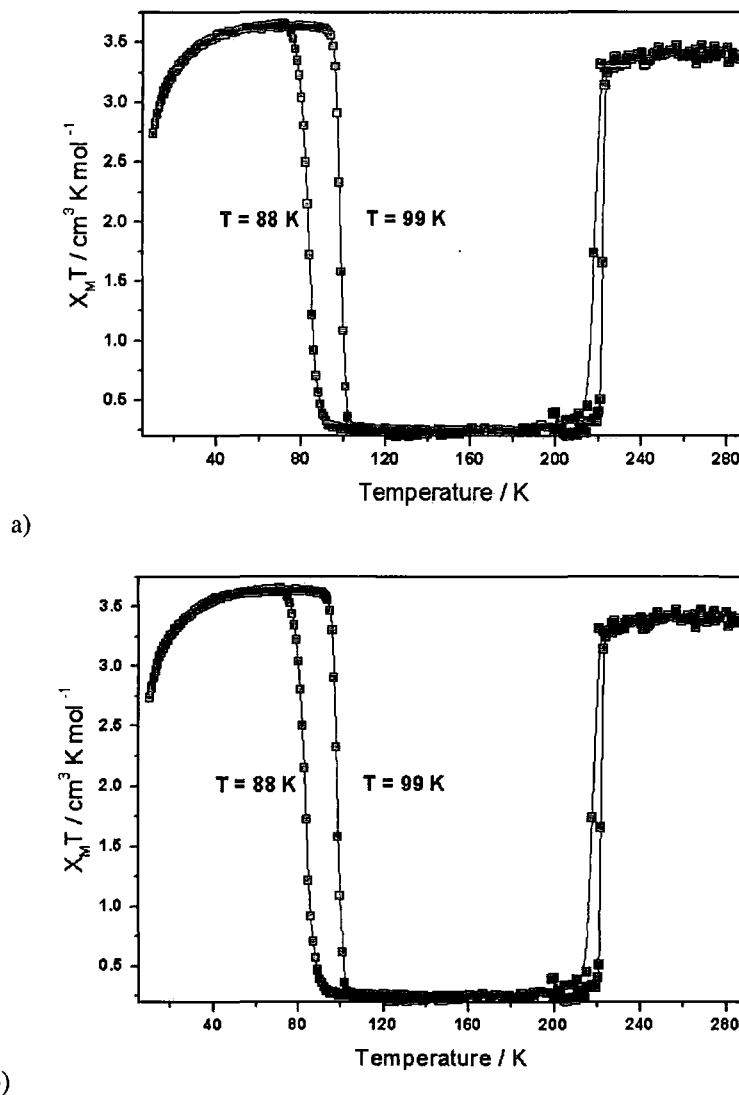


Figure 7.10: LITH experiment, the temperature dependence of $\chi_M T$ recorded in the warming and cooling modes with irradiation a) $[\text{FeL}_6]_2(\text{BF}_4)_2$; b) $[\text{FeL}_6]_2(\text{ClO}_4)_2$

The results of detailed kinetic experiments into the photomagnetic behaviour of $[\text{FeL}_6]_2(\text{BF}_4)_2$ and $[\text{FeL}_6]_2(\text{ClO}_4)_2$ have been reported elsewhere [8] and a detailed discussion of these findings lies beyond the scope of this thesis. To summarise these results; SQUID data were collected at temperatures accessible using the available equipment at the ICMCB in Bordeaux, between 10 K and 300 K. Analysis of these data showed that at temperatures below 70 K and 80 K for $[\text{FeL}_6]_2(\text{BF}_4)_2$ and $[\text{FeL}_6]_2(\text{ClO}_4)_2$ respectively, the systems showed so little loss of high spin population with time that it was not possible to measure the

temperature dependence. Below these temperatures (70 K and 80 K) relaxation of the system took place by temperature independent tunnelling. On raising the temperature above these threshold values the compounds enter the temperature dependent zone and the relaxation shows strong deviation from the sigmoidal behaviour that would be predicted for systems following Arrhenius decay. This deviation from simple Arrhenius behaviour is expected for systems which show self acceleration, a result of strong cooperative effects. There is an upper temperature limit for a particular compound above which it is not possible to collect meaningful kinetic data as the relaxation occurs more quickly than the SQUID time frame. The limiting temperatures for these systems are 83 K for $[\text{FeL}_6_2](\text{BF}_4)_2$ and 90 K for $[\text{FeL}_6_2](\text{ClO}_4)_2$.

7.4 Conclusions

The structure of $[\text{FeL}_6_2](\text{ClO}_4)_2$ in the high spin state at room temperature has been determined from powder X-ray diffraction data. The compound is found to be isostructural with $[\text{FeL}_1_2](\text{BF}_4)_2$, Chapter 3. However, unlike this compound, $[\text{FeL}_6_2](\text{ClO}_4)_2$ has been shown to undergo a crystallographic phase transition coincident with the thermal spin transition. The doubling of the unit cell volume, which is a feature of this phase transition, results in both a very large degree of peak overlap in the powder diffraction pattern and, assuming the crystal retains its symmetry, a asymmetric unit containing six independent fragments. The complex nature of the low spin state has meant that it has not been possible to determine its structure from the available powder diffraction data.

Examination of a polycrystalline sample of $[\text{FeL}_6_2](\text{BF}_4)_2$ using X-ray powder diffraction has shown that it is not isostructural with $[\text{FeL}_6_2](\text{ClO}_4)_2$ at room temperature in the high spin state. In fact it appears to crystallise in a unit cell similar to that observed for the low temperature, low spin phase of $[\text{FeL}_6_2](\text{ClO}_4)_2$ and for the reasons described above it has not been possible to determine the structure of this compound. The low spin structure of $[\text{FeL}_6_2](\text{BF}_4)_2$ has been determined at 120 K from a very poor quality, single crystal. This study shows the low spin state to crystallise in the monoclinic space group $P2_1$ and to be isostructural with the high spin phase of $[\text{FeL}_6_2](\text{ClO}_4)_2$.

Photomagnetic measurements of $[\text{FeL}_6_2](\text{BF}_4)_2$ and $[\text{FeL}_6_2](\text{ClO}_4)_2$ show that both compounds have long lived LIESST states at low temperature, with $T(\text{LIESST})$ values of 91 K and 100 K respectively. Taken in conjunction with $[\text{FeL}_1_2](\text{BF}_4)_2$ which has $T(\text{LIESST})$

of 80 K these compounds show agreement with the inverse relationship known to exist between $T_{1/2}$ and $T(\text{LIESST})$. From these results it can be postulated that the metastable high spin states for these compounds formed as a result of the LIESST transition, show a high degree of cooperativity. This is demonstrated by the abrupt nature of the relaxation curves and the existence of LITH loops under constant irradiation.

7.5 References

1. J. Elhaïk, V. A. Money, S. A. Barrett, C. A. Kilner, I. Radosavljevic Evans and M. A. Halcrow, *Dalton Trans.*, 2003, 2053 – 2060
2. J. W. Visser, *J. Appl. Cryst.*, 1969, **2**, 89 - 95
3. Cambridge Crystallographic Data Centre, (2002). DASH. Version 2.1. Cambridge Crystallographic Data Centre, 12, Union Road, Cambridge, CB2 1EZ, UK
4. F. H. Allen, *Acta Cryst.*, 2002 **B58**, 380 - 388
5. H. Rietveld, *J. Appl. Cryst.*, 1969, **2**, 65 – 71
6. A. C. Larson and R. B. von Dreele, 1994, *GSAS*, LANSCE, Los Alamos National Laboratory, NM, USA
7. G. A. Pawley, *J. Appl. Cryst.*, 1981, **14**, 357 - 361
8. V. A. Money, J. Sánchez Costa, S. Marcén, G. Chastanet, J. Elhaïk, M. A. Halcrow, J. A. K. Howard and J.-F. Létard, *Chem. Phys. Lett.*, 2004, 273 - 277
9. A. Hauser, *Coord. Chem. Rev.*, 1991, **111**, 275 - 290
10. A. Desaix, O. Roubeau, J. Jeftic, J. G. Hassnoot, K. Boukheddaden, E. Codjovi, J. Linares, M. Nogues and F. Varret, *Eur. Phys. B.*, 1998, **6**, 183 - 193

8 Conclusions and Perspectives

8.1 Conclusions

With the drive for ever faster and smaller computers there is considerable economic pressure to develop new materials for use in switching and memory devices. One of the most promising and exciting areas of research at the present time is that of spin crossover compounds in which a memory effect may be introduced by a change in temperature, or pressure, or by irradiation. Whilst the thermal spin transition has been well documented, and thoroughly studied, for a wide range of compounds containing first row transition metals, particularly iron (II), structural studies of the spin crossover phenomenon induced by raised pressure and by laser irradiation are much less common. In this thesis, a detailed crystallographic study has been made of the family of complexes derived from the 2,6-(dipyrazol-1-yl)pyridine ligand. The thermal spin transitions and LIESST behaviour of these compounds have been studied in detail; the first examination of this class of materials at raised pressure has also been made with the crystallographic and magnetic study of $[\text{FeL}_2](\text{BF}_4)_2$.

Full structural analyses of iron (II) complexes in the metastable high spin state (HS-2) have been reported for $[\text{FeL}_2](\text{BF}_4)_2$, $[\text{Fe}(\text{L}3)_2](\text{BF}_4)_2$, $[\text{Fe}(\text{L}3)_2](\text{ClO}_4)_2$ and $[\text{Fe}(\text{L}4)_2](\text{BF}_4)_2$, Chapters 3,5 and 6. These studies have shown that, at least for this family of materials, the HS-2 state is structurally identical to the high spin state reached as a result of the thermal spin transition (HS-1). This is in contrast with results reported for $[\text{Fe}(\text{phen})_2(\text{NCS})_2]$ and $[\text{Fe}(\text{phen})_2(\text{NCSe})_2]$ (where phen = 1,10-phenanthroline) [1,2] in which there were significant differences between the structures of the HS-1 and HS-2 states, leading to the metastable high spin state showing a higher level of cooperativity than the HS-1. Unit cell parameters showing the existence of a LIESST state have been recorded for $[\text{FeL}_2](\text{BF}_4)_2$ and $[\text{FeL}_2](\text{ClO}_4)_2$, Chapter 4, although relaxation was too fast to allow for the collection of a full set of diffraction data. These results are important in that they throw further light on a novel way to introduce bistability into these systems which in turn opens new applications in the areas of optical computing. Work on this family of compounds has shown that the inverse law between $T_{1/2}$ and $T(\text{LIESST})$ holds true for these materials as well as those studied by Létard *et al* [3]. These current studies into the effect of the LIESST transition have added greatly to the small number of materials in which the structure of the metastable high spin

state is known. This has not only increased the essential information available for those studying this fascinating facet of the spin crossover phenomenon, but has aided in the development of the techniques required for the study of these materials under these conditions.

An important feature of spin crossover materials is cooperativity, which is a measure of the degree to which a spin transition in one atom affects neighbouring atoms. High levels of cooperativity promote abrupt transitions with hysteresis loops, both of which are essential for potential applications. Although the critical nature of cooperativity has been demonstrated frequently, using methods such as dilute metal systems, [4] the exact nature of the phenomenon is still not clearly understood. By detailed crystallographic examination of spin crossover systems, it is possible to assess the effect of intermolecular interactions on the spin transition and so determine more fully the role they play in controlling the cooperativity and the course of the transition. The compounds presented in Chapter 4, $[\text{FeL}_2]_2(\text{BF}_4)_2$ and $[\text{FeL}_2]_2(\text{ClO}_4)_2$, show unusual spin transition curves with changes in gradient at the temperatures at which the spin transition is 50% complete. A detailed variable temperature crystallographic study has shown that the rate of transition is controlled by an order – disorder transition in one of the anions. In the high spin state, one of the anions in both compounds is thermally disordered, on cooling the anion is found to become fully ordered at the temperature at which the transition is 50% complete, this is the same temperature as that at which the spin transition curves show a change in gradient to become more gradual. The order – disorder transition in the anions causes a lengthening of the crystallographic c parameter, which in turn increases the distance between iron centres, weakening the hydrogen bonding between the anions and cations, and so reducing the cooperativity, giving rise to a more gradual conversion from high to low spin over the second half of the spin transition curve. As far as I am aware this is the first time that counter ions have been shown to exhibit this type of control over the spin transition and in which the behaviour can be so clearly seen.

Given the paramount importance of cooperative interactions in determining the course of the spin transition, it is somewhat surprising that the comparison between the hydrated and dehydrated crystals of $[\text{FeL}_2]_2(\text{BF}_4)_2$ reveals such similar spin crossover behaviour, Chapter 6. This is primarily due to the close similarities between the intermolecular packing in both systems. However, it was observed that the presence of water acts to stabilise the high spin state. This system also shows an extremely unusual partial spin transition from fully high spin to one third low spin on cooling. What is so unique about this transition is that the spin states become ordered in the solid state. This results in a trebling of the unit cell volume and the asymmetric unit which changes from containing only one formula unit to containing three,

with two high spin cations and one low spin. In the majority of cases, examination of the crystal structure of a mixed spin state phase yields cation structures with average values of bond lengths and angles.

Although the majority of materials discussed in this thesis have been studied using single crystal X-ray diffraction, we were unable to grow diffraction quality crystals of the materials discussed in the preceding chapter. The high spin structure of $[\text{FeL}_6\text{L}_2](\text{ClO}_4)_2$ at room temperature has been solved *ab initio* from laboratory powder X-ray diffraction data using the DASH programme from the Cambridge Crystallographic Data Centre [5]. The compound was found to be isostructural with $[\text{FeL}_1\text{L}_2](\text{BF}_4)_2$, crystallising in the monoclinic space group $P2_1$ with an asymmetric unit consisting of one cation and two anions. This structure solution of a material with three independent atoms in the asymmetric unit represents one of the most complicated materials solved by this simulated annealing programme to date (44 independent non hydrogen atoms). A variable temperature X-ray powder diffraction study (294 K and 128 K) of the unit cell parameters for this compound has shown that it undergoes a crystallographic phase transition between 217 K and 195 K coincident with the thermal spin transition, and this involves a doubling of the crystallographic c parameter.

One of the major physical effects of the spin transition is the decrease in the atomic radius of the metal centre, associated with the change in electronic configuration on going from the high to the low spin state. This decrease gives rise to a marked reduction in metal ligand bond length and therefore in the volume of the coordination polyhedron and the unit cell. It should, therefore, come as no surprise that spin crossover compounds are commonly extremely sensitive to changes in pressure, either internal or external. The results of the first study of the effect of pressure on the derivatives of the 2,6-(dipyrazol-1-yl)pyridine ligand are presented in Chapter three (3.3.3). The spin transition in $[\text{FeL}_1\text{L}_2](\text{BF}_4)_2$ can be induced at room temperature by application of a comparatively small increase in pressure. The low spin state formed in this way is isostructural with that formed on cooling. A study of the effect on the thermal spin transition of increasing the pressure was performed using SQUID magnetometry. This has confirmed that the temperature of the thermal spin transition increases with increasing pressure as is predicted for spin crossover compounds, since the volume of the low spin state is less than that of the high spin state. Investigation of other spin crossover compounds has shown that the width of the hysteresis loop can either increase or decrease on increasing the pressure but, in the case of this study it was not possible to draw concrete conclusions as to the effect of pressure on the hysteresis loop. It was noted that the spin transition remains abrupt, rather than becoming more gradual as observed for a number of the other examples of pressure effects on spin crossover complexes.

8.2 Future perspectives

Although the spin crossover phenomenon was first discovered in the 1930s, it was only relatively recently that the full industrial potential of this family of materials came to be realised. One of the most critical areas of research for the aim of producing devices which utilise any of the effects of the spin transition, from the change in colour to the change in magnetism, is the design of a library of materials with a wide range of well understood spin crossover behaviour. The complexes discussed herein offer an example of the way in which systematic changes can be used not only to build up such a library, but simultaneously to increase the knowledge which lies behind our understanding of these processes. With this aim in mind, continued structural studies will play an essential role in the development of devices. Nonetheless, structural studies alone are inadequate for complete understanding of spin crossover; kinetic behaviour and concrete affirmation of the percentage of material in each spin state can only be determined using techniques such as magnetometry. For this reason the approach followed during this course of research of combining detailed crystallographic studies with detailed SQUID magnetometry has proved very powerful.

There are a number of ways in which the work described here could be continued. Although mononuclear spin crossover compounds have been found which display transitions with hysteresis loops near to room temperature, there has been increasing interest recently in the development of spin-transition polymers in which the metal centres are linked by covalent bonds. It is thought that linking the metal centres in this fashion will yield greater levels of communication and so improve cooperativity leading to abrupt transitions and wide hysteresis loops. The ligands used in this study could be altered such that they allow formation of polymeric systems which should show interesting spin crossover properties. A dimeric system, similar to those described herein, in which the iron centres are linked by a pyrazolato bridge has recently been reported which shows a one step spin transition [6]. Helical binuclear complexes have been developed which contain one lanthanide ion and one six coordinate iron (II) centre, the identity of the lanthanide ion has a marked effect on the thermal spin transition in the iron atom and this has been accounted for by the effect of cooperativity through the linking ligands [7]. Generation of helical complexes of this sort will give rise to both asymmetric and symmetric isomers which may be expected to show different spin crossover behaviour and this will not only provide systems with improved cooperativity but may help to answer some of the fundamental questions about cooperative effects which, at the present time, remain unanswered. This will be aided by comparison with the spin crossover behaviour of mononuclear complexes in which the iron coordination

environment is the same as that in the polymeric and binuclear systems, thus showing how the spin transition in the metal ions is disturbed by communication with neighbouring atoms.

By far the greatest number of reported spin crossover materials have been iron (II) compounds in which the iron is coordinated to six nitrogen donors. Although spin transitions have been reported for all the first row transition metals with the correct electronic configurations there have been very few systematic studies into the phenomenon in metal centres other than iron (II). Extension of this research to include both new iron (II) coordination environments and other metal centres would be a valuable addition to the work being performed in this area at present. Iron (III) salts of the ligand shown in Figure 8.1 are known to show spin crossover transitions in solution, and as the spin transition is a molecular phenomenon, it is reasonable to suppose that they would also show this behaviour in the solid state [8,9]. In addition there is evidence of short lived LIESST states in these materials [10]. Study of compounds related to these is likely to yield iron (III) compounds with interesting thermal and light induced spin transitions. The only iron (II) spin crossover compound with an N_4O_2 donor set is also ligated by this type of ligand [11]. This raises the possibility of finding systems in which both iron (II) and iron (III) centres undergo spin transitions. Structural examination of spin crossover compounds which have the same ligation, but in which the metal centres have different oxidation states, would be a very important result. It is also realistic to suppose that this line of research would yield the first full structural determination of an iron (III) compound in the metastable high spin state, resulting from irradiation at low temperature.

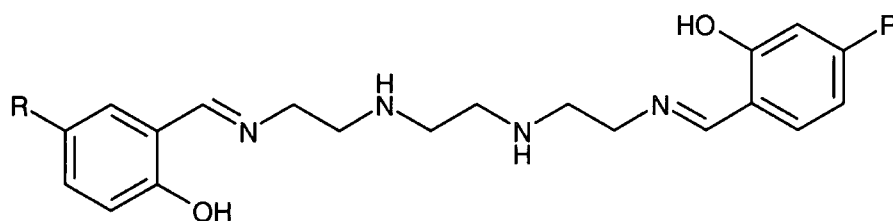


Figure 8.1: R = H, NO₂, OMe or Ph. Fe (III) complexes of this ligand show spin crossover in solution and LIESST behaviour. When R = NO₂ the Fe (II) complex is the only example of a Fe(II) compound with a N_4O_2 donor set to show spin crossover.

The improvement in experimental techniques which is certain to take place over the coming years, will greatly widen the accessible areas of research. It has been proposed that electron-phonon coupling may provide the basis for the cooperative effects so essential to the course of the spin transition [12], but at the present time spin crossover compounds are too complicated

to carry out studies into the behaviour of phonons. It is possible that examination of phonon behaviour over the course of a thermal spin transition will determine whether this is indeed the driving force behind the cooperative effect. Further development of the techniques for structure solution from powder diffraction data will enable examination of the structure compounds for which single crystals are not available. This is particularly pertinent in the area of research into polymeric systems where it can reasonably be expected, that while polycrystalline samples may be available, large single crystals will not.

With a view to device development, there is need for further investigation of methods for tuning the transition. O. Khan *et al* have patented polymeric systems, based on the 1,2,4-triazole ligand, which undergo spin transitions in which the hysteresis loops span room temperature. They also discovered that creation of a spin crossover alloy, in which the proportion of two different 1,2,4-triazole based ligands along the polymer chain is controlled, gave rise to spin crossover behaviour that was dependent on the relative proportions of each ligand. For example a 1:1 mixture of two ligands along the polymer chain will give rise to a material with $T_{1/2}$ half way between those of the two compounds which contain 100% of each ligand. This approach allows the controlled synthesis of spin crossover materials with spin transition temperatures which fall in a desired range, but has the draw back that the spin transitions exhibited by the alloys occur over a wide temperature range. In the same manner the spin transition may also be controlled by altering the ratio of different counter ions in the system [13]. In principle, this method provides an attractive way in which to fine tune the spin transition temperature, to give the desired properties for a particular application.

Another intrinsic draw back of spin crossover materials is the fact that they are usually obtained as crystalline solids which raises problems for the shaping of components. Recently Lee *et al* reported the development of composite materials in which an iron (II) spin crossover system containing the 4-heptyl-1,2,4-triazole ligand was blended with poly(methyl methacrylate). The spin crossover behaviour was retained in systems that contained more than 10% by weight of the iron complexes [14]. This avenue of research has the potential to lead to the development of a wide range of spin crossover materials which can be readily processed whilst retaining their magnetic properties. This would be of immense value in the design of devices based on the bistability of the magnetic properties or colour change associated with these systems.

Despite the considerable amount of research interest which has been focussed on spin crossover materials since their discovery, their full potential has not yet been realised. Fundamental questions still remain, particularly with regard to the role of cooperativity in the

spin transition. The discovery of the LIESST effect has generated a large amount of interest, but to the present time, information on the structure of the metastable high spin state and the kinetics of the relaxation to the low spin ground state remains relatively rare. Much work in this area is still to be done before utilisation of these materials in devices becomes possible. These compounds have the potential to overcome the limit to the speed of computer processing that the current silicon technology is fast approaching by providing access to much smaller bit size and fast read/write times. Kahn *et al* have also postulated that these materials may find use in medical applications in procedures such as those in which tumours are treated with heat, but care needs to be taken that the patient is not harmed by too high a temperature. These systems would be low spin, and therefore diamagnetic at low temperature, but the transition to a paramagnetic high spin form could provide a warning of a temperature limit being reached. This magnetic transition would show up clearly on a magnetic resonance imaging scan. Preliminary results into the effectiveness of using a polymeric spin crossover system based on Fe(II) triazole and aminotriazole complexes as a contrast agent show promise in this area [15]. Addition of the contrast agent is found to "spoil" MRI images above the spin transition temperature which may be modified to physiological temperature by substituting triazole for aminotriazole in different ratios, as described above. To summarise; continued research into this area is likely to provide not only new and exciting insights into the theory behind the spin crossover phenomenon but also open up new avenues of potential application. I firmly believe that detailed crystallographic studies such as those reported here coupled with complementary magnetometry have a critical role to play in the future research and development of this field.

8.3 References

1. M. Marchivie, P. Guionneau, J. A. K. Howard, A. E. Goeta, G. Chastanet, J-F. Létard and D. Chasseau, *J. Am. Chem. Soc.*, 2002, **124**, 194 - 195
2. E. J. MacLean, C.M. McGrath, C. J. O'Conner, C. Sangregorio, J. M. W. Seddon, E. Sinn, F. E. Sowrey, S. J. Teat, A. E. Terry, G. B. M. Vaughan, N. A. Young, *Chem. Eur. J.*, 2003, **921**, 5314 - 5322
3. A. Hauser. *Coord. Chem. Rev.*, 1991, **111**, 275 - 290
4. I. Sanner, E. Meissner, H. Köppen, H. Spiering and P. Gülich, *Chem. Phys.*, 1984, **86**, 227
5. Cambridge Crystallographic Data Centre, (2002). DASH. Version 2.1. Cambridge Crystallographic Data Centre, 12, Union Road, Cambridge, CB2 1EZ, UK

6. K. Nakamo, N. Suemura, S. Kawata, A. Fuyuhiko, T. Yagi, S. Nasu, S. Morimoto and S. Kaizaki, *Dalton Trans.*, 2004, 982 - 988
7. J-C. G. Bünzli and C. Piguet, *Chem. Rev.*, 2002, **102**, 1897 - 1928
8. M. F. Tweedle and L. J. Wilson, *J. Am. Soc.*, 1976, **98**, 4824 - 4835
9. E. Sinn, G. Sim, E. V. Dose, M. F. Tweedle and L. J. Wilson, *J. Am. Soc.*, 1978, **100**, 3375 - 3390
10. S. Schenker, A. Hauser, R. M. Dyson, *Inorg. Chem.*, 1996, **35**, 4676 - 4682
11. D. Boinnard, A. Boisseksou, A. Dworkin, J-M. Savariault, F. Varret and J-P. Tuchagues, *Inorg. Chem.*, 1994, **33**, 271 - 280
12. R. Zimmermann, *J. Phys. Chem. Solids*, 1983, **44**, 151 - 158
13. O. Kahn and C. J. Martinez, *Science*, 1998, **279**, 44 - 48
14. S-W. Lee, J-W. Lee, S-H. Jeong, I-W. Park, Y-M. Kim and J-I. Jin, *Synth. Met.*, 2004, **142**, 243 - 249
15. R. N. Muller, L. Vander Elst and S. Laurent, *J. Am. Chem. Soc.*, 2003, **125**, 8405-8407

A. Selected crystallographic parameters

A.1. $[\text{FeL1}_2](\text{BF}_4)_2$

290 K in the high spin state

Table 1.1: Atomic coordinates ($\times 10^4$) and equivalent isotropic displacement parameters ($\text{\AA}^2 \times 10^3$). $U(\text{eq})$ is defined as one third of the trace of the orthogonalized U^{ij} tensor.

	x	y	z	U(eq)
Fe(1)	7385(1)	3210(4)	2476(1)	52(1)
N(1)	5028(6)	2321(8)	2106(3)	53(1)
N(2)	4752(6)	2220(8)	1393(3)	52(1)
C(1)	3710(9)	1796(10)	2353(4)	63(2)
C(2)	2616(9)	1332(10)	1800(5)	76(2)
C(3)	3295(9)	1624(10)	1201(5)	68(2)
N(3)	7213(5)	3247(9)	1356(2)	45(1)
C(4)	5941(7)	2709(8)	976(3)	49(1)
C(5)	5802(10)	2662(10)	246(4)	65(2)
C(6)	7078(10)	3162(13)	-81(3)	71(2)
C(7)	8414(10)	3740(10)	295(4)	65(2)
C(8)	8412(8)	3762(8)	1021(3)	50(2)
N(4)	9688(6)	4322(8)	1482(3)	55(1)
N(5)	9598(7)	4174(9)	2186(3)	59(1)
C(9)	11005(10)	5115(11)	1349(5)	76(2)
C(10)	11792(10)	5459(12)	1990(6)	90(3)
N(6)	6497(7)	5567(8)	2682(3)	59(1)
N(7)	6316(6)	5858(8)	3370(3)	58(1)
C(11)	10892(9)	4876(11)	2484(5)	73(2)
C(12)	5976(9)	6859(11)	2347(5)	75(2)
C(13)	5450(10)	7946(12)	2803(6)	89(3)
C(14)	5682(10)	7277(10)	3456(6)	78(2)
N(8)	7359(5)	3401(9)	3589(2)	46(1)
C(15)	6822(7)	4702(9)	3877(4)	52(2)

C(16)	6774(9)	4884(11)	4589(4)	66(2)
C(17)	7291(9)	3649(11)	5014(4)	68(2)
C(18)	7868(9)	2302(11)	4735(4)	62(2)
C(19)	7874(7)	2232(9)	4008(3)	47(1)
N(9)	8444(6)	952(8)	3643(3)	51(1)
N(10)	8394(6)	1033(8)	2926(3)	53(1)
C(20)	9141(9)	-378(11)	3893(4)	70(2)
C(21)	9559(10)	-1194(11)	3330(4)	74(2)
C(22)	9067(9)	-287(10)	2745(4)	65(2)
B(1)	2037(2)	3780(2)	9227(1)	70(2)
F(1)	3070(3)	4421(4)	8797(2)	87(3)
F(2)	515(2)	4065(5)	8948(2)	118(5)
F(3)	2281(5)	4445(4)	9884(1)	84(3)
F(4)	2283(5)	2191(2)	9279(2)	104(4)
F(1A)	3452(2)	4162(5)	8982(2)	79(4)
F(2A)	939(4)	4914(5)	9025(5)	117(6)
F(3A)	2231(6)	3685(13)	9948(1)	260(20)
F(4A)	1528(6)	2360(5)	8952(5)	310(30)
B(2)	7366(1)	8553(1)	5727(1)	86(3)
F(5)	6722(3)	8618(4)	5039(1)	94(2)
F(6)	6993(3)	9897(2)	6070(1)	88(4)
F(7)	6772(3)	7277(2)	6051(1)	232(10)
F(8)	8978(1)	8419(4)	5747(2)	227(14)
F(5A)	6612(4)	8624(5)	5058(1)	600(50)
F(6A)	6527(3)	9399(4)	6175(2)	134(7)
F(7A)	7468(5)	7018(2)	5944(2)	180(19)
F(8A)	8857(2)	9170(5)	5729(2)	122(6)

Table 1.2: Selected bond lengths [Å] and angles [°].

Fe(1)-N(3)	2.125(4)	N(3)-Fe(1)-N(8)	173.1(3)
Fe(1)-N(8)	2.131(5)	N(3)-Fe(1)-N(5)	73.4(2)
Fe(1)-N(5)	2.173(6)	N(8)-Fe(1)-N(5)	108.5(2)
Fe(1)-N(10)	2.182(6)	N(3)-Fe(1)-N(10)	113.2(2)
Fe(1)-N(1)	2.191(6)	N(8)-Fe(1)-N(10)	73.5(2)
Fe(1)-N(6)	2.194(7)	N(5)-Fe(1)-N(10)	96.0(2)
		N(3)-Fe(1)-N(1)	73.3(2)

N(8)-Fe(1)-N(1)	104.3(2)	N(8)-Fe(1)-N(6)	73.3(2)
N(5)-Fe(1)-N(1)	146.7(2)	N(5)-Fe(1)-N(6)	91.2(2)
N(10)-Fe(1)-N(1)	98.3(2)	N(10)-Fe(1)-N(6)	146.6(2)
N(3)-Fe(1)-N(6)	100.1(2)	N(1)-Fe(1)-N(6)	93.1(2)

Symmetry transformations used to generate equivalent atoms:

120 K in the low spin state

Table 1.3: Atomic coordinates ($\times 10^4$) and equivalent isotropic displacement parameters ($\text{\AA}^2 \times 10^3$). U(eq) is defined as one third of the trace of the orthogonalized U^{ij} tensor.

	x	y	z	U(eq)
Fe(1)	7862(1)	1092(1)	7536(1)	14(1)
N(1)	10010(2)	145(2)	7807(1)	17(1)
N(2)	10354(2)	-135(2)	8555(1)	18(1)
C(1)	11294(3)	-335(3)	7530(1)	20(1)
C(2)	12466(3)	-920(3)	8086(1)	23(1)
C(3)	11841(3)	-769(3)	8730(1)	22(1)
N(3)	7905(2)	894(2)	8569(1)	15(1)
C(4)	9192(2)	297(3)	8989(1)	17(1)
C(5)	9293(3)	153(3)	9744(1)	21(1)
C(6)	7983(3)	672(3)	10059(1)	22(1)
C(7)	6644(3)	1316(3)	9634(1)	21(1)
C(8)	6667(2)	1408(2)	8885(1)	16(1)
N(4)	5476(2)	2050(2)	8355(1)	18(1)
N(5)	5755(2)	1979(2)	7634(1)	17(1)
C(9)	4070(3)	2786(3)	8404(1)	22(1)
C(10)	3416(3)	3194(3)	7707(1)	24(1)
N(6)	6876(2)	-930(2)	7170(1)	17(1)
N(7)	6692(2)	-1040(2)	6412(1)	17(1)
C(11)	4496(3)	2669(3)	7246(1)	20(1)
C(12)	6223(3)	-2225(3)	7392(1)	20(1)
C(13)	5596(3)	-3168(3)	6785(1)	24(1)
C(14)	5919(3)	-2378(3)	6174(1)	23(1)
N(8)	7818(2)	1368(2)	6503(1)	16(1)

C(15)	7223(2)	244(3)	6032(1)	17(1)
C(16)	7136(3)	399(3)	5281(1)	20(1)
C(17)	7700(3)	1803(3)	5027(1)	21(1)
C(18)	8306(3)	2996(3)	5502(1)	21(1)
C(19)	8338(2)	2711(3)	6243(1)	17(1)
N(9)	8888(2)	3741(2)	6827(1)	18(1)
N(10)	8761(2)	3227(2)	7527(1)	17(1)
C(20)	9453(3)	5239(3)	6838(1)	22(1)
C(21)	9693(3)	5704(3)	7560(1)	24(1)
C(22)	9238(3)	4421(3)	7963(1)	21(1)
B(1)	7846(3)	6730(4)	4458(2)	26(1)
F(1)	8619(2)	6859(2)	5183(1)	29(1)
F(2)	8372(3)	5384(2)	4146(1)	53(1)
F(3)	8172(2)	8035(2)	4048(1)	31(1)
F(4)	6198(2)	6676(2)	4472(1)	42(1)
B(2)	6994(3)	6476(3)	9395(1)	24(1)
F(5)	7317(2)	7001(2)	10127(1)	34(1)
F(6)	8205(2)	6962(2)	9007(1)	28(1)
F(7)	6943(2)	4841(2)	9401(1)	37(1)
F(8)	5539(2)	7086(3)	9068(1)	48(1)

Table 1.4: Selected bond lengths [\AA] and angles [$^\circ$].

Fe(1)-N(3)	1.8995(17)	N(8)-Fe(1)-N(10)	80.19(8)
Fe(1)-N(8)	1.9074(18)	N(5)-Fe(1)-N(10)	90.10(8)
Fe(1)-N(5)	1.9660(19)	N(3)-Fe(1)-N(1)	80.16(8)
Fe(1)-N(10)	1.972(2)	N(8)-Fe(1)-N(1)	100.66(8)
Fe(1)-N(1)	1.9828(19)	N(5)-Fe(1)-N(1)	160.29(7)
Fe(1)-N(6)	1.988(2)	N(10)-Fe(1)-N(1)	92.14(8)
		N(3)-Fe(1)-N(6)	101.94(8)
N(3)-Fe(1)-N(8)	178.01(9)	N(8)-Fe(1)-N(6)	79.86(8)
N(3)-Fe(1)-N(5)	80.15(8)	N(5)-Fe(1)-N(6)	91.35(8)
N(8)-Fe(1)-N(5)	99.02(8)	N(10)-Fe(1)-N(6)	159.97(7)
N(3)-Fe(1)-N(10)	97.98(8)	N(1)-Fe(1)-N(6)	93.19(8)

Symmetry transformations used to generate equivalent atoms:

30 K in the low spin state

Table 1.5: Atomic coordinates ($\times 10^4$) and equivalent isotropic displacement parameters ($\text{\AA}^2 \times 10^3$). $U(\text{eq})$ is defined as one third of the trace of the orthogonalized U^{ij} tensor.

	x	y	z	U(eq)
Fe(1)	2862(1)	6793(1)	7537(1)	8(1)
N(1)	5024(2)	7737(2)	7816(1)	10(1)
N(2)	5376(2)	8016(2)	8569(1)	9(1)
C(1)	6316(3)	8219(3)	7540(1)	11(1)
C(2)	7495(3)	8804(3)	8103(1)	12(1)
C(3)	6864(3)	8651(3)	8744(1)	11(1)
N(3)	2903(2)	6988(3)	8572(1)	9(1)
C(4)	4200(3)	7587(3)	8999(1)	10(1)
C(5)	4291(3)	7724(3)	9754(1)	11(1)
C(6)	2972(3)	7207(3)	10063(1)	11(1)
C(7)	1632(3)	6571(3)	9640(1)	12(1)
C(8)	1653(3)	6477(3)	8888(1)	10(1)
N(4)	459(2)	5829(3)	8353(1)	10(1)
N(5)	742(2)	5904(3)	7631(1)	10(1)
C(9)	-947(3)	5087(3)	8401(1)	11(1)
C(10)	-1604(3)	4681(3)	7697(1)	13(1)
N(6)	3761(2)	4653(2)	7532(1)	10(1)
N(7)	3891(2)	4125(2)	6829(1)	11(1)
C(11)	-517(3)	5217(3)	7240(1)	11(1)
C(12)	4234(3)	3447(3)	7972(1)	11(1)
C(13)	4693(3)	2151(3)	7572(1)	13(1)
C(14)	4455(3)	2621(3)	6848(1)	12(1)
N(8)	2823(2)	6506(2)	6504(1)	9(1)
C(15)	3341(3)	5153(3)	6243(1)	10(1)
C(16)	3303(3)	4865(3)	5502(1)	12(1)
C(17)	2695(3)	6051(3)	5020(1)	12(1)
C(18)	2137(3)	7468(3)	5276(1)	11(1)
C(19)	2223(3)	7634(3)	6026(1)	9(1)
N(9)	1694(2)	8931(2)	6406(1)	10(1)
N(10)	1876(2)	8828(2)	7167(1)	10(1)
C(20)	918(3)	10267(3)	6164(1)	12(1)
C(21)	588(3)	11074(3)	6778(1)	12(1)

C(22)	1214(3)	10126(3)	7383(1)	11(1)
B(1)	8001(3)	6406(3)	610(2)	11(1)
F(1)	6784(2)	5901(2)	999(1)	14(1)
F(2)	9479(2)	5803(2)	940(1)	18(1)
F(3)	7683(2)	5878(2)	-125(1)	15(1)
F(4)	8046(2)	8057(2)	608(1)	14(1)
B(2)	2883(3)	1124(4)	4464(2)	14(1)
F(5)	3653(2)	978(2)	5197(1)	14(1)
F(6)	3177(2)	-212(2)	4057(1)	13(1)
F(7)	3445(2)	2471(2)	4149(1)	19(1)
F(8)	1219(2)	1242(2)	4472(1)	17(1)

Table 1.6: Selected bond lengths [\AA] and angles [$^\circ$].

Fe(1)-N(3)	1.8956(18)	N(8)-Fe(1)-N(5)	99.00(8)
Fe(1)-N(8)	1.9014(19)	N(6)-Fe(1)-N(5)	90.11(9)
Fe(1)-N(6)	1.965(2)	N(3)-Fe(1)-N(1)	80.14(8)
Fe(1)-N(5)	1.966(2)	N(8)-Fe(1)-N(1)	100.72(8)
Fe(1)-N(1)	1.982(2)	N(6)-Fe(1)-N(1)	92.00(8)
Fe(1)-N(10)	1.988(2)	N(5)-Fe(1)-N(1)	160.23(8)
		N(3)-Fe(1)-N(10)	102.08(9)
N(3)-Fe(1)-N(8)	177.68(10)	N(8)-Fe(1)-N(10)	80.05(8)
N(3)-Fe(1)-N(6)	97.83(9)	N(6)-Fe(1)-N(10)	160.00(8)
N(8)-Fe(1)-N(6)	80.01(8)	N(5)-Fe(1)-N(10)	91.39(9)
N(3)-Fe(1)-N(5)	80.11(8)	N(1)-Fe(1)-N(10)	93.29(9)

Symmetry transformations used to generate equivalent atoms:

30 K after irradiation in the high spin state

Table 1.7: Atomic coordinates ($\times 10^4$) and equivalent isotropic displacement parameters ($\text{\AA}^2 \times 10^3$). $U(\text{eq})$ is defined as one third of the trace of the orthogonalized U^{ij} tensor.

	x	y	z	U(eq)
Fe(1)	2419(1)	8964(1)	2465(1)	9(1)
N(1)	3(2)	9761(2)	2065(1)	10(1)
N(2)	-287(2)	9832(2)	1330(1)	10(1)
C(1)	-1330(2)	10256(3)	2296(1)	11(1)
C(2)	-2480(3)	10691(3)	1718(1)	13(1)
C(3)	-1778(2)	10392(3)	1114(1)	12(1)
N(3)	2230(2)	8845(3)	1324(1)	10(1)
C(4)	918(2)	9369(2)	916(1)	10(1)
C(5)	773(2)	9419(3)	178(1)	11(1)
C(6)	2082(2)	8919(3)	-143(1)	11(1)
C(7)	3460(2)	8373(3)	262(1)	11(1)
C(8)	3451(2)	8349(3)	1000(1)	10(1)
N(4)	4729(2)	7773(2)	1487(1)	10(1)
N(5)	4654(2)	7974(2)	2207(1)	11(1)
C(9)	6024(2)	6900(3)	1369(1)	12(1)
C(10)	6824(2)	6537(3)	2029(1)	13(1)
N(6)	3455(2)	11133(2)	2962(1)	11(1)
N(7)	3466(2)	11189(2)	3694(1)	10(1)
C(11)	5939(2)	7233(3)	2529(1)	12(1)
C(12)	4157(2)	12469(3)	2793(1)	12(1)
C(13)	4638(2)	13396(3)	3410(1)	12(1)
C(14)	4173(2)	12548(3)	3970(1)	12(1)
N(8)	2350(2)	8706(2)	3592(1)	10(1)
C(15)	2870(2)	9874(3)	4044(1)	10(1)
C(16)	2839(2)	9788(3)	4781(1)	11(1)
C(17)	2241(2)	8392(3)	5039(1)	11(1)
C(18)	1720(2)	7140(3)	4584(1)	12(1)
C(19)	1801(2)	7376(3)	3863(1)	11(1)
N(9)	1325(2)	6221(2)	3327(1)	11(1)
N(10)	1543(2)	6550(2)	2636(1)	12(1)
C(20)	699(2)	4742(3)	3387(1)	13(1)

C(21)	513(2)	4080(3)	2712(1)	13(1)
C(22)	1062(2)	5255(3)	2268(1)	12(1)
B(1)	2210(3)	3428(3)	5694(1)	12(1)
F(1)	1544(1)	3371(2)	4970(1)	14(1)
F(2)	1739(2)	4820(2)	6008(1)	23(1)
F(3)	1749(2)	2094(2)	6056(1)	16(1)
F(4)	3881(1)	3399(2)	5713(1)	19(1)
B(2)	2971(3)	3286(3)	784(1)	12(1)
F(5)	2740(1)	2663(2)	84(1)	14(1)
F(6)	1874(2)	2628(2)	1196(1)	14(1)
F(7)	2769(2)	4944(2)	748(1)	14(1)
F(8)	4520(1)	2922(2)	1095(1)	18(1)

Table 1.8: Selected bond lengths [\AA] and angles [$^\circ$].

Fe(1)-N(3)	2.1278(17)	N(8)-Fe(1)-N(6)	73.66(7)
Fe(1)-N(8)	2.1335(17)	N(5)-Fe(1)-N(6)	95.62(7)
Fe(1)-N(5)	2.1737(18)	N(3)-Fe(1)-N(10)	96.88(7)
Fe(1)-N(6)	2.175(2)	N(8)-Fe(1)-N(10)	73.11(7)
Fe(1)-N(10)	2.189(2)	N(5)-Fe(1)-N(10)	90.01(7)
Fe(1)-N(1)	2.1920(18)	N(6)-Fe(1)-N(10)	146.39(7)
		N(3)-Fe(1)-N(1)	73.73(7)
N(3)-Fe(1)-N(8)	169.68(8)	N(8)-Fe(1)-N(1)	103.35(7)
N(3)-Fe(1)-N(5)	73.57(7)	N(5)-Fe(1)-N(1)	147.15(7)
N(8)-Fe(1)-N(5)	108.26(7)	N(6)-Fe(1)-N(1)	101.67(7)
N(3)-Fe(1)-N(6)	116.51(7)	N(10)-Fe(1)-N(1)	90.74(7)

Symmetry transformations used to generate equivalent atoms:

A.2. [FeL₁₂](PF₆)₂**290 K in the high spin state****Table 2.1:** Atomic coordinates ($\times 10^4$) and equivalent isotropic displacement parameters ($\text{\AA}^2 \times 10^3$). U(eq) is defined as one third of the trace of the orthogonalized U^{ij} tensor.

	x	y	z	U(eq)
Fe(1)	10000	3148(2)	2500	33(1)
N(1)	8969(6)	1438(10)	2267(4)	39(2)
N(2)	8936(6)	864(9)	1658(4)	38(2)
C(1)	8485(8)	557(13)	2582(6)	48(3)
C(2)	8141(9)	-570(13)	2183(7)	53(3)
C(3)	8440(8)	-352(12)	1599(6)	49(3)
N(3)	9903(6)	2647(9)	1464(4)	33(2)
C(4)	9407(7)	1556(10)	1203(5)	36(2)
C(5)	9349(8)	1154(12)	554(5)	45(2)
C(6)	9855(9)	1938(13)	171(5)	50(3)
C(7)	10374(8)	3078(13)	422(5)	47(3)
C(8)	10356(7)	3405(11)	1076(4)	36(2)
N(5)	10692(6)	4833(9)	2030(4)	40(2)
N(4)	10790(6)	4593(9)	1389(4)	39(2)
C(11)	11043(9)	6109(12)	2161(6)	50(3)
C(10)	11356(9)	6696(13)	1611(7)	57(3)
C(9)	11183(8)	5717(13)	1130(6)	51(3)
P(1)	2786(1)	253(2)	830(1)	47(1)
F(1)	1741(2)	-251(10)	820(4)	38(4)
F(2)	3077(5)	-514(7)	1523(2)	65(15)
F(3)	2997(7)	-1171(5)	461(3)	118(16)
F(4)	2496(5)	1007(7)	135(2)	90(20)
F(5)	2572(18)	1669(10)	1206(3)	54(5)
F(6)	3832(2)	745(10)	837(4)	103(12)
F(1A)	1707(2)	165(9)	877(4)	43(9)
F(2A)	3022(5)	-427(7)	1547(2)	60(30)
F(3A)	2743(6)	-1288(4)	511(3)	90(20)
F(4A)	2550(6)	934(7)	114(2)	60(20)

F(5A)	2828(6)	1794(4)	1149(4)	72(16)
F(6A)	3864(2)	341(9)	784(4)	120(30)
F(1B)	1871(3)	-673(7)	819(4)	65(13)
F(2B)	3187(5)	-374(8)	1537(2)	120(40)
F(3B)	3257(5)	-1009(6)	487(4)	90(20)
F(4B)	2384(5)	881(8)	124(2)	80(30)
F(5B)	2314(5)	1516(6)	1173(4)	59(14)
F(6B)	3700(3)	1180(7)	842(4)	120(30)

Table 2.2: Selected bond lengths [\AA] and angles [$^\circ$].

Fe(1)-N(3)#1	2.170(7)	N(3)-Fe(1)-N(5)	72.0(3)
Fe(1)-N(3)	2.170(7)	N(5)#1-Fe(1)-N(5)	86.6(5)
Fe(1)-N(5)#1	2.195(9)	N(3)#1-Fe(1)-N(1)	89.6(3)
Fe(1)-N(5)	2.195(9)	N(3)-Fe(1)-N(1)	71.7(3)
Fe(1)-N(1)	2.218(9)	N(5)#1-Fe(1)-N(1)	106.4(3)
Fe(1)-N(1)#1	2.218(9)	N(5)-Fe(1)-N(1)	141.4(3)
		N(3)#1-Fe(1)-N(1)#1	71.7(3)
N(3)#1-Fe(1)-N(3)	154.7(4)	N(3)-Fe(1)-N(1)#1	89.6(3)
N(3)#1-Fe(1)-N(5)#1	72.0(3)	N(5)#1-Fe(1)-N(1)#1	141.4(3)
N(3)-Fe(1)-N(5)#1	128.9(3)	N(5)-Fe(1)-N(1)#1	106.4(3)
N(3)#1-Fe(1)-N(5)	128.9(3)	N(1)-Fe(1)-N(1)#1	86.1(5)

Symmetry transformations used to generate equivalent atoms:

#1 -x+2,y,-z+1/2

120 K in the high spin state

Table 2.3: Atomic coordinates ($\times 10^4$) and equivalent isotropic displacement parameters ($\text{\AA}^2 \times 10^3$). U(eq) is defined as one third of the trace of the orthogonalized U^{ij} tensor.

	x	y	z	U(eq)
Fe(1)	10000	3172(1)	2500	12(1)
N(1)	8947(1)	1450(2)	2265(1)	16(1)
N(2)	8920(1)	863(2)	1656(1)	15(1)

C(1)	8467(2)	557(2)	2586(1)	18(1)
C(2)	8127(2)	-592(2)	2189(1)	20(1)
C(3)	8430(2)	-373(2)	1600(1)	19(1)
N(3)	9902(1)	2659(2)	1462(1)	13(1)
C(4)	9399(2)	1557(2)	1200(1)	15(1)
C(5)	9340(2)	1148(2)	552(1)	17(1)
C(6)	9858(2)	1936(2)	163(1)	19(1)
C(7)	10384(2)	3093(2)	418(1)	19(1)
C(8)	10362(2)	3422(2)	1068(1)	14(1)
N(4)	10801(1)	4623(2)	1386(1)	15(1)
N(5)	10696(1)	4869(2)	2025(1)	16(1)
C(9)	11196(2)	5750(2)	1126(1)	19(1)
C(10)	11365(2)	6743(2)	1607(1)	22(1)
C(11)	11043(2)	6151(2)	2160(1)	20(1)
P(1)	2787(1)	267(1)	841(1)	18(1)
F(1)	1710(1)	-229(2)	838(1)	26(1)
F(2)	3089(1)	-461(2)	1551(1)	27(1)
F(3)	3009(1)	-1162(2)	491(1)	45(1)
F(4)	2482(1)	984(2)	134(1)	29(1)
F(5)	2560(1)	1700(2)	1198(1)	30(1)
F(6)	3862(1)	776(2)	860(1)	45(1)

Table 2.4: Selected bond lengths [\AA] and angles [$^\circ$].

Fe(1)-N(3)	2.1737(18)	N(3)#1-Fe(1)-N(5)#1	71.94(7)
Fe(1)-N(3)#1	2.1737(18)	N(5)-Fe(1)-N(5)#1	85.90(10)
Fe(1)-N(5)	2.2032(19)	N(3)-Fe(1)-N(1)	71.80(7)
Fe(1)-N(5)#1	2.2032(19)	N(3)#1-Fe(1)-N(1)	88.98(7)
Fe(1)-N(1)	2.2208(19)	N(5)-Fe(1)-N(1)	141.29(7)
Fe(1)-N(1)#1	2.2208(19)	N(5)#1-Fe(1)-N(1)	107.36(7)
		N(3)-Fe(1)-N(1)#1	88.98(7)
N(3)-Fe(1)-N(3)#1	154.10(10)	N(3)#1-Fe(1)-N(1)#1	71.80(7)
N(3)-Fe(1)-N(5)	71.94(7)	N(5)-Fe(1)-N(1)#1	107.36(7)
N(3)#1-Fe(1)-N(5)	129.64(7)	N(5)#1-Fe(1)-N(1)#1	141.29(7)
N(3)-Fe(1)-N(5)#1	129.64(7)	N(1)-Fe(1)-N(1)#1	85.07(10)

Symmetry transformations used to generate equivalent atoms: #1 $-x+2, y, -z+1/2$

30 K in the high spin state

Table 2.5: Atomic coordinates ($\times 10^4$) and equivalent isotropic displacement parameters ($\text{\AA}^2 \times 10^3$) for $[\text{Fe}(\text{L}1)_2](\text{PF}_6)_2$ at 30 K. $U(\text{eq})$ is defined as one third of the trace of the orthogonalized U^{ij} tensor.

	x	y	z	U(eq)
Fe(1)	10000	3177(1)	2500	7(1)
N(1)	8940(3)	1441(4)	2268(2)	11(1)
N(2)	8917(3)	865(4)	1656(2)	9(1)
C(1)	8467(3)	549(5)	2587(2)	10(1)
C(2)	8128(3)	-605(5)	2189(2)	11(1)
C(3)	8425(3)	-380(5)	1599(2)	11(1)
N(3)	9906(3)	2660(4)	1463(2)	10(1)
C(4)	9395(3)	1558(5)	1198(2)	11(1)
C(5)	9341(3)	1144(5)	551(2)	10(1)
C(6)	9856(3)	1937(5)	157(2)	11(1)
C(7)	10384(3)	3099(5)	412(2)	10(1)
C(8)	10363(3)	3426(4)	1066(2)	9(1)
N(4)	10807(3)	4626(4)	1383(2)	9(1)
N(5)	10697(3)	4875(4)	2023(2)	10(1)
C(9)	11202(3)	5753(5)	1123(2)	10(1)
C(10)	11369(3)	6752(5)	1606(2)	11(1)
C(11)	11049(3)	6153(5)	2163(2)	11(1)
P(1)	2788(1)	262(1)	845(1)	9(1)
F(1)	1693(2)	-226(3)	837(1)	11(1)
F(2)	3084(2)	-474(3)	1561(1)	13(1)
F(3)	3012(2)	-1171(3)	490(1)	15(1)
F(4)	2491(2)	992(3)	135(1)	13(1)
F(5)	2561(2)	1703(3)	1203(1)	13(1)
F(6)	3881(2)	772(3)	869(1)	14(1)

Table 2.6: Selected bond lengths [\AA] and angles [$^\circ$] for $[\text{Fe}(\text{L}1)_2](\text{PF}_6)_2$ at 30 K.

Fe(1)-N(3)	2.166(4)	Fe(1)-N(1)	2.225(4)
Fe(1)-N(3)#1	2.166(4)	Fe(1)-N(1)#1	2.225(4)
Fe(1)-N(5)	2.201(4)		
Fe(1)-N(5)#1	2.201(4)	N(3)-Fe(1)-N(3)#1	153.8(2)

N(3)-Fe(1)-N(5)	71.86(14)	N(5)-Fe(1)-N(1)	141.46(14)
N(3)#1-Fe(1)-N(5)	130.02(14)	N(5)#1-Fe(1)-N(1)	107.61(13)
N(3)-Fe(1)-N(5)#1	130.02(14)	N(3)-Fe(1)-N(1)#1	88.43(14)
N(3)#1-Fe(1)-N(5)#1	71.86(14)	N(3)#1-Fe(1)-N(1)#1	72.06(14)
N(5)-Fe(1)-N(5)#1	85.83(19)	N(5)-Fe(1)-N(1)#1	107.61(13)
N(3)-Fe(1)-N(1)	72.06(14)	N(5)#1-Fe(1)-N(1)#1	141.46(14)
N(3)#1-Fe(1)-N(1)	88.43(14)	N(1)-Fe(1)-N(1)#1	84.45(19)

Symmetry transformations used to generate equivalent atoms:

#1 -x+2,y,-z+1/2

A.3. [CoL₁₂](BF₄)₂

120 K in the high spin state

Table 3.1: Atomic coordinates ($\times 10^4$) and equivalent isotropic displacement parameters ($\text{\AA}^2 \times 10^3$). U(eq) is defined as one third of the trace of the orthogonalized U^{ij} tensor.

	x	y	z	U(eq)
Co(1)	2632(1)	8471(1)	2535(1)	17(1)
N(1)	3450(4)	10832(4)	2389(2)	20(1)
N(2)	3692(4)	11150(4)	1699(2)	19(1)
C(1)	3941(5)	12109(5)	2759(3)	24(1)
C(2)	4499(5)	13254(6)	2318(2)	28(1)
C(3)	4331(5)	12602(5)	1647(3)	27(1)
N(3)	2682(4)	8687(5)	1434(2)	18(1)
C(4)	3204(5)	10008(5)	1162(2)	19(1)
C(5)	3257(5)	10231(5)	442(2)	23(1)
C(6)	2723(5)	8980(5)	-9(2)	22(1)
C(7)	2136(5)	7599(5)	254(2)	21(1)
C(8)	2147(5)	7526(5)	989(2)	19(1)
N(4)	1558(4)	6224(4)	1345(2)	19(1)
N(5)	1571(4)	6318(4)	2076(2)	21(1)
C(9)	845(5)	4880(5)	1079(2)	26(1)
C(10)	412(5)	4058(6)	1645(2)	27(1)

C(11)	876(5)	4994(5)	2252(2)	21(1)
N(6)	4982(4)	7561(4)	2896(2)	18(1)
N(7)	5292(4)	7432(4)	3623(2)	17(1)
C(12)	6314(5)	7080(5)	2650(2)	21(1)
C(13)	7458(5)	6616(5)	3223(3)	26(1)
C(14)	6780(5)	6855(5)	3835(2)	23(1)
N(8)	2800(3)	8443(5)	3643(2)	18(1)
C(15)	4106(5)	7888(5)	4046(2)	19(1)
C(16)	4260(5)	7817(5)	4784(2)	23(1)
C(17)	2964(5)	8322(6)	5109(2)	25(1)
C(18)	1600(5)	8899(5)	4706(2)	24(1)
C(19)	1580(5)	8941(5)	3970(2)	18(1)
N(9)	310(4)	9530(4)	3481(2)	19(1)
N(10)	389(4)	9376(4)	2758(2)	20(1)
C(20)	-1006(5)	10370(5)	3594(3)	27(1)
C(21)	-1784(6)	10736(6)	2930(3)	30(1)
C(22)	-874(5)	10098(6)	2436(2)	25(1)
B(1)	2776(7)	3938(6)	9341(3)	31(1)
B(2)	2008(7)	4034(6)	4270(3)	25(1)
F(5)	2307(4)	4583(3)	4976(1)	37(1)
F(6)	3155(3)	4625(3)	3871(1)	34(1)
F(7)	2115(4)	2397(3)	4284(2)	37(1)
F(8)	513(4)	4499(5)	3962(2)	55(1)
F(4)	3484(3)	4003(3)	10058(1)	34(1)
F(3)	3244(3)	5245(4)	8971(2)	45(1)
F(1)	1128(3)	4045(4)	9322(2)	54(1)
F(2)	3199(6)	2586(4)	9029(2)	77(1)

Table 3.2: Selected bond lengths [\AA] and angles [$^\circ$].

Co(1)-N(8)	2.070(3)	N(8)-Co(1)-N(3)	173.28(15)
Co(1)-N(3)	2.083(3)	N(8)-Co(1)-N(10)	75.54(13)
Co(1)-N(10)	2.145(3)	N(3)-Co(1)-N(10)	107.41(13)
Co(1)-N(1)	2.150(4)	N(8)-Co(1)-N(1)	99.14(15)
Co(1)-N(6)	2.161(3)	N(3)-Co(1)-N(1)	75.02(15)
Co(1)-N(5)	2.164(4)	N(10)-Co(1)-N(1)	90.07(14)
		N(8)-Co(1)-N(6)	75.11(13)

N(3)-Co(1)-N(6)	101.74(13)	N(3)-Co(1)-N(5)	75.03(14)
N(10)-Co(1)-N(6)	150.65(13)	N(10)-Co(1)-N(5)	92.72(13)
N(1)-Co(1)-N(6)	94.19(13)	N(1)-Co(1)-N(5)	149.34(13)
N(8)-Co(1)-N(5)	111.12(15)	N(6)-Co(1)-N(5)	98.09(13)

Symmetry transformations used to generate equivalent atoms:

30 K in the high spin state

Table 3.3: Atomic coordinates ($\times 10^4$) and equivalent isotropic displacement parameters ($\text{\AA}^2 \times 10^3$). $U(\text{eq})$ is defined as one third of the trace of the orthogonalized U^{ij} tensor.

	x	y	z	U(eq)
Co(1)	2375(1)	6362(1)	2464(1)	10(1)
N(1)	3430(4)	8520(5)	2925(2)	11(1)
N(2)	3447(4)	8606(4)	3662(2)	10(1)
C(1)	4140(5)	9851(5)	2755(3)	13(1)
C(2)	4599(5)	10778(6)	3363(2)	14(1)
C(3)	4159(5)	9955(6)	3933(2)	15(1)
N(3)	2322(4)	6143(5)	3565(2)	12(1)
C(4)	2864(5)	7304(5)	4018(2)	10(1)
C(5)	2854(5)	7213(5)	4753(2)	13(1)
C(6)	2263(5)	5819(6)	5012(2)	14(1)
C(7)	1738(5)	4574(5)	4556(2)	13(1)
C(8)	1793(5)	4807(5)	3835(2)	12(1)
N(4)	1318(4)	3665(4)	3298(2)	10(1)
N(5)	1569(4)	3992(5)	2611(2)	12(1)
C(9)	669(5)	2202(5)	3348(3)	14(1)
C(10)	505(5)	1563(6)	2666(2)	14(1)
C(11)	1095(5)	2708(5)	2230(3)	13(1)
N(6)	4629(4)	5458(4)	2247(2)	12(1)
N(7)	4704(4)	5289(4)	1520(2)	11(1)
C(12)	5907(5)	4732(5)	2572(2)	12(1)
C(13)	6814(6)	4060(6)	2079(2)	16(1)
C(14)	6022(5)	4435(5)	1412(2)	12(1)
N(8)	2213(4)	6368(5)	1352(2)	11(1)

C(15)	3422(5)	5870(5)	1028(2)	11(1)
C(16)	3421(5)	5920(5)	288(2)	12(1)
C(17)	2036(5)	6497(6)	-119(2)	12(1)
C(18)	736(5)	6989(5)	203(2)	14(1)
C(19)	902(5)	6927(5)	945(2)	12(1)
N(9)	-305(4)	7377(4)	1361(2)	10(1)
N(10)	15(4)	7252(4)	2101(2)	11(1)
C(20)	-1793(5)	7951(5)	1152(3)	13(1)
C(21)	-2476(5)	8198(5)	1758(3)	14(1)
C(22)	-1330(5)	7751(5)	2334(3)	12(1)
B(1)	3008(7)	800(7)	738(3)	14(1)
F(1)	2714(3)	217(3)	24(1)	18(1)
F(2)	2867(3)	2440(3)	718(1)	15(1)
F(3)	1859(3)	167(3)	1138(1)	15(1)
F(4)	4522(3)	351(4)	1048(1)	23(1)
B(2)	7820(6)	5830(6)	4354(3)	14(1)
F(5)	6150(3)	5824(3)	4328(1)	22(1)
F(6)	8251(3)	4494(3)	3991(1)	18(1)
F(7)	8320(4)	7194(3)	4033(2)	26(1)
F(8)	8523(3)	5779(3)	5079(1)	16(1)

Table 3.4: Selected bond lengths [\AA] and angles [$^\circ$].

Co(1)-N(8)	2.071(3)	N(3)-Co(1)-N(6)	107.47(14)
Co(1)-N(3)	2.079(3)	N(5)-Co(1)-N(6)	89.93(15)
Co(1)-N(5)	2.146(4)	N(8)-Co(1)-N(10)	75.72(14)
Co(1)-N(6)	2.147(4)	N(3)-Co(1)-N(10)	101.35(14)
Co(1)-N(10)	2.153(4)	N(5)-Co(1)-N(10)	93.98(15)
Co(1)-N(1)	2.158(4)	N(6)-Co(1)-N(10)	150.93(14)
		N(8)-Co(1)-N(1)	111.51(16)
N(8)-Co(1)-N(3)	172.97(16)	N(3)-Co(1)-N(1)	75.09(15)
N(8)-Co(1)-N(5)	98.86(16)	N(5)-Co(1)-N(1)	149.17(14)
N(3)-Co(1)-N(5)	74.83(15)	N(6)-Co(1)-N(1)	92.74(14)
N(8)-Co(1)-N(6)	75.21(14)	N(10)-Co(1)-N(1)	98.33(14)

Symmetry transformations used to generate equivalent atoms:

A.4. $[\text{FeL}_2](\text{BF}_4)_2$

290 K in the high spin state

Table 4.1: Atomic coordinates ($\times 10^4$) and equivalent isotropic displacement parameters ($\text{\AA}^2 \times 10^3$). $U(\text{eq})$ is defined as one third of the trace of the orthogonalized U^{ij} tensor.

	x	y	z	U(eq)
Fe(1)	0	10000	5000	32(1)
N(1)	1763(3)	8601(3)	5352(1)	41(1)
N(2)	1866(3)	8436(3)	6131(1)	40(1)
C(1)	2997(6)	7712(6)	4211(2)	83(2)
C(2)	2797(3)	7793(3)	5066(3)	51(1)
C(3)	3553(4)	7110(4)	5650(2)	61(1)
C(4)	2972(4)	7520(4)	6302(2)	59(1)
N(3)	0	10000	6208(2)	35(1)
N(4)	0	10000	7769(2)	51(1)
C(5)	937(3)	9201(3)	6593(2)	34(1)
C(6)	932(3)	9197(3)	7381(2)	45(1)
B(1)	5000	10000	7500	42(2)
F(1)	4353(3)	8968(3)	7947(2)	75(1)
B(2)	10000	5000	7500	98(5)
F(2)	10564(16)	3691(9)	7440(11)	196(4)
F(2A)	9646(19)	4371(14)	6846(9)	194(8)

Table 4.2: Selected bond lengths [\AA] and angles [$^\circ$].

Fe(1)-N(3)#1	2.124(3)	N(3)#1-Fe(1)-N(1)#1	73.52(6)
Fe(1)-N(3)	2.124(3)	N(3)-Fe(1)-N(1)#1	106.48(6)
Fe(1)-N(1)#1	2.184(3)	N(3)#1-Fe(1)-N(1)#2	73.52(6)
Fe(1)-N(1)#2	2.184(3)	N(3)-Fe(1)-N(1)#2	106.48(6)
Fe(1)-N(1)	2.184(3)	N(1)#1-Fe(1)-N(1)#2	147.05(12)
Fe(1)-N(1)#3	2.184(3)	N(3)#1-Fe(1)-N(1)	106.48(6)
		N(3)-Fe(1)-N(1)	73.52(6)
N(3)#1-Fe(1)-N(3)	180.0	N(1)#1-Fe(1)-N(1)	94.61(3)

N(1)#2-Fe(1)-N(1)	94.61(3)	N(1)#1-Fe(1)-N(1)#3	94.61(3)
N(3)#1-Fe(1)-N(1)#3	106.48(6)	N(1)#2-Fe(1)-N(1)#3	94.61(3)
N(3)-Fe(1)-N(1)#3	73.52(6)	N(1)-Fe(1)-N(1)#3	147.05(12)

Symmetry transformations used to generate equivalent atoms:

- #1 $y-1, -x+1, -z+1$ #2 $-y+1, x+1, -z+1$ #3 $-x, -y+2, z$
 #4 $-y+3/2, x+1/2, -z+3/2$ #5 $y-1/2, -x+3/2, -z+3/2$
 #6 $-x+1, -y+2, z$ #7 $y+1/2, -x+3/2, -z+3/2$ #8 $-y+3/2, x-1/2, -z+3/2$
 #9 $-x+2, -y+1, z$

270 K in a mixed spin state

Table 4.3: Atomic coordinates ($\times 10^4$) and equivalent isotropic displacement parameters ($\text{\AA}^2 \times 10^3$).
 $U(\text{eq})$ is defined as one third of the trace of the orthogonalized U^{ij} tensor.

	x	y	z	U(eq)
Fe(1)	10000	10000	5000	29(1)
N(1)	8223(3)	11381(3)	4653(1)	40(1)
N(2)	8112(3)	11561(3)	3877(1)	37(1)
C(1)	6951(5)	12221(6)	5796(2)	73(1)
C(2)	7172(3)	12175(3)	4949(3)	49(1)
C(3)	6408(4)	12861(4)	4364(2)	58(1)
C(4)	7001(4)	12455(4)	3700(2)	54(1)
N(3)	10000	10000	3799(1)	32(1)
N(4)	10000	10000	2237(2)	45(1)
C(5)	9056(3)	10792(3)	3409(2)	32(1)
C(6)	9061(3)	10805(3)	2623(2)	41(1)
B(1)	5000	10000	2500	36(2)
F(1)	5655(2)	11031(3)	2053(2)	66(1)
B(2)	10000	15000	2500	90(4)
F(2)	9406(16)	16316(10)	2470(11)	178(5)
F(2A)	10496(18)	15747(13)	3091(9)	211(7)

Table 4.4: Selected bond lengths [\AA] and angles [$^\circ$].

Fe(1)-N(3)	2.114(3)	N(3)#1-Fe(1)-N(1)#2	73.70(6)
Fe(1)-N(3)#1	2.114(3)	N(1)#1-Fe(1)-N(1)#2	147.39(12)
Fe(1)-N(1)#1	2.174(3)	N(3)-Fe(1)-N(1)	73.70(6)
Fe(1)-N(1)#2	2.174(3)	N(3)#1-Fe(1)-N(1)	106.30(6)
Fe(1)-N(1)	2.174(3)	N(1)#1-Fe(1)-N(1)	94.52(3)
Fe(1)-N(1)#3	2.174(3)	N(1)#2-Fe(1)-N(1)	94.52(3)
		N(3)-Fe(1)-N(1)#3	73.70(6)
N(3)-Fe(1)-N(3)#1	180.000(1)	N(3)#1-Fe(1)-N(1)#3	106.30(6)
N(3)-Fe(1)-N(1)#1	106.30(6)	N(1)#1-Fe(1)-N(1)#3	94.52(3)
N(3)#1-Fe(1)-N(1)#1	73.70(6)	N(1)#2-Fe(1)-N(1)#3	94.52(3)
N(3)-Fe(1)-N(1)#2	106.30(6)	N(1)-Fe(1)-N(1)#3	147.39(12)

Symmetry transformations used to generate equivalent atoms:

- #1 $y, -x+2, -z+1$ #2 $-y+2, x, -z+1$ #3 $-x+2, -y+2, z$
 #4 $-x+1, -y+2, z$ #5 $y-1/2, -x+3/2, -z+1/2$ #6 $-y+3/2, x+1/2, -z+1/2$
 #7 $-y+5/2, x+1/2, -z+1/2$ #8 $y-1/2, -x+5/2, -z+1/2$
 #9 $-x+2, -y+3, z$

240 K in a mixed spin state

Table 4.5: Atomic coordinates ($\times 10^4$) and equivalent isotropic displacement parameters ($\text{\AA}^2 \times 10^3$).

U(eq) is defined as one third of the trace of the orthogonalized U^{ij} tensor.

	x	y	z	U(eq)
Fe(1)	10000	10000	5000	23(1)
N(1)	8708(3)	8200(3)	5281(2)	35(1)
N(2)	8480(3)	8044(3)	6048(2)	34(1)
C(1)	7911(6)	6876(6)	4119(3)	60(1)
C(2)	7975(3)	7095(3)	4967(4)	46(1)
C(3)	7284(4)	6250(4)	5524(3)	54(1)
C(4)	7640(4)	6872(4)	6214(3)	50(1)
N(3)	10000	10000	6137(2)	28(1)
N(4)	10000	10000	7691(2)	38(1)
C(5)	9221(3)	9026(3)	6527(2)	29(1)
C(6)	9197(4)	9035(4)	7307(2)	34(1)

B(1)	0	5000	7500	37(2)
F(1)	682(3)	6040(3)	7047(2)	55(1)
B(2)	5000	10000	7500	45(3)
F(2)	5817(3)	9058(4)	7066(2)	96(1)

Table 4.6: Selected bond lengths [\AA] and angles [$^\circ$].

Fe(1)-N(3)	2.011(3)	N(3)#1-Fe(1)-N(1)	103.76(7)
Fe(1)-N(3)#1	2.011(3)	N(1)#2-Fe(1)-N(1)	152.48(15)
Fe(1)-N(1)#2	2.088(3)	N(3)-Fe(1)-N(1)#3	103.76(7)
Fe(1)-N(1)	2.088(3)	N(3)#1-Fe(1)-N(1)#3	76.24(7)
Fe(1)-N(1)#3	2.088(3)	N(1)#2-Fe(1)-N(1)#3	93.24(3)
Fe(1)-N(1)#1	2.088(3)	N(1)-Fe(1)-N(1)#3	93.24(3)
		N(3)-Fe(1)-N(1)#1	103.76(7)
N(3)-Fe(1)-N(3)#1	180.0	N(3)#1-Fe(1)-N(1)#1	76.24(7)
N(3)-Fe(1)-N(1)#2	76.24(7)	N(1)#2-Fe(1)-N(1)#1	93.24(3)
N(3)#1-Fe(1)-N(1)#2	103.76(7)	N(1)-Fe(1)-N(1)#1	93.24(3)
N(3)-Fe(1)-N(1)	76.24(7)	N(1)#3-Fe(1)-N(1)#1	152.48(15)

Symmetry transformations used to generate equivalent atoms:

#1 $y, -x+2, -z+1$ #2 $-x+2, -y+2, z$ #3 $-y+2, x, -z+1$

#4 $-x, -y+1, z$ #5 $y-1/2, -x+1/2, -z+3/2$ #6 $-y+1/2, x+1/2, -z+3/2$

#7 $-y+3/2, x+1/2, -z+3/2$ #8 $y-1/2, -x+3/2, -z+3/2$

#9 $-x+1, -y+2, z$

30 K in the low spin state

Table 4.7: Atomic coordinates ($\times 10^4$) and equivalent isotropic displacement parameters ($\text{\AA}^2 \times 10^3$).

$U(\text{eq})$ is defined as one third of the trace of the orthogonalized U^{ij} tensor.

	x	y	z	U(eq)
Fe(1)	0	0	5000	8(1)
N(1)	1261(3)	1787(3)	4786(1)	11(1)
N(2)	1495(3)	1993(3)	4015(1)	10(1)
C(1)	1996(4)	3100(4)	5974(2)	16(1)
C(2)	1957(3)	2927(3)	5128(2)	11(1)

C(3)	2624(3)	3842(3)	4568(2)	12(1)
C(4)	2313(4)	3228(4)	3876(2)	12(1)
N(3)	0	0	3918(2)	9(1)
N(4)	0	0	2349(2)	11(1)
C(5)	783(3)	999(3)	3527(2)	10(1)
C(6)	818(3)	990(4)	2733(2)	10(1)
B(1)	10000	5000	2500	10(2)
F(1)	9313(2)	3932(2)	2958(1)	14(1)
B(2)	5000	0	2500	12(2)
F(2)	4170(2)	974(2)	2957(1)	16(1)

Table 4.8: Selected bond lengths [\AA] and angles [$^\circ$].

Fe(1)-N(3)#1	1.898(3)	N(3)-Fe(1)-N(1)#2	79.25(7)
Fe(1)-N(3)	1.898(3)	N(1)-Fe(1)-N(1)#2	158.49(14)
Fe(1)-N(1)	2.010(3)	N(3)#1-Fe(1)-N(1)#1	79.25(7)
Fe(1)-N(1)#2	2.010(3)	N(3)-Fe(1)-N(1)#1	100.75(7)
Fe(1)-N(1)#1	2.010(3)	N(1)-Fe(1)-N(1)#1	92.00(3)
Fe(1)-N(1)#3	2.010(3)	N(1)#2-Fe(1)-N(1)#1	92.00(3)
		N(3)#1-Fe(1)-N(1)#3	79.25(7)
N(3)#1-Fe(1)-N(3)	180.0	N(3)-Fe(1)-N(1)#3	100.75(7)
N(3)#1-Fe(1)-N(1)	100.75(7)	N(1)-Fe(1)-N(1)#3	92.00(3)
N(3)-Fe(1)-N(1)	79.25(7)	N(1)#2-Fe(1)-N(1)#3	92.00(3)
N(3)#1-Fe(1)-N(1)#2	100.75(7)	N(1)#1-Fe(1)-N(1)#3	158.49(14)

Symmetry transformations used to generate equivalent atoms:

#1 $y, -x, -z+1$ #2 $-x, -y, z$ #3 $-y, x, -z+1$ #4 $-x+2, -y+1, z$

#5 $y+1/2, -x+3/2, -z+1/2$ #6 $-y+3/2, x-1/2, -z+1/2$

#7 $-y+1/2, x-1/2, -z+1/2$ #8 $-x+1, -y, z$ #9 $y+1/2, -x+1/2, -z+1/2$

A.5. $[\text{FeL}_2](\text{ClO}_4)_2$

290 K in the high spin state

Table 5.1: Atomic coordinates ($\times 10^4$) and equivalent isotropic displacement parameters ($\text{\AA}^2 \times 10^3$). $U(\text{eq})$ is defined as one third of the trace of the orthogonalized U^{ij} tensor.

	x	y	z	U(eq)
Fe(1)	0	5000	2500	33(1)
N(1)	1687(4)	6457(4)	2135(1)	41(1)
N(2)	1813(3)	6602(4)	1367(1)	40(1)
N(3)	0	5000	1290(1)	34(1)
N(4)	0	5000	-273(1)	51(1)
C(1)	2856(6)	7448(6)	3263(2)	78(2)
C(2)	2673(3)	7310(3)	2426(2)	50(1)
C(3)	3412(5)	8000(5)	1839(2)	61(1)
C(4)	2837(5)	7547(5)	1182(2)	55(1)
C(5)	908(5)	5801(5)	899(1)	36(1)
C(6)	898(5)	5817(6)	117(1)	48(1)
Cl(1)	5000	5000	0	50(1)
O(1)	3933(5)	4351(4)	454(3)	78(1)
Cl(2)	0	0	0	72(1)
O(2)	581(14)	1331(11)	176(8)	146(5)
O(2A)	-20(20)	720(20)	678(11)	192(10)

Table 5.2: Selected bond lengths [\AA] and angles [$^\circ$].

Fe(1)-N(3)	2.135(2)	N(3)-Fe(1)-N(1)#2	72.95(5)
Fe(1)-N(3)#1	2.135(2)	N(3)#1-Fe(1)-N(1)#2	107.05(5)
Fe(1)-N(1)#2	2.196(2)	N(3)-Fe(1)-N(1)	72.95(5)
Fe(1)-N(1)	2.196(2)	N(3)#1-Fe(1)-N(1)	107.05(5)
Fe(1)-N(1)#1	2.196(2)	N(1)#2-Fe(1)-N(1)	145.90(11)
Fe(1)-N(1)#3	2.196(2)	N(3)-Fe(1)-N(1)#1	107.05(5)
		N(3)#1-Fe(1)-N(1)#1	72.95(5)
N(3)-Fe(1)-N(3)#1	180.0	N(1)#2-Fe(1)-N(1)#1	94.93(3)

N(1)-Fe(1)-N(1)#1	94.93(3)	N(1)#2-Fe(1)-N(1)#3	94.93(3)
N(3)-Fe(1)-N(1)#3	107.05(5)	N(1)-Fe(1)-N(1)#3	94.93(3)
N(3)#1-Fe(1)-N(1)#3	72.95(5)	N(1)#1-Fe(1)-N(1)#3	145.90(11)

Symmetry transformations used to generate equivalent atoms:

#1 $y-1/2, -x+1/2, -z+1/2$ #2 $-x, -y+1, z$ #3 $-y+1/2, x+1/2, -z+1/2$

#4 $-x+1, -y+1, z$ #5 $-y+1, x, -z$ #6 $y, -x+1, -z$

#7 $-y, x, -z$ #8 $y, -x, -z$ #9 $-x, -y, z$

210 K in a mixed spin state

Table 5.3: Atomic coordinates ($\times 10^4$) and equivalent isotropic displacement parameters ($\text{\AA}^2 \times 10^3$).

$U(\text{eq})$ is defined as one third of the trace of the orthogonalized U^{ij} tensor.

	x	y	z	U(eq)
Fe(1)	0	5000	2500	25(1)
N(1)	1724(3)	6429(3)	2142(1)	31(1)
N(2)	1842(3)	6593(3)	1368(1)	30(1)
N(3)	0	5000	1292(1)	26(1)
N(4)	0	5000	-275(1)	40(1)
C(1)	2923(6)	7383(6)	3270(2)	62(2)
C(2)	2732(3)	7265(3)	2432(2)	40(1)
C(3)	3491(4)	7956(4)	1843(2)	48(1)
C(4)	2898(4)	7523(4)	1185(2)	42(1)
C(5)	922(4)	5795(4)	900(1)	28(1)
C(6)	921(5)	5796(5)	118(2)	37(1)
Cl(1)	5000	5000	0	35(1)
O(1)	3925(4)	4342(4)	469(2)	51(1)
Cl(2)	0	10000	10000	60(1)
O(2)	1378(11)	9472(13)	9844(8)	111(6)
O(2A)	712(18)	10380(30)	9363(13)	238(17)

Table 5.4: Selected bond lengths [\AA] and angles [$^\circ$].

Fe(1)-N(3)#1	2.132(2)	Fe(1)-N(1)#2	2.194(3)
Fe(1)-N(3)	2.132(2)	Fe(1)-N(1)	2.194(3)

Fe(1)-N(1)#3	2.194(3)	N(3)#1-Fe(1)-N(1)#3	73.25(6)
Fe(1)-N(1)#1	2.194(3)	N(3)-Fe(1)-N(1)#3	106.75(6)
		N(1)#2-Fe(1)-N(1)#3	94.77(3)
N(3)#1-Fe(1)-N(3)	180.0	N(1)-Fe(1)-N(1)#3	94.77(3)
N(3)#1-Fe(1)-N(1)#2	106.75(6)	N(3)#1-Fe(1)-N(1)#1	73.25(6)
N(3)-Fe(1)-N(1)#2	73.25(6)	N(3)-Fe(1)-N(1)#1	106.75(6)
N(3)#1-Fe(1)-N(1)	106.75(6)	N(1)#2-Fe(1)-N(1)#1	94.77(3)
N(3)-Fe(1)-N(1)	73.25(6)	N(1)-Fe(1)-N(1)#1	94.77(3)
N(1)#2-Fe(1)-N(1)	146.49(12)	N(1)#3-Fe(1)-N(1)#1	146.49(12)

Symmetry transformations used to generate equivalent atoms:

#1 $y-1/2, -x+1/2, -z+1/2$ #2 $-x, -y+1, z$ #3 $-y+1/2, x+1/2, -z+1/2$

#4 $-x+1, -y+1, z$ #5 $-y+1, x, -z$ #6 $y, -x+1, -z$

#7 $-x, -y+2, z$ #8 $y-1, -x+1, -z+2$ #9 $-y+1, x+1, -z+2$

180 K in a mixed spin state

Table 5.5: Atomic coordinates ($\times 10^4$) and equivalent isotropic displacement parameters ($\text{\AA}^2 \times 10^3$).

$U(\text{eq})$ is defined as one third of the trace of the orthogonalized U^{ij} tensor.

	x	y	z	$U(\text{eq})$
Fe(1)	0	10000	5000	18(1)
N(1)	1774(3)	8697(3)	5262(1)	27(1)
N(2)	1938(3)	8484(3)	6028(1)	28(1)
C(1)	3047(5)	7923(5)	4102(2)	49(1)
C(2)	2865(3)	7966(3)	4944(3)	35(1)
C(3)	3717(4)	7288(4)	5507(2)	42(1)
C(4)	3117(4)	7632(4)	6178(2)	36(1)
N(3)	0	10000	6116(1)	23(1)
N(4)	0	10000	7666(1)	29(1)
C(5)	973(3)	9221(3)	6500(2)	23(1)
C(6)	959(4)	9195(4)	7283(2)	29(1)
Cl(1)	5000	10000	7500	26(1)
O(1)	4298(3)	8910(4)	7966(2)	39(1)
Cl(2)	10000	5000	7500	32(1)
O(2)	10982(4)	5805(3)	7041(2)	58(1)

Table 5.6: Selected bond lengths [\AA] and angles [$^\circ$].

Fe(1)-N(3)#1	1.983(2)	N(3)-Fe(1)-N(1)#2	102.95(6)
Fe(1)-N(3)	1.983(2)	N(1)#1-Fe(1)-N(1)#2	154.09(13)
Fe(1)-N(1)#1	2.078(3)	N(3)#1-Fe(1)-N(1)	102.95(6)
Fe(1)-N(1)#2	2.078(3)	N(3)-Fe(1)-N(1)	77.05(6)
Fe(1)-N(1)	2.078(3)	N(1)#1-Fe(1)-N(1)	92.88(3)
Fe(1)-N(1)#3	2.078(3)	N(1)#2-Fe(1)-N(1)	92.88(3)
		N(3)#1-Fe(1)-N(1)#3	102.95(6)
N(3)#1-Fe(1)-N(3)	180.0	N(3)-Fe(1)-N(1)#3	77.05(6)
N(3)#1-Fe(1)-N(1)#1	77.05(6)	N(1)#1-Fe(1)-N(1)#3	92.88(3)
N(3)-Fe(1)-N(1)#1	102.95(6)	N(1)#2-Fe(1)-N(1)#3	92.88(3)
N(3)#1-Fe(1)-N(1)#2	77.05(6)	N(1)-Fe(1)-N(1)#3	154.09(13)

Symmetry transformations used to generate equivalent atoms:

#1 $y-1, -x+1, -z+1$ #2 $-y+1, x+1, -z+1$ #3 $-x, -y+2, z$

#4 $-y+3/2, x+1/2, -z+3/2$ #5 $y-1/2, -x+3/2, -z+3/2$

#6 $-x+1, -y+2, z$ #7 $-x+2, -y+1, z$ #8 $-y+3/2, x-1/2, -z+3/2$

#9 $y+1/2, -x+3/2, -z+3/2$

30 K in the low spin state

Table 5.7: Atomic coordinates ($\times 10^4$) and equivalent isotropic displacement parameters ($\text{\AA}^2 \times 10^3$).

$U(\text{eq})$ is defined as one third of the trace of the orthogonalized U^{ij} tensor.

	x	y	z	$U(\text{eq})$
Fe(1)	0	0	5000	10(1)
N(1)	1282(3)	1761(3)	4782(1)	12(1)
N(2)	1511(3)	1947(3)	4011(1)	14(1)
C(1)	2025(4)	3052(4)	5953(2)	16(1)
C(2)	1989(3)	2864(3)	5108(2)	16(1)
C(3)	2662(3)	3765(4)	4554(2)	16(1)
C(4)	2350(4)	3158(4)	3864(2)	15(1)
N(3)	0	0	3918(1)	12(1)
N(4)	0	0	2356(1)	14(1)
C(5)	778(3)	986(3)	3527(2)	13(1)

C(6)	808(4)	965(4)	2739(2)	15(1)
Cl(1)	10000	5000	2500	11(1)
O(1)	9303(3)	3898(3)	2972(1)	16(1)
Cl(2)	5000	0	2500	14(1)
O(2)	4178(3)	1006(3)	2970(1)	19(1)

Table 5.8: Selected bond lengths [\AA] and angles [$^\circ$].

Fe(1)-N(3)#1	1.913(2)	N(3)-Fe(1)-N(1)	79.03(6)
Fe(1)-N(3)	1.913(2)	N(1)#2-Fe(1)-N(1)	158.05(13)
Fe(1)-N(1)#2	2.026(3)	N(3)#1-Fe(1)-N(1)#1	79.03(6)
Fe(1)-N(1)	2.026(3)	N(3)-Fe(1)-N(1)#1	100.97(6)
Fe(1)-N(1)#1	2.026(3)	N(1)#2-Fe(1)-N(1)#1	92.08(2)
Fe(1)-N(1)#3	2.026(3)	N(1)-Fe(1)-N(1)#1	92.08(2)
		N(3)#1-Fe(1)-N(1)#3	79.03(6)
N(3)#1-Fe(1)-N(3)	180.0	N(3)-Fe(1)-N(1)#3	100.97(6)
N(3)#1-Fe(1)-N(1)#2	100.97(6)	N(1)#2-Fe(1)-N(1)#3	92.08(2)
N(3)-Fe(1)-N(1)#2	79.03(6)	N(1)-Fe(1)-N(1)#3	92.08(2)
N(3)#1-Fe(1)-N(1)	100.97(6)	N(1)#1-Fe(1)-N(1)#3	158.05(13)

Symmetry transformations used to generate equivalent atoms:

#1 $y, -x, -z+1$ #2 $-x, -y, z$ #3 $-y, x, -z+1$ #4 $-x+2, -y+1, z$

#5 $y+1/2, -x+3/2, -z+1/2$ #6 $-y+3/2, x-1/2, -z+1/2$

#7 $-y+1/2, x-1/2, -z+1/2$ #8 $-x+1, -y, z$ #9 $y+1/2, -x+1/2, -z+1/2$

A.6. $[\text{FeL}_3\text{O}_2](\text{BF}_4)_2$

300 K in the low spin state

Table 6.1: Atomic coordinates ($\times 10^4$) and equivalent isotropic displacement parameters ($\text{\AA}^2 \times 10^3$). U(eq) is defined as one third of the trace of the orthogonalized U^{ij} tensor.

	x	y	z	U(eq)
Fe(1)	6000(1)	1779(1)	1069(1)	41(1)
N(1)	7674(5)	1133(4)	1367(3)	49(1)
N(2)	8021(4)	1137(4)	2049(3)	46(1)
C(1)	8562(6)	756(6)	1128(4)	58(2)
C(2)	9462(6)	522(7)	1644(5)	68(2)
C(3)	9117(5)	779(6)	2201(4)	58(2)
N(3)	6292(5)	1817(4)	2110(3)	41(1)
C(4)	7300(5)	1543(5)	2455(3)	42(1)
C(5)	7560(6)	1659(5)	3130(3)	48(1)
C(6)	6762(6)	2088(5)	3463(3)	47(1)
C(7)	7020(7)	2300(8)	4220(3)	65(2)
O(1)	7954(13)	2851(17)	4410(8)	87(4)
O(1A)	8164(12)	2101(18)	4509(7)	84(4)
C(8)	5720(6)	2364(5)	3127(3)	50(2)
C(9)	5521(5)	2226(5)	2447(3)	40(1)
N(4)	4514(4)	2513(4)	2025(2)	43(1)
N(5)	4492(4)	2446(4)	1353(3)	47(1)
C(10)	3532(6)	2870(7)	2161(4)	61(2)
C(11)	2839(6)	3019(7)	1594(5)	67(2)
C(12)	3479(6)	2771(6)	1088(4)	55(2)
N(10)	6592(5)	3362(4)	777(3)	49(1)
N(9)	6456(4)	3526(4)	109(3)	45(1)
C(13)	4967(6)	-756(5)	1013(4)	58(2)
C(14)	4576(8)	-1512(6)	518(5)	66(2)
C(15)	4658(6)	-994(5)	-75(4)	57(2)
N(8)	5740(5)	1772(4)	18(3)	38(1)
C(16)	5362(5)	869(5)	-324(3)	42(1)
C(17)	5289(5)	799(5)	-1007(3)	47(1)

C(18)	5617(6)	1694(5)	-1341(4)	50(2)
C(19)	5608(8)	1642(7)	-2083(4)	68(2)
O(2)	6040(20)	761(13)	-2283(7)	74(4)
O(2A)	5291(14)	543(12)	-2379(6)	91(4)
C(20)	5982(6)	2651(5)	-998(3)	49(1)
C(21)	6062(5)	2637(5)	-303(3)	41(1)
N(7)	5087(4)	25(4)	94(2)	44(1)
N(6)	5263(5)	179(4)	758(3)	48(1)
C(22)	6730(7)	4564(6)	-28(4)	67(2)
C(23)	7096(7)	5102(6)	559(5)	69(2)
C(24)	6958(6)	4332(5)	1037(4)	62(2)
B(1)	3847(9)	4236(7)	4148(5)	63(2)
F(1)	3249(10)	4063(9)	3543(5)	157(3)
F(2)	3052(8)	4670(9)	4467(4)	146(3)
F(3)	4456(10)	3473(8)	4441(6)	172(5)
F(4)	4512(7)	5060(10)	3984(8)	205(7)
B(2)	2604(9)	191(8)	2996(6)	67(2)
F(5)	1730(9)	768(10)	2672(6)	183(5)
F(6)	2530(11)	-227(9)	3626(5)	177(5)
F(7)	2893(10)	-693(8)	2662(4)	153(4)
F(8)	3414(9)	915(8)	3194(7)	184(6)

Table 6.2: Selected bond lengths [\AA] and angles [$^\circ$].

Fe(1)-N(3)	2.101(6)	N(8)-Fe(1)-N(1)	105.0(2)
Fe(1)-N(8)	2.119(6)	N(5)-Fe(1)-N(1)	148.5(2)
Fe(1)-N(5)	2.163(6)	N(3)-Fe(1)-N(10)	104.6(2)
Fe(1)-N(1)	2.165(6)	N(8)-Fe(1)-N(10)	74.02(19)
Fe(1)-N(10)	2.167(5)	N(5)-Fe(1)-N(10)	94.4(2)
Fe(1)-N(6)	2.185(5)	N(1)-Fe(1)-N(10)	93.5(2)
		N(3)-Fe(1)-N(6)	107.8(2)
N(3)-Fe(1)-N(8)	178.5(2)	N(8)-Fe(1)-N(6)	73.54(19)
N(3)-Fe(1)-N(5)	74.2(2)	N(5)-Fe(1)-N(6)	95.0(2)
N(8)-Fe(1)-N(5)	106.5(2)	N(1)-Fe(1)-N(6)	94.5(2)
N(3)-Fe(1)-N(1)	74.3(2)	N(10)-Fe(1)-N(6)	147.6(2)

Symmetry transformations used to generate equivalent atoms:

30 K in the low spin state

Table 6.3: Atomic coordinates ($\times 10^4$) and equivalent isotropic displacement parameters ($\text{\AA}^2 \times 10^3$). $U(\text{eq})$ is defined as one third of the trace of the orthogonalized U^{ij} tensor.

	x	y	z	U(eq)
Fe(1)	5996(1)	1735(1)	1070(1)	7(1)
N(1)	7569(2)	1118(2)	1285(2)	11(1)
N(2)	7978(2)	1111(2)	1974(2)	11(1)
C(1)	8439(3)	764(3)	998(2)	14(1)
C(2)	9391(3)	528(3)	1484(2)	17(1)
C(3)	9088(3)	746(3)	2103(2)	15(1)
N(3)	6223(3)	1775(2)	2038(2)	10(1)
C(4)	7239(3)	1509(3)	2400(2)	10(1)
C(5)	7515(3)	1665(3)	3092(2)	10(1)
C(6)	6655(3)	2117(3)	3425(2)	11(1)
C(7)	6928(3)	2348(3)	4172(2)	14(1)
O(1)	8028(2)	2867(2)	4352(1)	15(1)
C(8)	5589(3)	2378(3)	3051(2)	12(1)
C(9)	5420(3)	2188(3)	2360(2)	12(1)
N(4)	4438(2)	2468(2)	1892(2)	12(1)
N(5)	4518(2)	2374(2)	1218(2)	11(1)
C(10)	3398(3)	2863(3)	1979(2)	12(1)
C(11)	2795(3)	3035(3)	1339(2)	13(1)
C(12)	3528(3)	2733(3)	885(2)	15(1)
N(10)	6592(3)	3250(2)	927(2)	11(1)
N(9)	6476(3)	3535(2)	256(2)	12(1)
C(13)	4972(3)	-684(3)	1134(2)	13(1)
C(14)	4574(3)	-1500(3)	637(2)	14(1)
C(15)	4684(3)	-1029(3)	25(2)	14(1)
N(8)	5803(3)	1773(2)	103(2)	10(1)
C(16)	5415(3)	868(3)	-265(2)	9(1)
C(17)	5336(3)	817(3)	-962(2)	12(1)
C(18)	5667(3)	1780(3)	-1286(2)	11(1)
C(19)	5637(3)	1769(3)	-2048(2)	13(1)
O(2)	6050(2)	740(2)	-2275(1)	15(1)

C(20)	6043(3)	2733(3)	-915(2)	11(1)
C(21)	6096(3)	2684(3)	-219(2)	11(1)
N(7)	5133(2)	16(2)	158(2)	11(1)
N(6)	5313(3)	230(2)	845(2)	11(1)
C(22)	6789(3)	4616(3)	177(2)	14(1)
C(23)	7117(3)	5043(3)	813(2)	14(1)
C(24)	6982(3)	4166(3)	1267(2)	13(1)
B(1)	3830(3)	4345(3)	4062(2)	10(1)
F(1)	3278(2)	3994(2)	3407(1)	18(1)
F(2)	3022(2)	4849(2)	4395(1)	19(1)
F(3)	4305(2)	3413(2)	4422(1)	20(1)
F(4)	4675(2)	5108(2)	3972(1)	23(1)
B(2)	2692(3)	225(3)	3098(2)	9(1)
F(5)	1667(2)	558(2)	2710(1)	21(1)
F(6)	2517(2)	-66(2)	3760(1)	20(1)
F(7)	3121(2)	-718(2)	2808(1)	20(1)
F(8)	3477(2)	1091(2)	3155(1)	26(1)

Table 6.4: Selected bond lengths [Å] and angles [°].

Fe(1)-N(8)	1.909(3)	N(3)-Fe(1)-N(5)	79.43(13)
Fe(1)-N(3)	1.912(3)	N(10)-Fe(1)-N(5)	91.10(12)
Fe(1)-N(10)	1.980(3)	N(8)-Fe(1)-N(1)	100.15(13)
Fe(1)-N(5)	1.986(3)	N(3)-Fe(1)-N(1)	79.79(13)
Fe(1)-N(1)	1.991(3)	N(10)-Fe(1)-N(1)	91.27(12)
Fe(1)-N(6)	1.992(3)	N(5)-Fe(1)-N(1)	159.22(12)
		N(8)-Fe(1)-N(6)	79.47(12)
N(8)-Fe(1)-N(3)	176.99(12)	N(3)-Fe(1)-N(6)	103.54(12)
N(8)-Fe(1)-N(10)	79.48(12)	N(10)-Fe(1)-N(6)	158.95(12)
N(3)-Fe(1)-N(10)	97.50(12)	N(5)-Fe(1)-N(6)	92.41(12)
N(8)-Fe(1)-N(5)	100.58(13)	N(1)-Fe(1)-N(6)	92.75(12)

Symmetry transformations used to generate equivalent atoms:

30 K after irradiation in the high spin state

Table 6.5: Atomic coordinates ($\times 10^4$) and equivalent isotropic displacement parameters ($\text{\AA}^2 \times 10^3$).
 $U(\text{eq})$ is defined as one third of the trace of the orthogonalized U^{ij} tensor.

	x	y	z	U(eq)
Fe(1)	6019(1)	1762(1)	1070(1)	8(1)
N(1)	7718(2)	1129(2)	1410(1)	11(1)
N(2)	8027(2)	1140(2)	2098(1)	10(1)
C(1)	8627(2)	738(2)	1166(2)	11(1)
C(2)	9514(3)	506(2)	1693(2)	13(1)
C(3)	9105(2)	766(2)	2275(2)	12(1)
N(3)	6254(2)	1839(2)	2139(1)	8(1)
C(4)	7244(2)	1572(2)	2503(2)	10(1)
C(5)	7492(2)	1710(2)	3189(2)	10(1)
C(6)	6635(2)	2154(2)	3522(2)	10(1)
C(7)	6876(2)	2361(2)	4279(2)	11(1)
O(1)	7980(2)	2806(2)	4478(1)	13(1)
C(8)	5594(2)	2435(2)	3155(2)	11(1)
C(9)	5453(2)	2260(2)	2464(2)	10(1)
N(4)	4457(2)	2538(2)	2022(1)	10(1)
N(5)	4485(2)	2497(2)	1341(1)	10(1)
C(10)	3432(2)	2889(2)	2157(2)	12(1)
C(11)	2775(2)	3092(2)	1549(2)	11(1)
C(12)	3465(2)	2838(2)	1057(2)	11(1)
N(10)	6645(2)	3390(2)	801(1)	10(1)
N(9)	6452(2)	3603(2)	120(1)	10(1)
C(13)	4891(2)	-764(2)	970(2)	11(1)
C(14)	4465(3)	-1502(3)	444(2)	14(1)
C(15)	4592(2)	-952(2)	-144(2)	11(1)
N(8)	5759(2)	1830(2)	1(1)	9(1)
C(16)	5386(2)	936(2)	-368(2)	10(1)
C(17)	5311(2)	887(2)	-1065(2)	10(1)
C(18)	5654(3)	1832(2)	-1394(2)	11(1)
C(19)	5634(3)	1812(2)	-2151(2)	10(1)
O(2)	5995(2)	764(2)	-2384(1)	14(1)
C(20)	6022(2)	2784(2)	-1019(2)	10(1)

C(21)	6066(2)	2725(2)	-325(2)	10(1)
N(7)	5074(2)	54(2)	37(1)	10(1)
N(6)	5263(2)	173(2)	724(1)	10(1)
C(22)	6684(2)	4689(2)	-15(2)	12(1)
C(23)	7042(2)	5194(2)	597(2)	13(1)
C(24)	7003(2)	4356(2)	1085(2)	12(1)
B(1)	3686(3)	4388(2)	4121(2)	8(1)
F(1)	3050(2)	4085(2)	3488(1)	16(1)
F(2)	2978(2)	4845(2)	4535(1)	17(1)
F(3)	4208(2)	3428(2)	4415(1)	17(1)
F(4)	4507(2)	5149(2)	3989(1)	18(1)
B(2)	2735(3)	98(3)	3034(2)	7(1)
F(5)	1722(2)	523(2)	2697(1)	18(1)
F(6)	2549(2)	-319(2)	3672(1)	17(1)
F(7)	3119(2)	-770(2)	2663(1)	17(1)
F(8)	3539(2)	941(2)	3145(1)	18(1)

Table 6.6: Selected bond lengths [\AA] and angles [$^\circ$].

Fe(1)-N(8)	2.117(3)	N(3)-Fe(1)-N(6)	110.26(10)
Fe(1)-N(3)	2.119(3)	N(5)-Fe(1)-N(6)	96.14(9)
Fe(1)-N(5)	2.178(2)	N(8)-Fe(1)-N(1)	108.71(10)
Fe(1)-N(6)	2.179(2)	N(3)-Fe(1)-N(1)	73.81(10)
Fe(1)-N(1)	2.184(3)	N(5)-Fe(1)-N(1)	147.58(10)
Fe(1)-N(10)	2.189(3)	N(6)-Fe(1)-N(1)	96.87(9)
		N(8)-Fe(1)-N(10)	73.84(9)
N(8)-Fe(1)-N(3)	175.17(8)	N(3)-Fe(1)-N(10)	102.11(9)
N(8)-Fe(1)-N(5)	103.40(10)	N(5)-Fe(1)-N(10)	91.79(9)
N(3)-Fe(1)-N(5)	73.84(10)	N(6)-Fe(1)-N(10)	147.62(10)
N(8)-Fe(1)-N(6)	73.78(10)	N(1)-Fe(1)-N(10)	92.90(9)

Symmetry transformations used to generate equivalent atoms:

A.7. $[\text{FeL}_3_2](\text{ClO}_4)_2$

340 K in the high spin state

Table 7.1: Atomic coordinates ($\times 10^4$) and equivalent isotropic displacement parameters ($\text{\AA}^2 \times 10^3$). U(eq) is defined as one third of the trace of the orthogonalized U^{ij} tensor.

	x	y	z	U(eq)
Fe(1)	6001(1)	1801(1)	1068(1)	47(1)
N(1)	7671(5)	1183(5)	1384(3)	51(1)
N(2)	8003(5)	1178(5)	2054(3)	48(1)
C(1)	8538(8)	805(8)	1146(5)	64(2)
C(2)	9431(7)	605(8)	1641(6)	72(3)
C(3)	9064(6)	848(8)	2220(5)	61(2)
N(3)	6300(5)	1875(5)	2116(3)	43(2)
C(4)	7278(5)	1593(5)	2457(4)	42(2)
C(5)	7544(7)	1739(6)	3129(4)	52(2)
C(6)	6748(7)	2161(7)	3458(4)	53(2)
C(7)	7002(9)	2376(9)	4205(4)	75(3)
O(1)	7920(20)	2810(20)	4415(10)	102(7)
O(1A)	8070(20)	2160(20)	4486(9)	98(7)
C(8)	5720(7)	2419(7)	3125(4)	52(2)
C(9)	5519(6)	2273(6)	2434(4)	45(2)
N(4)	4534(5)	2545(5)	2016(3)	51(1)
N(5)	4485(5)	2460(5)	1352(3)	51(1)
C(10)	3567(7)	2912(8)	2146(5)	62(2)
C(11)	2877(8)	3043(9)	1571(6)	77(3)
C(12)	3502(7)	2772(7)	1104(5)	63(2)
N(6)	5297(5)	209(6)	778(3)	54(2)
N(7)	5110(5)	28(5)	113(3)	44(1)
C(13)	4980(8)	-728(7)	1039(5)	66(2)
C(14)	4611(9)	-1461(8)	540(6)	76(3)
C(15)	4698(7)	-999(7)	-41(4)	60(2)
N(8)	5779(5)	1760(5)	41(4)	41(2)
C(16)	5394(6)	864(5)	-303(3)	43(1)
C(17)	5337(6)	748(6)	-977(4)	49(2)

C(18)	5643(7)	1649(7)	-1320(4)	52(2)
C(19)	5609(9)	1600(8)	-2055(5)	70(2)
O(2A)	5660(17)	553(9)	-2304(5)	167(6)
C(20)	6021(7)	2601(7)	-976(4)	53(2)
C(21)	6072(6)	2616(6)	-316(4)	47(2)
N(9)	6471(5)	3496(5)	102(3)	49(1)
N(10)	6569(6)	3362(6)	762(3)	57(2)
C(22)	6761(8)	4525(7)	-50(5)	70(3)
C(23)	7093(9)	5069(8)	508(6)	78(3)
C(24)	6962(8)	4314(8)	1032(5)	73(3)
Cl(1)	3837(2)	4310(2)	4176(1)	74(1)
O(3)	3327(15)	4115(13)	3530(6)	177(6)
O(4)	3040(12)	4715(11)	4489(6)	145(4)
O(5)	4479(14)	3524(12)	4534(9)	175(6)
O(6)	4540(10)	5120(14)	3987(10)	211(9)
Cl(2)	2596(2)	245(2)	2963(1)	77(1)
O(7)	1734(12)	762(16)	2615(10)	217(9)
O(8)	2330(30)	-165(14)	3546(12)	293(17)
O(9)	2903(16)	-675(11)	2642(8)	191(7)
O(10)	3414(14)	1017(13)	3174(12)	257(13)

Table 7.2: Selected bond lengths [\AA] and angles [$^\circ$].

Fe(1)-N(8)	2.087(7)	N(3)-Fe(1)-N(6)	108.1(3)
Fe(1)-N(3)	2.127(7)	N(10)-Fe(1)-N(6)	147.5(3)
Fe(1)-N(10)	2.161(7)	N(8)-Fe(1)-N(1)	104.6(2)
Fe(1)-N(6)	2.171(7)	N(3)-Fe(1)-N(1)	73.6(2)
Fe(1)-N(1)	2.179(6)	N(10)-Fe(1)-N(1)	93.4(3)
Fe(1)-N(5)	2.194(7)	N(6)-Fe(1)-N(1)	94.8(3)
		N(8)-Fe(1)-N(5)	107.8(2)
N(8)-Fe(1)-N(3)	177.4(3)	N(3)-Fe(1)-N(5)	74.0(2)
N(8)-Fe(1)-N(10)	73.7(2)	N(10)-Fe(1)-N(5)	94.8(3)
N(3)-Fe(1)-N(10)	104.4(2)	N(6)-Fe(1)-N(5)	94.9(3)
N(8)-Fe(1)-N(6)	73.8(2)	N(1)-Fe(1)-N(5)	147.7(2)

Symmetry transformations used to generate equivalent atoms:

30 K in the low spin state**Table 7.3:** Atomic coordinates ($\times 10^4$) and equivalent isotropic displacement parameters ($\text{\AA}^2 \times 10^3$).U(eq) is defined as one third of the trace of the orthogonalized U^{ij} tensor.

	x	y	z	U(eq)
Fe(1)	5993(1)	1761(1)	1072(1)	8(1)
N(1)	7572(8)	1163(9)	1306(5)	15(2)
N(2)	7982(8)	1162(9)	1990(5)	15(2)
C(1)	8437(11)	765(11)	1038(7)	16(2)
C(2)	9386(11)	593(11)	1531(7)	18(3)
C(3)	9076(10)	814(11)	2136(7)	16(2)
N(3)	6216(8)	1832(8)	2043(6)	11(2)
C(4)	7232(9)	1572(10)	2410(6)	11(2)
C(5)	7501(9)	1748(10)	3091(6)	10(2)
C(6)	6647(8)	2205(9)	3404(6)	8(2)
C(7)	6898(9)	2446(10)	4158(6)	12(2)
O(1)	7998(7)	2894(8)	4347(5)	17(2)
C(8)	5587(9)	2459(10)	3039(6)	9(2)
C(9)	5422(9)	2253(9)	2341(6)	9(2)
N(4)	4455(8)	2531(9)	1890(5)	13(2)
N(5)	4507(9)	2402(9)	1211(6)	16(2)
C(10)	3432(10)	2908(10)	1976(6)	12(2)
C(11)	2808(10)	3078(11)	1327(7)	16(2)
C(12)	3521(10)	2765(11)	891(7)	15(2)
N(6)	5326(8)	229(9)	853(5)	12(2)
N(7)	5139(8)	19(9)	172(5)	13(2)
C(13)	4988(10)	-655(11)	1136(7)	15(2)
C(14)	4564(11)	-1460(11)	652(7)	18(3)
C(15)	4700(10)	-1008(11)	44(7)	16(2)
N(8)	5796(8)	1749(8)	106(6)	10(2)
C(16)	5418(9)	851(10)	-255(6)	12(2)
C(17)	5345(9)	784(10)	-957(6)	13(2)
C(18)	5686(10)	1743(10)	-1278(7)	14(2)
C(19)	5654(11)	1697(10)	-2023(7)	15(2)
O(2)	6009(7)	641(8)	-2248(5)	17(2)
C(20)	6052(10)	2698(11)	-910(6)	15(2)
C(21)	6082(9)	2654(10)	-213(6)	12(2)

N(9)	6469(9)	3538(9)	234(6)	15(2)
N(10)	6559(9)	3270(8)	910(6)	13(2)
C(22)	6770(10)	4615(11)	154(7)	18(2)
C(23)	7097(11)	5048(12)	782(7)	19(3)
C(24)	6937(9)	4191(11)	1245(6)	13(2)
Cl(1)	3810(2)	4398(2)	4079(2)	13(1)
O(3)	3233(7)	4005(8)	3419(5)	19(2)
O(4)	2987(8)	4921(9)	4407(5)	22(2)
O(5)	4309(8)	3457(8)	4479(5)	19(2)
O(6)	4658(8)	5181(8)	3958(5)	21(2)
Cl(2)	2721(2)	263(2)	3078(2)	15(1)
O(7)	1679(8)	640(9)	2679(6)	26(2)
O(8)	2537(8)	-44(9)	3756(5)	23(2)
O(9)	3132(9)	-720(9)	2771(6)	29(2)
O(10)	3541(9)	1139(10)	3146(6)	33(2)

Table 7.4: Selected bond lengths [\AA] and angles [$^\circ$] for $[\text{FeL}_3\text{}_2](\text{ClO}_4)_2$.

Fe(1)-N(8)	1.915(11)	N(3)-Fe(1)-N(5)	79.2(4)
Fe(1)-N(3)	1.926(11)	N(10)-Fe(1)-N(5)	90.6(4)
Fe(1)-N(10)	1.978(10)	N(8)-Fe(1)-N(1)	100.5(4)
Fe(1)-N(5)	2.000(10)	N(3)-Fe(1)-N(1)	79.4(4)
Fe(1)-N(1)	2.000(10)	N(10)-Fe(1)-N(1)	91.7(4)
Fe(1)-N(6)	2.021(10)	N(5)-Fe(1)-N(1)	158.7(5)
		N(8)-Fe(1)-N(6)	78.3(4)
N(8)-Fe(1)-N(3)	177.7(4)	N(3)-Fe(1)-N(6)	103.9(4)
N(8)-Fe(1)-N(10)	80.0(4)	N(10)-Fe(1)-N(6)	158.3(4)
N(3)-Fe(1)-N(10)	97.7(4)	N(5)-Fe(1)-N(6)	93.0(4)
N(8)-Fe(1)-N(5)	100.8(4)	N(1)-Fe(1)-N(6)	92.7(4)

Symmetry transformations used to generate equivalent atoms:

30 K after irradiation in the high spin state

Table 7.5: Atomic coordinates ($\times 10^4$) and equivalent isotropic displacement parameters ($\text{\AA}^2 \times 10^3$).
 $U(\text{eq})$ is defined as one third of the trace of the orthogonalized U^{ij} tensor.

	x	y	z	U(eq)
Fe(1)	6001(1)	1801(1)	1068(1)	47(1)
N(1)	7671(5)	1183(5)	1384(3)	51(1)
N(2)	8003(5)	1178(5)	2054(3)	48(1)
C(1)	8538(8)	805(8)	1146(5)	64(2)
C(2)	9431(7)	605(8)	1641(6)	72(3)
C(3)	9064(6)	848(8)	2220(5)	61(2)
N(3)	6300(5)	1875(5)	2116(3)	43(2)
C(4)	7278(5)	1593(5)	2457(4)	42(2)
C(5)	7544(7)	1739(6)	3129(4)	52(2)
C(6)	6748(7)	2161(7)	3458(4)	53(2)
C(7)	7002(9)	2376(9)	4205(4)	75(3)
O(1)	7920(20)	2810(20)	4415(10)	102(7)
O(1A)	8070(20)	2160(20)	4486(9)	98(7)
C(8)	5720(7)	2419(7)	3125(4)	52(2)
C(9)	5519(6)	2273(6)	2434(4)	45(2)
N(4)	4534(5)	2545(5)	2016(3)	51(1)
N(5)	4485(5)	2460(5)	1352(3)	51(1)
C(10)	3567(7)	2912(8)	2146(5)	62(2)
C(11)	2877(8)	3043(9)	1571(6)	77(3)
C(12)	3502(7)	2772(7)	1104(5)	63(2)
N(6)	5297(5)	209(6)	778(3)	54(2)
N(7)	5110(5)	28(5)	113(3)	44(1)
C(13)	4980(8)	-728(7)	1039(5)	66(2)
C(14)	4611(9)	-1461(8)	540(6)	76(3)
C(15)	4698(7)	-999(7)	-41(4)	60(2)
N(8)	5779(5)	1760(5)	41(4)	41(2)
C(16)	5394(6)	864(5)	-303(3)	43(1)
C(17)	5337(6)	748(6)	-977(4)	49(2)
C(18)	5643(7)	1649(7)	-1320(4)	52(2)
C(19)	5609(9)	1600(8)	-2055(5)	70(2)
O(2A)	5660(17)	553(9)	-2304(5)	167(6)

C(20)	6021(7)	2601(7)	-976(4)	53(2)
C(21)	6072(6)	2616(6)	-316(4)	47(2)
N(9)	6471(5)	3496(5)	102(3)	49(1)
N(10)	6569(6)	3362(6)	762(3)	57(2)
C(22)	6761(8)	4525(7)	-50(5)	70(3)
C(23)	7093(9)	5069(8)	508(6)	78(3)
C(24)	6962(8)	4314(8)	1032(5)	73(3)
Cl(1)	3837(2)	4310(2)	4176(1)	74(1)
O(3)	3327(15)	4115(13)	3530(6)	177(6)
O(4)	3040(12)	4715(11)	4489(6)	145(4)
O(5)	4479(14)	3524(12)	4534(9)	175(6)
O(6)	4540(10)	5120(14)	3987(10)	211(9)
Cl(2)	2596(2)	245(2)	2963(1)	77(1)
O(7)	1734(12)	762(16)	2615(10)	217(9)
O(8)	2330(30)	-165(14)	3546(12)	293(17)
O(9)	2903(16)	-675(11)	2642(8)	191(7)
O(10)	3414(14)	1017(13)	3174(12)	257(13)

Table 7.6: Selected bond lengths [Å] and angles [°].

Fe(1)-N(8)	2.087(7)	N(3)-Fe(1)-N(6)	108.1(3)
Fe(1)-N(3)	2.127(7)	N(10)-Fe(1)-N(6)	147.5(3)
Fe(1)-N(10)	2.161(7)	N(8)-Fe(1)-N(1)	104.6(2)
Fe(1)-N(6)	2.171(7)	N(3)-Fe(1)-N(1)	73.6(2)
Fe(1)-N(1)	2.179(6)	N(10)-Fe(1)-N(1)	93.4(3)
Fe(1)-N(5)	2.194(7)	N(6)-Fe(1)-N(1)	94.8(3)
		N(8)-Fe(1)-N(5)	107.8(2)
N(8)-Fe(1)-N(3)	177.4(3)	N(3)-Fe(1)-N(5)	74.0(2)
N(8)-Fe(1)-N(10)	73.7(2)	N(10)-Fe(1)-N(5)	94.8(3)
N(3)-Fe(1)-N(10)	104.4(2)	N(6)-Fe(1)-N(5)	94.9(3)
N(8)-Fe(1)-N(6)	73.8(2)	N(1)-Fe(1)-N(5)	147.7(2)

Symmetry transformations used to generate equivalent atoms:

A.8. $[\text{FeL}_4\text{O}_2](\text{ClO}_4)_2$ **290 K in the predominately high spin state****Table 8.1:** Atomic coordinates ($\times 10^4$) and equivalent isotropic displacement parameters ($\text{\AA}^2 \times 10^3$).
U(eq) is defined as one third of the trace of the orthogonalized U^{ij} tensor.

	x	y	z	U(eq)
Fe(1)	6263(1)	6448(1)	8683(1)	41(1)
N(1)	5902(2)	7038(4)	9344(3)	57(1)
N(2)	5691(2)	8070(5)	9010(4)	64(1)
C(1)	6006(3)	5726(7)	10522(5)	101(3)
C(2)	5821(2)	6788(6)	10001(5)	78(2)
C(3)	5553(3)	7614(9)	10100(6)	103(3)
C(4)	5489(3)	8411(8)	9500(6)	94(3)
N(3)	6007(1)	8004(4)	8097(3)	52(1)
C(5)	5746(2)	8595(5)	8339(4)	59(1)
C(6)	5543(2)	9616(5)	7935(5)	75(2)
C(7)	5625(2)	9997(6)	7251(5)	84(2)
C(8)	5897(2)	9417(5)	7007(5)	78(2)
C(9)	6083(2)	8413(4)	7461(4)	55(1)
N(4)	6375(2)	7717(4)	7298(3)	58(1)
N(5)	6500(1)	6681(3)	7743(3)	48(1)
C(10)	6547(3)	7861(8)	6750(5)	89(2)
C(11)	6793(3)	6916(7)	6826(5)	84(2)
C(12)	6759(2)	6194(5)	7448(4)	61(2)
C(13)	6963(2)	5053(6)	7768(5)	80(2)
N(6)	5842(1)	5158(5)	7909(3)	61(1)
N(7)	5981(2)	4013(4)	8168(4)	71(2)
C(14)	5252(3)	6096(9)	6746(6)	120(3)
C(15)	5486(2)	5054(8)	7228(4)	80(2)
C(16)	5383(3)	3882(10)	7050(7)	122(4)
C(17)	5695(4)	3247(8)	7636(7)	116(4)
N(8)	6532(1)	4873(4)	9217(3)	51(1)
C(18)	6357(2)	3862(5)	8865(4)	62(2)
C(19)	6544(3)	2785(6)	9149(6)	85(2)

C(20)	6933(3)	2813(7)	9830(6)	94(3)
C(21)	7124(2)	3842(6)	10188(5)	74(2)
C(22)	6910(2)	4863(6)	9875(4)	58(1)
N(9)	7041(2)	5982(4)	10174(3)	59(1)
N(10)	6812(2)	6929(4)	9759(3)	52(1)
C(23)	7369(2)	6343(8)	10918(5)	90(2)
C(24)	7325(2)	7536(8)	10950(5)	96(2)
C(25)	6985(2)	7874(6)	10238(4)	67(2)
C(26)	6816(3)	9060(6)	9994(5)	86(2)
Cl(1)	6850(1)	1298(1)	7569(1)	72(1)
O(1)	5199(10)	1670(30)	8830(20)	173(17)
O(2)	5433(12)	1360(30)	10220(30)	270(20)
O(3)	5554(6)	2995(16)	9760(20)	212(15)
O(1A)	5181(5)	1370(20)	9110(20)	129(13)
O(2A)	5529(6)	2240(20)	10423(8)	138(9)
O(3A)	5613(7)	2870(20)	9255(15)	186(11)
O(4)	5894(2)	1217(5)	9788(4)	122(2)
Cl(2)	5537(1)	1903(2)	9646(1)	68(1)
O(5)	6814(2)	591(4)	8206(3)	98(2)
O(6)	6486(2)	1947(7)	7198(6)	166(3)
O(7)	7168(2)	2107(6)	7960(5)	146(3)
O(8)	6940(4)	611(6)	7038(7)	236(6)

Table 8.2: Selected bond lengths [Å] and angles [°].

Fe(1)-N(3)	2.056(4)	N(8)-Fe(1)-N(5)	101.17(16)
Fe(1)-N(8)	2.061(4)	N(6)-Fe(1)-N(5)	90.04(17)
Fe(1)-N(6)	2.126(5)	N(3)-Fe(1)-N(10)	105.44(19)
Fe(1)-N(5)	2.130(4)	N(8)-Fe(1)-N(10)	75.31(18)
Fe(1)-N(10)	2.135(5)	N(6)-Fe(1)-N(10)	151.12(19)
Fe(1)-N(1)	2.138(4)	N(5)-Fe(1)-N(10)	97.31(17)
		N(3)-Fe(1)-N(1)	75.73(19)
N(3)-Fe(1)-N(8)	176.60(17)	N(8)-Fe(1)-N(1)	107.64(18)
N(3)-Fe(1)-N(6)	103.4(2)	N(6)-Fe(1)-N(1)	97.77(17)
N(8)-Fe(1)-N(6)	75.88(19)	N(5)-Fe(1)-N(1)	151.17(18)
N(3)-Fe(1)-N(5)	75.47(17)	N(10)-Fe(1)-N(1)	89.13(18)

Symmetry transformations used to generate equivalent atoms:

120 K in a mixed spin state**Table 8.3:** Atomic coordinates ($\times 10^4$) and equivalent isotropic displacement parameters ($\text{\AA}^2 \times 10^3$).U(eq) is defined as one third of the trace of the orthogonalized U^{ij} tensor.

	x	y	z	U(eq)
Fe(1)	6266(1)	6456(1)	8715(1)	13(1)
N(1)	6520(1)	6604(3)	7848(2)	17(1)
N(2)	6386(1)	7638(4)	7370(2)	20(1)
C(1)	6983(2)	4876(5)	7867(3)	26(1)
C(2)	6776(2)	6065(4)	7540(3)	22(1)
C(3)	6815(2)	6767(5)	6891(3)	28(1)
C(4)	6565(2)	7744(5)	6787(3)	27(1)
N(3)	6015(1)	7926(3)	8181(2)	18(1)
C(5)	6096(1)	8360(4)	7529(3)	20(1)
C(6)	5907(2)	9383(5)	7083(4)	30(1)
C(7)	5623(2)	9969(5)	7352(4)	34(1)
C(8)	5538(2)	9557(4)	8030(4)	30(1)
C(9)	5744(1)	8506(4)	8431(3)	23(1)
N(4)	5704(1)	7926(4)	9117(3)	22(1)
N(5)	5928(1)	6871(4)	9399(2)	18(1)
C(10)	5505(2)	8259(5)	9638(4)	33(1)
C(11)	5604(2)	7413(6)	10256(4)	35(1)
C(12)	5867(2)	6555(5)	10099(3)	27(1)
C(13)	6070(2)	5471(6)	10606(4)	41(2)
N(6)	6781(1)	7058(3)	9693(2)	16(1)
N(7)	7048(1)	6126(4)	10145(2)	20(1)
C(14)	6743(2)	9238(5)	9920(3)	28(1)
C(15)	6941(2)	8039(5)	10164(3)	22(1)
C(16)	7305(2)	7733(5)	10906(3)	28(1)
C(17)	7365(2)	6535(5)	10879(3)	28(1)
N(8)	6527(1)	4979(4)	9211(2)	17(1)
C(18)	6911(1)	4960(4)	9856(3)	17(1)
C(19)	7132(2)	3917(5)	10188(3)	24(1)
C(20)	6931(2)	2842(5)	9820(4)	30(1)
C(21)	6531(2)	2832(5)	9152(3)	28(1)
C(22)	6343(2)	3933(4)	8856(3)	21(1)
N(9)	5833(1)	5313(4)	7938(2)	18(1)

N(10)	5956(1)	4130(4)	8163(3)	23(1)
C(23)	5666(2)	3372(5)	7606(4)	41(2)
C(24)	5357(2)	4045(6)	7019(4)	40(2)
C(25)	5471(2)	5247(5)	7236(3)	29(1)
C(26)	5240(2)	6323(6)	6755(3)	35(1)
Cl(1)	5542(1)	1817(1)	9689(1)	23(1)
O(1)	5168(3)	1095(8)	9430(7)	44(2)
O(2)	5587(3)	2530(8)	10430(6)	41(2)
O(3)	5559(3)	2502(10)	9039(7)	60(3)
O(1A)	5150(3)	1540(9)	8920(7)	45(2)
O(2A)	5475(4)	1558(15)	10409(7)	84(4)
O(3A)	5580(3)	3112(8)	9612(9)	70(4)
O(4)	5906(1)	1082(5)	9834(4)	74(2)
Cl(2)	6835(1)	1279(1)	7563(1)	23(1)
O(5)	6457(1)	1994(4)	7282(3)	41(1)
O(6)	6836(2)	566(4)	6870(3)	64(2)
O(7)	6847(1)	506(4)	8253(2)	34(1)
O(8)	7200(1)	2054(4)	7874(3)	39(1)

Table 8.4: Selected bond lengths [\AA] and angles [$^\circ$].

Fe(1)-N(8)	1.903(4)	N(3)-Fe(1)-N(9)	99.23(16)
Fe(1)-N(3)	1.904(4)	N(6)-Fe(1)-N(9)	159.97(16)
Fe(1)-N(6)	1.995(4)	N(8)-Fe(1)-N(1)	97.57(15)
Fe(1)-N(9)	2.001(4)	N(3)-Fe(1)-N(1)	79.92(16)
Fe(1)-N(1)	2.001(4)	N(6)-Fe(1)-N(1)	94.86(15)
Fe(1)-N(5)	2.006(4)	N(9)-Fe(1)-N(1)	89.70(15)
		N(8)-Fe(1)-N(5)	102.78(16)
N(8)-Fe(1)-N(3)	177.47(17)	N(3)-Fe(1)-N(5)	79.74(16)
N(8)-Fe(1)-N(6)	79.67(16)	N(6)-Fe(1)-N(5)	87.91(15)
N(3)-Fe(1)-N(6)	100.78(16)	N(9)-Fe(1)-N(5)	94.58(15)
N(8)-Fe(1)-N(9)	80.40(16)	N(1)-Fe(1)-N(5)	159.63(16)

Symmetry transformations used to generate equivalent atoms:

30 K in the predominately low spin state

Table 8.5: Atomic coordinates ($\times 10^4$) and equivalent isotropic displacement parameters ($\text{\AA}^2 \times 10^3$).
 $U(\text{eq})$ is defined as one third of the trace of the orthogonalized U^{ij} tensor.

	x	y	z	U(eq)
Fe(1)	1267(1)	1469(1)	3722(1)	8(1)
Cl(2)	1829(1)	6290(1)	2557(1)	12(1)
N(1)	1519(2)	1612(5)	2852(3)	11(1)
N(3)	1013(2)	2941(5)	3186(4)	15(1)
N(9)	832(2)	315(5)	2950(4)	13(1)
N(8)	1528(2)	-10(5)	4217(3)	12(1)
N(6)	1782(2)	2083(5)	4692(3)	11(1)
N(4)	702(2)	2939(5)	4127(4)	19(1)
N(2)	1386(2)	2663(5)	2375(3)	13(1)
C(2)	1774(2)	1072(6)	2534(5)	17(1)
N(5)	928(2)	1883(5)	4410(3)	13(1)
C(5)	1093(2)	3374(6)	2533(4)	16(1)
N(7)	2051(2)	1154(5)	5149(4)	15(1)
N(10)	960(2)	-866(5)	3178(4)	14(1)
C(17)	2370(2)	1569(7)	5885(5)	21(2)
C(15)	1939(2)	3078(7)	5168(4)	15(1)
C(18)	1918(2)	-20(6)	4866(4)	13(1)
C(19)	2139(2)	-1067(6)	5198(4)	15(1)
C(12)	869(2)	1557(8)	5113(4)	23(2)
C(25)	470(2)	244(7)	2250(5)	24(2)
C(1)	1976(2)	-141(6)	2858(5)	18(1)
C(9)	742(2)	3520(7)	3447(5)	19(1)
C(3)	1808(2)	1776(7)	1877(5)	21(2)
C(22)	1348(2)	-1060(6)	3874(4)	15(1)
C(14)	1737(2)	4274(6)	4917(4)	19(2)
C(21)	1539(2)	-2163(7)	4166(5)	20(2)
C(20)	1943(2)	-2146(7)	4842(5)	21(2)
C(8)	534(2)	4570(7)	3044(6)	26(2)
C(26)	240(2)	1316(8)	1762(5)	27(2)
C(11)	601(2)	2425(9)	5269(5)	30(2)
C(4)	1562(2)	2761(7)	1784(4)	17(1)

C(6)	906(2)	4413(6)	2095(5)	24(2)
C(16)	2305(2)	2772(7)	5908(4)	20(2)
C(10)	503(2)	3268(8)	4652(5)	28(2)
C(24)	361(2)	-962(8)	2029(6)	36(2)
C(7)	620(2)	5003(7)	2366(6)	30(2)
C(23)	671(2)	-1638(7)	2628(6)	34(2)
C(13)	1074(2)	471(9)	5618(5)	35(2)
Cl(1)	547(1)	6825(1)	4700(1)	14(1)
O(5)	1851(2)	5485(5)	3247(3)	20(1)
O(6)	2201(2)	7060(5)	2851(3)	21(1)
O(7)	1449(2)	7024(4)	2309(3)	19(1)
O(8)	1814(2)	5581(5)	1835(3)	26(1)
O(2)	599(3)	7541(10)	5466(6)	20(2)
O(2A)	492(3)	6531(12)	5437(7)	31(3)
O(1A)	579(3)	8157(9)	4622(7)	24(2)
O(1)	565(3)	7540(10)	4060(7)	24(2)
O(3)	138(3)	6552(9)	3914(7)	17(2)
O(3A)	166(3)	6102(9)	4441(7)	19(2)
O(4)	889(3)	6252(11)	4604(8)	19(2)
O(4A)	927(4)	5938(11)	4997(8)	18(3)

Table 8.6: Selected bond lengths [\AA] and angles [$^\circ$].

Fe(1)-N(8)	1.898(6)	N(3)-Fe(1)-N(1)	80.1(2)
Fe(1)-N(3)	1.902(6)	N(6)-Fe(1)-N(1)	94.8(2)
Fe(1)-N(6)	1.989(5)	N(8)-Fe(1)-N(9)	80.2(2)
Fe(1)-N(1)	1.992(5)	N(3)-Fe(1)-N(9)	99.2(2)
Fe(1)-N(9)	2.000(6)	N(6)-Fe(1)-N(9)	160.1(2)
Fe(1)-N(5)	2.001(5)	N(1)-Fe(1)-N(9)	89.6(2)
		N(8)-Fe(1)-N(5)	102.7(2)
N(8)-Fe(1)-N(3)	177.5(2)	N(3)-Fe(1)-N(5)	79.7(2)
N(8)-Fe(1)-N(6)	80.0(2)	N(6)-Fe(1)-N(5)	88.0(2)
N(3)-Fe(1)-N(6)	100.7(2)	N(1)-Fe(1)-N(5)	159.8(2)
N(8)-Fe(1)-N(1)	97.5(2)	N(9)-Fe(1)-N(5)	94.5(2)

Symmetry transformations used to generate equivalent atoms:

A.9. $[\text{FeL}_4\text{}_2](\text{BF}_4)_2$

200 K in the high spin state

Table 9.1: Atomic coordinates ($\times 10^4$) and equivalent isotropic displacement parameters ($\text{\AA}^2 \times 10^3$). $U(\text{eq})$ is defined as one third of the trace of the orthogonalized U^{ij} tensor.

	x	y	z	U(eq)
Fe(1)	8702(1)	4595(1)	8733(1)	25(1)
N(1)	8918(1)	6132(2)	8224(1)	29(1)
N(2)	8937(1)	7219(2)	8502(1)	28(1)
C(1)	9176(2)	5413(3)	7310(2)	45(1)
C(2)	9120(1)	6376(3)	7734(1)	32(1)
C(3)	9262(1)	7603(3)	7701(1)	37(1)
C(4)	9137(1)	8104(3)	8192(1)	36(1)
N(3)	8635(1)	6163(2)	9234(1)	25(1)
C(5)	8760(1)	7253(3)	9044(1)	29(1)
C(6)	8724(2)	8300(3)	9350(1)	44(1)
C(7)	8532(2)	8185(3)	9873(2)	49(1)
C(8)	8389(2)	7064(3)	10078(1)	39(1)
C(9)	8456(1)	6071(3)	9747(1)	29(1)
N(4)	8368(1)	4861(3)	9903(1)	30(1)
N(5)	8546(1)	3946(2)	9576(1)	29(1)
C(10)	8158(2)	4392(4)	10370(1)	45(1)
C(11)	8208(2)	3176(4)	10340(1)	52(1)
C(12)	8451(2)	2916(3)	9842(1)	39(1)
C(13)	8603(2)	1706(4)	9616(2)	61(1)
N(6)	7810(1)	4158(2)	8454(1)	26(1)
N(7)	7748(1)	3087(2)	8167(1)	25(1)
C(14)	7170(2)	5625(3)	8856(2)	41(1)
C(15)	7277(1)	4490(3)	8553(1)	30(1)
C(16)	6878(1)	3615(3)	8328(1)	33(1)
C(17)	7189(1)	2749(3)	8085(1)	33(1)
C(18)	8242(1)	2477(3)	8023(1)	26(1)
N(8)	8727(1)	2959(2)	8268(1)	26(1)
C(19)	8233(1)	1483(3)	7680(1)	34(1)
C(20)	8756(1)	952(3)	7607(1)	37(1)

C(21)	9265(1)	1402(3)	7871(1)	34(1)
C(22)	9225(1)	2422(3)	8195(1)	28(1)
N(9)	9701(1)	3012(2)	8483(1)	30(1)
N(10)	9608(1)	4045(2)	8778(1)	32(1)
C(23)	10269(1)	2771(3)	8493(1)	39(1)
C(24)	10551(1)	3662(3)	8799(1)	42(1)
C(25)	10126(1)	4451(3)	8971(1)	36(1)
C(26)	10193(2)	5589(4)	9300(2)	51(1)
B(1)	7601(2)	4113(4)	6666(2)	39(1)
F(1)	8044(1)	3665(2)	6374(1)	56(1)
F(2)	7290(1)	4953(3)	6337(1)	68(1)
F(3)	7258(1)	3151(2)	6799(1)	60(1)
F(4)	7834(1)	4666(2)	7152(1)	52(1)
B(2)	5409(2)	4527(4)	8820(2)	44(1)
F(5)	5461(1)	4831(2)	8267(1)	62(1)
F(6)	4892(1)	4973(3)	8958(1)	70(1)
F(7)	5859(1)	5036(3)	9146(1)	91(1)
F(8)	5436(2)	3306(3)	8855(2)	115(1)

Table 9.2: Selected bond lengths [Å] and angles [°].

Fe(1)-N(3)	2.117(2)	N(8)-Fe(1)-N(6)	74.05(9)
Fe(1)-N(8)	2.121(2)	N(1)-Fe(1)-N(6)	105.32(9)
Fe(1)-N(1)	2.175(3)	N(3)-Fe(1)-N(10)	108.58(9)
Fe(1)-N(6)	2.180(2)	N(8)-Fe(1)-N(10)	73.55(9)
Fe(1)-N(10)	2.192(3)	N(1)-Fe(1)-N(10)	88.14(10)
Fe(1)-N(5)	2.212(2)	N(6)-Fe(1)-N(10)	147.51(10)
		N(3)-Fe(1)-N(5)	73.41(9)
N(3)-Fe(1)-N(8)	175.85(9)	N(8)-Fe(1)-N(5)	102.97(9)
N(3)-Fe(1)-N(1)	73.75(10)	N(1)-Fe(1)-N(5)	146.50(10)
N(8)-Fe(1)-N(1)	110.07(9)	N(6)-Fe(1)-N(5)	88.63(9)
N(3)-Fe(1)-N(6)	103.60(9)	N(10)-Fe(1)-N(5)	96.14(10)

Symmetry transformations used to generate equivalent atoms:

130 K in the mixed spin state

Table 9.3: Atomic coordinates ($\times 10^4$) and equivalent isotropic displacement parameters ($\text{\AA}^2 \times 10^3$).
 U(eq) is defined as one third of the trace of the orthogonalized U^{ij} tensor.

	x	y	z	U(eq)
Fe(1)	801(1)	2916(1)	428(1)	14(1)
N(1)	1040(1)	1620(2)	348(1)	16(1)
N(2)	960(1)	469(2)	425(1)	18(1)
C(1)	1431(1)	2473(3)	233(1)	26(1)
C(2)	1274(1)	1454(3)	312(1)	18(1)
C(3)	1342(1)	200(3)	366(1)	24(1)
C(4)	1140(1)	-395(3)	433(1)	22(1)
N(3)	618(1)	1493(2)	485(1)	16(1)
C(5)	720(1)	377(3)	477(1)	17(1)
C(6)	597(1)	-693(3)	533(1)	23(1)
C(7)	358(1)	-561(3)	587(1)	25(1)
C(8)	245(1)	584(3)	584(1)	22(1)
C(9)	386(1)	1587(3)	535(1)	16(1)
N(4)	317(1)	2824(2)	544(1)	17(1)
N(5)	503(1)	3681(2)	551(1)	17(1)
C(10)	104(1)	3371(3)	597(1)	25(1)
C(11)	155(1)	4586(3)	641(1)	27(1)
C(12)	404(1)	4759(3)	613(1)	22(1)
C(13)	548(1)	5942(3)	657(1)	31(1)
N(6)	1040(1)	3096(3)	1051(1)	22(1)
N(7)	1199(1)	4114(3)	1094(1)	24(1)
C(14)	1011(1)	1361(4)	1535(1)	33(1)
C(15)	1127(1)	2524(4)	1442(1)	26(1)
C(16)	1338(1)	3181(4)	1737(1)	35(1)
C(17)	1379(1)	4175(4)	1510(1)	37(1)
C(18)	1166(1)	4822(3)	714(1)	22(1)
N(8)	980(1)	4348(2)	362(1)	19(1)
C(19)	1305(1)	5852(3)	682(1)	31(1)
C(20)	1243(1)	6395(3)	265(1)	32(1)
C(21)	1048(1)	5936(3)	-98(1)	27(1)
C(22)	918(1)	4909(3)	-32(1)	21(1)

N(9)	713(1)	4301(2)	-348(1)	19(1)
N(10)	627(1)	3230(2)	-219(1)	16(1)
C(23)	574(1)	4583(3)	-776(1)	24(1)
C(24)	394(1)	3678(3)	-928(1)	24(1)
C(25)	433(1)	2842(3)	-574(1)	19(1)
C(26)	289(1)	1679(3)	-576(1)	26(1)
Fe(2)	2514(1)	3260(1)	1296(1)	17(1)
N(11)	2728(1)	3724(3)	1986(1)	19(1)
N(12)	2647(1)	4788(3)	2124(1)	19(1)
C(27)	3092(1)	2282(3)	2280(1)	28(1)
C(28)	2946(1)	3415(3)	2311(1)	20(1)
C(29)	3002(1)	4287(3)	2657(1)	23(1)
C(30)	2809(1)	5142(3)	2529(1)	22(1)
N(13)	2342(1)	4897(2)	1433(1)	17(1)
C(31)	2425(1)	5379(3)	1840(1)	18(1)
C(32)	2305(1)	6364(3)	1963(1)	23(1)
C(33)	2096(1)	6878(3)	1636(1)	24(1)
C(34)	2012(1)	6425(3)	1208(1)	22(1)
C(35)	2142(1)	5413(3)	1124(1)	18(1)
N(14)	2076(1)	4821(3)	709(1)	20(1)
N(15)	2209(1)	3787(3)	676(1)	21(1)
C(36)	1883(1)	5069(3)	322(1)	24(1)
C(37)	1890(1)	4161(4)	32(1)	28(1)
C(38)	2096(1)	3382(3)	261(1)	24(1)
C(39)	2186(1)	2227(4)	106(1)	38(1)
N(16)	2275(1)	1680(3)	1318(1)	20(1)
N(17)	2370(1)	589(3)	1226(1)	20(1)
C(40)	1871(1)	2377(4)	1419(1)	29(1)
C(41)	2041(1)	1416(3)	1332(1)	22(1)
C(42)	1985(1)	161(3)	1249(1)	26(1)
C(43)	2198(1)	-334(3)	1186(1)	26(1)
N(18)	2713(1)	1691(3)	1182(1)	18(1)
C(44)	2611(1)	570(3)	1173(1)	21(1)
C(45)	2734(1)	-479(3)	1109(2)	36(1)
C(46)	2974(1)	-330(4)	1062(2)	42(1)
C(47)	3087(1)	810(3)	1079(1)	29(1)
C(48)	2944(1)	1802(3)	1130(1)	19(1)
N(19)	3016(1)	3027(3)	1117(1)	19(1)

N(20)	2838(1)	3934(3)	1104(1)	20(1)
C(49)	3231(1)	3522(3)	1055(1)	27(1)
C(50)	3191(1)	4752(3)	1007(1)	30(1)
C(51)	2945(1)	4983(3)	1034(1)	25(1)
C(52)	2807(1)	6169(3)	1002(1)	34(1)
Fe(3)	860(1)	2401(1)	2981(1)	17(1)
N(21)	591(1)	1886(3)	2340(1)	24(1)
N(22)	448(1)	857(3)	2353(1)	27(1)
C(53)	591(1)	3454(4)	1792(1)	38(1)
C(54)	492(1)	2317(4)	1927(1)	29(1)
C(55)	285(1)	1544(4)	1678(1)	38(1)
C(56)	263(1)	636(4)	1950(1)	36(1)
N(23)	689(1)	782(3)	3086(1)	21(1)
C(57)	499(1)	250(3)	2758(1)	24(1)
C(58)	368(1)	-776(3)	2824(1)	30(1)
C(59)	437(1)	-1230(3)	3252(1)	30(1)
C(60)	635(1)	-704(3)	3595(1)	25(1)
C(61)	757(1)	291(3)	3492(1)	20(1)
N(24)	969(1)	892(3)	3794(1)	20(1)
N(25)	1050(1)	1980(3)	3669(1)	22(1)
C(62)	1118(1)	572(3)	4211(1)	25(1)
C(63)	1303(1)	1463(3)	4360(1)	27(1)
C(64)	1254(1)	2332(3)	4017(1)	25(1)
C(65)	1397(1)	3484(4)	4002(1)	35(1)
N(26)	1200(1)	1750(3)	2849(1)	23(1)
N(27)	1371(1)	2695(3)	2859(1)	24(1)
C(66)	1210(1)	-499(4)	2834(2)	55(1)
C(67)	1334(1)	736(4)	2856(1)	35(1)
C(68)	1589(1)	1008(4)	2878(2)	47(1)
C(69)	1607(1)	2251(4)	2880(1)	37(1)
N(28)	1045(1)	3975(3)	2869(1)	19(1)
C(70)	1276(1)	3894(3)	2812(1)	21(1)
C(71)	1395(1)	4899(3)	2700(1)	27(1)
C(72)	1264(1)	6013(4)	2636(1)	36(1)
C(73)	1026(1)	6118(4)	2694(1)	33(1)
C(74)	924(1)	5053(3)	2815(1)	22(1)
N(29)	685(1)	4995(3)	2876(1)	24(1)
N(30)	605(1)	3887(3)	2990(1)	24(1)

C(75)	507(1)	5885(4)	2843(1)	32(1)
C(76)	306(1)	5357(4)	2936(1)	36(1)
C(77)	372(1)	4116(4)	3024(1)	32(1)
C(78)	217(1)	3112(4)	3131(1)	42(1)
B(1)	1991(1)	8151(4)	151(1)	31(1)
F(1)	2027(1)	9384(3)	107(1)	71(1)
F(2)	1776(1)	7993(2)	298(1)	37(1)
F(3)	2205(1)	7632(2)	468(1)	40(1)
F(4)	1937(1)	7572(3)	-253(1)	48(1)
B(2)	1347(1)	8030(4)	1556(1)	28(1)
F(5)	1109(1)	7942(3)	1232(1)	49(1)
F(6)	1351(1)	8607(4)	1924(1)	90(1)
F(7)	1512(1)	8500(6)	1378(1)	157(3)
F(8)	1440(1)	6890(4)	1694(1)	134(2)
B(3)	2179(1)	3763(4)	2670(1)	27(1)
F(9)	1920(1)	4106(2)	2453(1)	37(1)
F(10)	2324(1)	4797(2)	2852(1)	38(1)
F(11)	2277(1)	3205(2)	2368(1)	33(1)
F(12)	2187(1)	2922(2)	3006(1)	40(1)
B(4)	289(1)	7218(5)	1750(2)	38(1)
F(13)	94(1)	7688(3)	1879(1)	57(1)
F(14)	522(1)	7635(4)	2053(1)	80(1)
F(15)	267(1)	5971(3)	1755(1)	110(2)
F(16)	261(1)	7587(4)	1328(1)	86(1)
B(5)	1129(1)	6915(4)	3949(1)	26(1)
F(17)	1387(1)	6552(2)	4164(1)	34(1)
F(18)	1034(1)	7463(2)	4254(1)	34(1)
F(19)	984(1)	5900(3)	3767(1)	55(1)
F(20)	1126(1)	7758(3)	3623(1)	64(1)
B(6)	521(1)	1828(4)	4378(1)	22(1)
F(21)	624(1)	2441(2)	4094(1)	29(1)
F(22)	506(1)	2638(2)	4705(1)	39(1)
F(23)	272(1)	1406(2)	4139(1)	31(1)
F(24)	677(1)	835(2)	4572(1)	35(1)

Table 9.4: Selected bond lengths [Å] and angles [°].

Fe(1)-N(3)	1.891(3)	N(5)-Fe(1)-N(1)	159.74(11)
Fe(1)-N(8)	1.891(3)	N(10)-Fe(1)-N(1)	95.36(10)
Fe(1)-N(6)	1.990(3)		
Fe(1)-N(5)	1.994(2)	N(18)-Fe(2)-N(13)	175.75(10)
Fe(1)-N(10)	1.994(3)	N(18)-Fe(2)-N(16)	73.74(10)
Fe(1)-N(1)	2.000(3)	N(13)-Fe(2)-N(16)	109.92(10)
		N(18)-Fe(2)-N(11)	103.19(10)
Fe(2)-N(18)	2.125(3)	N(13)-Fe(2)-N(11)	73.93(10)
Fe(2)-N(13)	2.132(3)	N(16)-Fe(2)-N(11)	105.98(10)
Fe(2)-N(16)	2.179(3)	N(18)-Fe(2)-N(15)	109.41(10)
Fe(2)-N(11)	2.181(3)	N(13)-Fe(2)-N(15)	73.30(10)
Fe(2)-N(15)	2.195(3)	N(16)-Fe(2)-N(15)	87.32(10)
Fe(2)-N(20)	2.197(3)	N(11)-Fe(2)-N(15)	147.15(10)
		N(18)-Fe(2)-N(20)	73.06(10)
Fe(3)-N(23)	2.079(3)	N(13)-Fe(2)-N(20)	103.61(10)
Fe(3)-N(28)	2.085(3)	N(16)-Fe(2)-N(20)	145.72(10)
Fe(3)-N(25)	2.142(3)	N(11)-Fe(2)-N(20)	89.71(10)
Fe(3)-N(30)	2.149(3)	N(15)-Fe(2)-N(20)	95.75(10)
Fe(3)-N(21)	2.157(3)		
Fe(3)-N(26)	2.167(3)	N(23)-Fe(3)-N(28)	177.38(10)
		N(23)-Fe(3)-N(25)	75.06(11)
N(3)-Fe(1)-N(8)	179.07(12)	N(28)-Fe(3)-N(25)	104.83(10)
N(3)-Fe(1)-N(6)	100.11(11)	N(23)-Fe(3)-N(30)	107.65(10)
N(8)-Fe(1)-N(6)	80.74(11)	N(28)-Fe(3)-N(30)	74.94(10)
N(3)-Fe(1)-N(5)	79.83(10)	N(25)-Fe(3)-N(30)	103.89(10)
N(8)-Fe(1)-N(5)	99.75(11)	N(23)-Fe(3)-N(21)	74.41(11)
N(6)-Fe(1)-N(5)	93.90(11)	N(28)-Fe(3)-N(21)	105.53(11)
N(3)-Fe(1)-N(10)	99.07(11)	N(25)-Fe(3)-N(21)	149.32(11)
N(8)-Fe(1)-N(10)	80.08(11)	N(30)-Fe(3)-N(21)	88.20(11)
N(6)-Fe(1)-N(10)	160.82(11)	N(23)-Fe(3)-N(26)	102.78(11)
N(5)-Fe(1)-N(10)	89.79(10)	N(28)-Fe(3)-N(26)	74.61(10)
N(3)-Fe(1)-N(1)	80.01(10)	N(25)-Fe(3)-N(26)	88.78(10)
N(8)-Fe(1)-N(1)	100.43(11)	N(30)-Fe(3)-N(26)	149.11(11)
N(6)-Fe(1)-N(1)	87.65(11)	N(21)-Fe(3)-N(26)	95.01(11)

Symmetry transformations used to generate equivalent atoms:

90 K in the low spin state**Table 9.5:** Atomic coordinates ($\times 10^4$) and equivalent isotropic displacement parameters ($\text{\AA}^2 \times 10^3$).U(eq) is defined as one third of the trace of the orthogonalized U^{ij} tensor.

	x	y	z	U(eq)
Fe(1)	8691(1)	4592(1)	8793(1)	12(1)
N(1)	8881(2)	5894(3)	8241(1)	16(1)
N(2)	8882(2)	7060(3)	8478(1)	16(1)
C(1)	9179(2)	5049(5)	7347(2)	23(1)
C(2)	9090(2)	6072(4)	7739(1)	18(1)
C(3)	9213(2)	7330(4)	7657(2)	22(1)
C(4)	9082(2)	7934(4)	8129(2)	22(1)
N(3)	8581(1)	6043(3)	9222(1)	15(1)
C(5)	8698(2)	7154(4)	9017(1)	16(1)
C(6)	8654(2)	8236(4)	9320(2)	24(1)
C(7)	8462(2)	8107(5)	9855(2)	27(1)
C(8)	8326(2)	6956(4)	10076(2)	19(1)
C(9)	8397(2)	5942(4)	9740(1)	15(1)
N(4)	8322(2)	4704(3)	9885(1)	14(1)
N(5)	8508(1)	3829(3)	9516(1)	14(1)
C(10)	8164(2)	4160(4)	10371(2)	21(1)
C(11)	8254(2)	2916(4)	10308(2)	24(1)
C(12)	8469(2)	2739(4)	9777(2)	20(1)
C(13)	8639(2)	1557(4)	9523(2)	30(1)
N(6)	7855(2)	4310(3)	8510(1)	15(1)
N(7)	7804(2)	3232(3)	8198(1)	15(1)
C(14)	7163(2)	5833(4)	8863(2)	25(1)
C(15)	7304(2)	4695(4)	8556(1)	17(1)
C(16)	6901(2)	3862(4)	8283(1)	19(1)
C(17)	7233(2)	2967(4)	8059(2)	19(1)
C(18)	8320(2)	2624(4)	8086(1)	16(1)
N(8)	8788(2)	3146(3)	8362(1)	15(1)
C(19)	8377(2)	1613(4)	7742(2)	22(1)
C(20)	8936(2)	1120(4)	7706(2)	25(1)
C(21)	9424(2)	1613(4)	8003(2)	25(1)
C(22)	9322(2)	2635(4)	8326(1)	18(1)
N(9)	9748(2)	3305(3)	8650(1)	20(1)

N(10)	9560(2)	4358(3)	8923(1)	18(1)
C(23)	10349(2)	3185(5)	8707(2)	27(1)
C(24)	10550(2)	4181(5)	9018(2)	26(1)
C(25)	10051(2)	4875(4)	9144(2)	21(1)
C(26)	10036(2)	6050(5)	9464(2)	28(1)
B(1)	7612(2)	4289(5)	6691(2)	22(1)
F(1)	8107(1)	3912(3)	6406(1)	24(1)
F(2)	7289(1)	5109(3)	6344(1)	38(1)
F(3)	7277(1)	3252(3)	6806(1)	35(1)
F(4)	7798(1)	4894(3)	7176(1)	24(1)
B(2)	5426(2)	4500(5)	8845(2)	25(1)
F(6)	5603(2)	5276(4)	8419(2)	56(1)
F(7)	5830(2)	4620(4)	9288(1)	60(1)
F(8)	5457(2)	3313(4)	8645(2)	66(1)
F(5)	4861(1)	4783(3)	8972(1)	42(1)

Table 9.6: Selected bond lengths [Å] and angles [°].

Fe(1)-N(8)	1.898(3)	N(3)-Fe(1)-N(10)	100.12(14)
Fe(1)-N(3)	1.905(3)	N(5)-Fe(1)-N(10)	93.48(13)
Fe(1)-N(5)	1.997(3)	N(8)-Fe(1)-N(1)	100.31(13)
Fe(1)-N(10)	1.999(4)	N(3)-Fe(1)-N(1)	79.77(13)
Fe(1)-N(1)	2.001(3)	N(5)-Fe(1)-N(1)	159.38(13)
Fe(1)-N(6)	2.005(4)	N(10)-Fe(1)-N(1)	86.95(13)
		N(8)-Fe(1)-N(6)	79.90(14)
N(8)-Fe(1)-N(3)	179.20(15)	N(3)-Fe(1)-N(6)	99.30(14)
N(8)-Fe(1)-N(5)	100.09(13)	N(5)-Fe(1)-N(6)	89.83(13)
N(3)-Fe(1)-N(5)	79.86(13)	N(10)-Fe(1)-N(6)	160.58(14)
N(8)-Fe(1)-N(10)	80.68(14)	N(1)-Fe(1)-N(6)	96.59(13)

Symmetry transformations used to generate equivalent atoms:

A.10. $[\text{FeL}_4\text{2}](\text{BF}_4)_2 \cdot \frac{1}{3}\text{H}_2\text{O}$ **200 K in the high spin state****Table 10.1:** Atomic coordinates ($\times 10^4$) and equivalent isotropic displacement parameters ($\text{\AA}^2 \times 10^3$).
U(eq) is defined as one third of the trace of the orthogonalized U^{ij} tensor.

	x	y	z	U(eq)
Fe(1)	8705(1)	4589(1)	8738(1)	27(1)
N(1)	8914(1)	6137(2)	8230(1)	30(1)
N(2)	8924(1)	7218(2)	8508(1)	30(1)
C(1)	9181(2)	5428(3)	7320(1)	48(1)
C(2)	9117(1)	6383(3)	7742(1)	33(1)
C(3)	9256(1)	7618(3)	7714(1)	40(1)
C(4)	9131(1)	8110(3)	8199(1)	40(1)
N(3)	8633(1)	6152(2)	9243(1)	28(1)
C(5)	8741(1)	7250(3)	9047(1)	31(1)
C(6)	8684(2)	8295(3)	9348(1)	49(1)
C(7)	8498(2)	8175(3)	9866(2)	57(1)
C(8)	8373(2)	7045(3)	10081(1)	44(1)
C(9)	8455(1)	6061(3)	9752(1)	30(1)
N(4)	8373(1)	4848(2)	9910(1)	34(1)
N(5)	8545(1)	3932(2)	9576(1)	33(1)
C(10)	8170(2)	4381(4)	10377(1)	49(1)
C(11)	8212(2)	3162(4)	10342(2)	59(1)
C(12)	8448(2)	2906(3)	9842(1)	45(1)
C(13)	8588(2)	1698(4)	9606(2)	69(1)
N(6)	7815(1)	4158(2)	8455(1)	29(1)
N(7)	7754(1)	3086(2)	8168(1)	27(1)
C(14)	7177(1)	5619(3)	8851(2)	44(1)
C(15)	7284(1)	4485(3)	8549(1)	31(1)
C(16)	6887(1)	3617(3)	8324(1)	35(1)
C(17)	7196(1)	2749(3)	8084(1)	35(1)
C(18)	8247(1)	2478(3)	8024(1)	28(1)
N(8)	8730(1)	2963(2)	8269(1)	27(1)
C(19)	8235(1)	1478(3)	7681(1)	36(1)

C(20)	8759(1)	949(3)	7607(1)	40(1)
C(21)	9263(1)	1403(3)	7869(1)	36(1)
C(22)	9226(1)	2431(3)	8195(1)	30(1)
N(9)	9697(1)	3020(2)	8477(1)	32(1)
N(10)	9607(1)	4048(2)	8776(1)	33(1)
C(23)	10266(1)	2782(3)	8487(1)	41(1)
C(24)	10544(1)	3674(3)	8789(1)	44(1)
C(25)	10125(1)	4452(3)	8966(1)	38(1)
C(26)	10191(2)	5587(3)	9298(2)	54(1)
B(1)	7610(2)	4128(4)	6673(2)	40(1)
F(1)	8052(1)	3672(2)	6384(1)	59(1)
F(2)	7306(1)	4969(2)	6341(1)	68(1)
F(3)	7265(1)	3170(2)	6805(1)	62(1)
F(4)	7841(1)	4681(2)	7161(1)	54(1)
B(2)	5422(2)	4533(4)	8826(2)	55(1)
F(5)	5451(1)	4818(2)	8277(1)	67(1)
F(6)	4900(1)	4963(3)	8972(1)	90(1)
F(7)	5859(1)	5075(4)	9145(1)	108(1)
F(8)	5463(2)	3323(3)	8874(2)	145(2)
O(1)	9948(4)	2085(8)	5093(4)	77(3)

Table 10.2: Selected bond lengths [\AA] and angles [$^\circ$]

Fe(1)-N(8)	2.118(2)	N(3)-Fe(1)-N(6)	103.18(9)
Fe(1)-N(3)	2.120(2)	N(1)-Fe(1)-N(6)	104.78(9)
Fe(1)-N(1)	2.178(2)	N(8)-Fe(1)-N(10)	73.48(9)
Fe(1)-N(6)	2.182(2)	N(3)-Fe(1)-N(10)	109.12(9)
Fe(1)-N(10)	2.188(2)	N(1)-Fe(1)-N(10)	88.15(9)
Fe(1)-N(5)	2.204(2)	N(6)-Fe(1)-N(10)	147.46(10)
		N(8)-Fe(1)-N(5)	102.99(9)
N(8)-Fe(1)-N(3)	175.63(9)	N(3)-Fe(1)-N(5)	73.37(9)
N(8)-Fe(1)-N(1)	110.02(9)	N(1)-Fe(1)-N(5)	146.67(9)
N(3)-Fe(1)-N(1)	73.83(9)	N(6)-Fe(1)-N(5)	88.33(9)
N(8)-Fe(1)-N(6)	74.04(9)	N(10)-Fe(1)-N(5)	97.02(10)

Symmetry transformations used to generate equivalent atoms:

130 K in the high spin state

Table 10.3: Atomic coordinates ($\times 10^4$) and equivalent isotropic displacement parameters ($\text{\AA}^2 \times 10^3$).U(eq) is defined as one third of the trace of the orthogonalized U^{ij} tensor.

	x	y	z	U(eq)
Fe(1)	8706(1)	4599(1)	8739(1)	21(1)
N(1)	8918(1)	6141(3)	8228(1)	23(1)
N(2)	8927(1)	7229(2)	8504(1)	22(1)
C(1)	9191(2)	5422(4)	7314(2)	37(1)
C(2)	9126(1)	6385(3)	7735(1)	26(1)
C(3)	9262(1)	7627(3)	7705(2)	31(1)
C(4)	9131(1)	8126(3)	8193(1)	29(1)
N(3)	8628(1)	6166(2)	9240(1)	21(1)
C(5)	8737(1)	7264(3)	9043(1)	24(1)
C(6)	8674(2)	8317(3)	9341(1)	34(1)
C(7)	8482(2)	8202(4)	9864(2)	40(1)
C(8)	8357(2)	7071(3)	10079(1)	31(1)
C(9)	8447(1)	6074(3)	9749(1)	21(1)
N(4)	8364(1)	4856(3)	9909(1)	25(1)
N(5)	8545(1)	3943(3)	9576(1)	25(1)
C(10)	8157(2)	4387(4)	10377(2)	36(1)
C(11)	8209(2)	3162(4)	10344(2)	45(1)
C(12)	8447(2)	2907(3)	9844(1)	35(1)
C(13)	8600(2)	1702(4)	9611(2)	50(1)
N(6)	7811(1)	4173(3)	8454(1)	22(1)
N(7)	7748(1)	3091(2)	8169(1)	22(1)
C(14)	7172(2)	5653(4)	8851(2)	34(1)
C(15)	7282(1)	4507(3)	8547(1)	25(1)
C(16)	6876(1)	3626(3)	8328(1)	28(1)
C(17)	7186(1)	2748(3)	8088(1)	27(1)
C(18)	8242(1)	2482(3)	8023(1)	22(1)
N(8)	8727(1)	2967(2)	8269(1)	22(1)
C(19)	8229(2)	1478(3)	7674(1)	28(1)
C(20)	8753(2)	948(3)	7597(1)	30(1)
C(21)	9261(2)	1397(3)	7861(1)	29(1)
C(22)	9227(1)	2430(3)	8193(1)	24(1)
N(9)	9700(1)	3021(3)	8477(1)	26(1)

N(10)	9611(1)	4048(3)	8782(1)	28(1)
C(23)	10274(1)	2773(4)	8489(2)	32(1)
C(24)	10554(2)	3666(4)	8799(2)	34(1)
C(25)	10133(2)	4453(3)	8976(2)	32(1)
C(26)	10196(2)	5583(4)	9312(2)	44(1)
B(1)	7609(2)	4141(4)	6679(2)	29(1)
F(1)	8053(1)	3679(2)	6385(1)	39(1)
F(2)	7300(1)	4992(2)	6346(1)	45(1)
F(3)	7258(1)	3182(2)	6811(1)	41(1)
F(4)	7849(1)	4695(2)	7171(1)	36(1)
B(2)	5410(2)	4570(5)	8836(2)	43(1)
F(5)	5448(1)	4817(2)	8278(1)	47(1)
F(6)	4881(1)	5012(3)	8974(1)	66(1)
F(7)	5853(1)	5116(4)	9155(1)	84(1)
F(8)	5442(2)	3346(3)	8907(2)	118(2)
O(1)	9927(3)	2127(8)	5085(4)	47(2)

Table 10.4: Selected bond lengths [Å] and angles [°].

Fe(1)-N(3)	2.112(3)	N(8)-Fe(1)-N(6)	74.00(10)
Fe(1)-N(8)	2.116(3)	N(1)-Fe(1)-N(6)	104.77(10)
Fe(1)-N(1)	2.170(3)	N(3)-Fe(1)-N(10)	109.55(11)
Fe(1)-N(6)	2.178(3)	N(8)-Fe(1)-N(10)	73.64(11)
Fe(1)-N(10)	2.184(3)	N(1)-Fe(1)-N(10)	88.34(10)
Fe(1)-N(5)	2.195(3)	N(6)-Fe(1)-N(10)	147.56(11)
		N(3)-Fe(1)-N(5)	73.57(10)
N(3)-Fe(1)-N(8)	175.27(10)	N(8)-Fe(1)-N(5)	102.81(10)
N(3)-Fe(1)-N(1)	73.89(10)	N(1)-Fe(1)-N(5)	146.86(10)
N(8)-Fe(1)-N(1)	110.01(10)	N(6)-Fe(1)-N(5)	88.30(10)
N(3)-Fe(1)-N(6)	102.62(10)	N(10)-Fe(1)-N(5)	96.69(11)

Symmetry transformations used to generate equivalent atoms:

90 K in the mixed spin state

Table 10.5: Atomic coordinates ($\times 10^4$) and equivalent isotropic displacement parameters ($\text{\AA}^2 \times 10^3$). $U(\text{eq})$ is defined as one third of the trace of the orthogonalized U^{ij} tensor.

	x	y	z	U(eq)
Fe(1)	806(1)	2915(2)	441(1)	14(1)
N(1)	1044(2)	1602(8)	364(3)	12(2)
N(2)	962(2)	437(8)	439(3)	11(2)
C(1)	1434(2)	2421(12)	251(4)	26(3)
C(2)	1275(2)	1424(11)	327(3)	15(2)
C(3)	1341(2)	131(11)	382(3)	21(3)
C(4)	1143(2)	-399(12)	449(3)	21(3)
N(3)	623(2)	1465(8)	510(3)	14(2)
C(5)	724(2)	355(10)	496(3)	13(2)
C(6)	594(2)	-705(12)	548(4)	23(3)
C(7)	359(2)	-570(12)	598(4)	26(3)
C(8)	246(2)	564(10)	602(3)	18(3)
C(9)	389(2)	1568(10)	557(3)	13(2)
N(4)	318(2)	2820(9)	565(3)	17(2)
N(5)	503(2)	3690(9)	568(3)	19(2)
C(10)	107(2)	3358(11)	619(3)	22(3)
C(11)	154(2)	4577(12)	648(4)	26(3)
C(12)	404(2)	4772(12)	625(4)	23(3)
C(13)	542(2)	5967(13)	659(4)	38(3)
N(6)	1046(2)	3113(10)	1063(3)	25(2)
N(7)	1208(2)	4111(10)	1099(3)	26(2)
C(14)	1017(2)	1388(13)	1559(4)	38(3)
C(15)	1129(2)	2490(12)	1454(4)	24(3)
C(16)	1342(2)	3168(13)	1744(4)	36(3)
C(17)	1392(3)	4155(14)	1526(4)	38(3)
C(18)	1172(2)	4811(12)	722(4)	28(3)
N(8)	984(2)	4352(8)	369(3)	13(2)
C(19)	1305(2)	5855(13)	693(4)	37(3)
C(20)	1248(2)	6423(14)	274(4)	38(3)
C(21)	1050(2)	5942(12)	-94(4)	31(3)
C(22)	921(2)	4892(12)	-19(4)	24(3)

N(9)	720(2)	4320(9)	-337(3)	18(2)
N(10)	633(2)	3232(9)	-204(3)	18(2)
C(23)	579(2)	4583(12)	-765(4)	25(3)
C(24)	400(2)	3691(11)	-912(3)	17(3)
C(25)	439(2)	2843(10)	-560(3)	15(2)
C(26)	300(2)	1693(11)	-549(4)	23(3)
Fe(2)	2514(1)	3209(2)	1289(1)	19(1)
N(11)	2724(2)	3672(9)	1981(3)	19(2)
N(12)	2645(2)	4784(9)	2115(3)	20(2)
C(27)	3086(2)	2273(12)	2273(4)	27(3)
C(28)	2938(2)	3353(11)	2302(4)	22(3)
C(29)	3000(2)	4253(11)	2649(4)	21(3)
C(30)	2805(2)	5110(12)	2520(4)	26(3)
N(13)	2344(2)	4828(9)	1437(3)	15(2)
C(31)	2426(2)	5346(11)	1837(3)	19(3)
C(32)	2306(2)	6333(12)	1962(4)	28(3)
C(33)	2095(2)	6850(12)	1637(4)	27(3)
C(34)	2011(2)	6381(10)	1217(3)	16(2)
C(35)	2136(2)	5351(12)	1122(4)	23(3)
N(14)	2077(2)	4748(9)	719(3)	21(2)
N(15)	2212(2)	3729(10)	677(3)	25(2)
C(36)	1881(2)	5008(12)	326(4)	30(3)
C(37)	1895(2)	4089(12)	42(4)	25(3)
C(38)	2098(2)	3339(12)	259(4)	24(3)
C(39)	2190(2)	2193(13)	114(4)	36(3)
N(16)	2279(2)	1657(9)	1321(3)	16(2)
N(17)	2380(2)	553(9)	1240(3)	19(2)
C(40)	1877(2)	2307(12)	1412(4)	29(3)
C(41)	2047(2)	1362(11)	1333(3)	17(3)
C(42)	1995(2)	75(11)	1257(3)	21(3)
C(43)	2206(2)	-372(13)	1198(4)	27(3)
N(18)	2713(2)	1649(8)	1179(3)	13(2)
C(44)	2623(2)	541(11)	1185(3)	19(3)
C(45)	2752(3)	-527(14)	1155(4)	41(4)
C(46)	2991(3)	-374(15)	1114(5)	50(4)
C(47)	3096(2)	788(12)	1099(4)	30(3)
C(48)	2945(2)	1777(11)	1126(3)	18(3)
N(19)	3013(2)	3028(9)	1104(3)	18(2)

N(20)	2835(2)	3890(9)	1095(3)	16(2)
C(49)	3226(2)	3528(12)	1029(4)	29(3)
C(50)	3185(2)	4719(14)	983(4)	37(3)
C(51)	2937(2)	4953(12)	1016(4)	24(3)
C(52)	2806(2)	6121(13)	1000(4)	38(3)
Fe(3)	866(1)	2373(2)	2993(1)	19(1)
N(21)	592(2)	1864(10)	2355(3)	27(2)
N(22)	453(2)	816(10)	2372(3)	25(2)
C(53)	593(2)	3439(13)	1805(4)	36(3)
C(54)	490(2)	2319(11)	1946(3)	19(3)
C(55)	285(2)	1524(12)	1702(4)	27(3)
C(56)	270(2)	627(12)	1981(4)	28(3)
N(23)	694(2)	771(9)	3104(3)	15(2)
C(57)	504(2)	234(11)	2778(3)	20(3)
C(58)	371(2)	-782(12)	2848(4)	27(3)
C(59)	440(2)	-1260(12)	3277(4)	26(3)
C(60)	639(2)	-736(11)	3612(4)	23(3)
C(61)	763(2)	227(11)	3504(3)	20(3)
N(24)	971(2)	834(9)	3804(3)	19(2)
N(25)	1051(2)	1893(9)	3684(3)	20(2)
C(62)	1118(2)	495(11)	4214(3)	21(3)
C(63)	1302(2)	1392(11)	4367(4)	19(3)
C(64)	1257(2)	2265(11)	4024(4)	20(3)
C(65)	1396(2)	3422(12)	4017(4)	28(3)
N(26)	1213(2)	1767(10)	2868(3)	31(3)
N(27)	1381(2)	2686(10)	2869(3)	27(2)
C(66)	1239(3)	-464(19)	2902(6)	82(6)
C(67)	1353(3)	740(14)	2898(4)	38(3)
C(68)	1610(3)	1099(15)	2918(4)	46(4)
C(69)	1615(3)	2299(13)	2889(4)	38(4)
N(28)	1053(2)	3952(9)	2874(3)	19(2)
C(70)	1282(2)	3893(12)	2820(4)	25(3)
C(71)	1402(2)	4912(12)	2709(4)	28(3)
C(72)	1274(2)	6054(13)	2661(4)	35(3)
C(73)	1041(2)	6094(14)	2722(4)	36(3)
C(74)	936(2)	5067(11)	2837(3)	18(3)
N(29)	696(2)	4979(9)	2888(3)	19(2)
N(30)	614(2)	3878(9)	3002(3)	22(2)

C(75)	521(2)	5892(13)	2848(4)	30(3)
C(76)	315(2)	5384(12)	2940(4)	31(3)
C(77)	383(2)	4126(12)	3029(4)	29(3)
C(78)	224(2)	3123(13)	3129(4)	35(3)
B(1)	1992(3)	8041(14)	153(4)	26(3)
F(1)	2037(2)	9312(9)	96(3)	69(3)
F(2)	1779(1)	7926(7)	294(2)	35(2)
F(3)	2207(1)	7614(7)	469(2)	39(2)
F(4)	1944(2)	7488(8)	-247(3)	50(2)
B(2)	1351(2)	8027(13)	1564(4)	18(3)
F(5)	1113(1)	7964(8)	1258(2)	43(2)
F(6)	1357(2)	8636(11)	1943(3)	85(3)
F(7)	1526(2)	8319(11)	1374(3)	89(3)
F(8)	1430(2)	6870(11)	1728(4)	94(4)
B(3)	2187(3)	3741(14)	2664(4)	25(3)
F(9)	1927(1)	4049(7)	2448(2)	34(2)
F(10)	2330(1)	4734(7)	2841(2)	37(2)
F(11)	2280(1)	3146(7)	2348(2)	33(2)
F(12)	2190(1)	2830(7)	2994(2)	33(2)
B(4)	266(3)	6964(15)	1726(5)	30(4)
F(13)	115(1)	7604(8)	1917(3)	48(2)
F(14)	509(2)	7031(12)	1964(4)	103(4)
F(15)	164(2)	5759(11)	1676(4)	94(4)
F(16)	222(2)	7451(9)	1297(3)	60(2)
B(5)	1130(2)	6885(13)	3963(4)	17(3)
F(17)	1388(1)	6520(6)	4177(2)	27(2)
F(18)	1034(1)	7406(6)	4273(2)	25(2)
F(19)	988(1)	5839(7)	3789(2)	37(2)
F(20)	1122(1)	7701(8)	3635(2)	47(2)
B(6)	520(2)	1834(13)	4378(4)	16(3)
F(21)	627(1)	2402(6)	4098(2)	25(2)
F(22)	500(1)	2607(7)	4706(2)	30(2)
F(23)	276(1)	1374(6)	4140(2)	24(2)
F(24)	678(1)	823(6)	4581(2)	27(2)
O(1)	808(3)	9040(20)	1992(6)	50(5)
O(2)	2569(4)	9850(20)	122(8)	75(7)

Table 10.6: Selected bond lengths [Å] and angles [°]

Fe(1)-N(8)	1.910(9)	N(6)-Fe(1)-N(5)	94.6(4)
Fe(1)-N(3)	1.935(9)	N(1)-Fe(1)-N(5)	159.2(4)
Fe(1)-N(10)	2.005(8)		
Fe(1)-N(6)	2.012(9)	N(18)-Fe(2)-N(13)	175.2(3)
Fe(1)-N(1)	2.019(9)	N(18)-Fe(2)-N(16)	74.2(3)
Fe(1)-N(5)	2.030(9)	N(13)-Fe(2)-N(16)	109.2(3)
		N(18)-Fe(2)-N(20)	73.6(4)
Fe(2)-N(18)	2.123(9)	N(13)-Fe(2)-N(20)	103.6(4)
Fe(2)-N(13)	2.132(9)	N(16)-Fe(2)-N(20)	146.7(4)
Fe(2)-N(16)	2.164(9)	N(18)-Fe(2)-N(11)	102.8(3)
Fe(2)-N(20)	2.189(9)	N(13)-Fe(2)-N(11)	73.2(3)
Fe(2)-N(11)	2.198(9)	N(16)-Fe(2)-N(11)	105.2(3)
Fe(2)-N(15)	2.199(9)	N(20)-Fe(2)-N(11)	89.8(3)
		N(18)-Fe(2)-N(15)	110.3(3)
Fe(3)-N(23)	2.079(9)	N(13)-Fe(2)-N(15)	73.6(3)
Fe(3)-N(28)	2.114(10)	N(16)-Fe(2)-N(15)	87.1(3)
Fe(3)-N(30)	2.163(10)	N(20)-Fe(2)-N(15)	96.4(3)
Fe(3)-N(25)	2.177(9)	N(11)-Fe(2)-N(15)	146.8(4)
Fe(3)-N(21)	2.183(9)		
Fe(3)-N(26)	2.189(11)	N(23)-Fe(3)-N(28)	177.4(4)
		N(23)-Fe(3)-N(30)	108.1(4)
N(8)-Fe(1)-N(3)	179.4(4)	N(28)-Fe(3)-N(30)	74.5(4)
N(8)-Fe(1)-N(10)	79.9(4)	N(23)-Fe(3)-N(25)	73.4(3)
N(3)-Fe(1)-N(10)	99.5(4)	N(28)-Fe(3)-N(25)	106.5(3)
N(8)-Fe(1)-N(6)	80.3(4)	N(30)-Fe(3)-N(25)	105.3(3)
N(3)-Fe(1)-N(6)	100.3(4)	N(23)-Fe(3)-N(21)	74.2(4)
N(10)-Fe(1)-N(6)	160.2(4)	N(28)-Fe(3)-N(21)	105.8(4)
N(8)-Fe(1)-N(1)	101.0(4)	N(30)-Fe(3)-N(21)	87.3(4)
N(3)-Fe(1)-N(1)	79.3(4)	N(25)-Fe(3)-N(21)	147.5(4)
N(10)-Fe(1)-N(1)	96.3(4)	N(23)-Fe(3)-N(26)	104.5(4)
N(6)-Fe(1)-N(1)	87.2(4)	N(28)-Fe(3)-N(26)	72.8(4)
N(8)-Fe(1)-N(5)	99.8(4)	N(30)-Fe(3)-N(26)	147.1(4)
N(3)-Fe(1)-N(5)	79.9(4)	N(25)-Fe(3)-N(26)	87.6(4)
N(10)-Fe(1)-N(5)	89.1(4)	N(21)-Fe(3)-N(26)	97.8(4)

30 K in the high spin state after flash freezing

Table 10.7: Atomic coordinates ($\times 10^4$) and equivalent isotropic displacement parameters ($\text{\AA}^2 \times 10^3$).

U(eq) is defined as one third of the trace of the orthogonalized U^{ij} tensor.

	x	y	z	U(eq)
Fe(1)	8709(1)	4607(1)	8736(1)	12(1)
N(1)	8928(1)	6150(2)	8226(1)	13(1)
N(2)	8931(1)	7246(2)	8502(1)	13(1)
C(1)	9210(1)	5416(3)	7313(1)	19(1)
C(2)	9139(1)	6396(3)	7735(1)	16(1)
C(3)	9272(1)	7646(3)	7700(1)	17(1)
C(4)	9137(1)	8157(3)	8191(1)	17(1)
N(3)	8629(1)	6185(2)	9240(1)	13(1)
C(5)	8737(1)	7289(3)	9040(1)	13(1)
C(6)	8669(2)	8352(3)	9336(1)	20(1)
C(7)	8467(2)	8233(3)	9860(1)	21(1)
C(8)	8345(1)	7094(3)	10078(1)	16(1)
C(9)	8441(1)	6092(3)	9750(1)	14(1)
N(4)	8361(1)	4872(2)	9908(1)	14(1)
N(5)	8550(1)	3949(2)	9578(1)	16(1)
C(10)	8149(2)	4404(3)	10379(1)	22(1)
C(11)	8205(2)	3160(3)	10348(1)	28(1)
C(12)	8457(2)	2911(3)	9846(1)	22(1)
C(13)	8624(2)	1700(3)	9616(2)	29(1)
N(6)	7808(1)	4181(2)	8451(1)	14(1)
N(7)	7741(1)	3087(2)	8167(1)	14(1)
C(14)	7169(1)	5671(3)	8851(1)	17(1)
C(15)	7277(1)	4509(3)	8548(1)	15(1)
C(16)	6868(1)	3624(3)	8333(1)	17(1)
C(17)	7180(1)	2743(3)	8091(1)	17(1)
C(18)	8236(1)	2482(3)	8021(1)	14(1)
N(8)	8726(1)	2964(2)	8268(1)	14(1)
C(19)	8217(1)	1476(3)	7667(1)	16(1)
C(20)	8746(1)	946(3)	7586(1)	18(1)
C(21)	9258(1)	1394(3)	7854(1)	16(1)
C(22)	9226(1)	2427(3)	8189(1)	14(1)
N(9)	9704(1)	3014(2)	8477(1)	15(1)

N(10)	9616(1)	4040(2)	8786(1)	16(1)
C(23)	10280(1)	2766(3)	8485(1)	18(1)
C(24)	10566(1)	3660(3)	8802(1)	19(1)
C(25)	10142(1)	4435(3)	8982(1)	18(1)
C(26)	10211(1)	5568(3)	9328(1)	23(1)
B(1)	7610(2)	4135(3)	6687(1)	15(1)
F(1)	8051(1)	3670(2)	6382(1)	18(1)
F(2)	7296(1)	5009(2)	6349(1)	19(1)
F(3)	7253(1)	3186(2)	6818(1)	19(1)
F(4)	7862(1)	4696(2)	7178(1)	17(1)
B(2)	5396(2)	4596(4)	8839(2)	31(1)
F(5)	5444(1)	4822(2)	8273(1)	26(1)
F(6)	4866(1)	5091(2)	8964(1)	35(1)
F(7)	5849(1)	5148(3)	9165(1)	53(1)
F(8)	5407(1)	3372(3)	8937(2)	67(1)
O(1)	9899(3)	2206(7)	5080(3)	25(2)

Table 10.8: Selected bond lengths [Å] and angles

Fe(1)-N(8)	2.117(3)	N(3)-Fe(1)-N(6)	102.23(9)
Fe(1)-N(3)	2.121(3)	N(1)-Fe(1)-N(6)	105.43(9)
Fe(1)-N(1)	2.170(3)	N(8)-Fe(1)-N(10)	73.60(10)
Fe(1)-N(6)	2.181(3)	N(3)-Fe(1)-N(10)	109.88(10)
Fe(1)-N(10)	2.187(3)	N(1)-Fe(1)-N(10)	88.26(9)
Fe(1)-N(5)	2.198(3)	N(6)-Fe(1)-N(10)	147.54(10)
		N(8)-Fe(1)-N(5)	102.52(9)
N(8)-Fe(1)-N(3)	174.87(9)	N(3)-Fe(1)-N(5)	73.59(9)
N(8)-Fe(1)-N(1)	110.30(9)	N(1)-Fe(1)-N(5)	146.79(9)
N(3)-Fe(1)-N(1)	73.93(9)	N(6)-Fe(1)-N(5)	88.07(10)
N(8)-Fe(1)-N(6)	74.05(10)	N(10)-Fe(1)-N(5)	96.32(10)

Symmetry transformations used to generate equivalent atoms:

30 K in the mixed spin state

Table 10.9: Atomic coordinates ($\times 10^4$) and equivalent isotropic displacement parameters ($\text{\AA}^2 \times 10^3$). U(eq) is defined as one third of the trace of the orthogonalized U^{ij} tensor.

	x	y	z	U(eq)
Fe(1)	805(1)	2892(1)	436(1)	10(1)
N(1)	1045(1)	1563(5)	363(2)	10(1)
N(2)	961(1)	404(6)	441(2)	12(1)
C(1)	1437(2)	2411(7)	252(3)	21(2)
C(2)	1280(2)	1377(7)	331(2)	17(2)
C(3)	1344(2)	123(8)	387(3)	22(2)
C(4)	1140(2)	-468(7)	453(2)	17(2)
N(3)	621(1)	1444(5)	502(2)	11(1)
C(5)	717(2)	329(7)	496(2)	13(2)
C(6)	593(2)	-740(7)	546(2)	16(2)
C(7)	355(2)	-623(7)	594(2)	16(2)
C(8)	247(2)	529(7)	595(2)	13(2)
C(9)	386(1)	1539(6)	551(2)	7(1)
N(4)	316(1)	2773(5)	558(2)	11(1)
N(5)	503(1)	3648(5)	569(2)	10(1)
C(10)	103(2)	3313(7)	606(2)	15(2)
C(11)	150(2)	4552(7)	644(2)	19(2)
C(12)	400(2)	4730(7)	623(2)	16(2)
C(13)	545(2)	5902(7)	661(3)	21(2)
N(6)	1047(2)	3091(7)	1064(2)	29(2)
N(7)	1205(2)	4068(7)	1101(2)	32(2)
C(14)	1010(2)	1353(9)	1549(3)	38(2)
C(15)	1126(2)	2452(9)	1458(3)	34(2)
C(16)	1341(2)	3061(11)	1745(4)	49(3)
C(17)	1392(2)	4044(10)	1539(3)	40(2)
C(18)	1173(2)	4782(9)	723(3)	33(2)
N(8)	980(1)	4343(6)	365(2)	20(1)
C(19)	1310(2)	5818(10)	687(3)	39(2)
C(20)	1251(2)	6369(10)	287(3)	43(3)
C(21)	1052(2)	5945(9)	-99(3)	35(2)
C(22)	921(2)	4901(8)	-27(3)	24(2)

N(9)	718(1)	4324(6)	-348(2)	18(1)
N(10)	630(1)	3228(6)	-222(2)	17(1)
C(23)	578(2)	4629(7)	-772(2)	18(2)
C(24)	395(2)	3729(7)	-923(2)	16(2)
C(25)	438(2)	2862(7)	-571(2)	17(2)
C(26)	298(2)	1694(7)	-563(2)	17(2)
Fe(2)	2515(1)	3162(1)	1292(1)	11(1)
N(11)	2728(1)	3636(5)	1986(2)	12(1)
N(12)	2648(1)	4719(6)	2121(2)	13(1)
C(27)	3086(2)	2184(7)	2278(2)	17(2)
C(28)	2941(2)	3324(7)	2304(2)	14(2)
C(29)	3002(2)	4211(7)	2653(2)	14(2)
C(30)	2811(2)	5072(7)	2524(2)	16(2)
N(13)	2349(1)	4792(6)	1435(2)	12(1)
C(31)	2426(2)	5310(7)	1840(2)	14(2)
C(32)	2308(2)	6291(7)	1965(2)	16(2)
C(33)	2101(2)	6803(7)	1642(2)	17(2)
C(34)	2016(2)	6331(7)	1212(2)	14(2)
C(35)	2144(2)	5320(7)	1124(2)	12(2)
N(14)	2079(1)	4719(6)	713(2)	13(1)
N(15)	2215(1)	3690(6)	673(2)	15(1)
C(36)	1887(2)	4959(7)	327(2)	18(2)
C(37)	1895(2)	4051(7)	34(2)	17(2)
C(38)	2102(2)	3278(7)	263(2)	15(2)
C(39)	2194(2)	2131(8)	103(3)	22(2)
N(16)	2278(1)	1583(5)	1316(2)	11(1)
N(17)	2377(1)	485(5)	1230(2)	11(1)
C(40)	1874(2)	2283(7)	1408(3)	20(2)
C(41)	2045(2)	1313(7)	1325(2)	12(2)
C(42)	1989(2)	42(7)	1243(2)	17(2)
C(43)	2205(2)	-449(7)	1190(2)	17(2)
N(18)	2714(1)	1586(5)	1178(2)	11(1)
C(44)	2620(2)	475(7)	1183(2)	13(2)
C(45)	2749(2)	-579(8)	1135(3)	25(2)
C(46)	2986(2)	-445(9)	1094(3)	28(2)
C(47)	3096(2)	709(7)	1095(2)	20(2)
C(48)	2948(2)	1702(6)	1129(2)	11(1)
N(19)	3019(1)	2937(6)	1111(2)	12(1)

N(20)	2839(1)	3846(6)	1099(2)	12(1)
C(49)	3231(2)	3444(7)	1046(2)	18(2)
C(50)	3191(2)	4672(8)	998(2)	20(2)
C(51)	2947(2)	4890(7)	1029(2)	16(2)
C(52)	2808(2)	6089(7)	1000(3)	21(2)
Fe(3)	864(1)	2362(1)	2986(1)	13(1)
N(21)	593(1)	1836(6)	2347(2)	15(1)
N(22)	449(1)	817(6)	2368(2)	16(1)
C(53)	593(2)	3407(8)	1794(3)	22(2)
C(54)	491(2)	2271(7)	1938(2)	17(2)
C(55)	284(2)	1503(7)	1689(3)	20(2)
C(56)	265(2)	605(8)	1973(3)	22(2)
N(23)	692(1)	723(6)	3101(2)	15(1)
C(57)	501(2)	201(7)	2777(2)	15(2)
C(58)	371(2)	-825(7)	2848(2)	18(2)
C(59)	441(2)	-1283(8)	3273(2)	20(2)
C(60)	640(2)	-767(7)	3615(2)	16(2)
C(61)	763(2)	229(7)	3507(2)	13(2)
N(24)	974(1)	830(6)	3804(2)	12(1)
N(25)	1053(1)	1925(6)	3678(2)	14(1)
C(62)	1121(2)	486(7)	4217(2)	18(2)
C(63)	1306(2)	1389(8)	4365(3)	21(2)
C(64)	1254(2)	2263(8)	4021(3)	22(2)
C(65)	1395(2)	3443(8)	4009(3)	25(2)
N(26)	1208(1)	1729(6)	2857(2)	20(1)
N(27)	1379(1)	2674(6)	2862(2)	18(1)
C(66)	1233(3)	-528(12)	2877(4)	60(3)
C(67)	1353(2)	729(9)	2886(3)	32(2)
C(68)	1605(2)	1031(9)	2905(3)	35(2)
C(69)	1613(2)	2253(8)	2884(3)	25(2)
N(28)	1049(1)	3950(6)	2869(2)	16(1)
C(70)	1279(2)	3881(7)	2813(2)	16(2)
C(71)	1405(2)	4881(7)	2714(2)	20(2)
C(72)	1273(2)	6019(8)	2655(3)	24(2)
C(73)	1039(2)	6101(8)	2716(3)	22(2)
C(74)	934(2)	5047(7)	2822(2)	16(2)
N(29)	691(1)	4980(6)	2879(2)	15(1)
N(30)	611(1)	3874(6)	2995(2)	18(1)

C(75)	512(2)	5862(8)	2843(2)	20(2)
C(76)	313(2)	5347(8)	2931(3)	23(2)
C(77)	378(2)	4087(8)	3022(3)	23(2)
C(78)	218(2)	3103(8)	3125(3)	29(2)
B(1)	1995(2)	8002(9)	141(3)	19(2)
F(1)	2040(1)	9236(5)	79(2)	38(1)
F(2)	1781(1)	7882(4)	288(2)	24(1)
F(3)	2210(1)	7520(4)	469(1)	23(1)
F(4)	1950(1)	7383(5)	-257(2)	35(1)
B(2)	1354(2)	7985(9)	1562(3)	20(2)
F(5)	1113(1)	7899(5)	1253(2)	34(1)
F(6)	1355(2)	8556(7)	1942(2)	67(2)
F(7)	1530(2)	8189(7)	1373(2)	70(2)
F(8)	1418(2)	6730(8)	1729(3)	76(2)
B(3)	2186(2)	3693(8)	2666(3)	18(2)
F(9)	1928(1)	4045(4)	2454(1)	20(1)
F(10)	2333(1)	4703(4)	2850(1)	22(1)
F(11)	2276(1)	3116(4)	2350(1)	20(1)
F(12)	2190(1)	2817(4)	3000(1)	21(1)
B(4)	264(2)	7022(11)	1729(4)	33(2)
F(13)	111(1)	7607(5)	1919(2)	31(1)
F(14)	514(2)	7136(12)	1987(4)	133(4)
F(15)	190(2)	5767(8)	1701(3)	76(2)
F(16)	228(1)	7428(6)	1297(2)	48(2)
B(5)	1130(2)	6860(8)	3965(3)	15(2)
F(17)	1385(1)	6480(4)	4175(1)	17(1)
F(18)	1034(1)	7400(4)	4276(1)	17(1)
F(19)	983(1)	5825(4)	3779(1)	22(1)
F(20)	1126(1)	7693(4)	3634(2)	26(1)
B(6)	526(2)	1808(8)	4378(3)	16(2)
F(21)	629(1)	2410(4)	4090(1)	20(1)
F(22)	505(1)	2620(4)	4709(1)	19(1)
F(23)	278(1)	1366(4)	4142(1)	16(1)
F(24)	681(1)	813(4)	4578(1)	18(1)
O(1)	811(3)	8950(16)	1993(5)	60(5)
O(2)	2578(4)	9806(17)	127(6)	65(5)

Table 10.10: Selected bond lengths [Å] and angles [°].

Fe(1)-N(8)	1.898(7)	N(5)-Fe(1)-N(10)	89.6(2)
Fe(1)-N(3)	1.920(6)	N(1)-Fe(1)-N(10)	97.0(2)
Fe(1)-N(6)	2.015(7)		
Fe(1)-N(5)	2.016(6)	N(13)-Fe(2)-N(18)	175.2(2)
Fe(1)-N(1)	2.019(6)	N(13)-Fe(2)-N(16)	110.4(2)
Fe(1)-N(10)	2.027(6)	N(18)-Fe(2)-N(16)	73.4(2)
		N(13)-Fe(2)-N(20)	102.9(2)
Fe(2)-N(13)	2.110(6)	N(18)-Fe(2)-N(20)	73.6(2)
Fe(2)-N(18)	2.124(6)	N(16)-Fe(2)-N(20)	146.0(2)
Fe(2)-N(16)	2.173(6)	N(13)-Fe(2)-N(11)	73.4(2)
Fe(2)-N(20)	2.190(6)	N(18)-Fe(2)-N(11)	103.0(2)
Fe(2)-N(11)	2.190(6)	N(16)-Fe(2)-N(11)	106.4(2)
Fe(2)-N(15)	2.191(6)	N(20)-Fe(2)-N(11)	89.1(2)
		N(13)-Fe(2)-N(15)	73.7(2)
Fe(3)-N(28)	2.097(7)	N(18)-Fe(2)-N(15)	109.7(2)
Fe(3)-N(23)	2.101(6)	N(16)-Fe(2)-N(15)	87.2(2)
Fe(3)-N(25)	2.153(6)	N(20)-Fe(2)-N(15)	95.9(2)
Fe(3)-N(30)	2.158(7)	N(11)-Fe(2)-N(15)	147.0(2)
Fe(3)-N(21)	2.166(6)		
Fe(3)-N(26)	2.175(7)	N(28)-Fe(3)-N(23)	177.3(3)
		N(28)-Fe(3)-N(25)	105.0(2)
N(8)-Fe(1)-N(3)	178.7(3)	N(23)-Fe(3)-N(25)	74.5(2)
N(8)-Fe(1)-N(6)	80.3(3)	N(28)-Fe(3)-N(30)	74.2(3)
N(3)-Fe(1)-N(6)	100.4(3)	N(23)-Fe(3)-N(30)	108.6(3)
N(8)-Fe(1)-N(5)	99.7(3)	N(25)-Fe(3)-N(30)	104.8(2)
N(3)-Fe(1)-N(5)	79.2(3)	N(28)-Fe(3)-N(21)	106.1(2)
N(6)-Fe(1)-N(5)	94.1(3)	N(23)-Fe(3)-N(21)	74.3(2)
N(8)-Fe(1)-N(1)	101.9(3)	N(25)-Fe(3)-N(21)	148.6(2)
N(3)-Fe(1)-N(1)	79.2(3)	N(30)-Fe(3)-N(21)	87.9(2)
N(6)-Fe(1)-N(1)	86.9(3)	N(28)-Fe(3)-N(26)	74.0(3)
N(5)-Fe(1)-N(1)	158.2(2)	N(23)-Fe(3)-N(26)	103.3(3)
N(8)-Fe(1)-N(10)	79.6(3)	N(25)-Fe(3)-N(26)	87.7(2)
N(3)-Fe(1)-N(10)	99.7(3)	N(30)-Fe(3)-N(26)	147.9(3)
N(6)-Fe(1)-N(10)	159.9(3)	N(21)-Fe(3)-N(26)	96.6(2)

Symmetry transformations used to generate equivalent atoms:

30 K in the high spin state after irradiation

Table 10.11: Atomic coordinates ($\times 10^4$) and equivalent isotropic displacement parameters ($\text{\AA}^2 \times 10^3$).

$U(\text{eq})$ is defined as one third of the trace of the orthogonalized U^{ij} tensor.

	x	y	z	U(eq)
Fe(1)	8711(1)	4606(1)	8727(1)	9(1)
N(1)	8936(1)	6148(2)	8215(1)	11(1)
N(2)	8939(1)	7245(1)	8493(1)	10(1)
C(1)	9213(1)	5421(2)	7298(1)	16(1)
C(2)	9144(1)	6396(2)	7724(1)	12(1)
C(3)	9276(1)	7646(2)	7687(1)	13(1)
C(4)	9141(1)	8151(2)	8181(1)	13(1)
N(3)	8632(1)	6183(2)	9231(1)	10(1)
C(5)	8742(1)	7285(2)	9033(1)	11(1)
C(6)	8672(1)	8349(2)	9329(1)	16(1)
C(7)	8467(1)	8232(2)	9852(1)	18(1)
C(8)	8339(1)	7096(2)	10069(1)	13(1)
C(9)	8439(1)	6094(2)	9740(1)	10(1)
N(4)	8355(1)	4873(2)	9903(1)	11(1)
N(5)	8552(1)	3955(2)	9576(1)	12(1)
C(10)	8138(1)	4415(2)	10370(1)	14(1)
C(11)	8194(1)	3176(2)	10344(1)	17(1)
C(12)	8455(1)	2924(2)	9847(1)	14(1)
C(13)	8621(1)	1712(2)	9621(1)	18(1)
N(6)	7802(1)	4188(2)	8449(1)	11(1)
N(7)	7733(1)	3092(2)	8167(1)	10(1)
C(14)	7165(1)	5681(2)	8851(1)	14(1)
C(15)	7268(1)	4518(2)	8553(1)	12(1)
C(16)	6856(1)	3631(2)	8342(1)	13(1)
C(17)	7168(1)	2748(2)	8099(1)	12(1)
C(18)	8229(1)	2486(2)	8018(1)	10(1)
N(8)	8724(1)	2960(2)	8262(1)	10(1)
C(19)	8212(1)	1482(2)	7664(1)	12(1)
C(20)	8740(1)	942(2)	7586(1)	13(1)
C(21)	9258(1)	1388(2)	7852(1)	12(1)
C(22)	9225(1)	2418(2)	8185(1)	10(1)
N(9)	9710(1)	2997(2)	8473(1)	11(1)

N(10)	9622(1)	4030(2)	8780(1)	11(1)
C(23)	10286(1)	2741(2)	8483(1)	13(1)
C(24)	10578(1)	3625(2)	8801(1)	14(1)
C(25)	10148(1)	4410(2)	8978(1)	12(1)
C(26)	10225(1)	5547(2)	9324(1)	18(1)
B(1)	7604(1)	4138(2)	6683(1)	13(1)
F(1)	8037(1)	3660(1)	6372(1)	15(1)
F(2)	7286(1)	5015(1)	6353(1)	17(1)
F(3)	7242(1)	3201(1)	6827(1)	16(1)
F(4)	7868(1)	4697(1)	7173(1)	15(1)
B(2)	5377(1)	4616(2)	8855(1)	19(1)
F(5)	5447(1)	4814(1)	8281(1)	19(1)
F(6)	4845(1)	5115(1)	8968(1)	20(1)
F(7)	5830(1)	5186(1)	9183(1)	31(1)
F(8)	5388(1)	3378(1)	8963(1)	38(1)
O(1)	9896(2)	2238(4)	5085(2)	11(1)

Table 10.12: Selected bond lengths [\AA] and angles [$^\circ$].

Fe(1)-N(8)	2.1161(17)	N(3)-Fe(1)-N(10)	109.79(6)
Fe(1)-N(3)	2.1204(17)	N(1)-Fe(1)-N(10)	88.55(7)
Fe(1)-N(1)	2.1745(17)	N(8)-Fe(1)-N(6)	74.07(7)
Fe(1)-N(10)	2.1853(18)	N(3)-Fe(1)-N(6)	102.00(7)
Fe(1)-N(6)	2.1863(18)	N(1)-Fe(1)-N(6)	105.52(6)
Fe(1)-N(5)	2.2054(17)	N(10)-Fe(1)-N(6)	147.77(6)
		N(8)-Fe(1)-N(5)	102.48(6)
N(8)-Fe(1)-N(3)	174.54(7)	N(3)-Fe(1)-N(5)	73.37(6)
N(8)-Fe(1)-N(1)	110.57(6)	N(1)-Fe(1)-N(5)	146.53(6)
N(3)-Fe(1)-N(1)	73.96(7)	N(10)-Fe(1)-N(5)	95.75(7)
N(8)-Fe(1)-N(10)	73.85(6)	N(6)-Fe(1)-N(5)	88.20(7)

Symmetry transformations used to generate equivalent atoms:

30 K in the low spin state

Table 10.13: Atomic coordinates ($\times 10^4$) and equivalent isotropic displacement parameters ($\text{\AA}^2 \times 10^3$). $U(\text{eq})$ is defined as one third of the trace of the orthogonalized U^{ij} tensor.

	x	y	z	U(eq)
Fe(1)	8692(1)	4561(1)	8787(1)	18(1)
N(1)	8889(2)	5922(6)	8248(2)	22(1)
N(2)	8876(2)	7077(5)	8495(2)	22(1)
C(1)	9194(3)	5101(9)	7360(3)	35(2)
C(2)	9093(3)	6089(8)	7751(2)	27(2)
C(3)	9218(3)	7350(8)	7682(3)	36(2)
C(4)	9077(3)	7962(8)	8154(3)	32(2)
N(3)	8583(2)	6027(6)	9233(2)	18(1)
C(5)	8692(3)	7160(7)	9029(2)	21(1)
C(6)	8617(3)	8199(7)	9325(3)	32(2)
C(7)	8437(4)	8093(7)	9862(3)	34(2)
C(8)	8314(3)	6935(7)	10084(3)	29(2)
C(9)	8400(3)	5937(7)	9751(2)	20(1)
N(4)	8326(3)	4713(6)	9907(2)	23(1)
N(5)	8516(2)	3818(5)	9540(2)	20(1)
C(10)	8161(3)	4179(8)	10383(3)	30(2)
C(11)	8259(3)	2930(7)	10325(3)	32(2)
C(12)	8470(4)	2751(8)	9805(3)	36(2)
C(13)	8642(4)	1558(8)	9557(3)	39(2)
N(6)	7845(2)	4228(6)	8493(2)	26(1)
N(7)	7799(3)	3163(6)	8192(2)	30(2)
C(14)	7150(4)	5764(9)	8841(3)	42(2)
C(15)	7298(3)	4626(7)	8545(3)	28(2)
C(16)	6892(3)	3783(9)	8277(3)	38(2)
C(17)	7224(3)	2878(8)	8061(3)	35(2)
C(18)	8308(3)	2541(7)	8071(3)	32(2)
N(8)	8784(3)	3085(7)	8346(2)	33(2)
C(19)	8361(4)	1567(8)	7739(3)	39(2)
C(20)	8902(5)	1066(9)	7689(4)	54(3)
C(21)	9394(4)	1554(10)	7979(4)	57(3)
C(22)	9308(4)	2618(8)	8311(3)	42(2)

N(9)	9736(3)	3273(8)	8626(3)	51(2)
N(10)	9563(3)	4318(7)	8917(3)	38(2)
C(23)	10364(4)	3199(12)	8687(4)	78(5)
C(24)	10532(5)	4168(13)	9001(4)	61(3)
C(25)	10056(4)	4844(12)	9137(4)	63(4)
C(26)	10049(4)	5990(11)	9461(4)	61(3)
B(1)	7610(3)	4253(7)	6695(3)	22(2)
F(1)	8111(2)	3858(4)	6408(2)	25(1)
F(2)	7291(2)	5062(4)	6354(2)	33(1)
F(3)	7283(2)	3202(4)	6804(2)	34(1)
F(4)	7807(2)	4826(4)	7191(2)	30(1)
B(2)	5426(4)	4491(8)	8844(3)	28(2)
F(5)	5521(4)	4943(8)	8334(3)	94(2)
F(6)	4862(3)	4693(5)	8974(2)	57(2)
F(7)	5843(4)	4797(8)	9213(4)	101(2)
F(8)	5482(5)	3242(10)	8686(4)	139(4)
O(1)	9908(8)	1633(19)	5155(8)	53(5)

Table 10.14: Selected bond lengths [Å] and angles [°].

Fe(1)-N(8)	1.938(7)	N(3)-Fe(1)-N(1)	78.5(2)
Fe(1)-N(3)	1.941(6)	N(10)-Fe(1)-N(1)	86.3(2)
Fe(1)-N(10)	2.006(6)	N(8)-Fe(1)-N(6)	78.4(2)
Fe(1)-N(1)	2.034(6)	N(3)-Fe(1)-N(6)	100.5(2)
Fe(1)-N(6)	2.041(6)	N(10)-Fe(1)-N(6)	158.9(3)
Fe(1)-N(5)	2.042(5)	N(1)-Fe(1)-N(6)	98.7(2)
		N(8)-Fe(1)-N(5)	101.1(2)
N(8)-Fe(1)-N(3)	178.7(2)	N(3)-Fe(1)-N(5)	78.1(2)
N(8)-Fe(1)-N(10)	80.4(3)	N(10)-Fe(1)-N(5)	93.6(2)
N(3)-Fe(1)-N(10)	100.6(3)	N(1)-Fe(1)-N(5)	156.2(2)
N(8)-Fe(1)-N(1)	102.3(2)	N(6)-Fe(1)-N(5)	90.0(2)

Symmetry transformations used to generate equivalent atoms:

A.11. [FeL5₂](ClO₄)₂**250 K in the high spin state****Table 11.1:** Atomic coordinates (x 10⁴) and equivalent isotropic displacement parameters (Å²x 10³). U(eq) is defined as one third of the trace of the orthogonalized U^{ij} tensor.

	x	y	z	U(eq)
Fe(1)	10000	0	0	46(1)
N(3)	10000	0	1195(3)	48(1)
C(4)	8491(7)	3446(6)	1294(4)	67(2)
N(2)	9056(5)	2181(5)	1101(3)	55(1)
N(1)	9205(4)	2027(5)	359(3)	52(1)
C(5)	9528(6)	1105(5)	1570(3)	52(1)
C(1)	8728(5)	3220(5)	74(4)	57(1)
C(7)	10000	0	2719(5)	102(4)
C(2)	8287(6)	4147(5)	629(4)	60(2)
C(3)	7687(7)	5582(7)	539(6)	92(2)
C(6)	9493(8)	1162(8)	2351(4)	76(2)
Cl(1)	-348(5)	5296(6)	3191(2)	99(2)
O(1)	1160(13)	5802(13)	3228(7)	202(5)
O(3)	-657(13)	6158(13)	3737(7)	101(3)
O(2)	-850(20)	5750(20)	2495(10)	157(5)

Table 11.2: Selected bond lengths [Å] and angles [°].

Fe(1)-N(3)#1	2.143(5)	N(3)-Fe(1)-N(1)#2	107.14(12)
Fe(1)-N(3)	2.143(5)	N(3)#1-Fe(1)-N(1)	107.14(12)
Fe(1)-N(1)#2	2.184(5)	N(3)-Fe(1)-N(1)	72.86(12)
Fe(1)-N(1)	2.184(5)	N(1)#2-Fe(1)-N(1)	94.98(7)
Fe(1)-N(1)#3	2.184(5)	N(3)#1-Fe(1)-N(1)#3	107.14(12)
Fe(1)-N(1)#1	2.184(5)	N(3)-Fe(1)-N(1)#3	72.86(12)
		N(1)#2-Fe(1)-N(1)#3	94.98(7)
N(3)#1-Fe(1)-N(3)	180.0	N(1)-Fe(1)-N(1)#3	145.7(2)
N(3)#1-Fe(1)-N(1)#2	72.86(12)	N(3)#1-Fe(1)-N(1)#1	72.86(12)

N(3)-Fe(1)-N(1)#1	107.14(12)	N(1)-Fe(1)-N(1)#1	94.98(7)
N(1)#2-Fe(1)-N(1)#1	145.7(2)	N(1)#3-Fe(1)-N(1)#1	94.98(7)

Symmetry transformations used to generate equivalent atoms:

#1 $y+1, -x+1, -z$ #2 $-y+1, x-1, -z$ #3 $-x+2, -y, z$

#4 $-x, -y+1, z$

30 K in the low spin state

Table 11.3: Atomic coordinates ($\times 10^4$) and equivalent isotropic displacement parameters ($\text{\AA}^2 \times 10^3$).

U(eq) is defined as one third of the trace of the orthogonalized U^{ij} tensor.

	x	y	z	U(eq)
Fe(1)	2974(2)	507(1)	1248(1)	5(1)
N(1)	1111(10)	-243(9)	1183(3)	11(2)
N(2)	736(10)	-520(11)	794(3)	13(2)
C(1)	0(11)	-656(11)	1395(3)	8(2)
C(2)	-1080(12)	-1153(12)	1140(3)	13(2)
C(3)	-2504(11)	-1677(11)	1262(4)	14(2)
C(4)	-542(12)	-1031(12)	753(4)	14(2)
N(3)	2876(9)	393(9)	682(2)	7(2)
C(5)	1750(11)	-156(11)	507(3)	9(2)
C(6)	1632(12)	-282(11)	100(3)	13(2)
C(7)	2771(13)	137(11)	-129(3)	16(2)
C(8)	3945(13)	699(12)	44(3)	16(2)
C(9)	3963(11)	802(11)	452(3)	11(2)
N(4)	5055(10)	1330(9)	698(3)	9(2)
N(5)	4841(10)	1243(10)	1105(3)	13(2)
C(10)	6351(14)	1789(13)	610(4)	19(3)
C(11)	6997(13)	2053(11)	964(3)	14(2)
C(12)	8425(12)	2607(12)	1016(4)	15(2)
C(13)	6008(11)	1713(11)	1265(3)	11(2)
N(6)	2206(10)	2391(9)	1357(3)	10(2)
N(7)	2039(10)	2632(9)	1756(3)	10(2)
C(14)	1723(11)	3534(11)	1174(3)	10(2)
C(15)	1229(11)	4502(12)	1461(3)	12(2)

C(16)	575(14)	5903(13)	1397(4)	21(3)
C(17)	1367(13)	3875(13)	1821(4)	18(2)
N(8)	2987(10)	506(9)	1818(2)	9(2)
C(18)	2462(12)	1571(11)	2021(3)	11(2)
C(19)	2335(12)	1599(12)	2425(3)	14(2)
C(20)	2815(11)	439(11)	2634(3)	12(2)
C(21)	3405(12)	-698(12)	2427(3)	14(2)
C(22)	3434(11)	-608(11)	2016(3)	9(2)
N(9)	3858(10)	-1648(10)	1748(3)	11(2)
N(10)	3699(10)	-1364(9)	1348(3)	10(2)
C(23)	4318(13)	-2977(12)	1800(4)	15(2)
C(24)	4510(13)	-3540(12)	1429(4)	14(2)
C(25)	5028(13)	-4995(12)	1340(4)	17(2)
C(26)	4115(12)	-2516(11)	1150(3)	12(2)
Cl(1)	2276(3)	5892(3)	189(1)	14(1)
O(1)	2481(9)	4416(9)	232(3)	24(2)
O(2)	3620(9)	6607(9)	219(3)	18(2)
O(3)	1660(8)	6174(8)	-195(2)	14(2)
O(4)	1368(10)	6382(9)	494(3)	21(2)
Cl(2)	8037(3)	1094(3)	2277(1)	16(1)
O(5)	8579(8)	-296(8)	2260(2)	14(2)
O(6)	6538(9)	1062(9)	2257(3)	19(2)
O(7)	8437(9)	1644(9)	2669(3)	16(2)
O(8)	8544(9)	1957(9)	1958(3)	20(2)

Table 11.4: Selected bond lengths [Å] and angles [°].

Fe(1)-N(3)	1.897(8)		
Fe(1)-N(8)	1.911(8)	N(3)-Fe(1)-N(8)	175.8(4)
Fe(1)-N(1)	1.941(9)	N(3)-Fe(1)-N(1)	79.7(4)
Fe(1)-N(10)	1.960(9)	N(8)-Fe(1)-N(1)	96.7(4)
Fe(1)-N(5)	1.985(10)	N(3)-Fe(1)-N(10)	97.8(4)
Fe(1)-N(6)	1.991(9)	N(8)-Fe(1)-N(10)	79.9(4)
N(1)-C(1)	1.342(14)	N(1)-Fe(1)-N(10)	90.2(4)
N(1)-N(2)	1.378(12)	N(3)-Fe(1)-N(5)	79.9(4)
N(2)-C(4)	1.329(15)	N(8)-Fe(1)-N(5)	103.6(4)
N(2)-C(5)	1.412(14)	N(1)-Fe(1)-N(5)	159.7(4)

N(10)-Fe(1)-N(5)	92.8(4)	N(1)-Fe(1)-N(6)	91.0(4)
N(3)-Fe(1)-N(6)	102.5(4)	N(10)-Fe(1)-N(6)	159.5(4)
N(8)-Fe(1)-N(6)	79.6(4)	N(5)-Fe(1)-N(6)	93.1(4)

Symmetry transformations used to generate equivalent atoms:

A.12. $[\text{FeL}_6]_2(\text{BF}_4)_2$

120 K in the low spin state

Table 12.1: Atomic coordinates ($\times 10^4$) and equivalent isotropic displacement parameters ($\text{\AA}^2 \times 10^3$).

U(eq) is defined as one third of the trace of the orthogonalized U^{ij} tensor.

	x	y	z	U(eq)
Fe(1)	7880(3)	7544(3)	7531(1)	9(1)
N(3)	7910(17)	7304(18)	8583(8)	16(3)
N(1)	5801(18)	8448(17)	7630(8)	13(3)
N(5)	10031(16)	6591(15)	7798(7)	6(2)
N(6)	6880(20)	5520(20)	7243(10)	20(3)
N(9)	8703(19)	9640(18)	7478(9)	15(3)
N(8)	7736(18)	7760(20)	6484(8)	17(3)
N(7)	6590(20)	5378(19)	6426(9)	19(3)
C(11)	11270(20)	6040(19)	7486(9)	10(3)
N(2)	5450(20)	8530(20)	8371(9)	21(3)
C(5)	6580(19)	7770(20)	9670(9)	14(3)
N(11)	7750(20)	7080(20)	10095(10)	27(4)
C(4)	6600(30)	7880(20)	8911(12)	28(5)
C(13)	5540(30)	3330(30)	6830(12)	27(4)
C(12)	6220(30)	4240(30)	7473(14)	32(5)
C(19)	8240(20)	9100(20)	6175(10)	13(3)
C(3)	4130(30)	9370(30)	8466(13)	29(5)
C(8)	9180(20)	6710(20)	9005(11)	18(4)
F(3)	8552(14)	3356(14)	9028(6)	21(2)
F(2)	7154(17)	1263(17)	9378(8)	34(3)
F(1)	5897(19)	3637(18)	9165(9)	41(4)

F(4)	7623(19)	3264(19)	10171(8)	41(3)
C(7)	9140(20)	6580(20)	9739(11)	20(4)
B(1)	7270(30)	2850(30)	9419(13)	25(5)
N(10)	8897(19)	10112(19)	6741(9)	17(3)
C(2)	3420(20)	9720(20)	7686(11)	18(4)
C(10)	12460(30)	5490(20)	8074(12)	25(4)
C(20)	9490(20)	11620(20)	6718(11)	18(4)
N(4)	10301(19)	6303(19)	8552(9)	17(3)
C(21)	9760(20)	12110(20)	7473(11)	22(4)
C(9)	11670(30)	5620(20)	8708(12)	22(4)
C(14)	5780(20)	4130(20)	6207(11)	19(4)
C(1)	4510(20)	9160(20)	7265(11)	19(4)
N(17)	7556(18)	8153(18)	4950(8)	12(3)
C(15)	7130(30)	6650(30)	6020(12)	24(4)
C(18)	8190(30)	9240(30)	5420(12)	25(4)
C(16)	7070(30)	6820(20)	5265(12)	23(4)
C(22)	9330(30)	10850(20)	7877(12)	24(4)
F(5)	1874(19)	9496(18)	5945(8)	39(3)
F(6)	3880(20)	8140(20)	5565(10)	52(4)
F(7)	1450(30)	6880(30)	5814(13)	78(6)
B(2)	2200(30)	8200(30)	5524(15)	27(5)
F(8)	1573(19)	8326(19)	4782(9)	42(4)

Table 12.2: Selected bond lengths [Å] and angles [°].

Fe(1)-N(8)	1.894(15)	N(3)-Fe(1)-N(1)	82.3(6)
Fe(1)-N(3)	1.912(15)	N(9)-Fe(1)-N(1)	88.0(6)
Fe(1)-N(9)	1.931(16)	N(8)-Fe(1)-N(6)	80.8(7)
Fe(1)-N(1)	1.939(15)	N(3)-Fe(1)-N(6)	97.4(7)
Fe(1)-N(6)	1.969(17)	N(9)-Fe(1)-N(6)	161.7(7)
Fe(1)-N(5)	1.996(13)	N(1)-Fe(1)-N(6)	90.7(7)
		N(8)-Fe(1)-N(5)	104.0(6)
N(8)-Fe(1)-N(3)	177.1(7)	N(3)-Fe(1)-N(5)	78.4(6)
N(8)-Fe(1)-N(9)	81.1(7)	N(9)-Fe(1)-N(5)	94.1(6)
N(3)-Fe(1)-N(9)	100.5(7)	N(1)-Fe(1)-N(5)	160.7(6)
N(8)-Fe(1)-N(1)	95.3(7)	N(6)-Fe(1)-N(5)	93.1(6)

Symmetry transformations used to generate equivalent atoms:

B. Courses, Seminars and Conferences attended

B.1 Courses

ISIS Neutron Training Course, 19th to 28th October 2001

Introduction to Structural Biology, Prof. Garry Taylor, University of Durham, 22nd January 2003

9th BCA Intensive Teaching School in X-ray Structure Analysis, 7th to 15th April 2003

34th Erice International School of Crystallography; High Pressure Crystallography, 4th to 15th 2003

8th Oxford School on Neutron Scattering, 8th to 18th September 2003

B.2 Seminars

2001

17th October: Dr P. Knowles, *Gauss-Poisson density representations for large-scale electronic structure computation*

24th October: Prof. B. Denning, *Photonic Crystals*

31st October: Dr Colin Raston, *Towards Benign Supramolecular Chemistry. Synthesis – self organisation.*

8th November: Dr. Sergi Kozhushkov; *Selected Chapters in Political Organic Chemistry: Fascinating Artificial Cyclopropane Architectures*

6th November: Dr. C. Ludman, *The Chemistry of Explosives*

5th December: Dr. Mike Eaton, *Drugs of the Future?*

2002

22nd January: Dr. Ian Fallis, *Size is Everything*

23rd January: Dr. W. Huck, *Control over polymeric materials at a submicron level*

29th January: Dr. Paul Monk, *Ozone; the good the bad and the ugly*

30th January: Dr. Peter Hore; *Chemistry in a spin: the effects of magnetic fields on chemical reactions*

31st January: Prof. Peter Day, *Some supramolecular chemistry of magnets and superconductors*

7th May: Kenneth Harris, *Understanding the properties of molecular solids; structure, dynamics and applied aspects*

8th May: Prof. Paul Madden, *“Covalent” effects in “Ionic” systems*

13th June: Dr. Garry McIntyre, *Single crystal neutron diffraction at the ILL: Science and facilities*

22nd July 2002: Dr. G. I. Nikonov, , *New types of nonclassical interligand H-Si interactions in transition metal hydrides*

2nd October 2002: Prof. Gideon Davies, *Structural enzymology of glycosyl transfer,*

10th October 2002: Prof. Jack Dunitz , *Are crystal structures predictable?*

15th October 2002: Prof. Mike Zawarotko, *Self assembly of crystals and nanocrystals: crystal engineering of nanoscale structures*

6th November 2002 : Prof. Steve Perkins, *Modelling large uncrystallisable protein structures using X-ray and neutron scattering*

2003

12th February 2003: Prof. Paul Raithby, *Adventures in Organometallic Polymer Chemistry*

21st March 2003 Prof. Patrick M. Woodward, *Manipulating the electronic structure of semiconducting metal oxides*

28th November 2003: Prof. Yu Wang, *Charge density studies of 3d transition metal complexes*

2004

18th February 2004, Prof. John Waltho, *Protein Folding and Misfolding from an NMR perspective*

25th February 2004, Prof. Robin Clarke, *Raman Spectroscopy a powerful technique for Inorganic Chemistry - surface analysis and pigment studies*

B.3 Conferences

BCA CCG Autumn meeting, Aston University, 14th November 2001

BCA Spring meeting, University of Nottingham, 25th to 28th March, 2002

19th Congress and General Assembly of the IUCr, Geneva, 6th to 15th August 2002

BCA CCG Autumn meeting, Kings College London, 13th November 2002

BCA Spring meeting, University of York, 15th to 17th April 2003

BCA Young Crystallographers Satellite Meeting, UMIST, 5th April 2004

BCA Spring meeting, UMIST, 6th to 8th April 2004

C. Publications

- 1. An iron(II) spin-crossover complex: a variable temperature crystallographic study**
V. A. Money, I. R. Evans, J. A. K. Howard, A. E. Goeta and M. A. Halcrow, *Acta Cryst.*, (2002) A58 (Supplement), C129
- 2. Light induced excited high spin state trapping in $[\text{FeL}_2](\text{BF}_4)_2$ (L = 2,6-di(pyrazol-1-yl)pyridine)**
V. A. Money, I. R. Evans, M. A. Halcrow, A. E. Goeta, and J. A. K. Howard, *Chem. Commun.*, 2003, 158
- 3. The spin-states and spin-crossover behaviour of iron(II) complexes of 2,6-dipyrazol-1-ylpyrazine derivatives**
J. Elhaïk, V. A. Money, S. A. Barrett, C. A. Kilner, I. R. Evans and M. A. Halcrow, *Dalton Discussion*, 2003, 2053
- 4. A study of the thermal and light induced spin transition in $[\text{FeL}_2](\text{BF}_4)_2$ and $[\text{FeL}_2](\text{ClO}_4)_2$ L = 2,6-di(3-methylpyrazol-1-yl)pyrazine**
V. A. Money, J. Elhaïk, M. A. Halcrow and J. A. K. Howard, *Dalton Trans.* 2004, 65
- 5. Crystal structure and unit cell variation with temperature of an iron(II) spin crossover complex determined from powder X-ray diffraction data**
V. A. Money, I. R. Evans, J. Elhaïk, M. A. Halcrow and J. A. K. Howard, *Acta Cryst.* B60, 41-45
- 6. The thermal and light induced spin transition in $[\text{FeL}_2](\text{BF}_4)_2$ (L = 2,6-dipyrazol-1-yl-4-hydroxymethylpyridine)**
V. A. Money, J. Elhaïk, M. A. Halcrow and J. A. K. Howard, *Dalton Trans.*, 2004, 1516-1518
- 7. A photomagnetic study of three iron (II) compounds containing ligands from the 2,6-di(pyrazol-1-yl)pyridine series**
V. A. Money, J. Sánchez Costa, S. Marcén, G. Chastanet, J. Elhaïk, M. A. Halcrow, J. A. K. Howard and J-F. Létard, *Chem. Phys. Lett.*, 391 (2004), 273-277
- 8. Structural Studies of Thermal and Light Induced Transitions in Iron(II) Spin Crossover Complexes**
A. L. Thompson, V. A. Money, A. E. Goeta and J. A. K. Howard, *C. R. Chimie*, in press

